UNIVERSITE D'AIX-MARSEILLE

ECOLE DOCTORALE 352 : Physique et Science de la matière

DEN, CEA Cadarache, DEC/SESC/LM2C

Thèse présentée pour obtenir le grade universitaire de docteur

Discipline : Physique et Sciences de la matière
Spécialité : Matière condensée et Nanosciences

Ibrahim CHEIK NJIFON

Modélisation des modifications structurales, électroniques et thermodynamiques induites par les défauts ponctuels dans les oxydes mixtes à base d'actinides $(U,Pu)O_2$

Soutenue le 06/11/2018 devant le jury :

Pär Olsson	Professeur KTH	Rapporteur
Fabien Bruneval	Chercheur CEA	Rapporteur
David Andersson	Chercheur LANL	Examinateur
Christine Guéneau	Chercheur CEA	Examinateur
Philippe Maugis	Professeur AMU	Examinateur
Roland Hayn	Professeur AMU	Directeur de thèse
Michel Freyss	Chercheur CEA	Co-Directeur de thèse

Résumé

(U,Pu)O_2 (aussi appelé MOX) est actuellement utilisé comme combustible dans les réacteurs nucléaires à eau pressurisée (REP) avec une teneur massique en Pu d'environ 10 %. Il est également envisagé comme combustible de référence pour les réacteurs à neutrons rapides à caloporteur sodium (RNR-Na), avec une teneur massique en Pu d'environ 25 %. En conditions opérationnelles, (U,Pu)O_2 est soumis à des réactions de fission qui génèrent une grande quantité de défauts et de produits de fission de diverse nature. Par migration, ces défauts et produits de fission gazeux peuvent s'agréger en nano-cavités, en dislocations et en bulles de gaz de fission, conduisant à une modification de la microstructure. Une meilleure description du comportement du combustible à l'échelle atomique, notamment des mécanismes élémentaires impliqués dans la diffusion des défauts et des produits de fission, est donc nécessaire pour affiner les modèles utilisés dans les codes de performance des combustibles utilisés pour simuler le comportement des combustibles à l'échelle macroscopique. Pour l'étude des propriétés de (U,Pu)O_2, nous avons effectué des calculs de structure électronique basés sur la méthode DFT+*U* combinée au contrôle des matrices d'occupation (OMC) des orbitales corrélées. Des minimisations d'énergie (calculs statiques) ainsi que la dynamique moléculaire ab initio ont été utilisées. Nous avons étudié dans un premier temps les propriétés du cristal (structurales, électroniques et thermodynamiques) de (U,Pu)O_2 pour différentes teneurs en Pu. Nous avons ensuite étudié la stabilité des défauts ponctuels ainsi que les modifications structurales et électroniques induites par ces défauts ponctuels dans (U,Pu)O_2 et (U,Ce)O_2, matériau utilisé comme simulant de (U,Pu)O_2. Enfin, nous avons étudié le piégeage et la solubilité des gaz de fission (Kr, Xe) et de l'hélium (He) dans la matrice de (U,Pu)O_2.

Mots clés : (U, Pu)O_2, calculs de structure électronique, DFT+*U*, dynamique moléculaire *ab initio*, thermodynamique, défauts ponctuels, gaz de fission, diffusion.

Abstract

$(U,Pu)O_2$ (commonly called MOX) is currently used as nuclear fuel in pressurized water reactors with a Pu content of around 10 wt.%, and is envisaged as the reference fuel in Generation IV sodium fast reactors (SFR) with a Pu content of around 25 wt.%. Under operation, $(U,Pu)O_2$ is submitted to fission reactions which generate a large quantity and variety of point defects, as well as fission products. By migrating, point defects and gaseous fission products can aggregate into nano-voids, dislocations and fission gas bubbles, which lead to the modification of the fuel microstructure. Therefore, a better description of the fuel behaviour at the atomic scale, and especially of the elementary mechanisms involved in the diffusion of point defects and fission products, is necessary to refine the models used in the fuel performance codes used to simulate the behaviour of fuels at the macroscopic scale. We use electronic structure calculations based on the DFT+*U* method combined with the occupation matrix control scheme (OMC) to investigate $(U,Pu)O_2$ properties for various Pu contents. Static energy minimizations and *ab initio* molecular dynamics were used. We have first determined bulk structural, electronic and thermodynamics properties of $(U,Pu)O_2$. We then studied the stability of point defects in $(U,Pu)O_2$ and $(U,Ce)O_2$, as well as the structural and electronic modifications induced by these point defects, in $(U,Pu)O_2$ and the common experimental surrogate $(U,Ce)O_2$. Finally, the fission gas (Kr and Xe) and helium (He) trapping and solubility in $(U,Pu)O_2$ matrix are investigated.

Keywords : $(U,Pu)O_2$, electronic structure calculations, DFT+*U*, *ab initio* molecular dynamics, thermodynamics, point defects, fission gases, diffusion.

Acknowledgements

I will first like to acknowledge DEN (Direction de l'Énergie Nucléaire), DEC (Département d'Étude des Combustibles), SESC (Service d'Etudes et de Simulation du Comportement des Combustibles), RCOMB project and INSPYRE European project, for their support and for giving me the opportunity to pursue a PhD. I also acknowledge LM2C (Laboratoire de Modélisation Multi-échelle des Combustibles), all their members for the scientific and friendly environment they offered me during my PhD.

I thank Michel Freyss, the co-director and the main supervisor of my PhD thesis at CEA of Cadarache. With you I have learnt and improved a lot of things necessary for my PhD study, especially the papers and reports writing, presentations, etc. You have also allowed me to improve my scientific rigor. You were always available when I was in need. You gave me a lot of advices relative to the preparation of scientific documents, how to anticipate the deadlines, etc., and this since the first day of my PhD internship. I have really appreciate this experience of working with you, it was a real pleasure. Thanks Michel.

I thank Roland Hayn, the director of my PhD thesis at IM2NP (Institut Matériaux Microélectroniques Nanosciences de Provence). You were always available for any question I had and have invested yourself in this work. You have helped me to discuss the results. You have also guided my way of analyzing the scientific results. I have appreciated all our meetings and the welcome you provided me at IM2NP.

I thank Marjorie Bertolus, my another supervisor at CEA of Cadarache. You have invested heavilly in this work, especially through many advices about the preparation of scientific documents, presentations, interpretation of results, etc. I have really appreciated your involvement and it was a pleasure to work closely with you.

I thank Gérald Jomard, the head of the SESC/LM2C laboratory. You have welcomed me and have given me many advices and also helped me in writing scientific reports and in preparing presentations. I have greatly appreciated working in your laboratory and in particular with you.

I thank my parents, my father Njifon Chouaibou and my mother Mfangam Zénabou, for having encouraged me in doing a PhD. I dedicate this work to you. You have supported me since the beginning and were an indispensable psychological lever during the difficult moments. I also associate to this acknowledgement my sisters and brothers who have also encouraged my decision of doing a PhD. We have always been so close to our hearts.

I finally thank my PhD colleagues at CEA Cadarache with whom I have spent a fantastic time during these 3 years. We lunched, played football, hiked, swam, played laser games and pintball, went canoeing and bowling together. Thank you for all these fantastic moments which have made the CEA an unforgettable institution for me.

Table of contents

Annex

Résumé étendu

L'oxyde mixte d'uranium et de plutonium $(U,Pu)O_2$ revêt un intérêt industriel majeur, notamment dans la production de l'énergie nucléaire. En effet, $(U,Pu)O_2$ est utilisé comme combustible dans les réacteurs à eau pressurisée (REP) avec une teneur en plutonium d'environ 10 %. Il est également envisagé comme combustible de référence dans les réacteurs à neutrons rapides à caloporteur sodium, dits de quatrième génération (GEN IV), avec une teneur accrue en plutonium (environ 25 %). La conception et la qualification de l'élément combustible à base d'$(U,Pu)O_2$ en vue de l'utilisation dans les réacteurs GEN IV nécessitent une bonne connaissance des propriétés matériaux de ce composé, ainsi que l'évolution de ces dernières sous irradiation. En conditions opérationnelles (sous irradiation aux neutrons dans le réacteur), les noyaux fissiles tels que l'^{235}U, le ^{239}Pu et le ^{241}Pu peuvent capturer un neutron et, par réaction de fission, se diviser en deux fragments appelés produits de fission, avec chacun une énergie comprise entre 65 MeV et 95 MeV. La décélération des fragments de fission se fait à travers les excitations électroniques ou par des chocs balistiques avec d'autres atomes du combustible. En particulier, les chocs balistiques engendrent des déplacements atomiques dans la matrice de l'oxyde mixte, conduisant à la création d'une large variété et quantité de défauts ponctuels. Par ailleurs, les défauts ponctuels peuvent être présent dans le combustible MOX $(U,Pu)O_2$ avant l'irradiation pour l'accommodation des déviations à la stœchiométrie. En effet, lors de la fabrication du combustible, la sous-stœchiométrie est introduite volontairement dans le combustible pour des raisons de sûreté. Les défauts ainsi présents dans le combustible vont, sous l'effet de la température et de l'irradiation, s'agréger en nano-cavités ou dislocations par diffusion atomique. Cette diffusion peut se faire via divers mécanismes élémentaires. Ces nano-cavités et dislocations vont fortement influencer la formation des bulles de gaz de fission ainsi que leur relâchement hors de la matrice du combustible. En effet, la plupart des produits de fission ayant une masse comprise entre 75 et 155 u.m.a sont gazeux ou volatiles. Les éléments gazeux sont par exemple le krypton (^{83}Kr, ^{84}Kr, ^{85}Kr et ^{86}Kr) et le xénon (^{129}Xe, ^{131}Xe, ^{132}Xe, ^{134}Xe and ^{136}Xe). L'hélium est aussi produit dans le matériau par émissions α ou fissions ternaire.

La présence des défauts ponctuels et les gaz de fission, leur migration et agrégation en nano-cavités ou dislocations (pour des défauts) ou en bulles (pour les gaz) ainsi que le relâchement des gaz de fission ont un impact important sur l'évolution des propriétés du combustible sous irradiation. On peut citer par exemple la décroissance de la conductivité thermique due aux interactions phonon-défauts; la croissance des grains et le fluage qui sont gouvernés entre autres par la diffusion atomique; et enfin le gonflement du combustible qui est lié à la rétention et le relâchement des gaz de fission. Au regard de tous ces changements, la problématique des défauts ponctuels et des gaz de fission est cruciale pour la conception et la qualification des combustibles tels que l'$(U,Pu)O_2$.

La description du comportement du combustible sous irradiation est rendu très complexe par le nombre important de phénomènes impliqués ainsi que des couplages complexes entre ces divers phénomènes. Au CEA, les études fondamentales visant à

décrire le comportement des défauts et des gaz de fission sont conduites au moyen des examens post-irradiation, des expériences à effets séparés ou de la modélisation à différentes échelles de temps et de longueur. Pour ce qui est des expériences à effets séparés, nous pouvons citer entre autres les implantations et irradiations aux ions qui permettent d'analyser la création des défauts ainsi que le piégeage et le relâchement des gaz de fission. La microscopie électronique à transmission (MET) ou à balayage (MEB) sont utilisées pour la caractérisation des défauts étendus, notamment les dislocations (vecteur de Burgers, plan de glissement et d'habitation) [1], et la porosité (géométrie et concentration des pores). La spectroscopie d'annihilation de positons (SAP) est également utilisée pour identifier la présence des lacunes dans le matériau. Lorsque la SAP est couplée aux calculs de structure électronique, la nature des lacunes qui sont présentes dans le matériau peut être révélée [2]. Enfin, la spectroscopie d'absorption X (SAX) est aussi utilisée pour sonder la structure électronique et l'environnement local des espèces chimique, pour déterminer notamment, la nature des défauts dans lesquels les produits de fission sont incorporés. Ces expériences sont couplées aux travaux de modélisation menés au DEC/SESC à différentes échelles. Les codes de performance ALCYONE et GERMINAL permettent, par exemple, de simuler le comportement des pastilles combustible des REPs et des RNRs, tel qu'entre autre les interactions pastille-gaine, le comportement des produits de fission, etc…. A l'échelle mésoscopique, les codes, tel que MARGARET [3], sont utilisés pour décrire le comportement des bulles de gaz de fission ; le modèle thermodynamique CALPHAD (CALculation of PHAse Diagram) permet de calculer les données thermodynamiques du combustible [4]. Ce dernier modèle est alimenté par les données issues soit de la modélisation atomistique ou des expériences à effets séparés. A l'échelle atomique, la dynamique moléculaire et le Monte Carlo moléculaire utilisant les potentiels interatomiques empiriques permettent de calculer les propriétés thermodynamiques ainsi que l'évolution des dégâts d'irradiation en fonction du temps et de la température à la même échelle. Les calculs de structure électronique permettent d'étudier avec une précision accrue, les mécanismes élémentaires précurseurs de l'évolution des propriétés du combustible sous irradiation. Ces mécanismes sont, par exemple, le transport atomique, la stabilité des défauts ponctuels, le piégeage des produits de fission par les défauts ponctuels ainsi que leur migration dans la matrice du combustible. Les calculs de structure électronique utilisent principalement les codes tels que VASP (Vienna *ab initio* simulation package) [5–7] et ABINIT [8].

Les calculs de structure électronique occupent une place importante dans la modélisation multi-échelle des combustibles nucléaires. En effet, en plus de fournir les données fiables aux modèles aux échelles supérieures, tels que ceux utilisant les potentiels interatomiques empiriques, la dynamique d'amas et le modèle DICTRA, les calculs de structure électronique constituent un appui aux expériences à effets séparés (SAP et SAX, par exemple), notamment pour l'interprétation des résultats. En outre, il est difficile jusqu'à présent de déterminer expérimentalement les énergies d'incorporation et de solution des gaz de fission dans le combustible. Ce travail est donc

dévolu aux calculs de structure électronique et constitue une étape indispensable pour l'interprétation des expériences, notamment l'identification des pièges et des mécanismes de diffusion des gaz de fission. Le lien entre les calculs de structure électronique et les modèles aux échelles supérieures [9], d'une part, et entre les calculs de structure électronique et les expériences à effets séparés [2, 10, 11] d'autre part, a été récemment amélioré pour UO_2 dans le cadre du projet européen F-BRIDGE (2008-2012). Des études similaires sont en cours sur l'oxyde mixte $(U,Pu)O_2$ dans le cadre du projet européen INSPYRE (2017-2021) et cette thèse s'inscrit dans ce projet.

Dans ce travail de thèse, nous utilisons le calcul de structure électronique basé sur la théorie de la fonctionnelle de la densité (DFT), pour l'étude des propriétés des dégâts d'irradiation dans l'oxyde mixte $(U,Pu)O_2$, en particulier les défauts ponctuels. Ce type d'étude a connu un essor favorable depuis les années 2000 sur l'oxyde d'uranium UO_2. L'ajout d'un terme *U* de type Hubbard à la fonctionnelle DFT standard (méthode DFT+*U*) permet de traiter les fortes corrélations électroniques des électrons *5f* des actinides. D'une part, bien que de nombreuses études DFT+*U* existent sur les défauts et le piégeage et migration des gaz de fission dans UO_2, il n'existe à notre connaissance pas d'étude de ce genre dans les oxydes mixte d'uranium et de plutonium. D'autre part, la DFT+*U* utilisant les fonctionnelles standards GGA ou LDA pour décrire les interactions d'échange et de corrélation ne prend pas en compte les corrélations non locales de type van der Waals. Les méthodes récemment développées telles que la vdW-DF (van der Waals Density Functional) [12, 13] et implémentées dans les codes de calcul de structure électronique, permettent de prendre en compte ces corrélations non locales.

Cette thèse a donc pour objectif d'utiliser la DFT+*U* et la vdW-DF pour étudier :

- Les propriétés matériaux du cristal parfait $(U,Pu)O_2$ à 0 K et à température finie. Les propriétés structurales électroniques, élastiques, énergétiques sont calculées à 0 K. Les propriétés thermodynamiques, quant à elles, sont calculées pour diverses températures au moyen de la dynamique moléculaire *ab initio* (DM *ab initio*).

- Les propriétés des défauts ponctuels, notamment les énergies de formation. Les modifications structurales et électroniques induites par la création des défauts sont analysées dans un second temps dans $(U,Pu)O_2$.

- Dans un troisième temps, les énergies de formation ainsi que les modifications structurales et électroniques induites par la création des défauts ponctuels sont analysées dans $(U,Ce)O_2$. Ce matériau est, en effet, couramment utilisé expérimentalement comme simulant de $(U,Pu)O_2$. Le but ici est de comparer les propriétés des dégâts d'irradiation dans ces deux composés.

- Enfin, une étude du comportement des gaz de fission krypton et xénon mais aussi de l'hélium, notamment leur piégeage dans les défauts de Schottky dans $(U,Pu)O_2$, est menée dans ce manuscrit. On s'est également intéressé aux

modifications structurales induites dans la matrice de $(U,Pu)O_2$ par l'incorporation des ces atomes gazeux.

Toutes ces thématiques sont regroupées en quatre chapitres respectivement, après un chapitre sur l'état de l'art sur $(U,Pu)O_2$ et un autre sur l'approche méthodologique. Il apparait ainsi clairement que le but ultime de ce travail est d'améliorer la compréhension du comportement du combustible MOX $(U,Pu)O_2$ sous irradiation. Les résultats obtenus de ce travail sont résumés dans les paragraphes ci-dessous.

Dans le chapitre (chapitre 3) dédié à l'étude des propriétés matériaux du cristal parfait $(U,Pu)O_2$ à température finie, nous avons d'abord montré l'efficacité de la méthode DFT+*U* dans la description de $(U,Pu)O_2$ pour les propriétés connues expérimentalement. Cela a permis de prédire de façon fiable par la suite les propriétés encore non connues expérimentalement. Parallèlement, nous avons analysé l'effet de la teneur en plutonium sur les propriétés étudiées. Pour les propriétés structurales, nous avons obtenu une évolution linéaire du paramètre de maille en fonction de la teneur en Pu (loi de Vegard [14]). En ce qui concerne les propriétés électroniques, nous avons prédit un caractère d'isolant de Mott pour $(U,Pu)O_2$, avec un rétrécissement de la bande interdite dans $(U,Pu)O_2$ comparé à ceux dans les oxydes purs UO_2 et PuO_2. Ce rétrécissement est expliqué par le décalage des densités d'états électroniques des orbitales *5f* du Pu en raison de son hybridation aux orbitales *2p* de l'oxygène. Ensuite, nous avons prédit les constantes élastiques de $(U,Pu)O_2$ pour différentes teneurs en Pu. Un autre sujet important abordé dans cette première partie est la prédiction des propriétés énergétiques de $(U,Pu)O_2$, telles que l'enthalpie de formation et l'enthalpie de mélange pour toutes les teneurs en Pu. L'enthalpie de formation des oxydes purs UO_2, PuO_2 et Pu_2O_3, dont des mesures expérimentales sont disponibles, ont été calculées avec une excellente précision. En particulier, lorsque l'on prend en compte les corrélations non locales à travers la vdW-DF, l'erreur relative sur l'enthalpie de formation devient inférieure à 0,4 % comparée aux valeurs expérimentales. Cela témoigne de la fiabilité de nos résultats. En ce qui concerne l'enthalpie de mélange de $(U,Pu)O_2$, nous avons trouvé des valeurs négatives sur toute la gamme de teneur en Pu. Ce résultat confirme que $(U,Pu)O_2$ forme une solution solide.

Le dernier aspect de ce chapitre porte sur le calcul des propriétés thermodynamiques à température finie en utilisant la DM *ab initio*. Dans un premier temps, nous avons analysé les fonctions de distribution radiale (RDF) des sous-réseaux oxygène et actinide de la structure fluorine de UO_2 et $(U, Pu)O_2$ à différentes températures, jusqu'à 2600 K. On observe pour $(U, Pu)O_2$ que la RDF du sous-réseau oxygène garde un caractère solide jusqu'à la température de 2100 K. Lorsqu'on passe à 2600 K, la RDF adopte un caractère liquide, traduisant ainsi la fusion du sous-réseau oxygène à cette température. De cette observation, on peut conclure que la fusion du sous-réseau oxygène débute à une température comprise entre 2100 K et 2600 K. Ce début de fusion du sous-réseau oxygène est la transition super-ionique ou transition de Bredig. Elle est en général observée à une température d'environ $0.8T_f$, où T_f est la température de fusion du

composé. Pour le sous-réseau actinide, jusqu'à la température de 2600 K, le caractère solide est toujours maintenu. Cela indique que la température de fusion de (U, Pu)O_2 n'est pas encore atteinte. La dilatation thermique linéaire de UO_2 et (U,Pu)O_2 à différentes teneurs en Pu a également été calculée pour des températures allant jusqu'à 2000 K. Nos résultats ont ensuite été comparés à la recommandation expérimentale de D. G. Martin [15] actuellement utilisée dans les codes de performance ALCYONE et GERMINAL. Nous avons obtenu un bon accord entre nos résultats et la recommandation jusqu'à la température de 1000 K. Au-delà de 1000 K, nos résultats sont supérieurs aux valeurs de la recommandation, mais restent dans la marge des incertitudes sur la recommandation. Par ailleurs, les valeurs élevées par rapport à la recommandation de D. G. Martin sont en accord avec des récentes mesures de la dilatation thermique de UO_2 [16]. Les résultats sur la variation d'enthalpie montrent aussi un très bon accord avec les recommandations expérimentales de Fink [17] pour UO_2 et (U, Pu)O_2. Pour (U, Pu)O_2 en particulier, on note une légère augmentation de la variation d'enthalpie par rapport à celle de UO_2 pour les températures supérieures à 1300 K. Enfin, la capacité calorifique de UO_2 et de (U, Pu)O_2 a été analysée pour des températures allant jusqu'à 2000 K. Les résultats ont également été confrontés aux recommandations expérimentales de Fink [17] pour UO_2 et PuO_2 ainsi qu'aux calculs CALPHAD. Nos résultats obtenus en DM *ab initio* présentent un bon accord avec les recommandations expérimentales et les calculs CALPHAD jusqu'à une température de l'ordre de 1600 K. À partir de cette température, l'augmentation rapide de la capacité calorifique avec la température n'est pas observée sur nos valeurs. Cette croissance rapide est liée à la création des paires de Frenkel dans le matériau. Son absence suggère donc que nos temps de simulation ne sont pas assez longs pour que ce phénomène de création des paires de Frenkel se produise. En définitive, tous ces résultats sur les propriétés du cristal parfait d'(U, Pu)O_2, notamment leur accord avec l'expérience et les résultats de modélisation aux échelles supérieures, illustrent la maturité des calculs de structure électronique ainsi que de la DM *ab initio* pour la description des propriétés en température finie des oxydes d'actinides. Etant donné la transférabilité de ces méthodes, des futures études sont envisagées sur les oxydes mixtes d'actinides innovants et complexes, notamment (U, Pu, Am)O_2, pour lesquels les propriétés thermodynamiques sont manquantes.

Le chapitre suivant (chapitre 4) de cette étude est dédiée aux défauts ponctuels et au transport atomiques dans PuO_2 et (U,Pu)O_2. Nous avons dans un premier temps analysé les modifications électroniques et structurales induites par la création des défauts ponctuels dans (U, Pu)O_2 e PuO_2. On distingue dans (U, Pu)O_2 trois catégories de défauts ponctuels: les défauts à caractère réducteur tels que les lacunes d'oxygène (V_O) et les interstitiels actinide (I_M), les défauts à caractère oxydant tels que les interstitiels oxygène (I_O) et les lacunes d'actinide (V_M), et les défauts à caractère neutre tel que les défauts de Schottky (BSD). Cette étude a montré que la présence des défauts réducteurs neutres entraine la réduction de deux cations Pu^{4+} (pour V_O) ou de quatre cations Pu^{4+} (pour I_M) en cations Pu^{3+}, accompagné de l'introduction d'un état électronique occupé associé au défaut dans la bande interdite. Les cations Pu^{3+} et l'état électronique de la

bande interdite disparaissent lorsque le défaut réducteur est sous son état de charge formelle (V_O^{2+} ou I_M^{4+}). Cela correspond au retrait de deux ou de quatre électrons de la supercellule contenant le défaut. Pour les défauts oxydants, sous état de charge neutre, on observe pour (U, Pu)O_2 une oxydation de deux cations U^{4+} (pour I_O) ou de quatre cations U^{4+} (pour V_M) en cations U^{5+}. Dans ce cas, il n'y a pas d'état électronique dans la bande interdite. Par contre, lorsque les défauts oxydants sont sous charge formelle (I_O^{2-} ou V_M^{4-}), ce qui correspond à un ajout de deux ou quatre électrons, les cations U^{5+} disparaissent et on obtient un état électronique vide qui se crée sur l'état *5f* de l'uranium. Cet état électronique n'est pas présent dans la bande interdite parce qu'il se trouve à une énergie plus haute comparée à celle du bas de la bande de conduction constitué par des états *5f* de Pu. Dans le cas de PuO_2, un état électronique vide est observé dans la bande interdite dans le cas d'un défaut oxydant. En effet, comme les cations Pu^{4+} ne peuvent pas s'oxyder en Pu^{5+}, un état électronique vide se crée sur les états *2p* de l'atome d'oxygène interstitiel neutre. Lorsque le défaut oxydant de PuO_2 est sous charge formelle, l'état vide précédent se transforme en état électronique occupé dans la bande interdite. Quant aux défauts à caractère neutre (défauts de Schottky), il ne créent pas de modifications électroniques dans (U, Pu)O_2. La création des défauts induit aussi des modifications structurales, notamment une distorsion spécifique du réseau cristallin pour chaque type de défaut. Les distorsions du réseau sont mesurées en termes de déplacements atomiques. Les déplacements atomiques affectent principalement les atomes d'oxygène premiers voisins du défaut, lesquels se déplacent vers le défaut dans le cas de la lacune d'oxygène, ou s'éloignent du défaut dans le cas de l'interstitiel oxygène ou de la lacune actinide. Pour ce qui est de l'interstitiel actinide, on note plutôt des déplacements atomiques des actinides premiers voisins du défaut. Ces derniers s'éloignent de l'interstitiel actinide. Tous ces déplacements suscités sont isotropes et se font suivant les directions <100> pour la lacune d'oxygène et l'interstitiel actinide, et <111> pour l'interstitiel oxygène et la lacune actinide. Parallèlement, la présence des défauts réducteurs entraine une dilatation du cristal tandis que les défauts oxydants entrainent plutôt une contraction cristal. Pour ce qui est des défauts de Schottky, on note une distorsion plus complexe dans deux directions distinctes, donc anisotropique. Premièrement, les atomes d'oxygène premiers voisins de la lacune actinide du BSD sont repoussés loin cette dernière suivant la direction <111>. Ensuite, les atomes d'oxygène premiers voisins des lacunes d'oxygène sont repoussés vers les lacunes oxygène suivant la direction <100>.

Le deuxième aspect de ce chapitre sur les défauts porte sur les propriétés énergétiques des défauts ponctuels dans PuO_2 et (U,Pu)O_2. L'étude de la stabilité des défauts ponctuels dans PuO_2 sous différents états de charge, et en fonction du potentiel chimique de l'oxygène, montre deux domaines distincts : le domaine de sous-stœchiométrie pour les potentiels chimiques de l'oxygène inférieurs à -5,12 eV et le domaine de sur-stœchiométrie lorsque le potentiel chimique de l'oxygène est supérieur à -5,12 eV. Notons au passage que le potentiel chimique de l'oxygène de -5,12 eV correspond à la stœchiométrie, point où on trouve autant de lacunes d'oxygène que

d'interstitiels oxygène. Dans PuO_2, dans le domaine sous-stœchiométrique, la lacune d'oxygène est le défaut le plus stable, donc majoritaire, tandis que dans le domaine sur-stœchiométrique l'interstitiel oxygène devient le défaut le plus stable. Tous ces défauts sont plus stables sous leur état de charge formelle, traduisant la stabilité des cations Pu^{4+} en présence des défauts. Pour la stabilité des défauts ponctuels dans $(U,Pu)O_2$, nous avons d'abord étudié l'influence de l'environnement chimique (nombre de cations Pu premiers voisins) sur les défauts oxygène (V_O et I_O). On a ainsi montré que l'énergie de formation de la lacune d'oxygène décroit lorsque le nombre de cations Pu augmente dans l'environnement chimique tandis que celle de l'interstitiel oxygène augmente avec l'augmentation du nombre de cations Pu dans l'environnement chimique. L'étude de l'influence de la teneur en Pu, dans un second temps, a montré que l'énergie de formation de la lacune d'oxygène dans l'oxyde mixte $(U, Pu)O_2$ est plus petite que celle dans les oxydes purs UO_2 et PuO_2. On note également pour l'oxyde mixte une tendance décroissante de l'énergie de formation de la lacune d'oxygène avec l'augmentation de la teneur en Pu. Les énergies de formation de l'interstitiel oxygène sont très proches de celle dans UO_2 et largement inférieures à celle dans PuO_2. L'influence de la teneur en Pu sur la formation de l'interstitiel oxygène dans $(U,Pu)O_2$ est négligeable. Enfin, sur la stabilité des défauts, la stœchiométrie est obtenue pour le potentiel chimique oxygène de -6,38 eV. Dans le domaine sous-stœchiométrique (potentiel chimique oxygène inférieure à -6,38 eV), la lacune d'oxygène est le défaut le plus stable sous état de charge neutre, tandis que dans le domaine sur-stœchiométrique, l'interstitiel oxygène devient le défaut le plus stable sous état de charge formelle. Les états de charge stables traduisent le fait qu'en présence des défauts réducteurs, les cations stables dans $(U, Pu)O_2$ sont U^{4+}, Pu^{4+} et Pu^{3+}. Ce résultat est en accord avec les résultats expérimentaux obtenus en spectroscopie d'absorption X [18]. Pour ce qui est des défauts oxydants, les cations les plus stables en présence sont U^{4+} et Pu^{4+}. Notons que ces résultats sont obtenus pour le niveau de Fermi situé au milieu de la bande interdite. Quant aux défauts de Schottky, la configuration la plus stable est celle pour laquelle les deux lacunes d'oxygène du défaut sont placées dans la direction <110>. Nous l'avons noté BSD2 dans cette étude. Par ailleurs, les BSDs constitués des lacunes Pu sont plus stables que ceux constitués des lacunes U.

Enfin, le dernier aspect de ce chapitre est dédié aux propriétés de transport atomique, notamment la migration assistée par les défauts ponctuels, ainsi que les énergies d'activation de la diffusion des différentes espèces atomiques dans $(U, Pu)O_2$. Les barrières de migration sont obtenues à travers la méthode nudged elastic band (NEB). Les barrières de migration de la lacune d'oxygène sous différents états de charge ont montré que cette dernière migre plus facilement sous charge formelle plutôt que sous charge neutre. Pour l'interstitiel oxygène, deux mécanismes de migration ont été testés : le mécanisme direct et le mécanisme indirect (interstitialcy). Le mécanisme indirect est plus favorable à la migration de l'interstitiel oxygène et dans ce mécanisme, la charge formelle est privilégiée. Le calcul des énergies d'activation de l'auto-diffusion de l'oxygène suivant les mécanismes lacunaire et interstitiel en fonction du potentiel

chimique d'oxygène montre que l'auto-diffusion de l'oxygène est assistée par la lacune d'oxygène en condition sous-stœchiométrique. En condition sur-stœchiométrique, la diffusion de l'oxygène est assistée par l'interstitiel oxygène, suivant le mécanisme indirect. Pour les cations actinide, la migration des lacunes et interstitiels cationiques neutres est plus favorable que ceux sous état de charge formelle. Par ailleurs, lorsque la teneur en Pu augmente, l'énergie de migration des lacunes cationiques augmente tandis que l'impact sur les interstitiels cationiques reste négligeable. Globalement, les énergies d'activation de l'auto-diffusion des cations actinides montrent que ces derniers diffusent suivant un mécanisme lacunaire. Cependant, les énergies d'activation de la diffusion restent très grandes par rapport à celle de l'oxygène.

Les résultats de cette partie sur les défauts et le transport atomique sont très importants pour les méthodes de modélisation du combustible MOX aux échelles supérieures. D'une part, les résultats sur les modifications structurales induites par les défauts ponctuels ainsi que les énergies de formation des défauts vont servir de données de référence pour le développement des potentiels interatomiques empiriques, mais aussi aux potentiels numériques, pour l'étude des défauts chargés dans (U, Pu)O_2. D'autre part, les résultats de la migration et de la diffusion sont utilisés dans la base de données des modèles thermocinétiques, notamment le modèle CALPHAD/DICTRA pour le calcul des coefficients d'auto-diffusion des espèces atomiques dans (U, Pu)O_2. Comme perspectives, l'analyse de l'influence des amas de défauts sur les énergies de migration et d'activation de la diffusion serait une étape très importante et permettrait de consolider nos conclusions sur les mécanismes de diffusion des différentes espèces atomiques. Actuellement, ce type d'étude reste inenvisageable en DFT+*U*, mais pourrait être possible dans peu de temps, étant donné le développement rapide des ressources informatiques. Néanmoins, au CEA-SESC/LM2C, on envisage de conduire cette étude en utilisant des méthodes basées sur les potentiels interatomiques empiriques. Ces méthodes, bien que moins précises par rapport à la DFT, ont l'avantage d'être très peu coûteuses en ressources informatiques. On peut également envisager d'étendre notre étude à une analyse beaucoup plus précise de l'effet de l'environnement chimique sur la formation et la migration des défauts ponctuels, en considérant par exemple les cations de la seconde et de la troisième sphère de coordination, mais également de faire une statistique des environnements les plus favorables. Cela nécessite l'emploi des supercellules plus grandes, et donc des méthodes de calcul peu couteuses telles que les potentiels empiriques. Enfin, l'effet des actinides mineurs tel que l'américium sur la formation et la migration des défauts dans les combustibles MOX constitue également une perspective faisant suite à notre étude. En effet, les actinides mineurs tels que l'Am sont toujours présents, avec une teneur non-négligeable, dans les combustibles MOX des réacteurs rapides. Il est donc important d'étudier leur impact sur la formation et la migration des défauts dans le combustible.

Le chapitre suivant (chapitre 5) est consacrée à l'étude de la formation des défauts ponctuels dans les oxydes mixtes d'uranium et de cérium, ainsi que leurs impacts sur les propriétés structurales et électroniques. Une comparaison minutieuse a été faite entre

les résultats obtenus sur (U, Ce)O_2 et ceux obtenus sur (U, Pu)$_2$. Cette étude est motivée par le fait que (U, Ce)O_2 soit considéré expérimentalement comme simulant non radiotoxique de (U, Pu)O_2. Il ressort de notre étude que les défauts réducteurs sous état de charge neutre et formelle induisent qualitativement les mêmes modifications électroniques que dans (U, Pu)O_2, où les cations Pu ont le même comportement que les cations Ce. La différence quantitative entre les deux composés est celle de la faible énergie de l'état électronique du défaut neutre dans la densité d'états de (U, Ce)O_2, ce qui est différent de celui observé dans (U, Pu)O_2. Pour les défauts oxydants, lorsqu'ils sont sous état de charge neutre, les modifications électroniques induites dans (U, Ce)O_2 sont similaires à celles dans (U, Pu)O_2. Par contre, pour les états de charge formelle, on observe en même temps la présence d'un cation U^{5+} et Ce^{3+}, ainsi que la présence d'un état électronique occupé du défaut dans la bande interdite, ce qui est différent de ce qui est observé dans (U, Pu)O_2 dans lequel seul les cations U^{5+} et Pu^{4+} sont observés. On peut donc conclure globalement que les modifications électroniques induites par la formation des défauts ponctuelle dans (U, Ce)O_2 sont différentes de celles obtenues dans (U, Pu)O_2. En ce qui concerne les modifications structurales, on obtient qualitativement les mêmes déplacements atomiques et donc les mêmes distorsions du réseau en présence des défauts ponctuels dans (U, Ce)O_2 que celles dans (U, Pu)O_2. Cependant, les amplitudes des distorsions ainsi que l'ampleur de la dilatation ou de la contraction de la maille cristalline autour des différents défauts sont différentes. Cette différence est à considérer pour les propriétés structurales des deux composés.

Dans le deuxième aspect de ce chapitre 5, nous avons étudier la stabilité des défauts ponctuels dans (U, Ce)O_2 sous différents états de charge et différents potentiels chimiques d'oxygène. On montre que, pour une même valeur de potentiel chimique d'oxygène, l'énergie de formation de la lacune d'oxygène est plus petite dans (U, Ce)O_2 que dans (U, Pu)O_2. L'énergie de formation de l'interstitiel oxygène dans (U, Ce)O_2 reste similaire à celle dans (U, Pu)O_2 pour la même valeur du potentiel chimique d'oxygène. Par ailleurs, dans tout le domaine de potentiel chimique accessible pour (U, Ce)O_2, la lacune d'oxygène neutre reste le défaut le plus stable, donc majoritaire. Cela suggère la stabilité des cations U^{4+}, Ce^{4+} et Ce^{3+} en présence des défauts réducteurs. De plus, pour les potentiels chimiques d'oxygène supérieurs à -6,86 eV, les lacunes de cérium deviennent plus favorables que les interstitiels d'oxygène alors que les lacunes d'oxygène restent toujours les défauts majoritaires. Ce comportement est très différent de celui observé dans (U, Pu)O_2 où l'interstitiel oxygène devient le défaut majoritaire pour les potentiels chimiques d'oxygène supérieurs à -6,38 eV. Nous avons aussi obtenu la stabilité de la configuration BSD2 parmi les défauts de Schottky ainsi que celui constitué de lacune Ce. Cependant, les énergies de formations diffèrent de celles dans (U, Pu)O_2. En particulier, les BSDs comportant les lacunes Ce dans (U, Ce)O_2 ont une énergie plus basse que ceux constitués de lacunes Pu dans (U, Pu)O_2. Quant aux BSDs constitués de lacunes U, l'énergie de formation est plus élevée dans (U, Ce)O_2 que dans (U, Pu)O_2.

Cette partie met en exergue les différences notables entre (U, Ce)O_2 et (U, Pu)O_2 sur les propriétés énergétiques des défauts ponctuels, ainsi que sur les modifications électroniques et structurales induites par le formation de ces défauts. Cela suggère que ces deux composés auraient différents comportements sous irradiation. Pour davantage cerner les similitudes et les différences entre (U, Pu)O_2 et (U, Ce)O_2, des études à venir devront prendre en compte la contribution de la partie entropique sur la formation des défauts, ainsi que le transport atomique dans (U, Ce)O_2. La prise en compte de ces éléments va améliorer la compréhension de la diffusion atomique, et ainsi établir si la restructuration de (U, Pu)O_2 sous irradiation peut être efficacement simuler en utilisant (U, Ce)O_2.

Dans le dernière chapitre (chapitre 6) de cette thèse, nous nous somme intéressé au piégeage et à la solubilité des gaz de fission (Xe et Kr) ainsi que de l'hélium dans les défauts de Schottky dans (U, Pu)O_2. L'incorporation du krypton est favorable dans le défaut de Schottky de configuration BSD1 (lacunes d'oxygène dans la direction <100>) comportant une lacune d'uranium (BSD1_U). Pour l'incorporation du xénon, les défauts BSD1_U et BSD3_Pu sont les plus favorables. Dans la configuration BSD3, les lacunes d'oxygène du défaut sont alignées suivant la direction <111>. Pour l'incorporation de l'hélium, les défauts BSD2_U et BSD3_Pu sont les plus favorables. Les énergies de solution obtenues sont toutes positives et assez élevée. Cela traduit le fait que Kr, Xe et He sont très insoluble dans le cristal parfait de (U, Pu)O_2. Cette insolubilité augmente lorsque les interactions de van der Waals sont prises en compte. La comparaison de nos résultats avec les valeurs obtenues dans UO_2 montre que les énergies de solution de ces gaz dans (U, Pu)O_2 sont du même ordre de grandeur que celles dans UO_2.

Les études à venir devront considérer l'incorporation de plusieurs atomes de gaz dans les BSDs ou dans les défauts plus étendus, ainsi que la migration des atomes de gaz dans (U, Pu)O_2. Cela permettra par exemple de comprendre le mécanisme de formation des bulles de gaz ainsi que de leur relâchement.

Dans cette thèse, nous avons démontré l'amélioration du caractère prédictif des calculs de structure électroniques. L'avenir des calculs de structure électronique s'annonce prometteur, avec le développement des fonctionnelles (telles que la vdW-DF) et des méthodes (comme la DMFT) présentant une meilleure précision que celles couramment utilisées, mais aussi avec le développement rapide des ressources informatiques. Dans cette perspective, la DFT+*U* couplée à la dynamique moléculaire *ab initio* va assez rapidement étendre son domaine d'application à la modélisation des défauts étendus et des phénomènes liés à la température dans les oxydes d'actinides et d'autres matériaux complexes. En effet, avec ces avancées, les entropies de formation et de migration des défauts pourraient être directement calculées en utilisant la méthode DFT. Ainsi, les coefficients de diffusion et les données thermodynamiques seront accessibles plus rapidement. Les amas de défauts (nano-cavités, dislocations, amas de gaz de fission) pourraient aussi être analysés. Le calcul des propriétés thermodynamiques en DM *ab initio*, qui est jusqu'à présent limité par le manque de ressources informatiques, va

aboutir sur une avancée importante dans la prédiction ou l'affinement des diagrammes de phases des matériaux innovants. En d'autres termes, dans un futur proche, l'on pourra prendre en compte les effets de température et minimiser au mieux les effets de taille des supercellules. Il sera ainsi possible de mettre en place une procédure fiable, pour une prédiction détaillée et *ab initio* d'un nombre conséquent de phénomènes, en lien direct avec l'évolution des propriétés des combustibles nucléaires à l'échelle mésoscopique. On pourra donc mieux soutenir les expériences à effets séparés et mieux alimenter divers modèles de simulations des combustibles aux échelles plus grandes.

Références

[1] Onofri, C., Legros, M., Léchelle, J., Palancher, H., Baumier, C., Bachelet, C., and Sabathier, C. Full characterization of dislocations in ion-irradiated polycrystalline UO_2. *J. Nucl. Mater.* **494,** 252–259 (2017).

[2] Wiktor, J. *et al.* Coupled experimental and DFT+*U* investigation of positron lifetimes in UO_2. *Phys. Rev. B* **90,** 184101 (2014).

[3] Noirot, L. MARGARET: An Advanced Mechanistic Model of Fission Gas Behavior in Nuclear Fuel. *J. Nucl. Sci. Technol.* **43,** 1149–1160 (2006).

[4] Guéneau, C. *et al.* Thermodynamic modelling of advanced oxide and carbide nuclear fuels: Description of the U–Pu–O–C systems. *J. Nucl. Mater.* **419,** 145–167 (2011).

[5] Blöchl, P. E. Projector augmented-wave method. *Phys. Rev. B* **50,** 17953–17979 (1994).

[6] Kresse, G. and Hafner, J. *Ab* initio molecular dynamics of liquid metals. *Phys. Rev. B* **47,** 558–561 (1993).

[7] Kresse, G. and Furthmüller, J. Efficiency of ab-initio total energy calculations for metals and semiconductors using a plane-wave basis set. *Comput. Mater. Sci.* **6,** 15–50 (1996).

[8] Gonze, X. *et al.* First-principles computation of material properties: the ABINIT software project. *Comput. Mater. Sci.* **25,** 478–492 (2002).

[9] Bertolus, M. *et al.* Linking atomic and mesoscopic scales for the modelling of the transport properties of uranium dioxide under irradiation. *J. Nucl. Mater.* **462,** 475–495 (2015).

[10] Dorado, B. *et al.* First-principles calculation and experimental study of oxygen diffusion in uranium dioxide. *Phys. Rev. B* **83,** 035126 (2011).

[11] Bès, R. *et al.* Experimental evidence of Xe incorporation in Schottky defects in UO_2. *Appl. Phys. Lett.* **106,** 114102 (2015).

[12] Klimeš, J., Bowler, D. R. and Michaelides, A. Chemical accuracy for the van der Waals density functional. *J. Phys. Condens. Matter* **22,** 022201 (2010).

[13] Klimeš, J., Bowler, D. R. and Michaelides, A. Van der Waals density functionals applied to solids. *Phys. Rev. B* **83,** 195131 (2011).

[14] Vegard, L. Die Konstitution der Mischkristalle und die Raumfüllung der Atome. *Z. Für Phys.* **5,** 17–26 (1921).

[15] Martin, D. G. The thermal expansion of solid UO_2 and (U, Pu) mixed oxides — a review and recommendations. *J. Nucl. Mater.* **152,** 94–101 (1988).

[16] Guthrie, M. *et al.* Thermal expansion in UO_2 determined by high-energy X-ray diffraction. *J. Nucl. Mater.* **479,** 19–22 (2016).

[17] Fink, J. K. Enthalpy and heat capacity of the actinide oxides. *Int. J. Thermophys.* **3,** 165–200 (1982).

[18] Vigier, J.-F. *et al.* Structural Investigation of $(U_{0.7}Pu_{0.3})O_{2-x}$ Mixed Oxides. *Inorg. Chem.* **54,** 5358–5365 (2015).

General introduction

$(U,Pu)O_2$ is of first concern for technology applications, especially in the nuclear industry. It is used as fuel in pressurized water reactor (PWR) with a plutonium content around 10 wt.%, and is envisaged as reference fuel for generation IV (GEN IV) sodium fast reactors (SFR) with a plutonium content of around 25 wt.%. The design and qualification of the fuel elements for these new generation reactors are based on the fuel material properties and its behaviour under irradiation. Under operating conditions, the capture of a neutron by fissile nuclei such as ^{235}U, ^{239}Pu or ^{241}Pu results in their instability and their splitting into two fragments with energy ranging from 65 MeV to 95 MeV. Most of the fission fragments, commonly called fission products, for which atomic mass is between 75 and 155, are gaseous or volatile elements. The gaseous elements are in particular krypton (^{83}Kr, ^{84}Kr, ^{85}Kr and ^{86}Kr) and xenon (^{129}Xe, ^{131}Xe, ^{132}Xe, ^{134}Xe and ^{136}Xe). Helium gas is also produced in the material through α emission or ternary fissions. The deceleration of these fragments takes place through electronic excitation and their collision with other atoms. The atomic collisions especially generate atomic displacements in the material, resulting in the creation of a large variety and a large quantity of point defects under irradiation. Point defects can also be of importance in $(U,Pu)O_2$ MOX fuel before irradiation to accommodate the hypo-stoichiometry introduced intentionally during fuel fabrication for safety purposes. The point defects created can aggregate into dislocations or nano-cavities by means of atomic diffusion driven by various elementary mechanisms.

The presence of point defects, their migration and aggregation, as well as the presence of fission gases, their aggregation into bubbles and their release from $(U,Pu)O_2$ matrix, have an important impact on fuel properties, especially the decrease in thermal conductivity through phonon-defect scattering, microstructural evolutions such as the grain growth and creep, which are among other governed by atomic diffusion, and the fuel swelling which is linked to the fission gases retention and release in the fuel matrix. All these changes in the properties of fuel related to the point defects and fission gases make these topics crucial for the design and qualification of fuels.

The behaviour of fuel under operating condition is very complex owing to the number of phenomena involved and the complex link between the various phenomena. Fundamental studies carried out on nuclear oxide fuels at CEA/DEN aiming at describing the defects and fission gases behaviour are largely focused on post irradiation experiments (PIE), separate effect experiments and modelling at different time and length scales. Separate effect experiments include ion implantation and irradiation for the study of defect creation, fission gas trapping and release. The ion irradiation is then followed by detailed characterisation using a variety of techniques. Techniques such as tracer diffusion spectrometry, electrical conductivity and secondary ion mass spectrometry (SIMS) yield data such as diffusion coefficients of atomic species, including fission gases. Transmission electronic microscopy (TEM) and scanning electronic microscopy (SEM) analyses are used to characterise extended defects such as dislocations (Burgers vectors, habit/slip planes)[1], porosities (geometry and concentration). Positon annihilation spectroscopy (PAS) is used to identify the presence

of vacancies in the material. This latter technique coupled to atomic scale modelling can reveal the type of vacancies in the material [2]. Finally, X-ray absorption spectroscopy (XAS) is also used to probe the electronic structure and the local environment of chemical species, especially for the determination of the nature of defects in which fission products are incorporated. These experiments are coupled to modelling investigations conducted at DEC/SESC at different scales. At the scale of the fuel element, the ALCYONE and GERMINAL codes of the PLEIADES platform is used to model the behaviour of PWR and fast breeder reactors (FBR) fuel pin, among other the fuel-cladding interactions, fission gas behaviour, etc. At the mesoscopic scale, models such as MARGARET [3] are used to describe the behaviour of fission gas in the fuel pellet. Thermodynamic models, developed using the CALPHAD method, are also used to provide relevant data on thermodynamic and thermochemical quantities [4]. These models are fed by results of atomic scale modelling or experimental data. From the atomic scale to the mesoscopic scale, empirical potentials coupled to classical molecular dynamics allow the evaluation of the evolution of irradiation damage as a function of time and temperature. At the atomic scale, the commonly used codes for electronic structure calculations are the Vienna *ab initio* Simulation Package (VASP) [5–7] and ABINIT [8]. These codes constitute essential tools for the description of the elementary mechanisms involved in the evolution of fuel behaviour.

Electronic structure calculations play a significant role in the multi-scale modelling approach. They provide reliable data on structural and energetic properties for higher scale methods such as empirical potentials classical molecular dynamics [9], cluster dynamics, rate theory and other methods. Moreover, if the PAS experimental technique can give information on the presence of vacancy defects in the material, it is very difficult to identify the exact nature of the vacancies without the coupling to electronic structure calculations. In addition, it is difficult up to now to determine the incorporation and migration energies of fission products at the atomic scale, as well as the atomic and fission gas diffusion mechanisms, using experiments. These tasks are assigned to the electronic structure calculations and constitute an important challenge for the interpretation of experiments. The links were recently improved between the atomic scale modelling, especially the electronic structure calculations and the mesoscopic scale calculations [10] and between the electronic structure calculations and experiments [2, 11, 12] for UO_2 in the framework of the F-BRIDGE European project [13]. Similar studies are on-going for $(U,Pu)O_2$ mixed oxides in the framework of the INSPYRE project [14], and this PhD is a part of this latter project.

Electronic structure calculations based on the Density Functional Theory (DFT) is the modelling technique used to investigate $(U,Pu)O_2$ properties of concern in this PhD. Numerous studies have been carried out since 2000 on point defects and fission gas behaviour in UO_2 using DFT. The addition of a Hubbard-like term U to the standard DFT (DFT+U) aiming at solving the strongly correlated *5f* electrons issue in actinide oxides has been widely applied during the last decade. Many DFT+U calculations have been carried out on both point defect properties and fission gases incorporation and diffusion

in UO_2. On the contrary, no result is available in the literature on point defects in $(U,Pu)O_2$. Moreover, recent methods developed and implemented in the electronic structure codes such as vdW-DF (van der Waals Density Functional) [15, 16], which allow to account for non-local correlations, are not considered in the majority of the DFT+*U* studies on UO_2.

This PhD study aims first at using DFT+*U* combined to recent vdW-DF functionals to analyse the energetic properties of point defects in $(U,Pu)O_2$ in various charge states for various stoichiometry conditions. The impact of the creation of point defects on structural and electronic properties is also analysed. Then, the incorporation energies of various fission gases such as krypton, xenon, as well as helium, in $(U,Pu)O_2$ are investigated. Another subject of interest in this work is the modelling of thermodynamic properties of perfect UO_2 and $(U,Pu)O_2$ for various plutonium contents, using *ab initio* molecular dynamics method. The aim is to validate the application of the method for actinide based oxides. This will enable the determination of thermodynamic data for complex mixed actinide materials such as $(U,Pu,Am)O_2$ for which thermodynamic data are not yet accessible experimentally. Additionally, the study of point defect properties is also conducted on $(U,Ce)O_2$ which is used as a $(U,Pu)O_2$ surrogate for separate effect experiments. The aim is to gain more insight into the comparison between these two oxides by analysing the similarities and differences in terms of defects properties.

This PhD study carries out a fine characterization of atomic scale irradiation damage in $(U,Pu)O_2$ for the first time using DFT based method, and also uses for the first time *ab initio* MD coupled to DFT+*U* to investigate the thermodynamic properties of actinide based oxides. The global goal of this PhD is thus to improve the understanding of the behaviour of $(U,Pu)O_2$ under irradiation, and to gain insight into the use of *ab initio* MD for the prediction of thermodynamic properties of actinide based materials in general and oxides in particular.

This manuscript is organized in six chapters. In the first chapter, a literature review on $(U,Pu)O_2$ as well as UO_2 and PuO_2 is presented. We review various material properties of $(U,Pu)O_2$ obtained experimentally and using various modelling techniques. Point defects properties in UO_2 and PuO_2, as well as atomic self-diffusion in UO_2, PuO_2 and $(U,Pu)O_2$, are also reviewed. In the second chapter the methods used in our study are presented. We detail the various DFT approximations used, including approaches adapted for the study of strongly correlated compounds. We also present the special quasirandom structures (SQS) method used for the modelling of solid solutions such as $(U,Pu)O_2$ and $(U,Ce)O_2$. *Ab initio* molecular dynamics (*ab initio* MD) is also presented in detail, as well as the thermostat and the barostat used for the calculations of thermodynamic properties. In addition, we present the procedure we use to determine the chemical potentials of the various species of $(U,Pu)O_2$ under different stoichiometry conditions. This is an important requirement for the subsequent calculations of formation energies of point defects. In chapter 3, the material properties calculated for pristine $(U,Pu)O_2$ are shown. The structural, electronic and elastic properties are investigated for various

plutonium contents. The energetic properties and the finite temperature properties such as radial distribution functions, linear thermal expansion, variation of enthalpy and heat capacity are also studied at various temperatures for UO_2 and $(U,Pu)O_2$. Chapter 4 is dedicated to the study of point defect properties in $(U,Pu)O_2$. In this chapter, the modifications on the electronic properties and on the structural properties induced by the creation of various point defects – especially the presence of defect states in the electronic density of states and the lattice distortion in the defect environment – are analysed in detail. The formation energies of point defects are investigated for various plutonium contents, taking into account the effect of various chemical environments of defects, various defect charge states, as well as the deviation from stoichiometry. The atomic transport properties, through the calculation of the migration barriers of point defects are also presented in this chapter. The combination of the formation energies and the migration energies has allowed us to access the activation energy for diffusion. This latter quantity is very important for the calculation of the self-diffusion coefficients of various atomic species in $(U,Pu)O_2$. In chapter 5, point defect properties in $(U,Ce)O_2$ and their impact on the electronic and structural properties are investigated in the same manner as in $(U,Pu)O_2$. We have therefore performed a thorough comparison between both $(U,Pu)O_2$ and $(U,Ce)O_2$ in terms of point defect energetic properties. Finally in chapter 6, the incorporation and solution of fission gases, especially Kr and Xe, as well as He, in bound Schottky defects (BSD) of $(U,Pu)O_2$ are investigated. The results are compared to those on UO_2 and PuO_2. Finally, a general conclusion is given, together with several perspectives to these studies.

Chapter 1: Literature review on $(U,Pu)O_2$ mixed oxides

1.1 Introduction

$(U,Pu)O_2$ is a nuclear fuel for pressurized water reactors in France with a plutonium content of around 10 wt.%. It is also planned to be used as the reference fuel in Generation IV sodium fast reactors with a higher plutonium content of around 25 wt.%. Before being loaded in GEN IV reactor, $(U,Pu)O_2$ MOX fuel has to be designed and qualified to meet safety requirements. The design and the qualification of fuels need a detailed knowledge of their properties [17]. To this aim, material bulk properties of $(U,Pu)O_2$ and their evolution under irradiation have to be investigated in detail.

Among relevant properties of interest, the structural properties are essential. The analysis of the evolution of the fuel structure under temperature and pressure as well as under irradiation improves the understanding of fuel restructuring under operation. Thermodynamic properties, such as the thermal expansion, heat capacity, thermal conductivity and melting temperature, are also of prime interest for the optimisation of the fuel performance and safety. Indeed, the thermal expansion contributes to the fuel swelling and thus to the pellet-cladding mechanical interactions, which can be detrimental for safety issues. The heat capacity is a key parameter for the thermal conductivity. Both properties are crucial for the heat transfer from the fuel to the coolant. The melting temperature has to be as high as possible than the operating temperature in order to guaranty the fuel integrity if an incidental increase in power happens during operation.

Fuel properties evolve under operation through elementary mechanisms that occur at various scales of the material, down to the atomic scale. At the atomic scale, these mechanisms are driven by defects and fission product formation, and atom diffusion. For instance, the deviation from stoichiometry is accommodated by the formation of point defects. Furthermore, atomic diffusion is assisted by point defects. Therefore, in order to predict the behaviour of fuel under irradiation, the study of phenomena occurring at the atomic scale, such as defect properties, atomic transport and fission gases behaviour, is required.

Many research groups, including at CEA, have been working on fuel property characterisation and irradiation effects. Studies have already been published on structural and microstructural properties and their evolution under irradiation, as well as atomic transport and fission gases for UO_2, PuO_2 and MOX fuel [3, 18–21]. This first chapter aims at presenting the studies published by various groups on material properties and irradiation effects of $(U,Pu)O_2$. For properties that are missing for the $(U,Pu)O_2$ MOX fuel, the results for the end members UO_2 and PuO_2 will be discussed.

This chapter is divided into two main parts. In the first part, the material properties of the perfect and defective $(U,Pu)O_2$ are presented. These are the phase diagram of the U-Pu-O system, structural, elastic, magnetic, electronic and thermodynamic properties. In the second part of this chapter, the defects stability will be reviewed for UO_2 and PuO_2

for which published studies are available. We will also present the atomic transport properties according to various models available in the literature. These models originate from both experiments, such as electrical conductivity, nuclear reaction and SIMS techniques, and from modelling, such as the DICTRA method.

1.2 Phase diagram of U-Pu-O system and bulk properties of $(U,Pu)O_2$

1.2.1 Phase diagram of U-Pu-O system

The phase diagram of a given system is the representation of the different stable phases as a function of the concentration of its constitutive elements, temperature and pressure conditions. Phase diagrams are used in materials research and engineering to understand the interrelationship of composition, microstructure, and processing conditions.

Since 1967, a considerable effort has been made for the experimental study of U-Pu-O systems, resulting in the construction of a phase diagram by Markin and Street [22] for different temperature ranges. Other experimental studies have been conducted later, especially by Sari *et al*. [23] and more recently by Belin *et al*. [24] and Truphémus *et al*. [25] for the comprehension of this system. Huge effort has also been made for the modelling studies, especially with the CALPHAD method [26, 27], resulting in the proposition of more precise phase diagram [4]. These calculations through the Thermo-Calc software were carried out using the database FUELBASE established since 2005. Now, the database TAF-ID [28] established since 2013 is used.

The experimental phase diagram of the U-Pu-O system from Markin and Street is presented in Figure 1. The phase diagram is plotted at 25°C for oxygen composition ranging from 60 % to 73 % and for the entire plutonium compositions. This phase diagram shows three remarkable regions: the face-centered cubic (fcc) phase region, the highly oxidized region constituted of the orthorhombic phases, and the highly reduced region constituted of body-centered cubic phase, metallic and cubic phases.

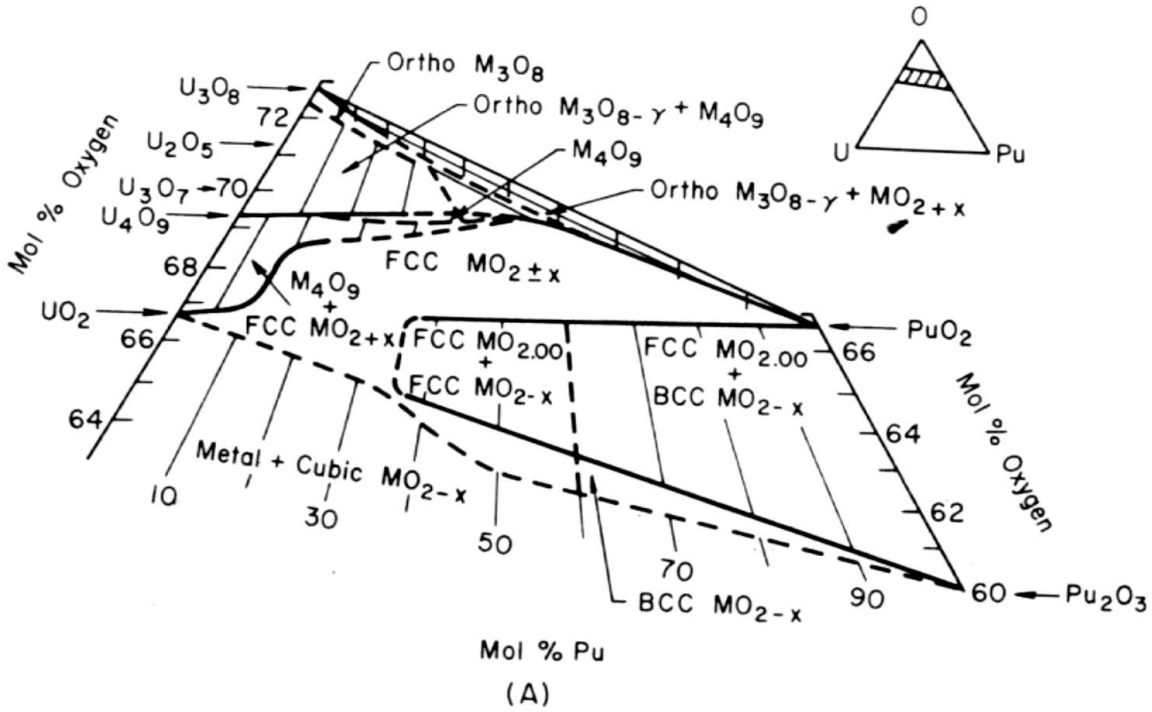

Figure 1 : Ternary phase diagram of the U-Pu-O system at 25°C from Markin and Street [22].

The U-Pu-O phase diagram has also been detailed through CALPHAD calculations for oxygen concentrations ranging from 60 % to 70 % and plutonium contents ranging from 0 to 40 %. The result of this study from Guéneau *et al.* [4] is reported in the Figure 2.

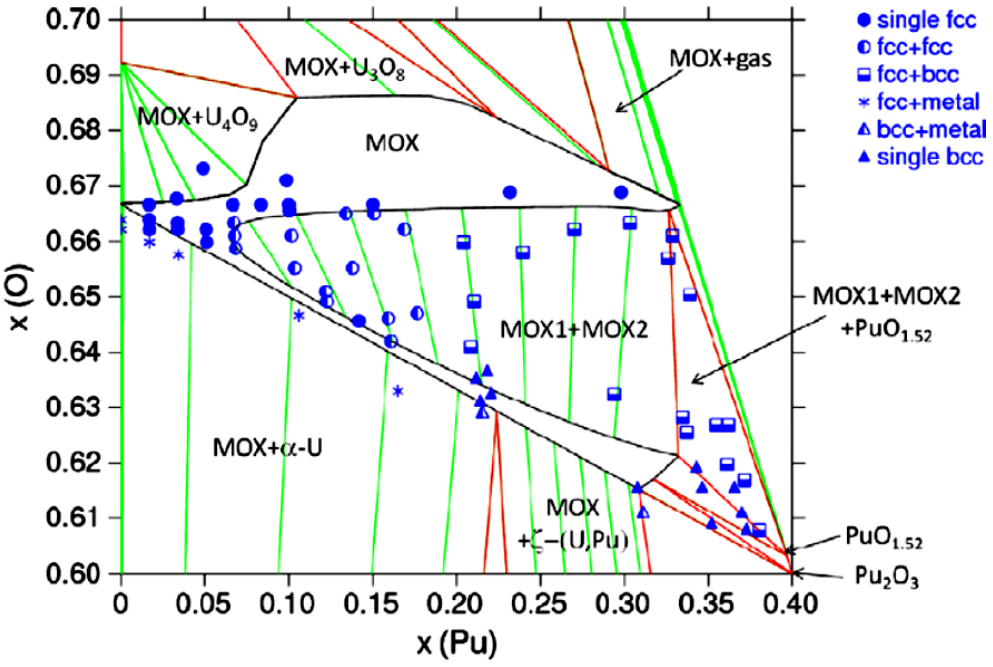

Figure 2 : Calculated phase diagram of U-Pu-O system at 200°C from Guéneau *et al.* [4].

In our DFT studies, the good understanding of the phase diagram in terms of phases obtained at each composition domain is essential since this data will be crucial for the determination of the chemical potentials for the calculation of point defect formation energies (Chapter 2, section 2.6). Therefore, the description of each phase in the hypo-stoichiometry and hyper-stoichiometry conditions, including oxidized and reduced phases is done below.

1.2.1.1 Hypo-stoichiometric domain: $(U,Pu)O_{2-x}$ and reduced phases

The hypo-stoichiometric region of the U-Pu-O system is the region where the O/(U+Pu) ratio is smaller than 2.00. It is constituted of the hypo-stoichiometric fluorite phases $(U,Pu)O_{2-x}$, reduced phases $PuO_{1.52}$ and Pu_2O_3 as well as the mixture of $(U,Pu)O_{2-x}$ and metallic phases.

At room temperature, depending on the Pu content, the phase diagram presents from the stoichiometric to the highly reduced phases the following domains, which are the most largely studied ones:

- A domain of a single *fcc* fluorite phase for low plutonium contents (less than 40% depending on temperature).
- A domain of a miscibility gap at intermediate plutonium contents, constituted of two fcc phases (*fcc1*+*fcc2*) in equilibrium, *fcc1* with a O/(U+Pu) close to 2.00 and *fcc2* being more reduced.
- At higher plutonium content, a two-phase region exists with a *fcc* phase in equilibrium with a α-Pu_2O_3 body-centered (*bcc*) phase.

Depending on authors, the boundaries of each region may vary. According to Markin and Street [22], the boundary between the single *fcc* phase and the miscibility gap (*fcc*/*(fcc1+fcc2)* limit) is reached for a plutonium content of 35 % and the transition from the miscibility gap to the fcc+bcc equilibrium for a plutonium content of 60 %. According to Sari *et al*. [23], the miscibility gap occurs for a plutonium content smaller than 20 % and the transition to the fcc+bcc equilibrium for a plutonium content between 45 % and 55 %. Guéneau *et al*. [4] have also predicted the miscibility gap to occur at a plutonium content smaller than 20 % in accordance with Sari *et al*. and also predicted the existence of the fcc+bcc equilibrium for large Pu contents. However, the authors emphasized that the boundary of this latter equilibrium cannot be accurately predicted since the solubility of uranium in the α-Pu_2O_3 is not taken into account in the thermodynamic model owing to the lack of experimental data.

Another interesting domain is the transition from fcc1+fcc2 to fcc+bcc. Indeed, according to the thermodynamic phase rule this transition passes through the intermediate domain of fcc1+fcc2+bcc triphasic equilibrium. This intermediate domain has been found experimentally for a plutonium content ranging from 45 % to 65 % by

Truphémus *et al*. [25], composed of two fcc phases and a α-Pu_2O_3-type phase. Guéneau *et al*. have also found this domain from CALPHAD calculations but for plutonium contents different from those of Truphémus *et al*.

The boundary of the single fcc phase shifts towards higher plutonium contents with the increase of temperature. This evolution has been observed with differential thermal analysis (DTA) studies [23, 29], high temperature X-ray diffraction experiments [22, 24, 30] and CALPHAD calculations [4].

Below these reduced phases discussed above, depending on the plutonium content, there exist the domains where the fcc fluorite phase is in equilibrium with metallic phases such as α-uranium (α-U) and the uranium-plutonium alloy ξ-(U,Pu). These equilibrium are not discussed in depth in the literature since there is no enough data on the metallic-oxide U-Pu-Pu_2O_3-UO_2 region of the U-Pu-O phase diagram and the solubility of the oxide phase in the metallic liquid (U,Pu) is not known [4].

1.2.1.2 Hyper-stoichiometric domain: $(U,Pu)O_{2+x}$ and oxidized phases

The hyper-stoichiometric region is characterized by the O/(U+Pu) ratio larger than 2.00. It is constituted of the hyper-stoichiometric fluorite phase $(U,Pu)O_{2+x}$ and oxidized phases written as M_4O_9 and M_3O_8. In the phase diagram, three relevant domains are observed depending on the plutonium and oxygen content [22] as indicated below:

- A domain of monophasic fluorite phase $(U,Pu)O_{2+x}$
- A domain of the equilibrium $(U,Pu)O_{2+x}$+M_4O_9
- A domain of the equilibrium $(U,Pu)O_2$ +M_3O_8

The boundary between the biphasic regions of each oxidized phase and the monophasic region appears at different O/(U+Pu) ratio depending on the plutonium content. The description of these domains is not yet established unequivocally and thus depends on the authors. Markin and Street [22] observe the phase separation between M_4O_9 and $(U,Pu)O_{2+x}$ for a plutonium content of 11 % at the O/(U+Pu) ratio larger than 2.10. For a plutonium content of 15 %, the O/(U+Pu) ratio at which this separation occurs is above 2.19. For a higher plutonium content, especially 42 %, the separation between the $(U,Pu)O_{2+x}$ fluorite phase and M_3O_8 hexagonal phase is observed for a O/(U+Pu) ratio at least equal to 2.33. In both phases, the Pu contents are different since plutonium is less soluble in M_3O_8 [23, 31]. Indeed, M_3O_8 is a plutonium-poor phase. According to Dean [30], the monophasic fluorite phase can be observed for a plutonium content of 30 % up to the O/(U+Pu) ratio of 2.2. The highest oxygen phase boundary of the $(U,Pu)O_{2+x}$ is also well reproduced by the CALPHAD model with a maximum O/(U+Pu) ratio equal to 2.2 for a Pu contents between 32 % and 60 % at 200°C [4]. However, the solubility of Pu in U_4O_9 and U_3O_8 oxides was not taken into account in this model.

We can thus conclude that when the plutonium content increases, the O/(U+Pu) ratio for the appearance of the $(U,Pu)O_{2+x}$+M_4O_9 increases too.

For a given Pu content, at O/(U+Pu) ratio higher than those mentioned above, the phase diagram shows at various temperatures the presence of M_4O_9, M_3O_8 and M_3O_7. All these phases have similar crystal structure to those found in the U-O system [32]. The formation of M_4O_9 and M_3O_7 phases, as in the U-O system, is the result of the ordered aggregation of oxygen defects into cuboctahedral structures [33]. M_3O_8 and M_3O_7 crystalize in a hexagonal phase and M_3O_8 results in the oxidation of M_3O_7. The plutonium content at which M_3O_8 is observed increases with the temperature [31].

The properties of the $(U,Pu)O_{2\pm x}$ fluorite phase are impacted by both plutonium concentration and the deviation form stoichiometry. The next section presents the description of structural properties of these fluorite phases.

1.2.2 Structural properties of $(U,Pu)O_2$

The structural properties of $(U,Pu)O_2$ described here include the crystal structure, lattice constant and interatomic distances. The stoichiometric $(U,Pu)O_2$ crystalizes in the fluorite-type structure [34, 35]. In this structure, actinide cations U(IV) and Pu(IV) are located in the face-centered cubic (fcc) structure sites, forming the cation sub-lattice and the oxygen atoms are located in the tetrahedral sites of this fcc structure, forming the oxygen sub-lattice with a simple cubic structure. This structure is presented in Figure 3.

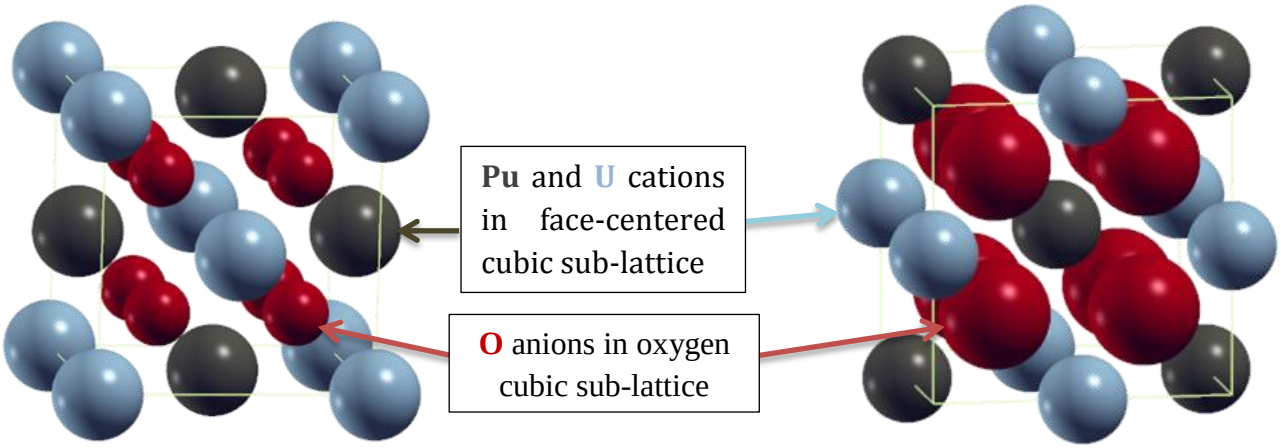

Figure 3 : Crystal structure of stoichiometric $(U,Pu)O_2$.

This fluorite-type structure is maintained for small deviations from stoichiometry as we mentioned above. Let us now present a literature review on the structural parameters of the stoichiometric $(U,Pu)O_2$ and the impact of the deviation from the stoichiometry on these parameters.

1.2.2.1 Lattice constant and interatomic distances of stoichiometric (U,Pu)O_2 at room temperature

X-ray diffraction experiments have been widely used to determine the lattice constant of the (U,Pu)O_2 fluorite structure at room temperature for various stoichiometry conditions. For the stoichiometric compound, the lattice constant is found to decrease with an increase in plutonium content. This lattice constant evolution follows a linear trend known as Vegard's law [36]. Figure 4 gives the lattice constant as a function of plutonium content from the experimental studies of Markin *et al*. [22], Thummler *et al*. [37], Brett *et al*. [38], Lyon *et al*. [39], Nakayama *et al*. [40], Jayadevan *et al*. [41], Durier *et al*. [42], Martin *et al*. [34], Grandjean *et al*. [43], Kato *et al*. [44], Beauvy [45] and Truphémus *et al*. [25], compared to the Vegard's law. The small deviations can be due to the difficulty to control the stoichiometry.

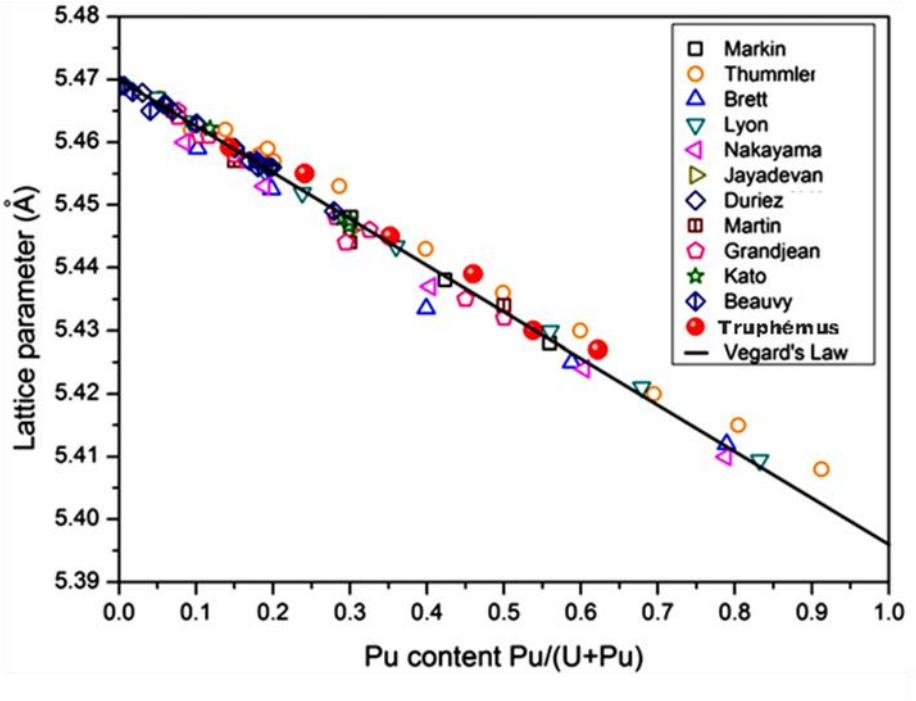

Figure 4 : Plot of lattice constant of (U,Pu)O_2 as a function of plutonium content at room temperature from Thruphémus *et al.* [25].

The Vegard's law has also been obtained through modelling studies using empirical potentials [46] and also validated by electronic structure calculations [47, 48]. However, for the electronic structure calculations, the correct description of the Vegard's law is sensitive to the description of magnetic properties of the compound as pointed out by Yang *et al*. [48]. The ferromagnetic (FM) order fails to reproduce the Vegard's law while the antiferromagnetic order (AFM) reproduces this tendency.

Experimental studies on the interatomic distances have been conducted on (U,Pu)O_2 for various plutonium contents by Martin *et al*. [34] using X-ray absorption spectroscopy (XAS-EXAFS). The results are summarized in Table 1. *N* is the coordination number of

neighbouring atoms and $\boldsymbol{\sigma^2}$ is the mean-square disorder of neighbour distances. *R* is the distance to the neighbouring atom. This study shows that in $(U,Pu)O_2$, the interatomic distances decrease linearly with respect to the plutonium content, in accordance to the Vegard's law of the lattice parameter. Moreover, the interatomic distances U-O and Pu-O in the first coordination shell are identical for a 50 % Pu content, in contrast to the pure UO_2 and PuO_2 where the U-O and the Pu-O distances are respectively different. At lower Pu content, the U-O distances vary (three values obtained), while the Pu-O distance remains identical for each Pu concentration. A similar value to that of Pu-O distance is found among the various U-O distances. The differences in U-O distances at lower Pu concentration are attributed to the presence of hyper-stoichiometric UO_{2+x} structures in the samples around U cations. For a 50 % plutonium content, the ideal solid solution structure is found, with the metal-oxygen distance being equal to 2.351(5) Å irrespective to the cation type. The same ideal solid solution structure is also found in the metal-metal shell with the metal-metal distance of 3.845(5) Å.

Pu content (%)	**First shell**						**Second shell**					
	Pu-O			**U-O**			**Pu-U/Pu**			**U-Pu/U**		
	R(Å)	**N**	**σ^2(10^{-3} Å^2)**	**R(Å)**	**N**	**σ^2(10^{-3} Å^2)**	**R(Å)**	**N**	**σ^2(10^{-3} Å^2)**	**R(Å)**	**N**	**σ^2(10^{-3} Å^2)**
0	--	--	--	2.370(5)	8.0(5)	8.0(5)	--	--	--	3.865 (5)	12.0 (5)	
7	2.366(5)	8.1(5)	9.0(5)	2.31(1) 2.36(1) 2.86(1)	1.5(5) 6.7(5) 1.1(5)	5.0(5) 14(1) 7.0(5)	3.868 (5)	12	6.0(5)	3.868 (5)	12	5.1(5)
15	2.351(5)	8.0(5)	8.8(5)	2.28(1) 2.36(1) 2.84(1)	1.0(5) 6.7(5) 1.0(5)	6.4(5) 17(1) 7.0(5)	3.857 (5)	12	5.8(5)	3.865 (5)	12	6.3(5)
30	2.353(5)	7.7(5)	9.8(5)	2.28(1) 2.35(1) 2.85(1)	1.1(5) 6.5(5) 0.7(5)	6.7(5) 19(1) 5.6(5)	3.845 (5)	12	4.5(5)	3.858 (8)	12	6.5(5)
50	2.351(5)	8.0(5)	8.1(5)	2.352(5)	8.1(5)	7.3(5)	3.845 (5)	12	3.0(3)	3.845 (5)	12	5.4(3)
100	2.333(5)	8.0(5)	6.4(5)	--	--	--	3.820 (5)	12.0 (5)	3.3(3)	--	--	--

Table 1 : Metric parameters extracted by fitting of EXAFS spectra measured at U and Pu L_{III} edges for $(U,Pu)O_2$ samples and UO_2 and PuO_2 reference compounds from Ref. [34].

For $(U,Pu)O_2$ with a 50 % Pu content, the local order has been suggested through these EXAFS analyses to correspond to that of an ideal solid solution.

Another method than XAS has been used by Vigier *et al*. [49] for a direct characterisation of the local environment of oxygen atoms in $(U,Pu)O_2$ with a plutonium content of 30 %. This method is ^{17}O Magical Angle Spinning Nuclear Magnetic Resonance (^{17}O MAS NMR). With this technique, the local environment of oxygen atoms is probed. Indeed, for oxygen atoms in $(U,Pu)O_2$, there are five possible environment listed as $O(U)_{4-z}(Pu)_z$ ($0 \leq z \leq 4$), where z is the number of neighbouring cations. For 30 % Pu, Vigier *et al*. found no $O(Pu)_4$ environment. Moreover, the proportion of each environment found experimentally agrees with the corresponding calculated value for

the random distributed uranium-plutonium model of ideal solid solution. The authors conclude that from the structural point of view, this data gives strong evidence of the solid solution ideality for the stoichiometric $U_{0.7}Pu_{0.3}O_2$, and the segregation of cations can be discarded.

Based on these experimental suggestions, the modelling of the stoichiometric $(U,Pu)O_2$ is done for this PhD work in the approximation of ideal solid solution in the whole plutonium content range. This approximation will be discussed in the next chapter.

Even if the crystal structure remains identical at a low deviation from stoichiometry, the structural parameters discussed above are sensitive to these deviations. This is the purpose of the next section.

1.2.2.2 Effect of the deviation from stoichiometry on the structural parameters of $(U,Pu)O_2$

The deviations from stoichiometry have an impact on the structural parameters, namely the lattice constants or the interatomic distances. Figure 5 gives the plot of the lattice constant as a function of the deviation from stoichiometry ***x*** ($x > 0$) of $(U,Pu)O_{2\pm x}$ from X-ray diffraction experiments with a plutonium content of 15 % and 30 % by Markin and Street [22] and with the plutonium content of 53 % and 70 % by Sali *et al*. [50].

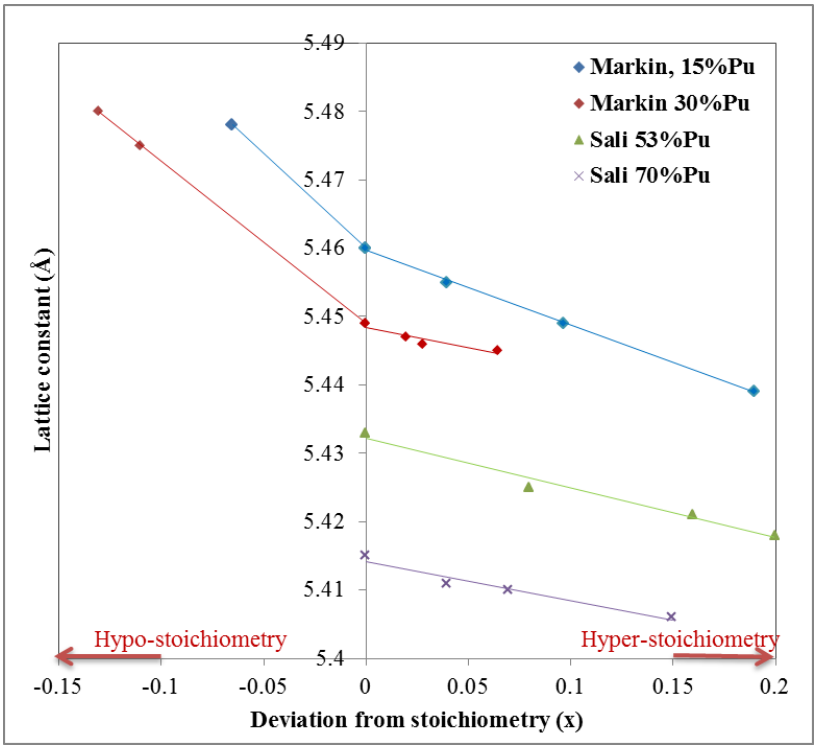

Figure 5 : Lattice constants as a function of deviation from stoichiometry for a Pu content of 15 %, 30 %, 53 % and 70 %.

In the hypo-stoichiometry region, the lattice constant increases linearly with the deviation from stoichiometry both from XRD experiment at room temperature (Figure 5) and from classical molecular dynamic from 300 K to 3000 K [51]. The evolution can be expressed as a function of the plutonium content and the deviation from stoichiometry according to the empirical recommendation of Vauchy *et al.* [52] deduced from Duriez *et al.* [42] as follows:

$$a(\text{Å}) = 5.47 - 0.074y + 0.32x \qquad (1)$$

where ***a*** is a lattice constant, ***y*** the plutonium content and ***x*** here is the absolute value of the deviation from stoichiometry.

Vigier *et al.* [49] measured in the hypo-stoichiometric $U_{0.7}Pu_{0.3}O_{2-x}$ the modification of the Pu-O interatomic distances due to the deviation from stoichiometry. The U-O distance remains identical to its value in the stoichiometric compound while a slight increase in Pu-O distance seems to occur. This is probably due to the presence of trivalent plutonium which exhibit a larger atomic radius.

Conversely in the hyper-stoichiometry region, the lattice constant decreases with the deviation from stoichiometry from XRD at room temperature (Figure 5). The reason of the decrease in lattice constant is the increase in the oxidation state of uranium from +IV to +V [50].

1.2.3 Magnetic, electronic and elastic properties of $(U,Pu)O_2$

Magnetic and electronic properties are important data for atomic scale studies using DFT calculations. The magnetic configuration for instance affects the ground state of the system and then other properties at the atomic scale, as mentioned in the previous section for the lattice constant found for the antiferromagnetic order in $(U,Pu)O_2$. Thus, the good and precise knowledge of magnetic properties of a material is required for an accurate validation of the approximations used in DFT calculations. As for the electronic properties, the band gap for instance is also a key parameter used to validate the accuracy of DFT calculations. The DFT in its standard approximations (LDA and GGA) has in particular been disqualified for the study of the strongly correlated materials since it fails to reproduce their electronic structure. It predicts for instance UO_2 to be metallic [53] instead of a Mott-Hubbard insulator as proven experimentally [54]. As to the elastic constants, they constitute input parameters for fuel performance codes for the modelling of mechanical properties. This section presents the literature review of these properties for $(U,Pu)O_2$ when available, and for UO_2 and PuO_2 when there are no available data for $(U,Pu)O_2$.

1.2.3.1 Magnetic properties of (U,Pu)O_2, UO_2 and PuO_2

To our knowledge, there is no experimental data on the magnetism of the uranium-plutonium mixed oxide (U,Pu)O_2. However, it has been established experimentally that UO_2 is antiferromagnetic below its Néel temperature which is 30.8 K [55]. For PuO_2, there is no experimental data evidencing its magnetic character. Crystal field calculations suggest that the ground state of PuO_2 is a non-magnetic singlet Γ1 [55–57]. However, the anomaly in the magnetic response of PuO_2 suggested the existence of an antiferromagnetic exchange interaction between plutonium cations [55]. On the other hand, from the DFT+*U* calculations, PuO_2 is energetically more stable in the antiferromagnetic configuration. Owing to the above information on the magnetic structure of the pure oxides UO_2 and PuO_2, it remains difficult to predict the magnetic structure of the uranium-plutonium mixed oxides. DFT+*U* studies aiming at the identification of the most stable magnetic structure have emerged (see Table 2). In these studies, some properties are evaluated and the selected magnetic structure is the one which better describes these properties.

Studies	**Pu content**	**Functionals An(*U* , *J*) (eV)**	**Magnetic order**	**Lattice constant (Å)**	**Band gap (eV)**	**ΔE (meV/atom)**	**E_{coh} (eV)**
Dorado *et al.* [47]	**12.5% SQS**	LDA+*U* U(4.5 , 0.54) Pu (4.0 , 0.7) *Liechtenstein*	AFM	5.410	1.6	1.7	24.5
			FM	5.410	1.1	0.0	24.5
			PM	5.405	1.5	3.2	24.5
	25% SQS		AFM	5.400	1.5	2.8	24.2
			FM	5.395	1.0	0.0	24.2
			PM	5.395	1.5	1.8	24.2
	12.5% Ordered		AFM	5.406	1.5	2.2	24.5
			FM	5.404	1.2	0.0	24.8
	25% Ordered		AFM	5.395	1.4	1.7	24.2
			FM	5.395	1.0	0.0	24.2
Yang *et al.* [48]	**25%**	LDA+*U* U(4.5 , 0.5) Pu(4.7 , 0.7) *Dudarev*	AFM	5.43	0.2	0.0	--
	50%		AFM	5.41	0.2	0.0	--
	75%		AFM	5.39	0.2	0.0	--
Ma *et al.* [58]	**50%, O/M=1.75**	Hybrid functionals with 25 % HF exchange	AFM	5.425	1.2	0.0	--
			FM	5.429	0.8	0.405 eV/unit cell	--
	50%, O/M=2.25		AFM	5.433	1.4	0,0	--
			FM	5.435	1.3	0.018 eV/unit cell	--

Table 2 : Lattice constant, band gap, bulk modulus, cohesive energy and energy differences of magnetic configurations AFM, FM and PM of (U,Pu)O_2 for various Pu contents. ΔE is the difference between the energy of a given magnetic configuration and that of the most stable one. An is an actinide cation and (*U, J*) are respectively the interaction and exchange terms of DFT+*U*. Results from Ma *et al*. are in eV/unit cell.

Dorado *et al*. [47] have studied the magnetic configuration stability in $(U,Pu)O_2$ modelled in both the approximations of ideal solid solution (SQS) and the ordered structure. They have therefore compared the stability of various magnetic orders, namely the ferromagnetic order (FM), the antiferromagnetic order (AFM) and the paramagnetic order (PM), for plutonium contents of 12.5 % and 25 %. The authors found using LDA+*U* the ferromagnetic order to be favourable energetically, with an energy difference for the antiferromagnetic order of 1.7 meV/atom for a plutonium content of 12.5 % and 2.8 meV/atom for a plutonium content of 25 %.

They also observe the change in the relative stability of the paramagnetic order which becomes more stable than the antiferromagnetic order for a plutonium content of 25 %. Even for the ordered compound, the ferromagnetic order remains the most favourable. Their results also show that the magnetic order has no impact on the lattice constant and the cohesive energy. However, the authors precise that the energy differences are very low and that the 1**k** antiferromagnetic order commonly found in the literature is a good approximation of the magnetic order and gives results close to experiments. In the 1**k** antiferromagnetic order, the magnetic spins are ordered in the same direction with alternatively opposite orientations from one crystallographic plane to the next.

Beside the assumption of Dorado *et al*. [47], Yang *et al*. [48] using LDA + *U* found the antiferromagnetic order to be more stable than the ferromagnetic order and the non-magnetic order. Moreover their lattice constants obtained from the FM configuration for various plutonium contents do not follow the Vegard's law contrary to those obtained from the AFM order. Ma *et al*. [58] have also analysed the relative stability of the AFM and the FM orders in over-stoichiometric $U_{0.5}Pu_{0.5}O_{2.25}$ and sub-stoichiometric $U_{0.5}Pu_{0.5}O_{1.75}$ using hybrid functionals. They also conclude on the stability of the AFM order with energy differences of 0.018 eV/unit cell for the over-stoichiometric compound and 0.405 eV/unit cell for the sub-stoichiometric one. They found the band gap to be smaller in the FM order and a very small impact of the magnetic order on the lattice constant.

All these LDA+*U* or hybrid functional calculations tend to validate the stability of the AFM rather than the FM or non-magnetic structures, except the one by Dorado *et al*. But even if the results of Dorado and co-workers tend to predict the stability of FM order, they argue that the small energy scale involved do not allow the rejection of the AFM structure suggested for UO_2 and $(U,Pu)O_2$ at 0 K. Moreover, for Dorado *et al.* [47], the AFM magnetic order remains a good approximation of the paramagnetic order found at higher temperature. In any case, the magnetic properties of $(U,Pu)O_2$ for the whole range of Pu contents remain unclear and need to be clarified by GGA+*U* studies as we will see later in this manuscript.

1.2.3.2 Electronic properties of (U,Pu)O_2, UO_2 and PuO_2

The electronic properties include the description of the density of state of the material and its band gap. These properties have been extensively studied in UO_2. Indeed, the first determination of the electronic structure of UO_2 has been performed in 1980 by Baer and Schoenes [59] using X-ray photoemission spectroscopy (XPS) and Bremsstrahlung isochromat spectroscopy (BIS). The spectrum obtained in their study shows a band gap of around 2.1 eV between the occupied and the empty *5f* states. Many experimental studies have also determined the band gap between the top of the valence band and the bottom of the conduction band of UO_2 to be 2.6 eV [60], 2.3 eV [61] and 2.14 eV [62] through the determination of the activation energy of the electrical conductivity, using the four-contact method.

Recently, Yu *et al*. [54] have confirmed the $f - f$ Mott insulating character of UO_2 by combining the X-ray absorption spectroscopy of the *4d – 5f* and *4f – 6d* transition of uranium and of the *1s – 2p* transition of oxygen. The results of their study presented in Figure 6 show that the empty *5f* states are localized at a lower energy than the empty *6d* states of UO_2. This confirms that UO_2 has a $f - f$ Mott insulating character. The same result has been obtained by Jollet *et al*. [63] and later by other authors [64, 65] from electronic structure calculations, with a band gap of 2.3 eV and 2.1 eV respectively.

For PuO_2, an experimental band gap of 1.8 eV [66] has been found, through the determination of the activation energy of the electrical conductivity. This value has been recently challenged by McCleskey *et al*. [67] who found an optical band gap of 2.8 eV. The latter authors argue that the first technique is very sensitive to the presence of defects in the material. However, the first value of 1.8 eV remains widely used as the reference band gap by many electronic structure calculations. Electronic structure calculations predict PuO_2 to be a charge-transfer insulator with the plutonium *5f* state and oxygen *2p* state being strongly hybridized at the top of the valence band [68–72].

Up to now, there is no experimental studies neither on the band gap nor on the density of states published for (U,Pu)O_2 to our knowledge. However, few electronic structure calculations on this compound have been published in the literature. The validity of these studies has been established through their accuracy in the description of electronic properties of UO_2 and PuO_2.

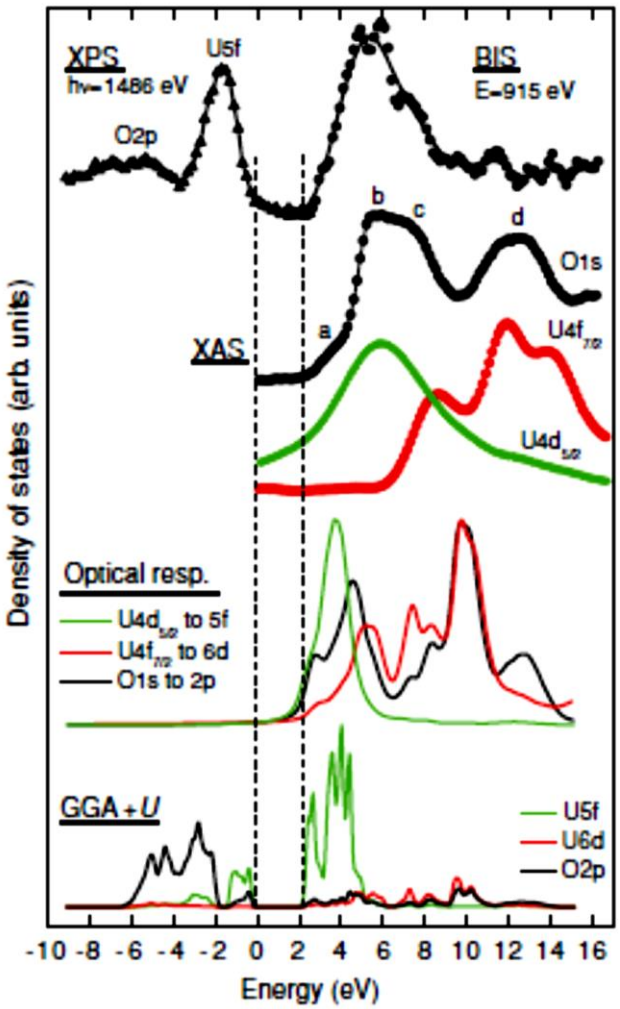

Figure 6 : Electronic density of states of UO_2 obtained from XAS, XPS, BIS and electronic structure calculation (DFT+*U*) from Yu *et al.* [54].

The available results on the electronic structure of $(U,Pu)O_2$ with 50 % Pu show a similar behaviour for the correlated *5f* orbitals of uranium and plutonium as in the pure oxides UO_2 and PuO_2. Indeed, the analysis of the electronic density of states of the three oxides obtained from LDA+*U* shows that the *5f* states of uranium and plutonium in $(U,Pu)O_2$ keep the same localized character, with the density of states of the actinide cations keeping the same hybridized character vis-à-vis the oxygen *2p* states as in the pure oxides [48]. Therefore, the density of states of $(U,Pu)O_2$ is the quasi-superposition of those of UO_2 and PuO_2 as presented in Figure 7 from Yang *et al*. [48].

The superposition of the density of states of UO_2 and PuO_2 in the electronic structure of $(U,Pu)O_2$ has a significant impact on the band gap. Indeed, $(U,Pu)O_2$ yield a smaller band gap [47, 48] compared to those of UO_2 and PuO_2. The top of the valence band is constituted of the *5f* state of uranium and the bottom of the conduction band constituted of the *5f* state of plutonium.

Up to now, there is no systematic study of the electronic structure of (U,Pu)O_2, namely the electronic density of states and the band gap, as a function of Pu content. This systematic study has been conducted in this PhD (see Chapter 3, Section 3.2.3).

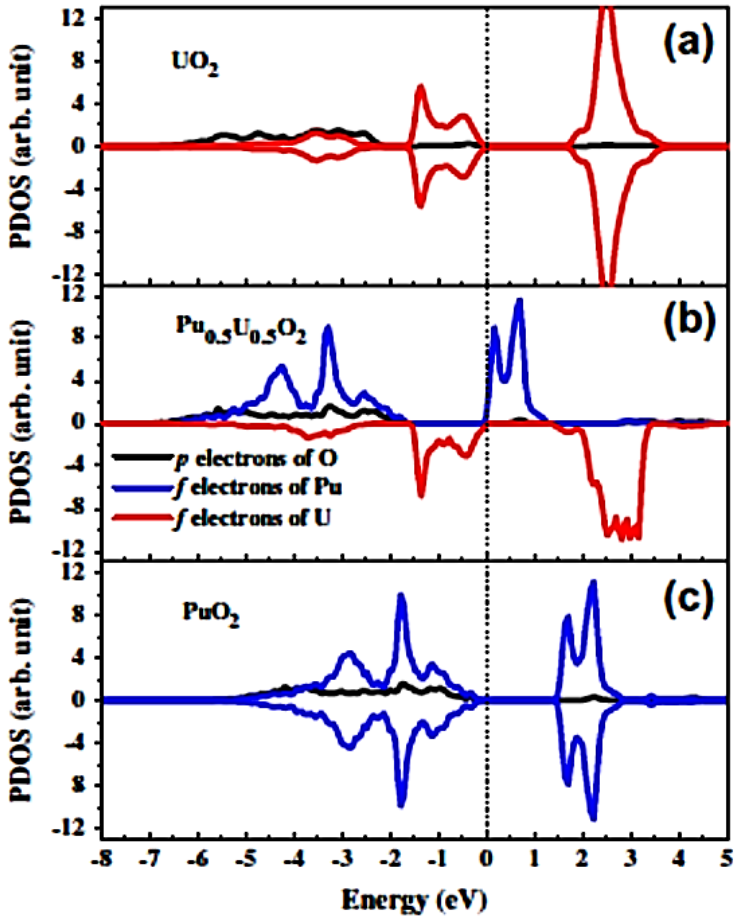

Figure 7 : The projected density of states (PDOSs) for the oxygen 2*p*, plutonium 5*f*, and uranium 5*f* electrons in (a) UO_2, (b) $Pu_{0.5}U_{0.5}O_2$, and (c) PuO_2. The Fermi energies are set to zero and denoted by a dotted line. The negative values represent spin-down electrons [46].

1.2.3.3 Elastic properties of (U,Pu)O_2, UO_2 and PuO_2

Elastic constants of materials are quantities that measure the materials resistance to elastic deformation. These are for instance the bulk modulus B, the shear modulus or modulus of rigidity G or μ, the Young's modulus E, isothermal compressibility β, and the Poisson's ratio ν. All these quantities can be derived from a unique elastic tensor, composed of elastic constants C_{ijk}.

The elastic constants and bulk modulus of UO_2 have been studied experimentally at room temperature in Ref [73–75], and also by first-principles studies in different

magnetic orders [47, 76, 77]. As for PuO_2, experimental data on elastic constants are scarce. The bulk modulus has been measured experimentally by Idiri *et al*. [75]. Elastic properties of PuO_2 have been also calculated by first-principles studies [69, 76, 77].

Experimental studies on the elastic constants of the uranium-plutonium mixed oxides are old to our knowledge. The available experimental elastic constants of this mixture are taken from the review of D. G. Martin [78] on polycrystalline $(U,Pu)O_2$ at room temperature and up to 1300 K. The values reviewed are presented in Table 3. It can be noted that the values obtained are sensitive to the experimental techniques, especially for the bulk modulus with the uncertainty larger than 30 % and for the Poisson's ratio with the uncertainty around 20 %.

Pu contents	E (GPa)	G (GPa)	B (GPa)	ν (GPa)	Experimental methods
20	210	82.4	156.9	0.277	RES
20	223	83.7	221	0.332	USV
20	259				RES
15	233			0.335	USV
RES = resonant frequency, USV = ultrasonic velocity					

Table 3 : Elastic constants for stoichiometric $(U,Pu)O_2$ [78].

The experimental elastic constants are also sensitive to the deviation from stoichiometry. Figure 8 shows the trend of D. G. Martin's recommendations for the impact of the deviation from stoichiometry on the Young's modulus and the Poisson's ratio, with experimental points used for the fit. This review shows that the Young's modulus of $(U,Pu)O_2$ decreases with the deviation from stoichiometry for both the hypo-stoichiometry or the hyper-stoichiometry. The Poison's ratio increases with the increase in the oxygen to metal ratio (O/M).

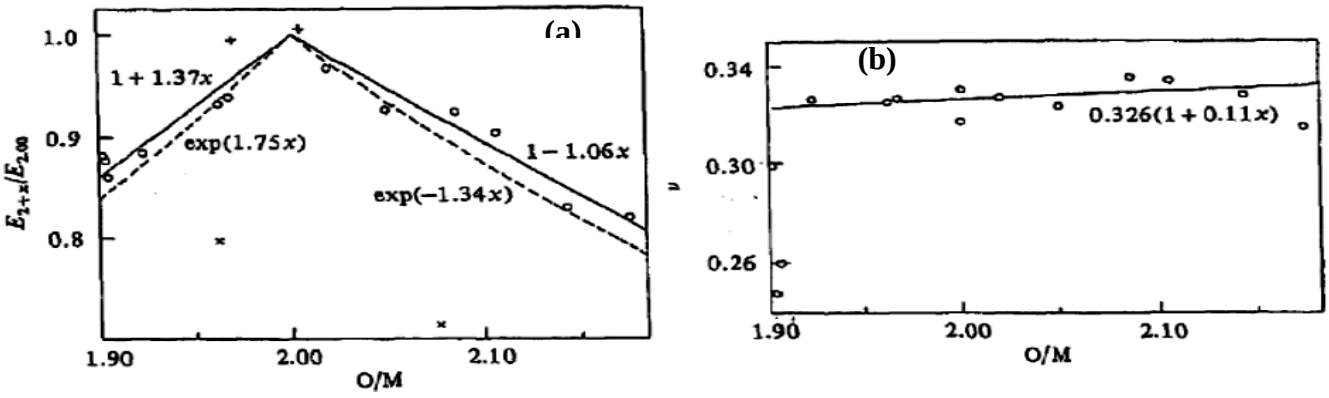

Figure 8 : (a) Young's modulus for $(U,Pu)O_{2+x}$ at room temperature, expressed as a ratio of the stoichiometric value as a function of the ratio O/M and (b) Poisson's ratio for $(U,Pu)O_{2+x}$ at room temperature as a function of the ratio O/M from D. G. Martin [78].

Few atomistic studies, such as DFT+*U* and studies using empirical potentials, have also investigated the elastic constants of the uranium-plutonium mixed oxides. The values obtained using electronic structure calculations are presented in Table 4.

Studies	**Pu content**	**Functionals An(*U* , *J*) (eV)**	**Magnetic order**	**B (GPa)**	**G (GPa)**	**ν (GPa)**	**C_{11} (GPa)**	**C_{12} (GPa)**	**C_{44} (GPa)**
Dorado *et al.* [47]	**12.5% SQS**	LDA+*U* U (4.5 , 0.54) Pu (4.0 , 0.7) *Lichtenstein*	AFM	237	--	--	416	147	101
			FM	235	--	--	419	143	98
			PM	221	--	--	396	133	71
	25% SQS		AFM	235	--	--	402	151	78
			FM	233	--	--	419	139	86
			PM	228	--	--	392	137	82
	12.5% Ordered		AFM	227	--	--	416	131	72
			FM	227	--	--	413	134	69
	25% Ordered		AFM	220	--	--	401	129	82
			FM	225	--	--	404	136	83
Yang *et al.* [48] **ordered**	**25%**	LDA+*U* U (4.5 , 0.5) Pu (4.7 , 0.7) *Dudarev*	AFM	210	112	0.27	320	191	136
	50%		AFM	219	107	0.29	329	203	131
	75%		AFM	223	117	0.28	366	187	132
Ma *et al.* [79]	**50 %**	Hybrid functionals with 40% HF exchange	AFM	198	--	--	--	--	--
			FM	196	--	--	--	--	--
			NM	216	--	--	--	--	--
			AFM-SOC	199	--	--	--	--	--
			FM-SOC	195	--	--	--	--	--
			NM-SOC	210	--	--	--	--	--
Ma *et al.* [58]	**50%, O/M=1.75**	Hybrid functionals with 25% HF exchange	AFM	223	--	--	--	--	--
			FM	210	--	--	--	--	--
	50%, O/M=2.25		AFM	206	--	--	--	--	--
			FM	201	--	--	--	--	--

Table 4: Elastic properties of $(U,Pu)O_2$ and $(U,Pu)O_{2\pm x}$ obtained from electronic structure calculations. NM means non-magnetic and SOC means that the spin-orbit coupling has been taken into account.

The elastic properties of $(U,Pu)O_2$ obtained from Dorado's study for plutonium contents of 12.5 % and 25 % seem to display no significant differences for the various magnetic orders AFM and FM. Differences appear for the paramagnetic order as mentioned by the

author. In addition, the impact of the plutonium content is negligible at least up to 30 % of plutonium. Conversely, the bulk modulus and the elastic constant C_{11} from Yang *et al*. [48] seem to increase with plutonium content. It is to be noted that Yang's values are different from the ones obtained by Dorado *et al*.

The Poisson's ratio obtained by Yang *et al*. [48] is consistent with the experimental value from D. G. Martin [78] recommendations.

The difference between Yang *et al*. [48] and Dorado *et al*. [47] is probably due to the control of metastable states by the latter authors (or the lack of the control of metastable states by Yang *et al*.), enabling the system to reach the ground state as we will discuss in the next chapter. Thus we are more confident in the Dorado *et al*. LDA+*U* study since in addition to be the most recent one, it takes into account the issue of metastable states.

Ma *et al*. [79] have calculated the bulk modulus of stoichiometric $(U,Pu)O_2$ and studied the effect of spin-orbit coupling (SOC), using a hybrid functional with 40 % of Hartree-Fock exchange. The results with plutonium content of 50 % show no impact of spin-orbit coupling on the bulk modulus. The study of the effect of the deviation from stoichiometry shows the decrease in the bulk modulus for O/M ratio ranging from 1.75 to 2.25.

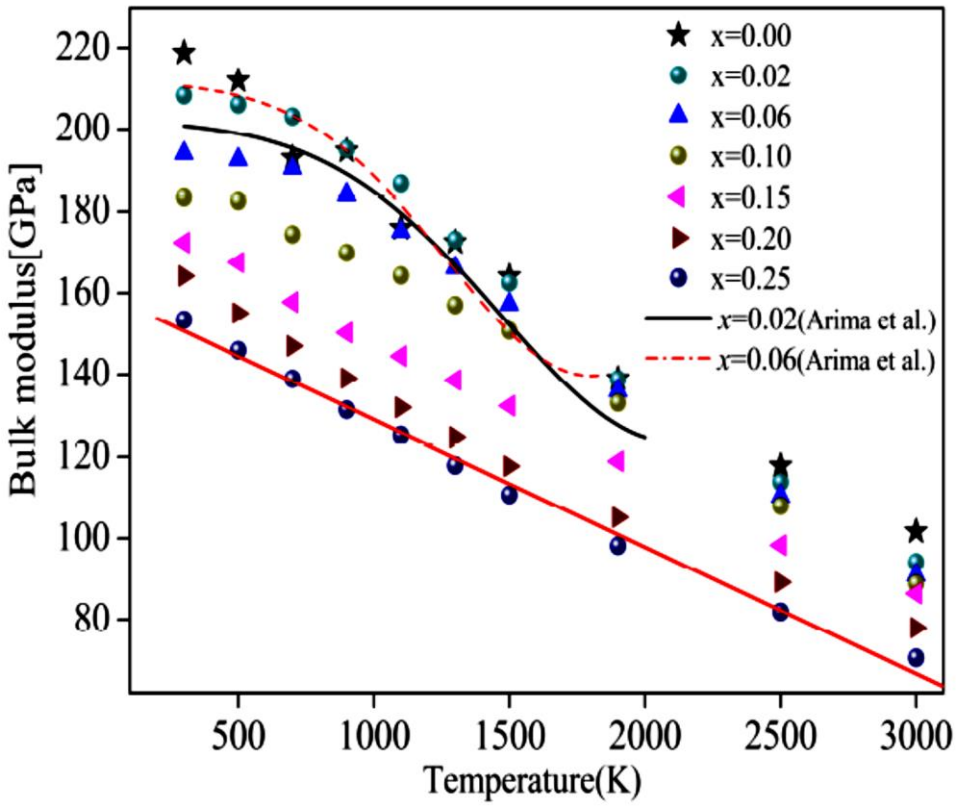

Figure 9 : Bulk modulus calculated using empirical potentials by Ma *et al*. [51] for $U_{0.75}Pu_{0.25}O_{2-x}$ and Arima *et al*. [80] for $U_{0.8}Pu_{0.2}O_{2-x}$ as a function of the deviation from stoichiometry *x* and temperature.

The bulk modulus of $(U,Pu)O_2$ has also been the subject of interest in empirical potential modelling. Ma *et al*. [51] and Arima *et al*. [80] have investigated the bulk modulus of hypo-stoichiometric $(U,Pu)O_{2-x}$ as a function of both O/M ratio and temperature. The results are shown in Figure 9. The bulk modulus does not vary significantly with the plutonium content. Moreover, the bulk modulus decreases with the deviation from stoichiometry. Also, the bulk modulus decreases with the increase in temperature.

More recently, Balboa *et al*. [81] have investigated the bulk modulus, Young's modulus and shear modulus as a function of temperature for various plutonium contents, using various empirical potentials. They also found that the plutonium content has no significant impact on these elastic properties. Once again the bulk modulus, the Young's modulus and the shear modulus decrease with the increase in temperature. Moreover, the authors recommend as reference the values yielded by Cooper's potential (CRG).

1.2.4 Thermodynamic properties of uranium-plutonium mixed oxides

The thermodynamic properties are characterized by quantities that describe the behaviour of the $(U,Pu)O_2$ with respect to the temperature. These quantities of interest are among others the melting point, the thermal expansion, the heat capacity, the thermal diffusivity and the thermal conductivity. The calculation of thermodynamic properties by first-principles method is one of the main points of this PhD study. In this section, the experimental and theoretical studies of thermodynamic quantities of $(U,Pu)O_2$, UO_2 and PuO_2 will be presented in detail.

1.2.4.1 Melting point of $(U,Pu)O_2$, UO_2 and PuO_2

The melting points of stoichiometric UO_2 and PuO_2 have been investigated in the literature. The values of 2805±15°C [82], 2876±7°C [83] and 2840±20°C [39] were reported for UO_2. Carbajo *et al.* [84] have recommended in their review the melting temperature of 2846.85±30 °C for stoichiometric UO_2. The values of 2400°C [85] and 2390±20°C [39] were reported for PuO_2. The recommendation of Carbajo *et al.* [84] for stoichiometric PuO_2 is 2427.85 ± 35 °C. These values are obtained from the thermal analysis of cooling curves using the thermal arrest method. Recently, De Bruycker *et al.* [86] have found a higher melting temperature for stoichiometry PuO_2 of 2743.85 ± 28 °C. They argue that previous results were affected by the interaction between PuO_2 and tungsten involved in the tungsten encapsulated samples of the thermal arrest method.

Lyon and Baily [39], using the thermal arrest method, have reported for $(U,Pu)O_2$ melting points at various plutonium contents. Their experimental values were

consolidated by the calculated solidus and liquidus curves as presented in Figure 10, through the ideal solid solution theory.

Lyon and Baily [39] also showed that the melting point may be sensitive to the deviation from stoichiometry, with an increase in the liquidus temperature by 85°C in the hypo-stoichiometric $U_{0.8}Pu_{0.2}O_{1.98}$ compared to the stoichiometric $U_{0.8}Pu_{0.2}O_2$.

Below a solid-liquid phase transition at the melting point, another phase transition has been pointed out experimentally by Hiernaut *et al*. [87] in UO_2 through the thermal analysis of cooling curves. This transition is known as premelting or Bredig or superionic transition and occurs near $0.85T_m$ where T_m is the melting temperature. A Bredig transition temperature of 2397±30°C was reported [87] for UO_2. Moreover, the transition temperature increases with the deviation from stoichiometry in the hypo-stoichiometric oxide, while in the hyper-stoichiometric oxide, no transition is detected. The Bredig transition is attributed to the sudden rise in the anionic diffusivity [88] and the premelting of the oxygen sublattice. There is no experimental value of the Bredig transition temperature reported in the literature for $(U,Pu)O_2$ and PuO_2 to our knowledge.

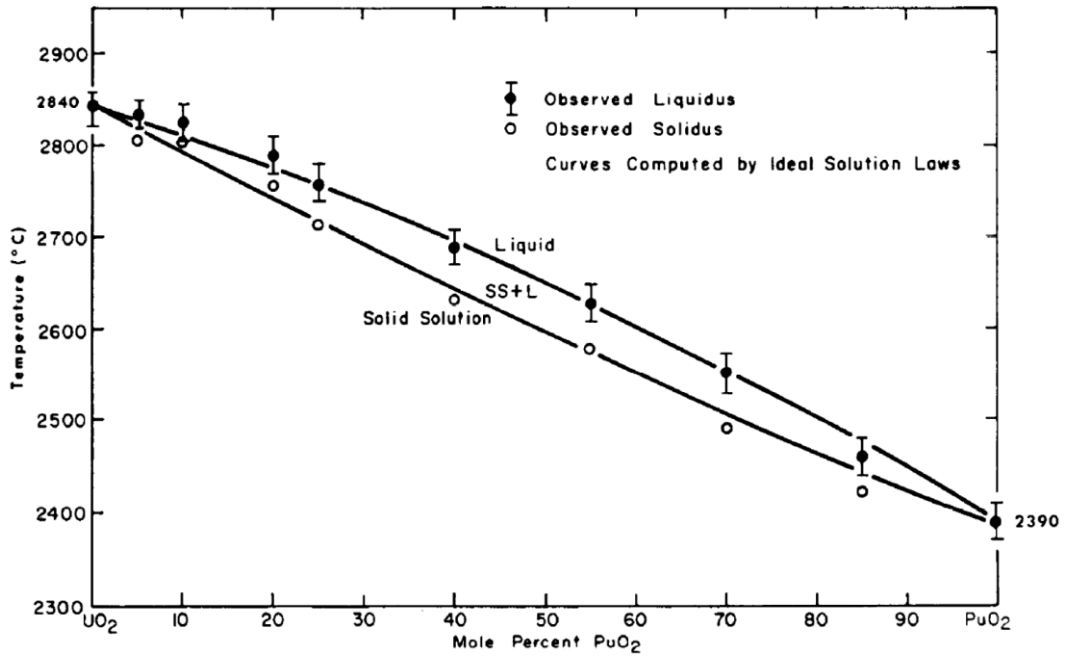

Figure 10 : Solid-liquid phase diagram for the UO_2-PuO_2 system [39].

Using empirical potential calculations, the Bredig transition temperatures of UO_2, PuO_2 and $(U,Pu)O_2$ for various plutonium contents were calculated. Using such a method, this transition is detected through the sudden changes in some properties such as thermal expansion and heat capacity. This is going to be discussed in the next sections.

1.2.4.2 Thermal expansion of uranium-plutonium mixed oxides

The thermal expansion is a key data for nuclear fuels as $(U,Pu)O_2$. Indeed, since the fuel operates at high temperature, the thermal expansion should be well monitored in order to minimise the pellet-cladding mechanical interaction [89–91]. The pellet-cladding interaction is detrimental to the mechanical strength of the cladding. The thermal expansion in $(U,Pu)O_2$ has been investigated experimentally using different methods such as the direct measurement of the linear expansion of macroscopic samples as a function of temperature or the measurement of lattice constant at various temperature ranges. All these techniques show almost the same results (see Ref. [90] for more details). In general, the linear thermal expansion for stoichiometric actinide oxides UO_2, PuO_2 and mixed actinide oxides $(U,Pu)O_2$ can be expressed as a function of temperature through the same third order polynomial relationship as proposed by D. G. Martin [90]. This relationship is known as Martin's recommendation and gives the sample length as a function of temperature as follows:

$$L = L_{273}(9.9734.10^{-1} + 9.802.10^{-6}T - 2.705.10^{-10}T^2 + 4.391.10^{-13}T^3) \qquad (2)$$

for $273\ K \leq T \leq 923\ K$ and

$$L = L_{273}(9.9672.10^{-1} + 1.179.10^{-5}T - 2.429.10^{-9}T^2 + 1.219.10^{-12}T^3) \qquad (3)$$

$$\text{for } 923\ K \leq T \leq 3120\ K$$

In these equations, L and L_{273} are the fuel lengths at the temperatures $T(K)$ and 273 K, respectively.

The above Martin's recommendations are used in the CEA fuel performance codes ALCYONE for pressurized water reactor fuels and GERMINAL for fast breeder reactor fuels. From these equations, the thermal expansion is calculated as follows:

$$\varepsilon = (L - L_{273})/L_{273} \qquad (4)$$

The empirical potential studies by Cooper *et al*. [46] and Arima *et al*. [80] report an increase in lattice parameter with temperature, with the conservation of Vegard's law up to 2000 K for $(U,Pu)O_2$. For temperatures higher than 2000 K, a deviation from Vegard's law is observed. Cooper *et al*. [46] attribute the deviation from the Vegard's law to the Bredig transition. Furthermore, they obtain the Bredig transition for UO_2, $U_{0.75}Pu_{0.25}O_2$, $U_{0.5}Pu_{0.5}O_2$, $U_{0.25}Pu_{0.75}O_2$ and PuO_2 at the temperature of 2600 K, 2500 K, 2450 K, 2375 K and 2320 K respectively. The transition temperature found in this study is consistent with the experimental value for UO_2 of 2670 K (2397°C) as mentioned in the previous section. Figure 11 below shows the evolution of the lattice constant and the deviation from Vegard's law as a function of temperature from Cooper *et al*. [46]. The experimental data for UO_2 [92], PuO_2 [93], $U_{0.75}Pu_{0.25}O_2$ and $U_{0.45}Pu_{0.55}O_2$ [39] are also included and show a good agreement with the calculated values.

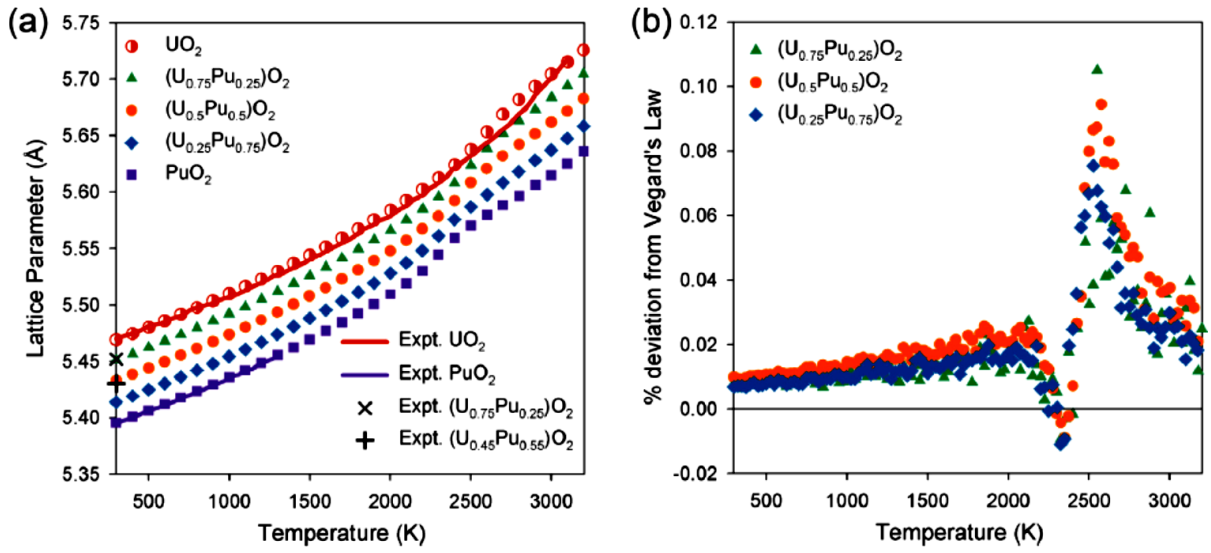

Figure 11 : Variation of (a) the lattice parameter and (b) the deviation from Vegard's law as a function of temperature for UO_2, PuO_2 and three compositions of the $U_{1-y}Pu_yO_2$ solid solution. Experimental data for UO_2, PuO_2, $U_{0.75}Pu_{0.25}O_2$ and $U_{0.45}Pu_{0.55}O_2$ are included [46].

The thermal expansion of uranium-plutonium mixed oxides depends on the deviation from stoichiometry. D. G. Martin recommends for the hypo-stoichiometry condition to multiply the thermal expansion of stoichiometric oxides by $[1 + 3.9(\pm 0.9)x]$ where x is the deviation from stoichiometry. Kato *et al*. [89] have proposed a recommendation taking into account both the contribution of plutonium content C_{Pu} and the deviation from stoichiometry x for hypo-stoichiometric $(U,Pu)O_{2-x}$, assuming the third order polynomial relationship as follows:

$$\varepsilon = a_0 + a_1 T + a_2 T^2 + a_3 T^3 \qquad (5)$$

In this expression the coefficients a_i (i = 0, 1, 2, 3) are expressed as a function of the plutonium content and the deviation from stoichiometry as follows:

$$a_i = b_{0i} + b_{1i}.C_{Pu} + b_{2i}.x + b_{3i}.C_{Pu}^2 + b_{4i}.x^2 + b_{5i}.C_{Pu}.x \qquad (6)$$

where C_{Pu} and x are the plutonium content and the deviation from stoichiometry respectively. The coefficients b_{ji} (j = 0, .., 5) were obtained by fitting experimental data [89, 94].

For both D. G. Martin's and Kato's recommendations, the thermal expansion increases with the deviation from stoichiometry for the hypo-stoichiometric oxides. There is no recommendation for the hyper-stoichiometry condition to our knowledge up to now.

1.2.4.3 Heat capacity of uranium-plutonium mixed oxides

The heat capacity of a given material is the energy needed to increase the temperature of one mole of this material by one degree Kelvin. This quantity is generally obtained indirectly through the derivative of the variation of enthalpy with respect to the temperature at constant pressure as follows:

$$C_P = (\frac{\partial H}{\partial T})_P \qquad (7)$$

For solid state materials, especially for actinide oxides, the heat capacity is the result of many contributions such as the lattice vibration which contributes by the term C_V, the thermal expansion by the term C_d, the Schottky term C_{Sch} due to the presence of Schottky defects, the electronic conductivity term C_e and the high temperature term due to the creation of oxygen Frenkel pairs C_{exc}. Thus the heat capacity is written as the sum of all these terms as follows:

$$C_P = C_V + C_d + C_{Sch} + C_e + C_{exc} \qquad (8)$$

There is a relationship between the thermal expansion term and the lattice vibration term expressed as follows:

$$C_d = \gamma . \alpha . T . C_V \qquad (9)$$

In this expression, γ is the Grüneisen coefficient, α the volumic thermal expansion coefficient and T is the temperature.

The vibrational term which is also known as the heat capacity at constant volume can be given by the Debye quasi-harmonic classical model from the classical kinetic theory as follows:

$$C_v = 9nR(\frac{T}{T_D})^3 \int_0^{T_D/T} \frac{x^4 e^x}{(e^x-1)^2} dx \qquad (10)$$

where n is the number of atoms per molecule, R is the constant of ideal gases and T_D is the Debye temperature.

Konings and Benes [95] have assessed the high temperature term due to the creation of Frenkel pairs for actinide oxides. The proposed expression is given as follows:

$$C_{exc} = \frac{\Delta H_{OFP}^2}{\sqrt{2}R.T^2} . exp\left(-\frac{\Delta H_{OFP}}{2RT}\right) . exp\left(\frac{\Delta S_{OFP}}{2R}\right) \qquad (11)$$

where ΔH_{OFP} and ΔS_{OFP} are both the variations of enthalpy and entropy of formation of oxygen Frenkel pairs respectively.

In general, the sum of C_V and C_d is sufficient to describe the heat capacity of a thermodynamic system under thermal equilibrium according to the four laws of thermodynamics. For the actinide mixed oxides, one has to take into account all

components, especially at high temperature where the formation of defects occurs. Indeed, by omitting the three last terms of the heat capacity in PuO_2 for instance, the calculation of Kato *et al*. [94] shows a lower heat capacity by 15 J/mol/K than the experimental value of Oetting [91]. By taking into account all components of heat capacity in their calculation and using the results of Nakamura *et al*. [96] on Schottky heat capacity, Kato *et al*. point out a better agreement between calculated heat capacities and experimental results for PuO_2 as shown in Figure 12. Therefore, for every calculations or fitting of heat capacity of actinide oxides, all the terms of the heat capacity as presented below have to be taken into account for an accurate description.

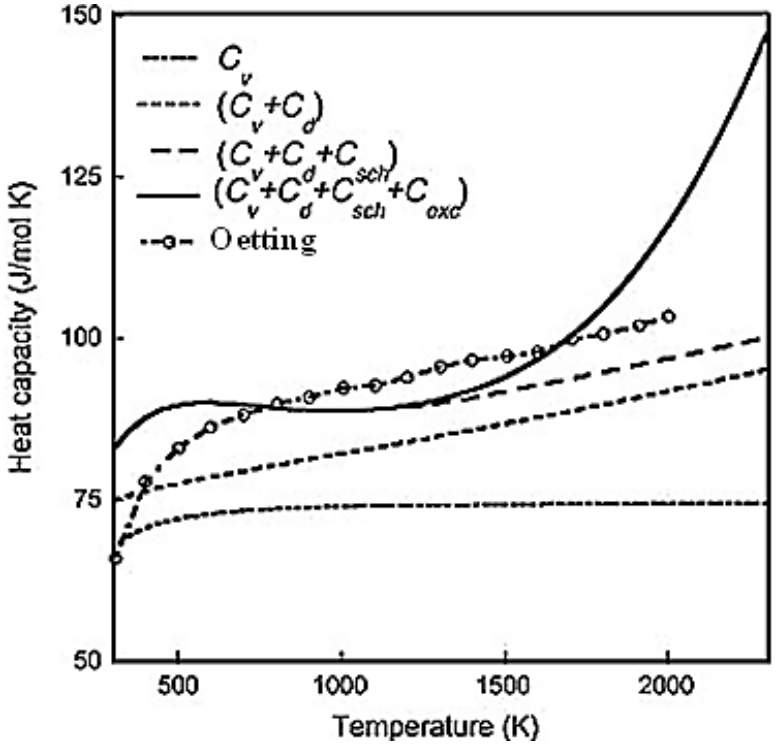

Figure 12 : Effect of different terms in the description of heat capacity of PuO_2 from Kato *et al.*[94].

The experimental heat capacities of the uranium-plutonium mixed oxides are scarce. Leibowitz *et al*. [97] and Gibby *et al*. [98] have investigated the heat capacity of $U_{0.8}Pu_{0.2}O_2$ from 2350 K to 3000 K and $U_{0.8}Pu_{0.2}O_2$ and $U_{0.75}Pu_{0.25}O_2$ from 298 K to 3000 K respectively. These data on $(U,Pu)O_2$ have been used by Fink [99], Harding *et al*. [100] and more recently by Carbajo *et al*. [84] to establish recommendations for heat capacity. The Fink's recommendation is shown in the following equation:

$$C_p(J.mol^{-1}.K^{-1}) = \frac{C_1\theta^2 e^{\theta/T}}{T^2(e^{\theta/T}-1)^2} + 2C_2T + C_3 k e^{-E_a/kT}\left(1+\frac{E_a}{kT}\right) \qquad (12)$$

This recommendation is used for UO_2, PuO_2 and $(U,Pu)O_2$ with values of the constants θ, C_1, C_2, C_3 and E_a given in Table 5. k is Boltzmann's constant. Some constants such as C_3 and E_a are lacking for PuO_2 since experimental data on PuO_2 are scarce and the few existing data are scattered according to Fink [99].

Compound	θ (K)	C_1 (J.mol^{-1}.K^{-1})	C_2 x 10^3 (J.mol^{-1}.K^{-2})	C_3 (J.mol^{-1}.eV^{-1})	Ea (eV)
UO_2	516.12	78.215	3.8609	3.4250 x 10^8	1.9105
PuO_2	587.41	87.394	3.9780		
$(U,Pu)O_{2-x}$	585.49	87.104	0.80048	2.6863 x 10^6	0.75748

Table 5 : Values of the constants used for Fink's recommendation of heat capacity [99].

The Fink's recommendation uses three terms which represent the contribution due to phonons (lattice vibrations), thermal expansion and electrons respectively.

Carbajo *et al*. [84] have recommended the application of the Neumann-Kopp rule for the uranium-plutonium mixed oxides as shown in the following equation:

$$C_p\left(T, U_{1-y}Pu_yO_2\right) = (1-y)C_p(T, UO_2) + yC_p(T, PuO_2) \qquad (13)$$

Since the experimental values of heat capacity of PuO_2 are scarce compared to UO_2 values, the authors recommend using the PuO_2 heat capacity from Fink's recommendation.

The use of Neumann-Kopp rule for the heat capacity of $(U,Pu)O_2$ means that the heat capacity of this compound increases with the plutonium content between the corresponding values for UO_2 and PuO_2. The experimental values of heat capacity of $(U,Pu)O_2$ with the plutonium contents of 21 %, 28 % and 40 % from Kandan *et al*. [101] re-assessed by Vasudeva *et al*. [102] tend to confirm this tendency. Indeed, the values of Vasudeva *et al*. presented in Table 6 show for a given temperature an increase in heat capacity with the increase in plutonium content. The difference in heat capacity between the 21 % and 40 % plutonium content (ΔC_p) also increases continuously with temperature. Cooper *et al*. [46] using empirical potentials have also shown an increase in heat capacity with plutonium content from the value for UO_2 to that of PuO_2. They also point out the Bredig transition with the rapid increase in C_P at around 2000 K. The same domain of transition has been reported by Basak *et al*. [88] through the specific heat analysis. Therefore, Fink's formula [99] is recommended for pure UO_2 and PuO_2 oxides and Carbajo's formula [84] is recommended for $(U,Pu)O_2$ since it agrees with experimental observation. This latter formula is the one recommended in the European catalogue on $(U,Pu)O_2$ properties for fast reactor's fuel within the ESNI II+ Project [17].

Temperature (K)	C_p ($J.K^{-1}.Kg^{-1}$)			
	$U_{0.79}Pu_{0.21}O_2$	$U_{0.72}Pu_{0.28}O_2$	$U_{0.6}Pu_{0.4}O_2$	ΔC_p
673	300.9	303.6	306.1	5.2
773	307.3	310.7	313.6	6.3
873	312.7	316.9	320.0	7.3
973	317.3	322.5	325.8	8.2
1073	321.4	327.7	331.2	9.8
1173	325.3	332.6	336.4	11.1
1273	329.0	337.4	341.3	12.3
1373	332.5	342.0	346.2	13.7
1473	336.1	346.5	350.9	14.8

Table 6 : Heat capacities of $U_{0.79}Pu_{0.21}O_2$, $U_{0.72}Pu_{0.28}O_2$ and $U_{0.6}Pu_{0.4}O_2$. ΔC_p is the increase in heat capacity between the plutonium contents of 21 % and 40 % [102].

1.2.4.4 Thermal conductivity of $(U,Pu)O_2$

Thermal conductivity is the material property which quantifies its ability to conduct heat. It is thus an important data for nuclear fuel performance for the evacuation of heat from the pellet central part to the coolant during operation in the nuclear reactors.

Thermal conductivity is related to many contributions such as the phonons, electron conductivity and radiative phenomena. Contrary to other material properties, the thermal conductivity does not obey the Neumann-Kopp's mixing law. It is obtained indirectly through the measurement of thermal diffusivity α, heat capacity C_p and density ρ using the following formula:

$$\lambda = \alpha \rho C_P \qquad (14)$$

The thermal diffusivity can be measured experimentally using the laser flash technique [42, 102, 103]. The results found in the literature are scattered, probably due to the difference in homogeneity of samples used and the sensitivity to the deviation from stoichiometry which is a difficult parameter to control experimentally.

The Green-Kubo [104] formula is also another way to calculate the thermal conductivity. This latter expression is for instance used in molecular dynamic calculations and represents the average of the heat flux self-correlation function [51]. The Green-Kubo's formula is given as follows:

$$\lambda = \frac{V}{3kT^2} \int_0^\infty J(t)J(0)dt \qquad (15)$$

where V is the simulation box volume, k the Boltzmann constant, T is the temperature and $J(t)$ the heat flux.

Experimental studies by Washington [105], Philipponneau [106] and Carbajo *et al*. [84] support that the thermal conductivity of uranium-plutonium mixed oxides is independent to the plutonium content. However, Vasudeva *et al*. [102] have found a decrease in thermal conductivity with the increase in plutonium content. They thus state that the effect of plutonium content is to be analysed for this mixed compound for an unambiguous conclusion. In both cases, the decrease in thermal conductivity with temperature is observed. Using empirical interatomic potential calculations, the thermal conductivity of $(U,Pu)O_2$ has been found to be lower than the values for pure UO_2 and PuO_2 [80, 107] at low temperature. This behaviour is due to the difference in cation type in the cation sublattice generating a phonon-defect scattering which is predominant at low temperature. At high temperature, the phonon-phonon scattering becomes predominant and the effect of plutonium content vanishes. The thermal conductivity becomes therefore identical to that of pure UO_2 and PuO_2 oxides as presented in Figure 13.

In order to take into account the substitutional alloy character of the cation sublattice in the thermal conductivity as it is the case for $(U,Pu)O_2$, Cooper *et al*. [107] have used the formula based on Klemens-Callaway's theory [108–112] established for the disordered alloyed semiconductors by Abeles [113]. The equivalent expression for the thermal conductivity of $A_yB_{1-y}C$ was defined by Adachi [114, 115] as follows:

$$\lambda = \frac{1}{yW_{AC}+(1-y)W_{BC}+y(1-y)C_{AC}} \qquad (16)$$

C_{AC} is the contribution of the random distribution of A and B in the sublattice. The thermal resistivity of end member AC and BC are written as follows:

$$W_{AC}= a_{AC} + b_{AC}T \quad \text{and} \quad W_{BC}= a_{BC} + b_{BC}T \qquad (17)$$

The values of the various constants in the expression of thermal resistivity obtained for $(U,Pu)O_2$ are given in Table 7.

Parameter	UO_2	PuO_2
a (mKW^{-1})	-1.36×10^{-2}	-1.96×10^{-2}
b ($m.W^{-1}$)	2.32×10^{-4}	2.13×10^{-4}
$C_{UPu} = 5.21 \times 10^{-2}$ mKW^{-1}		

Table 7 : Parameters that describe the equation of Adachi (where A = U, B = Pu and C = O_2) when fitted to the thermal conductivity data of $(U_yPu_{1-y})O_2$ as predicted from MD [107]. The fit is shown alongside the MD data in Figure 13 [107].

The thermal conductivity varies with the deviation from stoichiometry *x*. Philiponneau [106] has analysed the impact of the deviation from stoichiometry in hypo-stoichiometry conditions for $(U,Pu)O_2$ with 20 % plutonium, for *x* ranging from 0 to 0.1. He assumed that only the phonon-phonon interaction term of the thermal conductivity is affected by *x*. As to Carbajo *et al*. [84] recommendation, both phonon-phonon and

phonon-lattice interaction terms are affected by the deviation from stoichiometry. Ma *et al*. [51] have also pointed out the strong decrease in thermal conductivity at low temperature attributed to the phonon-defect interaction as mentioned above for the substitutional defects.

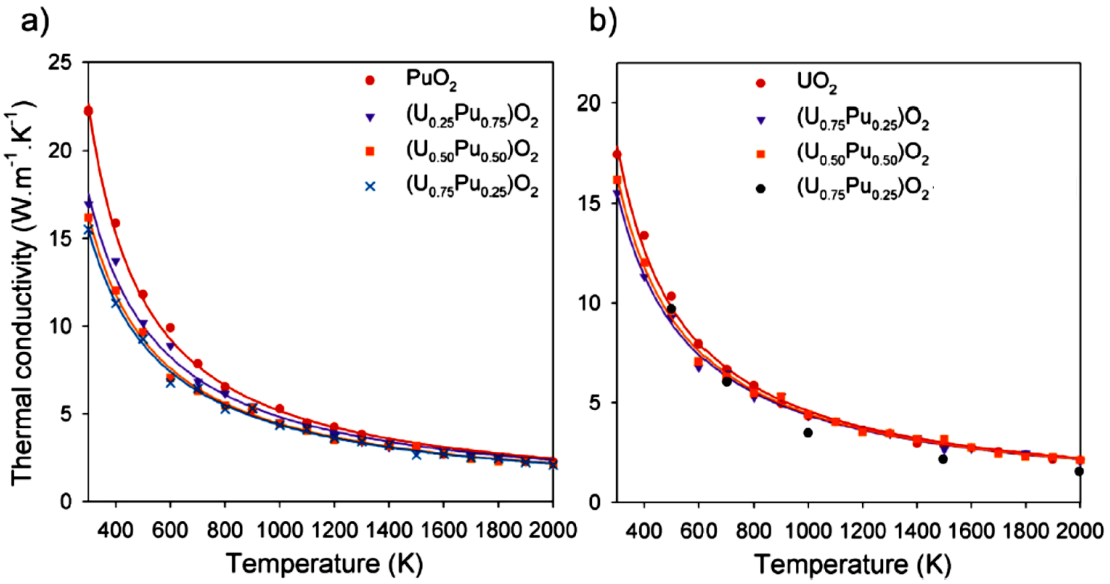

Figure 13 : Effect of the addition of a) U to PuO_2 and b) Pu to UO_2 for a range of $(U_{1-y}Pu_y)O_2$ compositions, as predicted using the non-equilibrium method [107].

1.3 Defects and atomic transport properties on UO_2, PuO_2 and $(U,Pu)O_2$

1.3.1 Defect structure and stability in UO_2, PuO_2 and $(U,Pu)O_2$

The analysis of point defect properties in nuclear fuels is an important issue that allows to improve the understanding of its thermomechanical, structural and kinetic properties at the scale of the atoms and of the microstructure. Indeed, point defects play an important role in atomic diffusion and the accommodation of stoichiometry variations that exist in actinide oxides and they constitute traps for fission products. Point defects can be classified in terms of intrinsic or extrinsic defects [116]. Intrinsic point defects are those which are created without the need of atoms to be brought or removed. These are for instance Frenkel pairs, formed by the simultaneous creation of

interstitial and vacancy of a given element in the material (V_α+I_α); Schottky defects formed by the simultaneous creation of one uranium/plutonium vacancy and two oxygen vacancies (V_{MO_2}) and anti-Schottky defects formed by the simultaneous creation of one uranium/plutonium interstitial and two oxygen interstitials (I_{MO_2}). The extrinsic point defects are those which are created by introducing or removing atoms in the material. These are for instance the oxygen/uranium/plutonium interstitials and vacancies. Defects in actinide oxides can also be neutral or charged. The charge state of defect has a significant impact on the deviation from stoichiometry x in UO_{2+x} with the oxygen partial pressure [117]. The stability of defects and thus their concentration as well as their migration can be very different between charged and neutral configurations [9, 65, 118–122]. The study of point defect stability and the effect of the charge state on formation and migration energies constitutes a key point in this manuscript. We extend the methods used for the point defect formation energies in UO_2 and PuO_2 for the study of defects in the more complex mixed oxide $(U,Pu)O_2$. Theoretical DFT studies on point defects on $(U,Pu)O_2$ are still missing and experimental defect model for this mixed compound not yet established as for UO_2 for example. Studies of defects population and concentration for end members UO_2 and PuO_2 are a first step for the analysis of defects properties on $(U,Pu)O_2$. In this section, we will present a brief literature review on point defects in UO_2 and PuO_2 and their impact on structural (interatomic distances, oxygen sublattice distortions…) and electronic properties (cation valences, Fermi-level, band gap, …).

1.3.1.1 Point defects formation energy in UO_2 and PuO_2

Experimental studies conducted on UO_2 and PuO_2, especially for the analysis of atomic transport properties have allowed to evaluate the formation energies of intrinsic defects such as oxygen/uranium/plutonium Frenkel pairs and Schottky defects [123–125]. The determination of migration energy of oxygen, uranium or plutonium vacancy and interstitial, knowing the activation energy of diffusion via vacancy or interstitial mechanism [123, 124, 126, 127], could lead to an estimation of the formation energies of extrinsic defects. However, the activation energy of diffusion may be affected by complex mechanisms such as clustering effects, deviation from stoichiometry and the simultaneous migration of vacancy and interstitial [128]. The separation of these effects is difficult to achieve experimentally.

Electronic structure calculations have been widely used for the investigation of point defects in UO_2 [9, 53, 64, 65, 76, 116–118, 120, 121, 129–134], and to a certain extent in PuO_2 [70, 135–138]. The formation energy of defects D_J with charge q is given by the following expression:

$$E_f^{D_J} = E_{tot}(D_J, q) - \sum_J n_J \mu_J + q\varepsilon_F + E_{corr} \qquad (18)$$

where $E_{tot}(D_J, q)$ is the total energy of the defective supercell, μ_J the chemical potential of element J, $\boldsymbol{\varepsilon}_F$ the Fermi energy and E_{corr} the correction term due to the defect image interaction [139].

The determination of point defect formation energies from first-principles calculations requires the knowledge of oxygen or actinide chemical potentials which constitute a key parameter in equation (18). This parameter is taken into account by different ways according to the authors.

The simplest estimates of chemical potentials consist of considering the oxygen-rich and poor regions based on the chemical potential of oxygen reference compound (O_2) for oxygen rich region, and actinide chemical potentials of reference compounds (α-uranium or α-plutonium) for oxygen-poor region. This approach is used by many if not most of authors, even for neutral or charged defects. Thus, the chemical potential of oxygen in the O-rich region is defined by the following expressions:

$$\mu_O^{MO_2} = \mu_O^{O_2} \qquad (19)$$

where M = (U or Pu) is an actinide atom whose chemical potential $\mu_M^{MO_2}$ is deduced from the chemical potential per formula unit of the constituent species:

$$\mu_M^{MO_2} + 2\mu_O^{MO_2} = \mu_{MO_2} \qquad (20)$$

Then, the chemical potentials of the constitutive atoms are directly derived from data calculated using first-principles calculations. In the oxygen-poor region, the chemical potential is taken from metallic α-phase of uranium or plutonium as written below, and the oxygen chemical potential deduced from the equation (19).

$$\mu_M^{MO_2} = \mu_M^{metal} \qquad (21)$$

The results on formation energies of point defects obtained using this approach in UO_2 and PuO_2 are shown in the following Table 8. Oxygen extrinsic defects are calculated for O-rich conditions and actinide extrinsic defects for O-poor conditions. I_j stands for interstitial of *j*-type atom, V_j for vacancy of *j*-type atom, FP_j for Frenkel pair of *j*-type atom and ISD for isolated Schottky defect. Energies are given for neutral defects in electron-volts (eV).

The standard DFT approximations (LDA and GGA) are known to give a wrong description of actinide oxides, they seem to give similar values of point defects formation energies when comparison is made between LDA and GGA-PBE functionals especially for UO_2. This tendency might be due to an error compensation [64].

Results from the DFT+*U* methods are largely scattered, especially for extrinsic defects, making these results difficult to compare. The discrepancy can be due to the values of chemical potential of reference elements, namely the oxygen and actinide chemical potentials calculated from O_2 and α-phases. However, even for intrinsic defects, the

formation energies largely scattered too, with difference in the order of magnitude of more than 1 eV. It is therefore difficult to make a clear conclusion on these values.

Compound	References	Approximation	I_O	I_{An}	V_O	V_{An}	FP_O	FP_{An}	ISD
UO_2	Crocombette [116]	LDA	-2.9	7.3	6.7	3.3	3.9	10.7	5.8
	Freyss [53]	PBE	-2.5	7.0	6.1	4.8	3.6	11.8	5.6
	Iwasawa [130]	PBE+U	-0.4	4.7	4.5	8.4	4.1	13.1	- -
	Nerikar [121]	PW91+U	-1.3	6.1	5.3	9.0	4.0	15.1	7.6
	Yu [133]	GGA+U	-2.4	2.5	5.1	4.5	2.6	7.0	3.6
	Dorado [64]	LDA+U	-0.05	5.38	5.36	10.43	4.96	15.81	10.66
PuO_2	Freyss [140]	GGA	0.1	4.9	5.3	9.2	5.3	14.1	9.1
	Tian [71]	PW91+U	--	--	--	--	9.78	19.78	14.92
	Tiwary [141]	GGA+U	--	--	--	--	3.9	11.9	--
	Lu [135]	LDA+U	1.95	--	--	--	6.05	15.85	12.88

Table 8 : Formation energies (in eV) of neutral point defects in UO_2 and PuO_2, using the oxygen chemical potential of O_2 and actinide chemical potentials of metallic α-phases.

A challenge for the determination of chemical potentials in the fluorite phase consists in bounding their values in the fluorite phase of AnO_2 in such a way that all oxidized and reduced phases in the phase diagram are excluded. This reasoning has been used by Na-Phattalung *et al*. [142] in TiO_2, Hong *et al*. [143] and Vathonne *et al*. [118] in UO_2 and Shi *et al*. [119] in CeO_2 for the investigation of point defects. This method proposes to calculate the deviation of chemical potential as a function of stoichiometry relative to the chemical potentials of the reference states, denoted by $\Delta\mu_U$, $\Delta\mu_{Pu}$ and $\Delta\mu_O$ for uranium, plutonium and oxygen. This deviation is a difference between chemical potential of atoms in AnO_2 and that of reference states. In this approach, the enthalpy of formation of An_xO_y is assumed constant up to the phase transition. Then, one can write:

$$\Delta H_f^{An_xO_y} = x\Delta\mu_{An} + y\Delta\mu_O \qquad (22)$$

Thus the boundary of the fluorite phase is determined through the condition of stability relative to oxidized and reduced phases. In fact, An_xO_y is stable if the following inequality is obeyed:

$$x\Delta\mu_{An} + y\Delta\mu_O \leq \Delta H_f^{An_xO_y} \qquad (23)$$

The curve of $\Delta\mu_O$ *vs.* $\Delta\mu_{An}$ is plotted for each An_xO_y phase and the chemical potential ranges where the fluorite phase AnO_2 is the most stable is deduced.

The use of this approach allows to improve the description of the oxygen and actinide chemical potentials in various stoichiometry conditions. The values of formation energies of point defects calculated for various charge states, for stoichiometric UO_2 by Vathonne *et al.* [118] and for hyper-stoichiometric PuO_2 by Lu *et al.* [135] are given in Figure 14.

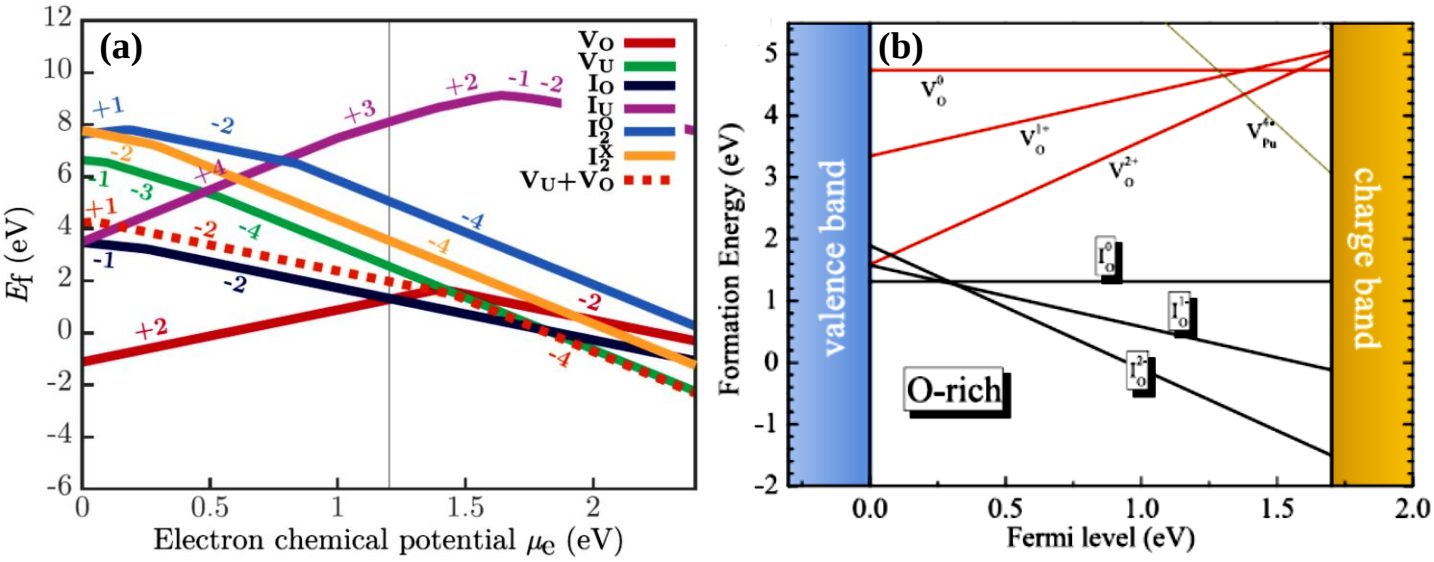

Figure 14 : Formation energies of point defects in (a) stoichiometric UO_2 and (b) oxygen-rich PuO_2. In UO_2, oxygen and uranium defects are plotted while for PuO_2, only oxygen defects are plotted, with plutonium vacancy charged +4 [118, 135].

In the stoichiometric UO_2, oxygen vacancy and interstitial in their formal charge states are stable defects and have the same formation energy in the middle of the band gap. Vathonne *et al.* [118] have shown that the deviation from stoichiometry is accommodated by oxygen defects. Oxygen interstitials in PuO_2 are found favourable in their formal charge state -2 for the Fermi level laying at the middle of the band gap under oxygen-rich condition. Under oxygen-poor condition, oxygen vacancies are found more favourable in their formal charge state +2 [135].

This previous approach takes into account the limits of stoichiometry domains for the fluorite phase. The accuracy of results given by this approach depends on the accuracy in the description of the chemical potentials of reference states of constitutive elements. These involve for oxygen element the description of the oxygen molecule O_2. However, DFT is known to provide a poor description of the oxygen molecule using the LDA or GGA functional. Thus another approach due to Finnis *et al.* [144] has been considered in the literature to circumvent the poor description of oxygen chemical potential in the reference state O_2. This approach is presented in the next paragraph. Nevertheless, we have demonstrated that the use of van der Waals vdW-DF functional [15] allows a better description of the oxygen dimer. This functional gives very similar enthalpy of

formation compared to experiments and CALPHAD calculations. Thus using this functional, we have extended the above approach to mixed actinide oxides. This will be discussed later in Chapters 2 and 3 in more details.

In the approach of Finnis *et al*. [144] which has also been used by Nerikar *et al*. [121] and more recently by Cooper *et al*. [9], the oxygen chemical potential is expressed as a function of temperature and oxygen partial pressure. This is made by using the ideal gas relations to extrapolate the oxygen chemical potential of the standard temperature and pressure. The following expression is thus obtained:

$$\mu_{O_2(g)}\left(P_{O_2},T\right)=\mu_{O_2(g)}\left(P^{\circ}_{O_2(g)},T^{\circ}\right)+\Delta\mu(T)+\frac{1}{2}k_B\mathrm{T}\log\left(\frac{P_{O_2}}{P^{\circ}_{O_2}}\right) \qquad (24)$$

$\Delta\mu(T)$ is defined as:

$$\Delta\mu(T)=-\frac{1}{2}\left(S^{\circ}_{O_2}-C^{\circ}_{P}\right)(T-T^{\circ})+C^{\circ}_{P}Tlog\left(\frac{T}{T^{\circ}}\right) \qquad (25)$$

where $S^{\circ}_{O_2}=0.0021\ eV/K$ and $C^{\circ}_{P}=7k_B=0.000302\ eV/K$ are the molecular entropy of O_2 at standard temperature T° and pressure P° (STP) and constant pressure specific heat, respectively.

In pure UO_2 or PuO_2 oxides, the STP oxygen chemical potential $\mu_{O_2(g)}\left(P^{\circ}_{O_2(g)},T^{\circ}\right)$ is obtained using the experimental Gibbs free energy of formation of the oxide. Thus, for UO_2 we can write:

$$\Delta G^{\circ}_{f,UO_2}\left(P^{\circ}_{O_2},T^{\circ}\right)=\mu_{UO_2(s)}-\mu_{U(s)}-\mu_{O_2(g)}\left(P^{\circ}_{O_2(g)},T^{\circ}\right) \qquad (26)$$

where $\mu_{UO_2(s)}$ and $\mu_{U(s)}$ are the chemical potentials of bulk UO_2 and uranium metal as calculated using DFT.

While the oxygen chemical potential is determined as a function of temperature and oxygen partial pressure, the uranium chemical potential can be deduced as a function of temperature and oxygen partial pressure from the following expression:

$$\mu_{UO_2(s)}=\mu_U\left(P_{O_2},T\right)+\mu_{O_2}\left(P_{O_2},T\right) \qquad (27)$$

Nerikar *et al*. [145] have shown using Finnis approach that, when only vacancy defects are considered, the oxygen vacancy in its formal +2 charge state is the most favourable for the Fermi level near the valence band, in accordance with the previous approach [118]. The advantage of the latter approach is the possibility to investigate the point defect formation energy at different temperature ranges and at different oxygen partial pressure, miming as possible the conditions used for experiments.

1.3.1.2 Defect concentration in UO_2 and PuO_2

In order to establish the relationship between defect concentration and temperature or oxygen partial pressure, a point defect model (PDM) has been introduced by Matzke and Lidiard [123, 146] for the closed regime. The aim is to analyse the variation of the population of point defects with stoichiometry x in $UO_{2\pm x}$. The PDM has been expanded by Crocombette *et al*. [116, 117] to deal with open regime (in which the system can exchange particle with the exterior) and charged defects. In this model, defects are non-interacting and the configurational entropy is given by the dilute limit approximation. A PDM has also recently been expanded by Garcia *et al.* [147] and Bruneval *et al.* [148] to take into account small oxygen defect clusters.

In the model for the closed regime, the combinations of isolated defects to form intrinsic defects are considered. These intrinsic defects are the oxygen Frenkel pair (FP_O), the uranium or plutonium Frenkel pair (FP_M) and Schottky defect (SD). The aim is to eliminate the ambiguity of the reference formation energies which are different for each extrinsic isolated defect. The defect concentrations are thus linked to the formation energy of each intrinsic defect:

$$[V_O][I_O] = \exp\left(-\frac{E_{FP_O}}{k_B T}\right) \qquad (28)$$

$$[V_M][I_M] = \exp\left(-\frac{E_{FP_M}}{k_B T}\right) \qquad (29)$$

$$[V_O]^2[V_M] = \exp\left(-\frac{E_{SD}}{k_B T}\right) \qquad (30)$$

The above equations are associated with the composition equation in point defect populations for the stoichiometry x :

$$x = 2([V_M] - [I_M]) + [I_O] - 2[V_O] \qquad (31)$$

In all the equations, $[D_X]$ represents the concentration of a point defect D (vacancy or interstitial) in the site X (oxygen or actinide) and x is the deviation from stoichiometry. The relationship between the deviation from stoichiometry and each defect concentration can thus be established through simple combinations between these equations.

The defect population in the closed system has been used by Geng *et al*. [149] and Crocombette *et al*. [116] in UO_2 and Lu *et al*. [135] in PuO_2 for oxygen vacancies and interstitials, and actinide vacancies. Their results are summarized in the following Figure 15 and Figure 16 respectively. The defect concentration in each oxide, obtained by Geng *et al.* and Lu *et al.*, agrees well with experimental assumption that the hypo-stoichiometry is accommodated by oxygen vacancy and the hyper-stoichiometry

accommodated by the oxygen interstitial. However, at hyper-stoichiometry, Crocombette *et al.* [116] found a predominance of uranium vacancy.

For charged defects with a given charge state q in AnO_2, the equations of the model are based on the mass conservation and charge neutrality [117]. The first condition is written as follows:

$$2\sum_q[V_{An}^q] + \sum_q[I_O^q] = 2\sum_q[I_{An}^q] + \sum_q[V_O^q] + x \qquad (32)$$

where $[D_X^q]$ is the concentration of defect D (=V or I) in site X (= O or An) with their different charge states q, and x is the deviation from stoichiometry.

The charge neutrality equation is:

$$\sum_q q[D_X^q] + p_v - n_c = 0 \qquad (33)$$

In this equation, the summation is taken over all charged defects. p_v is the concentration of holes in the valence band, and n_c is the concentration of electrons in the conduction band.

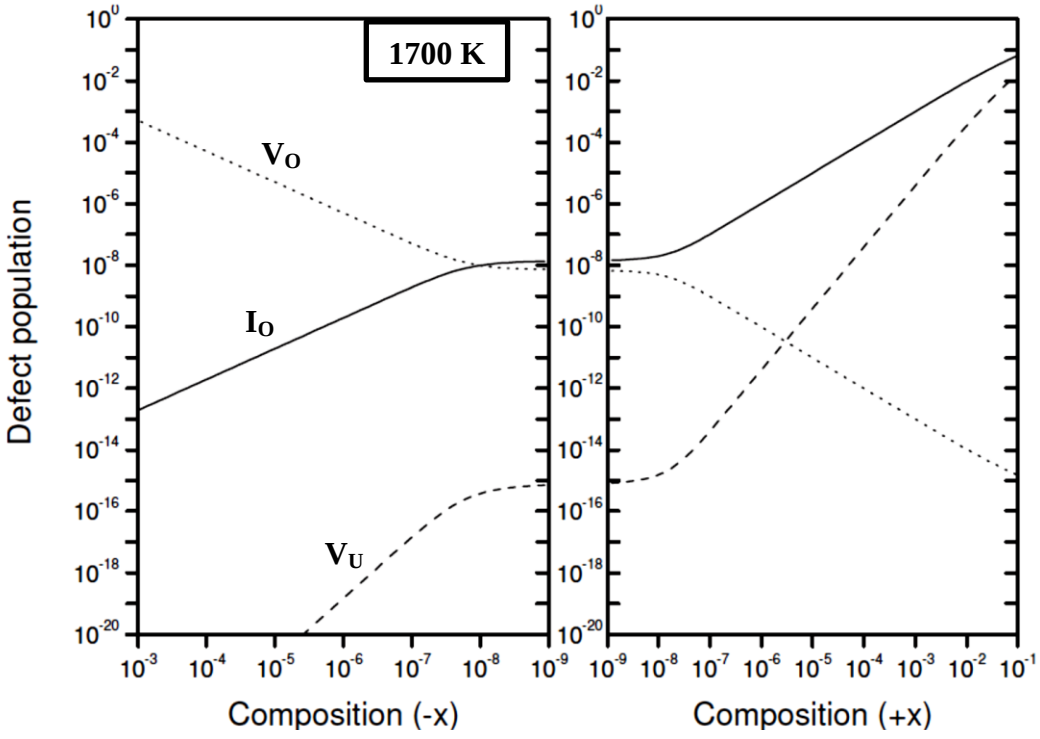

Figure 15 : Analysis of the point defect model for the neutral point defects in UO_2 at 1700K. Variation of point defect concentration with the deviation from stoichiometry. The Figure is taken from the study of Geng *et al.*[149].

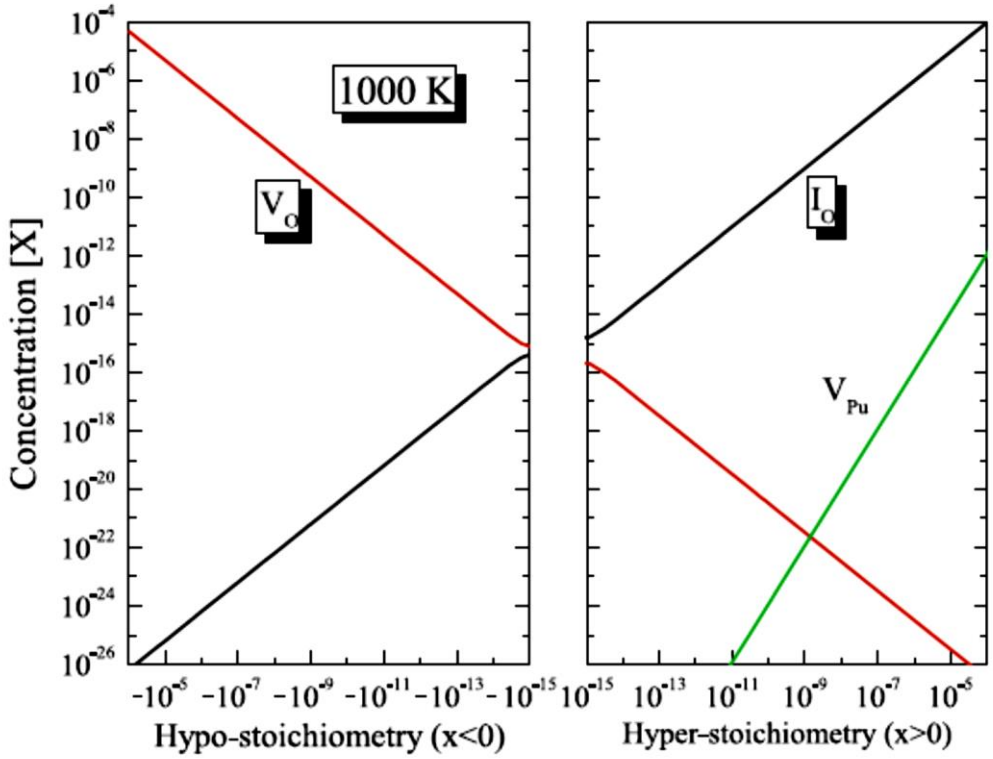

Figure 16 : Analysis of the point defect model for the neutral point defects in PuO_2 at 1000K. Variation of point defect concentration with the deviation from stoichiometry. The Figure is taken from the study of Lu *et al.*[135].

In the open regime of equilibrium of $AnO_{2\pm x}$ the concentrations of oxygen and actinide single defects can be expressed as a function of their formation energies, of temperature (T), Fermi level (ε_F) and oxygen partial pressure (P_{O_2}) [117, 135]:

$$\left[V_O^q\right] = 2 \times P_{O_2}^{-1/2} \exp\left(-\frac{E_{V_O^q}^R + q\varepsilon_F}{k_B T}\right) \quad (34)$$

$$\left[I_O^q\right] = P_{O_2}^{1/2} \exp\left(-\frac{E_{I_O^q}^R + q\varepsilon_F}{k_B T}\right) \quad (35)$$

$$\left[V_{An}^q\right] = P_{O_2} \exp\left(-\frac{E_{V_{An}^q}^R + q\varepsilon_F}{k_B T}\right) \quad (36)$$

$$\left[I_{An}^q\right] = P_{O_2}^{-1} \exp\left(-\frac{E_{I_{An}^q}^R + q\varepsilon_F}{k_B T}\right) \quad (37)$$

In the above equations, $E_{D_X^q}^R$ is the Gibbs free energy of formation of point defects which includes the enthalpy of formation (or the formation energy) and the entropy related to the formation of point defect D_X^q [9], without the contribution of the Fermi level.

The concentrations of holes and electrons both depend on Fermi level and temperature through basic Fermi statistics, given by the following equation:

$$\varepsilon_F = \frac{k_B T ln\left(\frac{n_c}{p_v}\right) + E_g}{2} \qquad (38)$$

where E_g is the band gap of AnO_2.

The latter approach has been applied to $UO_{2\pm x}$ by Crocombette *et al.* [117], Nerikar *et al.* [121] and Bruneval *et al.* [148] and to $PuO_{2\pm x}$ by Lu *et al.* [135] for the investigation of charged defects. The Brouwer diagram reported are presented by the following Figure 17 and Figure 18 respectively. Note that a similar work has been recently published by Cooper *et al.* [9], taking into account point defects formation entropy calculated through empirical potentials.

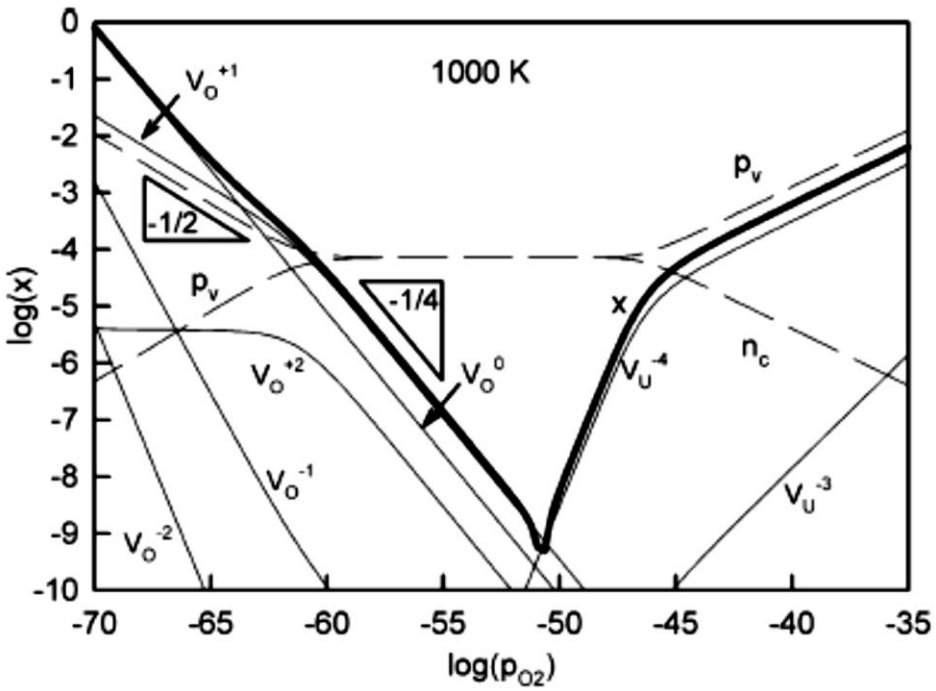

Figure 17 : Calculated Brouwer diagram as a function of the pressure of di-oxygen in equilibrium with UO_{2+x}, showing the concentrations of oxygen vacancy, interstitials and uranium vacancies in their various charge states. The concentration of electrons (e) and holes (h) are also shown. This diagram is taken from Crocombette *et al.* [117].

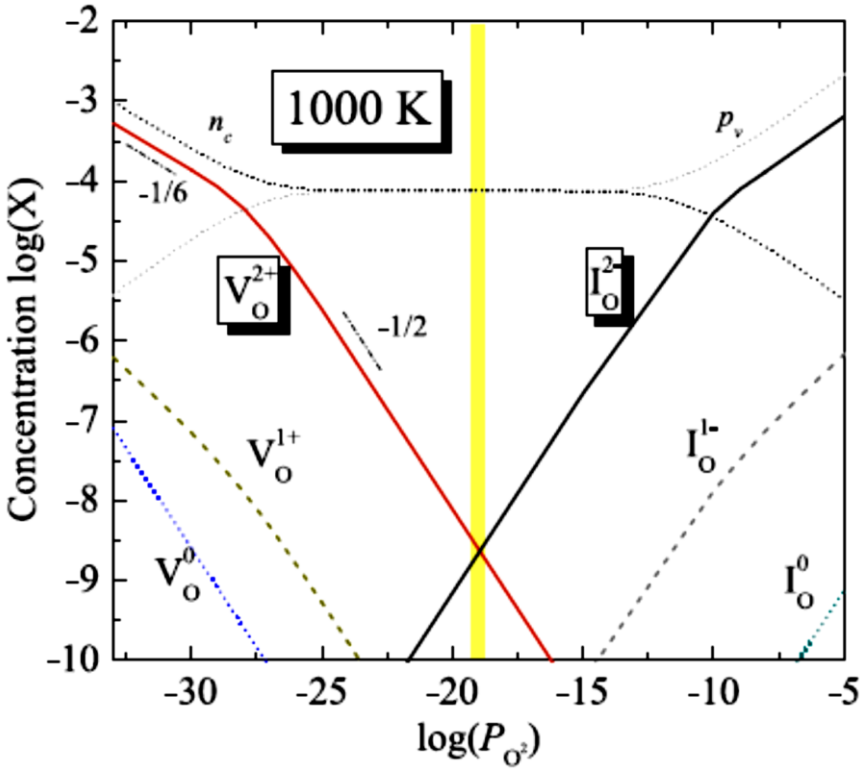

Figure 18 : Calculated Brouwer diagram as a function of the pressure of di-oxygen in equilibrium with PuO_{2+x}, showing the concentrations of oxygen vacancy, interstitials and uranium vacancies in their various charge states. The concentration of electrons (n_c) and holes (p_v) are also shown. This diagram is taken from Lu *et al.*[135].

The Brouwer diagrams for UO_2 and PuO_2 at 1000 K shows that stoichiometry is reached at higher oxygen partial pressure in PuO_2 than in UO_2. For the UO_2 compound, the calculated Brouwer diagram predicts the predominance of neutral oxygen vacancies at the hypo-stoichiometry. This result is consistent with the experiments which assume that the hypo-stoichiometry is accommodated by oxygen vacancies. However, at the hyper-stoichiometry, the model predicts the predominance of uranium vacancies in its formal charge state, contrary to the oxygen interstitial suggested by experiments. Even by considering the formation entropy [9] of uranium vacancies and oxygen interstitials, the hyper-stoichiometry is still poorly described, and the PDM predicts the predominance of uranium vacancy. This tendency is also obtained by Bruneval *et al.* [148]. Two possible limits of the defect model could explain this discrepancy. First, the oxygen clustering should play an important role in the hyper-stoichiometric oxide. Geng *et al.* [149] showed that oxygen clusters especially the cuboctahedral one [150] are more stable compared to isolated interstitials. The cuboctahedral configuration has also been identified in the PhD thesis by Ma [151], using neutron diffraction. Second, the configurational entropy implicit in the point-defect model corresponds to an infinite dilution of the defects. This can be inaccurate especially for non-negligible deviations from stoichiometry.

The model, for PuO_2, predicts the predominance of oxygen vacancies in its formal charge state +2 at the hypo-stoichiometry, and the predominance of oxygen interstitials in its formal charge state -2 at the hyper-stoichiometry [135].

In the present manuscript, the defect model, namely the evaluation of point defect formation energies, the determination of oxygen, uranium and plutonium chemical potentials, and the defect concentration is extended to the uranium-plutonium mixed oxides. This point is discussed in Chapter 4.

1.3.1.3 Structure of point defects in UO_2 and PuO_2

The presence of point defects in actinide oxides generates modifications in electronic properties and local structure. Table 9 below shows the atomic displacements and cation oxidation state induced by the neutral point defects in UO_2 [64] and formal charged defects in PuO_2 [135] as obtained from *ab initio* calculations. In this Table, X stands for defect type (Vo, Io, V_M and I_M).

In MO_2 containing neutral and charged oxygen vacancy defects, the oxygen atoms in the first coordination shell move closer to the vacancies. The displacements are about 0.1 Å in UO_2 [64] for neutral defect, accompanied by the formation of two reduced uranium cations U^{3+} in the first and second metallic coordination shell. The atomic displacements in PuO_2 have been calculated for formal charge state by Lu *et al*. [135]. This study reports the oxygen in the first coordination shell to come closer to the defect by 0.18 Å. The plutonium cations in the first coordination shell are also affected with displacements of around 0.13 Å farther from the defect.

In MO_2 containing oxygen interstitials, oxygen atoms in the first defect coordination shell are also pushed closer to the defect. The nearest neighbouring oxygen displacements in UO_2 around a neutral oxygen interstitial is of 0.16 Å [64]. The presence of a neutral oxygen interstitial in UO_2 leads to the oxidation of two uranium cations located in the second coordination shell from U^{4+} to U^{5+}[64]. The formally charged oxygen interstitial (I_O^{2+}) in PuO_2 was found to induce the displacement of the nearest neighbouring oxygen by 0.08 Å. In addition, the plutonium cations in the first coordination shell have been found to come closer to the oxygen interstitial with a displacement of around 0.12 Å. As the defect is formally charged in this case, all plutonium cations are Pu^{4+}.

In MO_2 containing an actinide (M) vacancy, oxygen atoms in the first coordination shell of the defect move farther from the defect site. For the neutral defect in UO_2, the displacement of oxygen is around +0.27 Å, accompanied by the oxidation of four first neighbouring cations into U^{5+}. The formally charged plutonium vacancy (V_{Pu}^{4-}) in PuO_2 induces the displacement of around 0.20 Å of oxygen atoms, away to the defect. The surrounding plutonium cations move closer to the plutonium vacancy by around 0.10 Å.

	Displacement and valence of cations	Site involved	Vo	Io	V_M	I_M	SD
UO_2 [64]	$d_{(X-O)}$	1rst neighbour	-0.1 Å	+0.16 Å	+0.27 Å	0	+0.25 Å
		2nd neighbour	0	0	0	0	--
	$d_{(X-U)}$	1rst neighbour	--	--	--	+0.23 Å	--
		2nd neighbour	--	--	--	--	--
	Valence of cations	1rst neighbour	1 U^{3+}	--	4 U^{5+}	distributed	U^{4+}
		2nd neighbour	1 U^{3+}	2 U^{5+}	--	--	U^{4+}
PuO_2 [135]	$d_{(X-O)}$	1rst neighbour	-0.18 Å	+0.08 Å	+0.20 Å	-0.02 Å	--
	$d_{(X-Pu)}$	1rst neighbour	+0.13 Å	-0.12 Å	-0.10 Å	+0.26 Å	--
	Valence of cations	1rst neighbour	Pu^{4+}				

Table 9 : Atomic displacements around point defects in UO_2 and PuO_2 from first-principles calculations [64, 135] and valence of cations.

In MO_2 containing an actinide interstitial, contrary to the actinide vacancy, oxygen atoms are not noticeably impacted. However, cations move further from the interstitial with an atomic displacement of around 0.23 Å in the neutral UO_2 and 0.26 Å for the formally charged plutonium interstitial in PuO_2.

The presence of defects also modifies the electronic structure of actinide oxides by inducing defect electronic states in the electronic density of states, depending on the defect charge state. In PuO_2 for instance, the presence of neutral oxygen vacancy leads to the formation of an occupied defect electronic states within the band gap [135]. This defect level is composed of plutonium *5f* vacancy neighbouring cations. This vacancy level shows a n-type doping effect [135], and disappears for the formally charged +2 defect. The electronic projected density of state showing this defect level is shown in Figure 19.

With the presence of the neutral oxygen interstitial in PuO_2, two unoccupied defect states are observed within the band gap nearby the valence band maximum (VBM). These states indicate that a neutral oxygen interstitial brings *p*-type doping effect to PuO_2. These defect states are due to two unoccupied *2p* states of the oxygen interstitial. When the defect is charged -2, four occupied peaks are observed within the band gap, indicating that an oxygen interstitial charged -2 brings n-type doping effect to PuO_2. The

projected density of states of PuO_2 containing an oxygen interstitial in two different charge states as described above are shown in the Figure 20 and Figure 21.

The structural and electronic modifications induced by point defects in $(U,Pu)O_2$ are of interest in this manuscript and will be discussed in Chapter 4 in comparison to those in pure oxides.

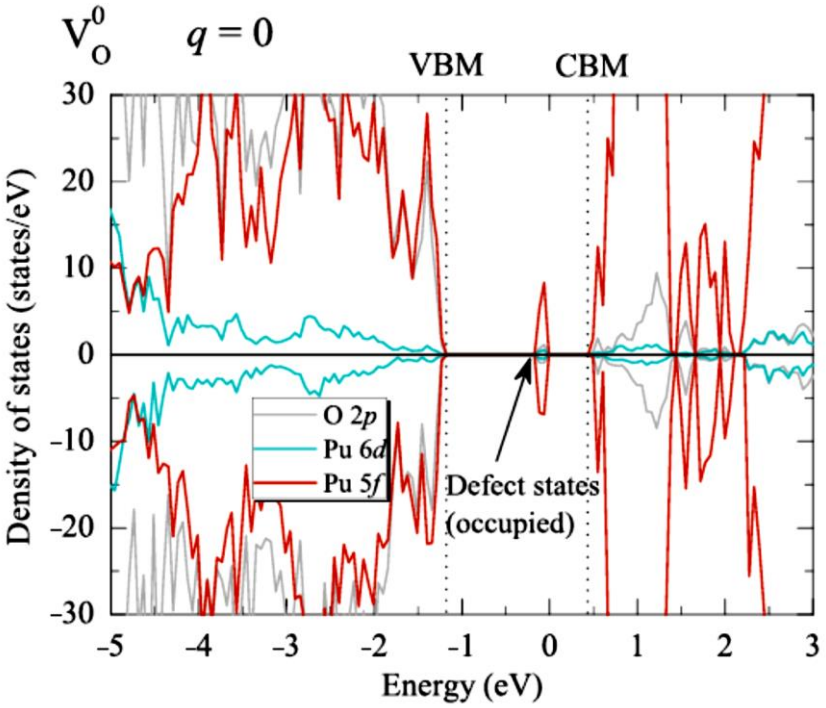

Figure 19 : Projected density of state of PuO_2 with a neutral oxygen vacancy by Lu *et al.* [135].

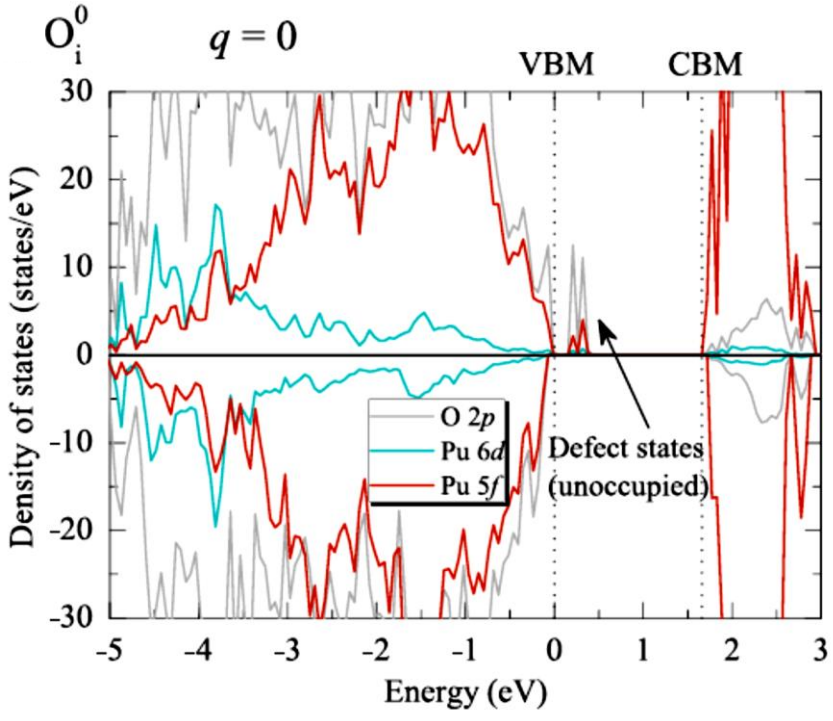

Figure 20 : Projected density of state of PuO_2 with a neutral oxygen interstitial by Lu *et al.* [135].

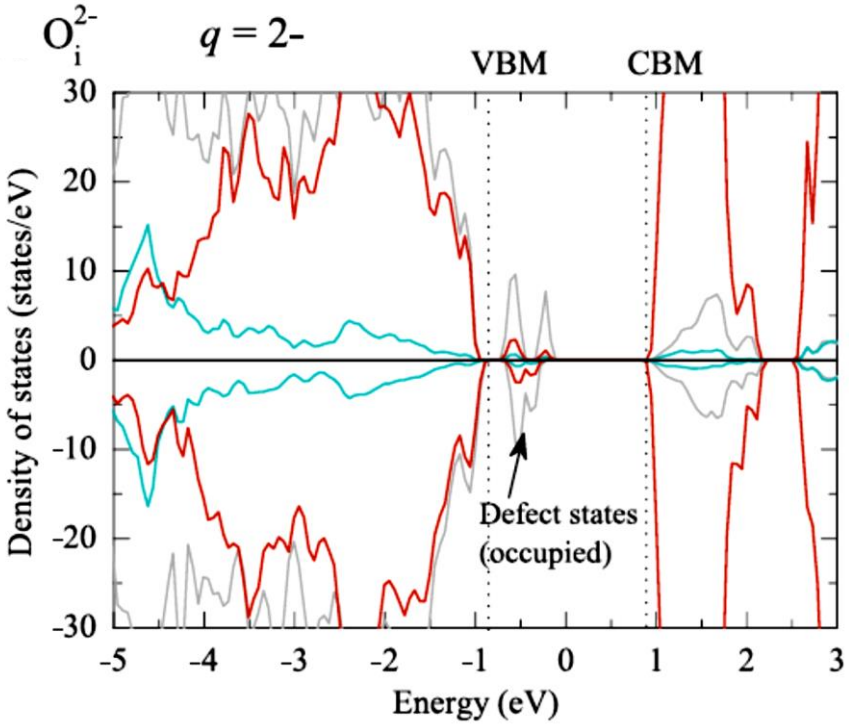

Figure 21 : Projected density of state of PuO_2 with a formally charged 2- oxygen interstitial by Lu *et al.* [135].

1.3.2 Atomic self-diffusion in UO_2, PuO_2 and $(U,Pu)O_2$

Atomic transport properties of fuel are of interest since they control the microstructural evolution under normal or accident conditions. The evolution consists for instance at the microscopic scale of the grain growth and formation of fission gas bubbles. The microstructure changes will further impact the material mechanical properties and can result in the embrittlement of fuel at the macroscopic scale. Transport properties are also of interest for fuel fabrication, especially for pellet sintering and densification processes. Diffusion properties of species are heavily influenced by the defect chemistry and respective oxidation states of the actinide elements [123]. These are for instance the self-diffusion quantified by the self-diffusion coefficient D*, the chemical diffusion quantified by the chemical diffusion coefficient $\widetilde{D}$, and the diffusion under thermal gradient. The chemical diffusion coefficient is proportional to the self-diffusion coefficient by the following relationship [123] where *F* is a Darken factor:

$$\widetilde{D} = F.D^* \text{ with } F \propto d(\Delta G(O_2))/dt \qquad (39)$$

In general, self-diffusion coefficients are written according to an exponential Arrhenius expression as follows:

$$D^* = D_o \exp(-\frac{E_a}{RT}) \qquad (40)$$

where D_o is a pre-factor which includes information concerning the atomic vibrational frequencies, entropy contribution and jump distances (interatomic spacing). E_a is the activation energy. It represents the energy needed for a defect to form and migrate. It can thus be expressed as a function of the migration energy and the formation energies of the defects assisting the diffusion. This quantity can be calculated through electronic structure calculations [11] and used to identify elementary diffusion mechanisms. This point is an important part of this PhD work, aiming at providing data such as activation energies and migration mechanisms for (U,Pu)O_2 to thermo-kinetic CALPHAD/DICTRA model [23, 148, 149] and to better validate empirical interatomic potentials.

Oxygen self-diffusion is usually measured using the stable ^{18}O isotope as a tracer. MO_2 samples are saturated with ^{18}O, often by means of an inert atmosphere containing the tracer. An annealing procedure is applied under a controlled atmosphere for a given duration, related to the sample size. Analysis methods may consist of spectrometry techniques such as secondary ion mass spectrometry (SIMS), electrical conductivity as well as nuclear reaction analysis (NRA) method which is used as a mean of non-destructive detection of oxygen profiles through measuring the emitted alpha particles [152]. The limitation of experimental measurements is its inability to determine unequivocally the elementary mechanism related to oxygen migration. Another difficulty is the simultaneous control of physical parameters which affect the material such as temperature, oxygen partial pressure and defects concentration [64].

As for the uranium self-diffusion, several isotopes such as ^{237}U [153], ^{233}U [154, 155], ^{235}U [154, 156, 157] are commonly used as tracers, and analysed using α-degradation methods as well as SIMS spectrometry [157]. Here again, the effect of temperature, oxygen partial pressure and defect concentration are difficult to monitor. Moreover, a significant surface effect caused by phenomena such as surface relaxation/smoothing or damage due to mechanical polishing are reported in the literature [123]. For UO_2 for instance, these effects may explain the scattered values of self-diffusion coefficients of uranium since they involve the faster penetration of tracers leading to the much higher values than expected.

In the following subsections, the transport properties of oxygen and actinide atoms are reviewed for UO_2, PuO_2 and (U,Pu)O_2. For a detailed overview on a CALPHAD/DICTRA model of atomic diffusion calculations, refer to Moore *et al*. [127, 128].

1.3.2.1 UO_2

In this subsection, results on the diffusion of oxygen and uranium species in UO_2 are reviewed separately.

Several experimental and theoretical studies have been conducted on the oxygen diffusion in uranium dioxide under stoichiometry, hypo-stoichiometry and hyper-stoichiometry conditions. Those studies have been reviewed in detail by Berthinier *et al*. [158]. The critical review of Moore *et al*. [128] has led to select data consistent to each other for DICTRA calculations. Table 10 below shows the oxygen diffusion properties obtained from different methods for various stoichiometry conditions (i.e O/M ratio) and temperatures ranges from both the review by Berthinier *et al.* and the more recent study by Moore *et al*. [128].

References	Method	O/U	Diffusion coefficient D* (m^2/s) and Ea (eV)	Temperature (K)
Kim and Olander [126]	^{18}O tracer, U liquid between UO_{2-x}	Phase boundary U-UO_{2-x} composition from Fryxel *et al.* [160]	$1.4x10^{-8}exp(-0.5/kT)$	1463 - 1838
Auskern and Belle [154]	^{18}O isotopic exchange via CO_2(g) Mass spectrometric analysis of the gas phase	O/U = 2.002 O/U = 2.004 O/U = 2.063	$1.2x10^{-1}exp(-2.8/kT)$ $7x10^{-10}exp(-1.3/kT)$ $2.06x10^{-7}exp(-1.3/kT)$	823-1053
Contamin *et al*. [161]	Single couple $^{18}O(p,\alpha)$ ^{15}N(0.6 MeV) Nuclear reaction Sectioning/analytical method SIMS analysis of ^{18}O Single crystal or sintered (no differences)	O/U = 2.006 O/U = 2.02 O/U = 2.1 O/U = 2.12 O/U = 2.16	$5x10^{-9}exp(-0.91/kT)$ $10x10^{-9}exp(-0.91/kT)$ $2.7x10^{-8}exp(-0.93/kT)$ $5x10^{-8}exp(-0.95/kT)$ $6x10^{-8}exp(-0.95/kT)$	673-1173 673-1073 773-1073 873-1073 1073-1183
Murch *et al*. [162]	$^{18}O(p,\alpha)$ ^{18}F(2.75 MeV) $^{17}O(d,n)$ ^{18}F(1.2 MeV) Nuclear reaction[a]	2.011 < O/U < 2.16±0.02	At mean O/U ≈ 2.08 $6.25(\pm5.03)x10^{-8}exp(-1.00\pm0.16/kT)$	833-1074
Matzke [123]	Experimental and theoretical review	O/U = 2	$0.26x10^{-4}exp(-2.60/kT)$	1000-2000
Garcial *et al*. [163]	Electrical conductivity mearsument and SIMS	O/U = 2	$5.4x10^{-19}$ to $1.8x10^{-17}$	1273-1573

Table 10 : Review of oxygen self-diffusion coefficients and activation energy of UO_2 from experiments and calculations.

The reviewed self-diffusion coefficients show scattered values of pre-factor D_o and activation energies E_a for a given stoichiometry condition. Therefore, it is difficult to determine a unique diffusion coefficient and identify the diffusion mechanism for UO_2. Nevertheless, the oxygen migration mechanism is assumed to be vacancy-assisted at the hypo-stoichiometry condition. An interstitial-assisted mechanism was found for a small

hyper-stoichiometric deviation using a combination of well controlled experiments and DFT calculations [11]. The scatter in the literature values is, however, probably due to the difficulties of experimental procedures in controlling all parameters involved as pointed out in the previous section. Indeed, as reported in the literature, even at very small hyper-stoichiometric deviation, the oxygen diffusion mechanisms are strongly affected by cluster formation. Oxygen interstitial defects can form clusters with special spatial configurations as mentioned by Willis [159].

Moore *et al*. [128] have demonstrated using CALPHAD/DICTRA calculations that the cluster formation has to be taken into account in the oxygen self-diffusion. Indeed, a simple fit without including cluster effects does not describe both temperature and composition dependence of the diffusion coefficient. When the cluster formation is taken into account both dependences are well described. The oxygen vacancy and interstitial migration energies are thus calculated and compared with other literature values as shown in Table 11.

Defect type	Migration energies (eV)					
	Matzke [123]	Dorado [11]	Morelon [164]	Kim and Orlander [126]	Berthinier [158]	Moore [128]
Oxygen vacancy	0.51	0.67	0.33	0.501	0.99	0.67
Oxygen interstitial	0.81-1.00	0.93	0.65	--	1.07	1.11

Table 11 : Migration energies of oxygen vacancy and interstitial in UO_2.

The uranium diffusion in UO_2 is less studied experimentally. The diffusion of uranium reviewed by Matzke [123] pointed out scattered values from experimental studies by Sabioni *et al*. [157], Auskern and Belle [154], Schmitz and Lindner [156], Alcock *et al*. [165], Matzke [166], Lindner and Schmitz [167] and Yajima *et al*. [153] for a stoichiometric UO_2. The same tendency is observed for hyper-stoichiometry conditions. Experimental data are missing for the hypo-stoichiometry conditions. This scatter is illustrated in the following Figure 22 from Moore *et al*. [128].

For the good reproduction of selected experimental diffusion coefficients, Moore *et al*. have added the mixing term to account for the mixed (U^{4+}, U^{5+}) cation valence states in hyper-stoichiometry condition. This model allows them to calculate the activation energy of uranium diffusion of 5.3 eV which decreases by nearly 2 eV from stoichiometric compositions to O/U = 2.20. Moreover, the accepted mechanism of migration as described by point defect models is that of uranium vacancies in the hyper-stoichiometric oxide. Table 12 below shows migration energies of uranium diffusion from various studies.

Defect type		Migration energies (eV)			
	Matzke [123]	Dorado [168]		Andersson [169]	Morelon [164]
		LDA+*U*	GGA+*U*	LDA+*U*	
Uranium vacancy	2.4	4.8	3.6	4.81	4.46

Table 12 : Migration energies of uranium vacancy in UO_2.

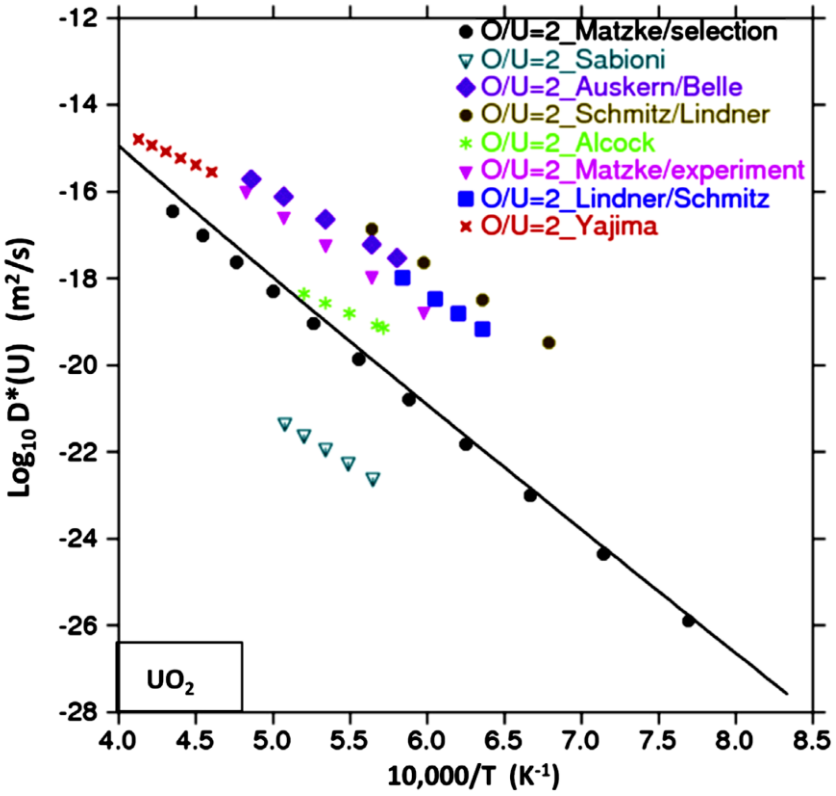

Figure 22 : Review of uranium self-diffusion coefficient as a function of temperature at O/U = 2 by Moore *et al.* [128].

1.3.2.2 PuO_2

Few studies on atomic diffusion in PuO_2, and much less than UO_2, have been conducted through experiments and modelling. In this subsection, we propose a brief review of oxygen diffusion in PuO_2 as done previously for UO_2.

Oxygen diffusion properties have been studied in the literature for both hypo-stoichiometric PuO_{2-x} and stoichiometric PuO_2. However, direct self-diffusion studies are only available for stoichiometric PuO_2 [124, 170], through the gas-solid exchange between PuO_2 and ^{18}O. The available diffusion coefficients for the hypo-stoichiometric PuO_{2-x} are the chemical diffusion coefficients [125, 171–173]. Both thermogravimetric technique and electrical conductivity measurements have been used in the latter case. The self-diffusion coefficients are then derived from an analytical relationship [174] between the chemical diffusion coefficients and the thermodynamic factor from a relevant thermodynamic description. These experimental data are reported in

Figure 23 from the assessment by Moore *et al*. [127].

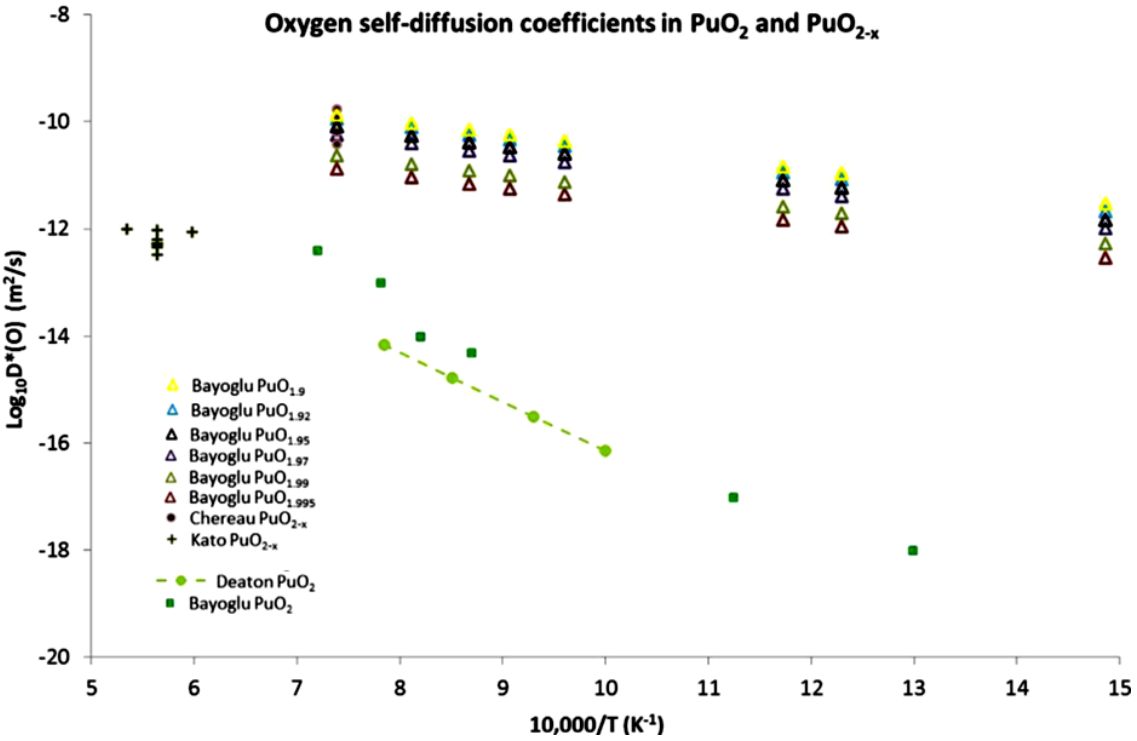

Figure 23 : Oxygen self-diffusion coefficient in hypo-stoichiometric PuO_{2-x} and stoichiometric PuO_2 [127].

The self-diffusion coefficients of the hypo-stoichiometric oxide, derived from chemical diffusion coefficients, are consistent to each other except the lower values from Kato *et al*. [173] who use the reducing atmosphere H_2/H_2O for reducing reaction. Moore *et al*. [127] argue about these lower values that the H_2/H_2O atmosphere could promote a deceleration of the measured diffusion coefficients due to possible formation of hydrates competing with oxygen departure during reduction. However, the increase

in diffusion coefficient with temperature is observed for both stoichiometric and hypo-stoichiometric oxides. The oxygen diffusion is higher in the hypo-stoichiometric than stoichiometric oxide due to the large concentration of oxygen vacancies, supporting that the oxygen diffusion in plutonium dioxide is vacancy assisted. Table 13 below shows the migration and activation energies for oxygen diffusion in PuO_2 and PuO_{2-x}. Moore's and Deaton's values are for the stoichiometric oxide. These results highlight that the oxygen migration energy in the stoichiometric PuO_2 (0.47 eV) is relatively smaller than for the stoichiometric UO_2 (0.67 eV).

	Moore [127]	Bayoglu [125]	Deaton [170]
Migration energy (eV)	0.47	0.46	--
Activation energy (eV)	1.81	1.94	1.83

Table 13 : Migration and activation energies of diffusion in PuO_2 and PuO_{2-x}.

1.3.2.3 $(U,Pu)O_2$

Experimental studies have widely focused on chemical diffusion rather than self-diffusion in uranium-plutonium mixed oxides. D'annuci and Sari [175], Sari [176] using thermogravimetry have evaluated the oxygen chemical diffusion in both hypo-stoichiometric and hyper-stoichiometric $U_{0.8}Pu_{0.2}O_2$. Bayoglu and Lorenzelli [177–179] have used thermogravimetry and dilatometry to study the oxygen chemical diffusion in hypo-stoichiometric and hyper-stoichiometric $U_{0.8}Pu_{0.2}O_2$. Oxygen chemical diffusion has also been investigated more recently by Kato *et al*. [180] through thermogravimetry for 20 % and 30 % of plutonium content. These data are shown in Figure 24 for hypo-stoichiometric oxides and Figure 25 for hyper-stoichiometric oxides. The only direct measurement of oxygen self-diffusion has been done recently by Vauchy *et al*. [181, 182] through the gas-solid isotope exchange. Table 14 shows the related values.

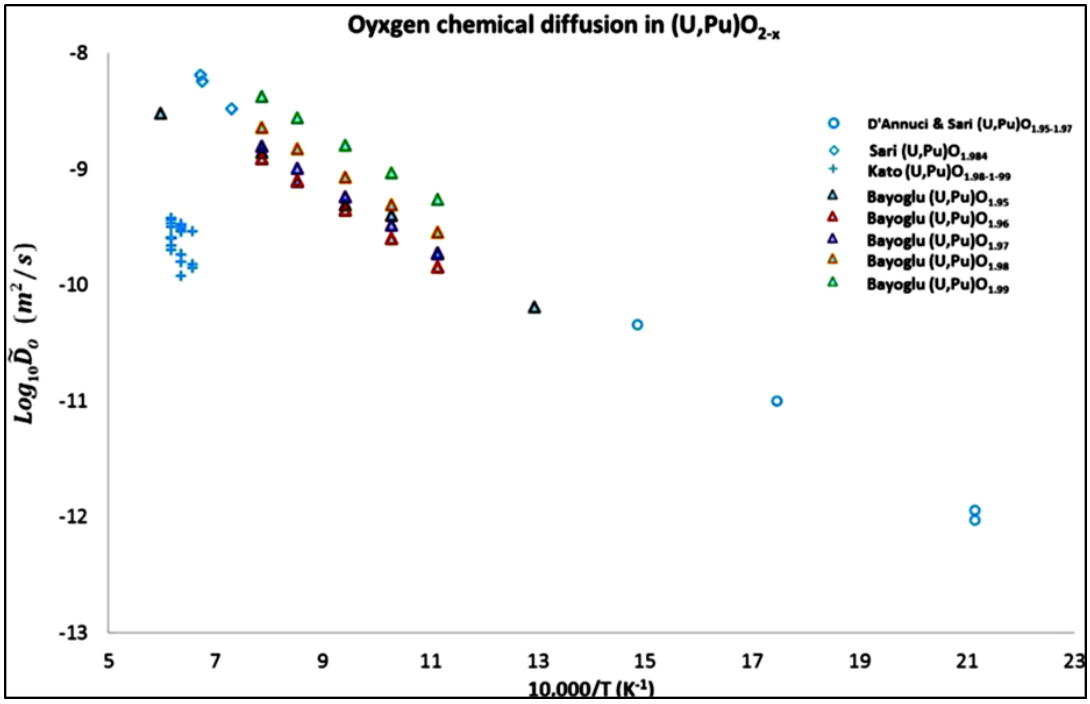

Figure 24 : Oxygen chemical diffusion coefficient of hypo-stoichiometric $U_{0.8}Pu_{0.2}O_{2-x}$ [127].

Experimental conditions	1073 K 3.2(5).10^{-23}bar	1273 K 2.7(1).10^{-18}bar	1273 K 2.2(1).10^{-17}bar	1273 K 3.4(2).10^{-16}bar
Self-diff. coeff D^* (m^2.s^{-1})	1.5(2).10^{-16}	3.7(2).10^{-14}	2.0(2).10^{-14}	4.5(2).10^{-15}

Table 14 : Oxygen self-diffusion coefficient in $U_{0.55}Pu_{0.45}O_2$ for various temperatures and oxygen partial pressures [181, 182].

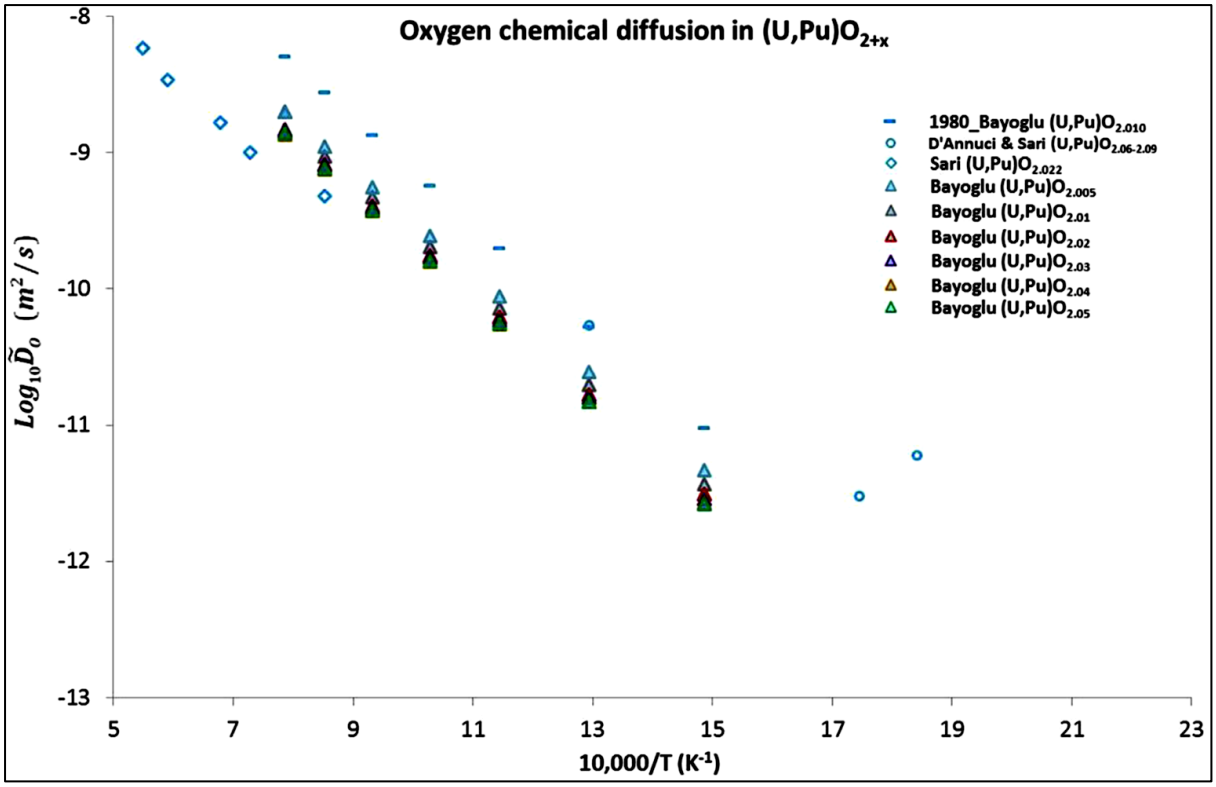

Figure 25 : Oxygen chemical diffusion coefficient of hyper-stoichiometric $U_{0.8}Pu_{0.2}O_{2+x}$ [127].

Still, Kato's values [180] for hypo-stoichiometric $U_{0.8}Pu_{0.2}O_2$ are lower than other experimental values, although similar atmospheric conditions as in Refs. [177, 179] were used. Moore *et al*. [127] argue that differences in the diffusion coefficients must be explained by the experimental procedure of the reduction *vs.* oxidation curves. Kato *et al*. [180] explain the higher values of the other experimental data by the fact that they use an oxidation procedure which does not follow the model of oxygen chemical diffusion.

The increase in diffusion coefficient with temperature is obtained in all cases for hypo-stoichiometric and hyper-stoichiometric $(U,Pu)O_2$ for both oxygen diffusion and uranium diffusion. Moreover, Vauchy *et al*. [181] have pointed out the fact that the oxygen self-diffusion coefficient decreases with the increase in oxygen partial pressure. They thus conclude on a vacancy-assisted diffusion mechanism for oxygen diffusion in $(U,Pu)O_2$. The experimental activation energies for oxygen diffusion from the literature are given in Table 15.

References		Kato [180]	Bayoglu [179]	Sari [176]
Activation energy (eV)	O/M < 2.00	0.62 0.91 (Pu/M=0.3)*	0.56	0.30
	O/M > 2.00	--	0.76	--

Table 15 : Activation energy of oxygen diffusion in hypo-stoichiometric (O/M < 2.00) and hyper-stoichiometric (O/M > 2.00) uranium-plutonium oxide with a plutonium content of 20 %. The star (*) is on the value obtained for 30 % Pu given by Kato.

Kato *et al*. [180] have obtained the oxygen chemical diffusion to be higher in $U_{0.8}Pu_{0.2}O_{2-x}$ (20 % Pu content) than in $U_{0.7}Pu_{0.3}O_{2-x}$ (30 % Pu content) with different activation energies in those plutonium compositions as shown in Table 15. The authors attribute this difference to the different types of point defects in $U_{0.8}Pu_{0.2}O_{2-x}$ and $U_{0.7}Pu_{0.3}O_{2-x}$ as shown in Ref. [183], since the diffusion coefficient is well known to be dependent on the defect chemistry [184].

The effect of plutonium content and temperature in oxygen diffusivity has been studied in detail by Cooper *et al*. [46], using empirical interatomic potential calculations (Figure 26). This study shows for $(U,Pu)O_2$ three mobility regimes for oxygen:

- A low mobility regime obtained for temperatures lower than the Bredig super-ionic transition temperature. This regime is characterized by higher activation enthalpies, higher than 4.5 eV at 2200 K (Figure 26-b). Moreover, the activation enthalpies are different from one composition to another, suggesting differences in oxygen diffusion mechanism for each Pu composition.
- A transition region, where an abrupt decrease in activation enthalpies of about 2.5 eV is observed. This transition corresponds to the Bredig transition (Figure 26-b).
- A high mobility regime obtained for temperatures higher than the Bredig transition temperature. This regime is characterized by lower and uniform activation enthalpies (less than 2 eV) for each plutonium composition (Figure 26-b). This means that at this regime, the diffusion mechanism is the same at all Pu compositions.

The difference in oxygen diffusion mechanisms below and above the Bredig transition temperature leads to the loss of Arrhenius's behaviour. An additional term for oxygen anions diffusion is then added to the standard exponential law as suggested by [88].

It is also to be noted that the oxygen diffusivity increases with the increase in plutonium content (Figure 26-a).

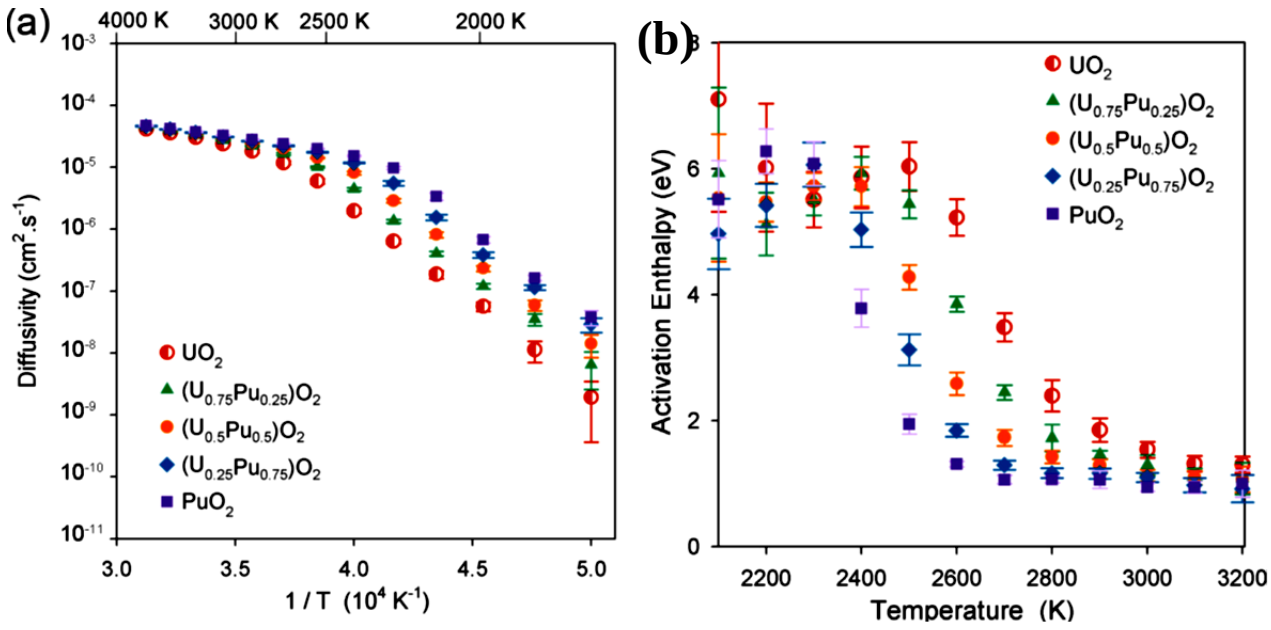

Figure 26 : Oxygen diffusivity and activation enthalpy of $(U,Pu)O_2$ with various plutonium contents assessed by Cooper *et al.* [46] using empirical potential calculations.

The diffusion properties of actinides U or Pu in $(U,Pu)O_2$ are scarce. Only very few and dated studies on the diffusion of Pu in $U_{0.8}Pu_{0.2}O_{2\pm x}$ are available, as mentioned by Matzke [123]. The diffusion of uranium and plutonium in $(U,Pu)O_2$ is slower than that of oxygen at most accessible temperatures ($D^M < 10^{-17}$ m²/s for T < 1500 K). Moreover, data on those phenomena are scare and somewhat not representative of the real bulk diffusion. As explained by Matzke [123], the main reasons for that are the high evaporation rates, the formation of striated surfaces due to the anisotropy of the surface energy.

The only relevant experimental measurements of actinide diffusion in $(U,Pu)O_2$ in the literature are those of Schmitz and Marajofsky [185] on the diffusion of Pu in $U_{0.8}Pu_{0.2}O_2$. They have applied a long annealing time in order to reduce errors due to the phenomena mentioned above. Figure 27 below shows the evolution of Pu self-diffusion in $(U,Pu)O_2$ as a function of the oxygen potential.

Matzke pointed out the faster diffusion of Pu in the hyper-stoichiometric oxide rather than the hypo-stoichiometric one. He also showed a minimum of D^{Pu} in the hypo-stoichiometric $(U,Pu)O_{2-x}$ at $x \approx -0.02$ and an increase again upon further reduction, for which a diffusion mechanism via metal interstitial and/or cluster mechanism was suggested [166, 186]. The cluster mechanism tends to be consolidated since Matzke has calculated the simple Pu^{3+}-Vo-Pu^{3+} defect to saturate for O/M= 1.95, which corresponds to oxygen contents for which D^{Pu} reaches a constant value. For $x \geq -0.02$, the vacancy mechanism is suggested.

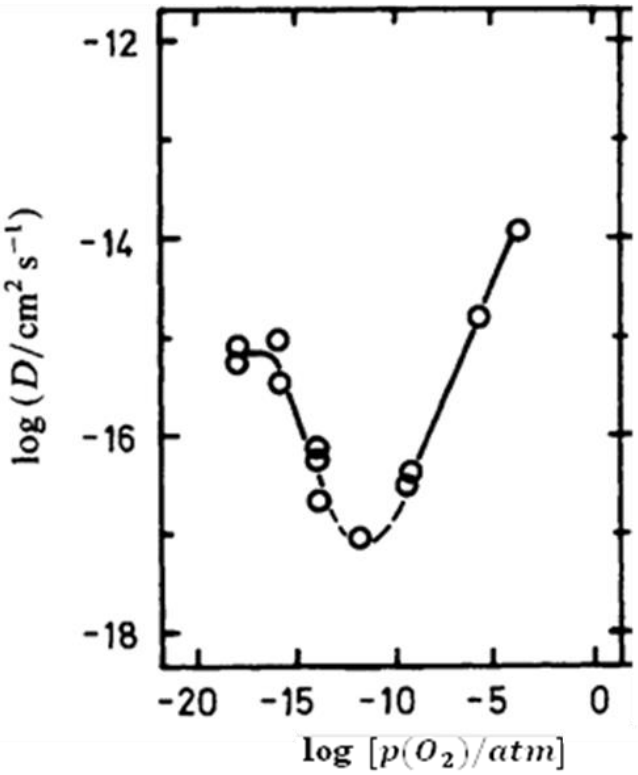

Figure 27 : The dependence of plutonium diffusion in $U_{0.8}Pu_{0.2}O_{2\pm x}$ *vs.* oxygen potential of annealing atmosphere by Schmitz and Marajofsky [185].

The increased diffusion of Pu in hypo-stoichiometric $(U,Pu)O_{2-x}$ for O/M below its value at the minimum of D^{Pu} may be partly due to the faster mobility of reduced Pu^{3+} ions compared to Pu^{4+}, as proven by Matzke [123] in single ThO_2 crystal. The faster mobility of Pu^{3+} has also been proven by theoretical calculations by Jackson *et al*. [187, 188] with the increase in activation energy by 31%.

Matzke reported unsuccessful attempts to measure the mobility of U in $(U,Pu)O_{2-x}$ owing to difficulties to measure the U-diffusion profiles in the presence of Pu.

1.4 Conclusion

We have reviewed in this chapter major and relevant studies on material properties of $(U,Pu)O_2$, UO_2, and PuO_2. On the first hand, the phase evolution of U-Pu-O system has been presented through the description of the phase diagram. The phase diagram will be important for the determination of atomic chemical potentials in $(U,Pu)O_2$ in our calculations of formation energies of point defects. Structural properties in terms of the

description of the evolution of the lattice constant with respect to Pu contents (Vegard's law) as well as the deviation from stoichiometry has also been shown. Moreover, we have presented available elastic, electronic and magnetic properties of $(U,Pu)O_2$, UO_2 and PuO_2. These results constitute the reference values for the validation of the approximations we use in our DFT calculations. Another topic reviewed in this chapter is the thermodynamic properties of $(U,Pu)O_2$ for various Pu contents as well as UO_2 and PuO_2, from both experiments and empirical potentials modelling. We have highlighted some discrepancies, especially concerning the melting temperature of PuO_2 for which recent measurements have pointed out a potential methodological interference on old values. The thermal expansions, the heat capacities and the thermal conductivities were also reviewed in detail, with a particular focus on the effect of Pu content. These values will be used to validate the implementation of *ab initio* molecular dynamics for actinide based materials. This point constitutes a challenging objective for this PhD study. To achieve that, we will calculate the thermal expansions, the variation of enthalpies and the heat capacities of UO_2 and $(U,Pu)O_2$ and compare to the reviewed values. The method will be applied in the future for the investigation of more complex systems such as $(U,Pu,Am)O_2$ for which thermodynamic data are missing. Next, we have reviewed point defects properties for UO_2 and PuO_2 as well as the methods used for their investigations. The investigation of defects in $(U,Pu)O_2$ constitutes a key point of this PhD research since it has never been done to our knowledge. Using the same techniques as for UO_2 and PuO_2, the defect properties in $(U,Pu)O_2$, especially the defect formation energies will be analysed. The results obtained will be compared to those for UO_2 and PuO_2. Finally, we have reviewed the atomic transport properties, especially oxygen, uranium and plutonium diffusion for UO_2 and PuO_2. Diffusion of oxygen in both UO_2 and PuO_2 were suggested to be vacancy and interstitial assisted at hypo-stoichiometry and hyper-stoichiometry respectively. The vacancy assisted mechanism was suggested for the diffusion of cations. Up to now, only very few and scattered measurements of the oxygen diffusion coefficient in $(U,Pu)O_2$ were found in the literature, and the most recent study by Vauchy *et al.* [181] suggests the vacancy assisted diffusion at the stoichiometry. Up to now, there are no theoretical studies in support of these experimental measurements as for UO_2. Moreover, there are no data concerning the diffusion of cations in $(U,Pu)O_2$. In this context, this PhD study will bring a major contribution for the understanding of atomic transport properties in $(U,Pu)O_2$. We will investigate the atomic transport properties of $(U,Pu)O_2$ in terms of the migration energies and the activation energies of diffusion of oxygen, uranium and plutonium atoms. These studies will be conducted using the DFT+*U* method as described in the next chapter.

Chapter 2: Methodological approach

2.1 Introduction

The electronic structure calculation method used in this PhD study is the Density Functional Theory (DFT) within the DFT+*U* approach. In general, the DFT method is based on the determination of the ground state total energy (or charge density) of multi-electronic systems using quantum theory. The quantum approaches used, as in many studies, is formulated around the resolutions of Schrödinger's equation for multi-electronic systems. When dealing with $(U,Pu)O_2$, one has to face two challenges: describe the strong electron correlations of *5f* states and describe an ideal solid solution which imply a random distribution of two cations species. These challenges are tackled by using on the one hand approaches beyond standard DFT (LDA and GGA) especially the DFT+*U* method. On the other hand, the so-called "Special Quasi-random Structures" (SQS) [189] are used for the modelling of the disorder in the cation sublattice. In the present chapter, the formalisms and various approximations of the DFT method are presented as well as methods beyond standard DFT, which are more adapted for the description of strongly correlated materials and van der Waals interactions. We also describe the formalism of the SQS method and some alternatives to this method. Another important part of the methodological approach is the use of *ab initio* molecular dynamics (*ab initio* MD) for actinide based materials. The approach allows the investigation of thermodynamic properties, taking into account the correlated *f* electrons. In our application, the DFT+*U* calculations and the SQS structures are coupled to the resolution of the equation of motion of ions in $(U,Pu)O_2$. This approach is also described in detail in this chapter.

2.2 Density functional theory (DFT) method and features

2.2.1 DFT formalism

The DFT method is the most popular method for the quantum description of the electronic structure of solids. Its modern formulation was developed through the formalism of Hohenberg and Kohn [190] in 1964, further by Kohn and Sham [191] in 1965. In the DFT method, the electronic density $n(\boldsymbol{r})$ plays an essential role. Indeed, the average values of observables such as the total energy of an electronic system are computed by the simple knowledge of the ground-state electronic density $n_0(\boldsymbol{r})$. Therefore, all the material properties linked to the ground-state energy (or charge density) can be determined. This method becomes very interesting since it reduces, for a system of N electrons, a problem of 3N variables to the problem of 3 variables, which are simply the coordinate $\boldsymbol{r}$ at which $n_0(\boldsymbol{r})$ is calculated.

The DFT formalism includes numerous approximations aiming at reducing as much as possible the degree of freedom of the standard Schrödinger equation, which is unsolvable for multi-electronic systems. The essence of these approximations is shown in the following sections.

2.2.1.1 Born Oppenheimer approximation

The first approximation is that of Born-Oppenheimer. This approximation aims at reducing the number of variables involved in the resolution of the Schrödinger equation. Indeed, in this approximation, the total wave function is split into two different contributions: the contribution of nuclei and the contribution of electrons. This splitting is justified by the fact that the nuclei mass is much larger than the electron mass. The total wave function is thus written as follows:

$$\Psi = \Psi_{electrons} \text{ x } \Psi_{nuclei} \qquad (41)$$

This separation enables the treatment of a system of N electrons moving in the external potential generated by the nuclei $v(\boldsymbol{r})$, with Coulomb repulsive interactions between electrons. In that case, the Hamiltonian of the system can be written as follows:

$$\hat{H} = \hat{T} + \hat{V} + \hat{U} = -\frac{\hbar^2}{2m_e}\sum_i \boldsymbol{\nabla}_i^2 + \sum_i v(\boldsymbol{r_i}) + \frac{1}{2}\sum_{i\neq j}\frac{e^2}{|\boldsymbol{r_i}-\boldsymbol{r_j}|} \qquad (42)$$

In Equation (42) the sum is over the N electrons of the system. Despite this simplification brought by Born-Oppenheimer approximation, it always remains very difficult to solve the electronic Hamiltonian for multi-electronic systems. The idea of Hohenberg and Kohn was thus to consider the electronic density $n(\boldsymbol{r})$ instead of the electronic wave function.

2.2.1.2 Hohenberg-Kohn theorem

The main ideas of the density functional theory are summarised by the two Hohenberg-Kohn theorems [190]. The first theorem proves that for a given system of particles in interaction in an external potential $v(\boldsymbol{r})$, the potential $v(\boldsymbol{r})$ is a unique functional of the electronic density $n(\boldsymbol{r})$. The external potential is therefore determined unequivocally by the ground state electronic density $n_0(\boldsymbol{r})$. Since $v(\boldsymbol{r})$ defines the Hamiltonian $\hat{H}$, the full many-particle ground state is a unique functional of $n(\boldsymbol{r})$. The total energy functional is then defined as follows:

$$E[n(\boldsymbol{r})] = \int v(\boldsymbol{r}).n(\boldsymbol{r}).d\boldsymbol{r} + F_{HK}[n(\boldsymbol{r})] \qquad (43)$$

where $F_{HK}[n(\boldsymbol{r})]$ is universal functional of Hohenberg and Kohn. This functional does not depend on the external potential $v(\boldsymbol{r})$. It represents the kinetic energy T of interacting electrons and the energy of the electron Coulomb repulsion U. It can be written as follows:

$$F_{HK}[n(\boldsymbol{r})] = T[n(\boldsymbol{r})] + U[n(\boldsymbol{r})] \qquad (44)$$

The second theorem states that for a given external potential ***v(r)***, the ground-state electronic density ***n_0(r)*** is the one for which the total energy is minimal. In another words, the true electronic (or charge) density of the system ensures the ground state of this system. The major complexity of the many-electron problem is associated with the determination of the universal functional $F_{HK}[n(\boldsymbol{r})]$ of Hohenberg and Kohn in the expression of ***E[n(r)]***. Kohn and Sham [191] proposed an effective potential for the calculation of $F_{HK}[n(\boldsymbol{r})]$ which corresponds to the ground state.

2.2.1.3 Kohn-Sham formalism

Kohn and Sham [191] have proposed to replace a complex system of N interacting electrons in an external potential ***v(r)*** by a fictive system of non-interacting electrons in a local effective potential $v_{eff}(\boldsymbol{r})$. Using the exact electronic density, $F_{HK}[n(\boldsymbol{r})]$ is written as follows:

$$F_{HK}[n(\boldsymbol{r})] = T_S[n(\boldsymbol{r})] + E_H[n(\boldsymbol{r})] + E_{XC}[n(\boldsymbol{r})] \qquad (45)$$

where $T_S[n(\boldsymbol{r})]$ is the kinetic energy functional of non-interacting electrons calculated using the exact electronic density ***n(r)***. $E_H[n(\boldsymbol{r})]$ is the Hartree term for the electron Coulomb repulsion and $E_{XC}[n(\boldsymbol{r})]$ is the exchange-correlation functional. This latter term accounts for the difference between the exact and effective kinetic energies as well as complex interactions (or exchange and correlations) between electrons. Therefore, the equation of state of the electronic system within the Kohn-Sham formalism, known as the Kohn-Sham equation is written as follows:

$$\left[-\frac{\hbar^2}{2m_e}\sum_{\boldsymbol{i}} \boldsymbol{\nabla_i^2} + v_{eff}(\boldsymbol{r})\right]\psi_i(\boldsymbol{r}) = \epsilon_i\psi_i(\boldsymbol{r}) \qquad (46)$$

where $\psi_i(\boldsymbol{r})$ is the mono-electronic wave function. The electronic density within this formalism is calculated as follows:

$$n(\boldsymbol{r}) = \sum_{\boldsymbol{i=1}}^{\boldsymbol{N}} |\psi_i(\boldsymbol{r})|^{\boldsymbol{2}} \qquad (47)$$

where N is the number of electrons of the system. The kinetic energy of non-interacting electrons is given as follows:

$$T_S[n(\boldsymbol{r})] = -\frac{\hbar^2}{2m_e}\sum_{i=1}^{N}\int \psi^*(\boldsymbol{r})\nabla^2\psi(\boldsymbol{r})d\boldsymbol{r} \qquad (48)$$

and the effective potential by,

$$v_{eff}(\boldsymbol{r}) = v(\boldsymbol{r}) + \frac{\delta E_H[n(\boldsymbol{r})]}{\delta n(\boldsymbol{r})} + \frac{\delta E_{XC}[n(\boldsymbol{r})]}{\delta n(\boldsymbol{r})} = v(\boldsymbol{r}) + \int \frac{n(\boldsymbol{r'})}{|\boldsymbol{r}-\boldsymbol{r'}|}d\boldsymbol{r'} + v_{XC}(\boldsymbol{r}) \qquad (49)$$

In the expression of $\boldsymbol{v_{eff}}(r)$, only the exchange-correlation potential $\boldsymbol{v_{XC}}(\boldsymbol{r})$ does not have an exact formulation as a function of the electronic density. The exchange correlation functional can only be approximated and the reliability of the DFT results depends on the quality of this approximation. The standard approximations of the exchange-correlation functional are the local density approximation (LDA) and the generalized gradient approximation (GGA). These approximations are presented in the following section.

2.2.1.4 Standard exchange and correlation functionals: LDA and GGA

In the LDA approximation, the exchange and correlation energy is considered as for a uniform electron gas with a density *n(**r**)*, where the density is treated locally. The exchange and correlation energy functional is then given as follows:

$$E_{XC}^{LDA}[n(\boldsymbol{r})] = \int \epsilon_{XC}^{LDA}[n(\boldsymbol{r})].\, n(\boldsymbol{r}) d\boldsymbol{r} \qquad (50)$$

There exist several LDA functionals which correspond to various parametrisations of the energy of a homogenous electron gas. The exchange component is known exactly and is given as follows:

$$e_{XC}^{hom}[n(\boldsymbol{r})] = -\frac{3q^2}{4}\left(\frac{3}{\pi}\right)^{1/3} n(\boldsymbol{r})^{4/3} \qquad (51)$$

The exact expression of the correlation component is not known. It has been estimated for the first time by Wigner [192] and more recently by Ceperley and Alder [193] using Monte Carlo method. Other functionals such as those developed by Hedin-Lundqvist [194], Barth-Hedin [195], Vosko-Wilk-Nusair [196], Perdew-Zunger [197] etc., can also be used to compute the correlation component.

The LDA approximation is reliable for systems in which the electronic density slightly varies. This is in general not the case for solids and molecular systems. The main limitation of the LDA approximation is a systematic overestimation of bounding energies in molecules and cohesive energies for solids. This limitation can be explained by the existence in both standard approximations of non-physical interaction of an electron with itself, which is known as the self-interaction, within the Coulomb term [197].

In the GGA approximation, the exchange and correlation functional at a given point is expressed as a function of both the electronic density and its gradient (or variation) at this point. It is formulated as follows:

$$E_{XC}^{GGA}[n(\boldsymbol{r})] = \int e_X^{hom}[n(\boldsymbol{r})] F_{XC}[n(\boldsymbol{r}), |\nabla n(\boldsymbol{r})|] d\boldsymbol{r} \qquad (52)$$

where e_X^{hom} is the exchange energy of a homogenous electron gas and F_{XC} a dimensionless functional. One of the first developed GGA functionals combines the exchange functional of Becke (B) [198] and the correlation functional of Lee, Yang and Parr (LYP) [199]. Other functionals were developed such as the one of Perdew Wang (PW91) [200] and Perdew, Burke and Ernzerhof (PBE) [201]. The two latter functionals are the most used in recent researches.

The use of the GGA approximation allows one to correct the overestimations in bonding and cohesive energies yielded by the LDA approximation, as well as the resulting underestimation of interatomic distances. However, both the LDA and the GGA approximations fail to describe materials having complex electronic structures. Especially, actinide based materials are not well describe within the standard LDA and GGA approximations, owing to the presence of strongly correlated *5f* electrons. The failure of these approximations and the adapted method proposed for correlated materials are presented in the next section.

2.2.1.5 Failure of LDA and GGA for specific features of actinide based materials: adapted DFT approaches

Both LDA and GGA give a wrong qualitative description of actinide oxides. They predict UO_2, PuO_2 and Pu_2O_3 to be conductors. Moreover, the LDA predicts UO_2 to be ferromagnetic. These predictions are contrary to experiments which show an insulating behaviour for these oxides [202–204], and antiferromagnetic character for UO_2. Indeed, one of the first electronic structure calculations using LDA and the LMTO method on actinide oxides was carried out by Kelly and Brooks [205, 206] on UO_2, PuO_2, CmO_2 and ThO_2. They predict a metallic character for all these oxides except for ThO_2 predicted as a charge-transfer insulator. Freyss *et al*. [53] have also found using GGA and a pseudopotential method a metallic character for UO_2. In order to correct these wrong descriptions of correlated materials, methods beyond standard LDA and GGA approximations have been developed. These are, for instance, the hybrid functionals [207], the self-interaction correction (SIC) [137, 197] , the DFT+DMFT and the DFT+*U* methods.

2.2.1.5.1 Hybrid functionals

Hybrid functionals are built through a linear combination of the exact Hartree-Fock exchange functional and the exchange and correlation functional of LDA or GGA. The weight of each functional is determined by an empirical parameter which is adjusted by comparison to experimental or reliable calculated properties. The currently most used hybrid functionals are PBE0 [208] and HSE [209]. The use of hybrid functionals is very

time consuming and thus prevents up to now its use for supercells containing more than few dozen atoms. This constitutes a limiting factor for the use of these functionals for the study of point defects and mixed oxides, as it is the case in this PhD study.

2.2.1.5.2 Self-interaction correction (SIC) method

LDA and GGA induce a self-interaction term which corresponds to the interaction of an electron with itself. This non physical term can have a significant impact on localized electrons. The SIC method [137, 197] introduces a correction term to the LDA or GGA energy in order to localize electrons on the dedicated orbitals. This correction cancels the self-interaction energy. Within this method, it is required to first determine the number of localized and itinerant electrons in the system.

2.2.1.5.3 Coupling dynamical mean field theory to the LDA: LDA+DMFT

The LDA or GGA gives a correct description of non correlated materials while the DFT+*U* (see the next section) is adapted for strongly correlated ones. The DMFT [210, 211] coupled to the LDA allows an accurate description of a set of materials going from weakly to strongly correlated ones. This is achieved by adding to the DFT formalism the consideration of the local quantum fluctuation of spin and charges [211]. The LDA+DMFT is very time consuming and also prevents the use of large supercells, thus the calculation of isolated point defects [65].

2.2.1.6 DFT+*U* approach

The DFT+*U* method is the most used approach for the treatment of strongly correlated *f* orbitals of actinide based materials. This approach is used in this PhD study since it provides an accurate description of strongly correlated materials and allows the use of larger supercells compared to other approaches as mentioned above. The DFT+*U* method has been proposed for the first time by Anisimov, Zaanen and Andersen [212]. It consists of replacing the repulsion energy of the LDA or GGA by a repulsive term depending on the orbitals. This repulsive term is the screened Coulomb interaction between correlated orbitals. The idea behind the DFT+*U* method is similar to that proposed by Mott [213] and Hubbard [214] which consists of opening a gap between the valence band and the conduction band, using a local Coulomb repulsive term which is dependent to two parameters. In the DFT+*U* approach, the Coulomb repulsion for localized electrons is represented by the Hubbard term while the delocalized states are described by the standard LDA or GGA exchange and correlation functionals. The energy of the DFT+*U* can thus be expressed as a function of the energy of the DFT as follows:

$$E_{DFT+U} = E_{DFT} + E_{Hub} - E_{DC} \quad (53)$$

where E_{DFT} is the standard DFT total energy, E_{Hub} accounts for the interactions between strongly correlated electrons and E_{DC} is a double counting term. The double counting term cancels the electronic correlations which are already taken into account by the standard LDA or GGA functionals within E_{DFT}. It is determined in this study through the full localized limit (FLL).

The term $\boldsymbol{E_{Hub}}$ contains two adjustable parameters which are conventionally denoted *U* and *J*. The *U* parameter represents the screened Coulomb interaction of correlated electrons and *J* is the exchange parameter. Two approaches for the description of E_{Hub} have been proposed by Lichtenstein *et al*. [215] and Dudarev *et al*. [216]. In the Lichtenstein approach, the *U* and *J* terms are considered separately while in the Dudarev approach, only the difference between the *U* and *J* parameters is considered (U_{eff} = *U-J*). For both approaches, the Hubbard term is expressed as follows:

$$E_{Hub} = \frac{1}{2}\sum_{m\sigma \neq m'\sigma'} W_{mm'}^{\sigma\sigma'} n_m^{\sigma} n_{m'}^{\sigma'} \quad (54)$$

where n_m^{σ} is the number of electrons on the correlated orbital (*m, σ*) and $W_{mm'}^{\sigma\sigma'}$ the component of the Coulomb interaction matrix between correlated electrons. $W_{mm'}^{\sigma\sigma'}$ represents the value of the Coulomb interaction between an electron having a spin *σ* localized on an orbital *m* with an electron having a spin *σ'* localized on an orbital *m'*. It is expressed as a function of the Coulomb and exchange contributions as follows:

$$W_{mm'}^{\sigma\sigma'} = (U_{mm'} - J_{mm'}\delta_{\sigma\sigma'}) \quad (55)$$

The interaction matrix *W* contains all the information of the Coulomb interactions between correlated electrons. For two electrons having different spins, the exchange interaction disappears.

The values of the *U* and *J* parameters can be extracted from photoemission spectrometry measurements or calculated using *ab initio* techniques [217].

Compound	*U* (eV)	*J* (eV)
UO_2 Kotani *et al*. [218]	4.50	0.54
PuO_2 Kotani *et al*. [218]	5.50	0.68
PuO_2 Jomard *et al*. [219]	4.00	0.71

Table 16 : Values of *U* and *J* parameters of UO_2 and PuO_2 extracted from experiments and DFT+*U* calculations.

They can also be adjusted empirically on experimental data. For UO_2 and PuO_2, the values of *U* and *J* for *5f* electrons have been extracted from the experimental

measurements by Kotani and Ogasawara [218]. Jomard *et al*. [219] have adjusted these parameters for PuO_2 and have obtained satisfactory results on PuO_2 compared to experiments, especially for the volume of the unit cell and the bulk modulus. These values are shown in Table 16. The values obtained by Jomard *et al*. [219] are used in this study for PuO_2 and Pu cations in $(U,Pu)O_2$. As for Ce *4f* states in $(U,Ce)O_2$, the values of U = 5.0 eV and J = 0.0 eV are used.

2.2.1.7 Metastable states and occupation matrix control scheme (OMC)

The DFT+*U* method, through the adding of the Hubbard term favours entire occupations of the correlated orbitals. This induces an orbital anisotropy and thus generates the proliferation of metastable states. The metastable states are due to the fact that two different electronic occupations of the seven *5f* orbitals of uranium for example do not correspond to the same energy level, and that during the numerical procedure, the electronic system can be trapped into a metastable state with an electronic occupation which differs to that of the ground state. The existence of metastable states has been evidence for UO_2 and PuO_2 by the fact that, using the same calculation parameters, two DFT+*U* calculations gave different results especially on bulk properties and defect formation energies [121, 132, 133]. Thus the issue of metastable states has to be monitor in order to ensure the ground state to be reached.

In order to overcome the issue of metastable states, we use the occupation matrix control (OMC) scheme. It has been implemented and used in perfect crystals by Amadon *et al*. [220] and Jomard *et al*. [219] on Ce and PuO_2. This technique has further been extended to point defects in UO_2 by Dorado [64], and also used by Vathonne [65], Wiktor [221] and Shi [122] for the investigation of charged defects and fission gas incorporation in UO_2 and CeO_2 respectively.

The OMC technique consists in imposing an initial filling of the occupation matrices of the correlated *5f* orbitals, corresponding to the electronic configuration of the ground state. The occupation matrices of UO_2 ground state has been determined by Dorado *et al*. [222] through a systematic investigation of different possible electronic filling of the uranium *5f* orbitals. A similar investigation has been carried out by Shi [122] for the occupation matrices of Ce^{3+} *4f* orbitals and by Jomard *et al*. [219] and Li [223] for Pu *5f* orbitals in PuO_2. These occupation matrices are used as prerequisites in this PhD study.

Other techniques aiming at overcoming the issue of metastable states exist in the literature. We can cite for instance the *U*-ramping method proposed by Meredig *et al*. [224]. This method consists in starting by a standard DFT calculation, followed by a progressive increase of the *U* parameter up to its final value. Thompson *et al*. [225] have, however, demonstrated that the convergence towards the ground state is not

guaranteed within this method. We can also cite the quasi-annealing (QA) method proposed by Geng *et al*. [226]. The idea behind this method is to heat the system with a spurious external potential. This spurious potential allows the system to cross the energy barrier from one local minimum to another and thus to determine the global minimum. Another technique is the controlled symmetry reduction (CSR) proposed by Gryaznov *et al*. [227]. Within this technique, specific displacements and/or distortions are imposed to the unit cell in order to compute the initial electronic density for the geometry optimisation. However, there is no guaranty that this electronic density corresponds to the ground state.

2.2.1.8 Non-local correlation functionals: vdW-DF

The description of non-local interactions are challenging for atoms or gas molecules having fully filled valence orbitals. It is for instance the case for noble gases. Indeed, it is well established that the standard LDA and GGA functionals are inadequate for the description of dispersive van der Waals interactions. This failure is due to the fact that these approximations are local or at best semi-local. Therefore, new functionals have been developed in order to account for non-local correlations [15, 16, 228, 229]. These functionals are implemented as the van der Waals density functionals (vdW-DF).

In the most sophisticated vdW-DF functional by Dion *et al*. [228], Langreth *et al*. [229] and Kliměs *et al*. [15, 16], the correlation functional is divided into a local component and a non local component as follows:

$$E_C[n(\boldsymbol{r})] = E_C^{DFT}[n(\boldsymbol{r})] + E_C^{nl}[n(\boldsymbol{r})] \qquad (56)$$

$E_C^{DFT}[n(\boldsymbol{r})]$ is a short range term evaluated through the standard LDA or GGA functionals and $\boldsymbol{E_C^{nl}[n(r)]}$ a long range term evaluated as follows:

$$E_C^{nl}[n(\boldsymbol{r})] = \frac{1}{2}\int d\boldsymbol{r} \int n(\boldsymbol{r})\phi(\boldsymbol{r},\boldsymbol{r}')n(\boldsymbol{r}')d\boldsymbol{r}' \qquad (57)$$

where $\phi(\boldsymbol{r},\boldsymbol{r}')$ is the interaction kernel depending on ***r*-*r'***, the density and its gradient in the neighbouring positions ***r*** and ***r'*** [229]. The exchange-correlation energy functional is thus written as follows:

$$E_{XC}^{DFT}[n(\boldsymbol{r})] = E_X^{DFT}[n(\boldsymbol{r})] + E_C^{DFT}[n(\boldsymbol{r})] + E_C^{nl}[n(\boldsymbol{r})] \qquad (58)$$

The exchange functional $E_X^{DFT}[n(\boldsymbol{r})]$ associated to the vdW-DF is GGA-revPBE for Dion *et al.* [228] and GGA-optPBE for Kliměs *et al*. [15, 16].

vdW-DF functionals give an improved description of energetic properties of dimers and molecules, as compared to standard DFT [15]. Further, even for solids in which dispersive interactions are weak, Kliměs *et al*. [16] also reported a systematic improvement of cohesive properties when non-local interactions are taken into account.

Vathonne [65] has also shown an improvement on the description of energetic properties of UO_2 such as the formation enthalpy. This improvement will also be highlighted for UO_2, PuO_2 and Pu_2O_3 in Chapter 3, section 3.3.1.1. Moreover, for the study of fission gas behaviour in actinides, the consideration of long range interactions is required since they are important for noble gases. Therefore, the vdW-DF functional parametrized by Kliměs *et al*. [15] has been considered in our study.

2.3 DFT calculation methods

2.3.1 Representation of wave functions

One of challenging issues of the Kohn-Sham formalism is the representation of the mono-electronic wave function $\psi_i(\boldsymbol{r})$. Indeed, the Kohn-Sham wave function oscillates rapidly close to the nuclei owing to the strong attractive potential of the nuclei and smoothly in the region between the nuclei. Two possible solutions exist for the representation of the wave function. The first possibility is to expand the wave function in a basis of localized waves and the second possibility is to expand the wave function in a basis of plane waves. For solids in general, the wave function is expanded in plane waves. This solution is privileged since crystals are periodic and plane waves are mathematically simple and they also simplify the calculation of forces acting on ions. Moreover, errors associated to the truncation of the basis can be easily overcome by adding more plane waves. The wave functions are built following the Bloch theorem presented in the next section.

2.3.1.1 Bloch theorem

In the Kohn-Sham formalism, the electronic system is treated as a system of itinerant electrons moving in an effective potential ***v(r)***. In the crystal system, this potential has the same periodicity as the lattice. This means that at a point ***r+R*** where ***R*** is a vector of the Bravais lattice, the potential verify the expression as follows:

$$v(\boldsymbol{r} + \boldsymbol{R}) = v(\boldsymbol{r}) \qquad (59)$$

On the other hand, as the Kohn-Sham electrons obey the Kohn-Sham equation, the Bloch theorem states that the wave function at ***r***+***R*** is given as follows:

$$\psi_{nk}(\boldsymbol{r} + \boldsymbol{R}) = exp(i\boldsymbol{k}.\boldsymbol{R})\psi_{nk}(\boldsymbol{r}) \qquad (60)$$

where *n* is the index of band and ***k*** a wave vector. Owing to the periodicity of the lattice, the wave vector is limited to the first Brillouin zone. In practice, this zone is sampled by a finite number of k-points usually by the Monkhorst-Pack scheme [230].

2.3.1.2 Plane wave representation

The wave function is periodic with the periodicity of the lattice, it can thus be expanded as a Fourier series within the basis exp(*i**G**.**r*). This complex exponential forms a complete basis of functions having the periodicity of the lattice. **G** represents a reciprocal lattice vector. Using the normalised plane waves, the Kohn-Sham wave functions can thus be written as follows:

$$\psi_j(\boldsymbol{r}) = \Omega^{-1/2} \sum_{\boldsymbol{G}} c_{j,\boldsymbol{G}} \exp(i\boldsymbol{G}.\boldsymbol{r}) \qquad (61)$$

Ω is the unit cell volume, **G** a wave vector and $c_{j,G}$ are expansion coefficients in the plane wave basis and *i* the complex number defined by $i^2 = -1$.

By introducing this expression in Equation (60), we obtain the wave function as a sum of plane waves as follows:

$$\psi_j(\boldsymbol{r}) = \Omega^{-1/2} \sum_{\boldsymbol{G}} c_{j,\boldsymbol{G}} \mathbf{e} \exp(i(\boldsymbol{G} + \boldsymbol{k}).\boldsymbol{r}) \qquad (62)$$

In practice, a truncation in the expansion the wave function is necessary. This is done such that the norm of the selected **G** vectors is smaller than a fixed threshold value G_{cut}. A wave vector **G** is associated to the kinetic energy of a free particle moving with the kinetic energy $\hbar^2 G^2/2m$. Therefore, imposing a cut-off value to the wave vector is equivalent to imposing a cut-off energy E_{cut}. Thus, the sum in Equation (62) is over **G** vectors which satisfy:

$$\frac{\hbar^2 \boldsymbol{G^2}}{2m} \leq E_{cut} \qquad (63)$$

Note that imposing a cut-off energy leads to the reduction of the degree of freedom for the convergence of the computed ground-state energy toward the exact ground-state energy. In practice, when the cut-off energy is increased, the computed total energy of the system better approaches the exact ground-state total energy. It is therefore important to choose the cut-off energy in such a manner that the variation of total energy as a function of the cut-off energy is negligible, or smaller than a required accuracy criterion. This is ensured through convergence tests.

The expansion over plane waves is not adapted for wave functions close to the nuclei. Indeed, in order to account for strong oscillations close to the nuclei, a large number of plane waves need to be considered. It is thus necessary to use more adapted methods such as pseudopotential methods or the projector augmented wave (PAW) method. These methods are presented in the next sections. In this PhD study, we use the PAW method.

2.3.1.3 Pseudopotential method

In general, within the pseudopotential method, the exact wave function is first replaced by a pseudo-function which has no oscillations near the nuclei and can be easily expanded over plane waves. Further, the Coulomb potential and the effect of the core electrons are described by a ionic effective potential (pseudo-potential) acting on the valence electrons. This transformation leads to the simplification of the DFT problem since only the valence electrons are considered. The core electrons are excluded (and "frozen") since their charge density is assumed not to be affected by a variation of the chemical environment [231]. Another advantage is that the relativistic effects which are mainly due to core electrons can be include in the pseudopotential. The main limitation of this method is the non-transferability of the pseudopotential. This method is less accurate than the PAW method shown in the next section.

2.3.1.4 Projected augmented wave method (PAW)

The projector augmented wave (PAW) [5, 232] is an efficient method which generalizes both the pseudopotential method and the linear augmented-plane-wave method. This method is used in this PhD for all calculations. The principle of the PAW method consists in dividing the wave function into two groups:

- A partial wave expansion within an atom-centered sphere Ω_R (PAW sphere). Within Ω_R, the wave function oscillates rapidly. The partial basis set ϕ_i is calculated through the resolution of the Schrödinger equation for an isolated atom.
- An envelope function outside Ω_R where the wave function is fairly smooth. The envelope function is expanded onto a plane waves basis set.

Envelope function and partial-wave expansions are then matched with value and derivative at the sphere radius.

The rapid oscillation of the real wave function next to the nuclei, however, remains numerically cumbersome. The idea is thus to use pseudo all-electron (PS) wave functions, which are linked to the real all-electron (AE) wave functions though a linear transformation [5, 232] as follows:

$$|\psi^{AE}\rangle = |\psi^{PS}\rangle + \sum_i (|\phi_i^{AE}\rangle - |\phi_i^{PS}\rangle)\langle p_i^{PS}|\psi^{PS}\rangle \qquad (64)$$

In the above equations, $|\psi^{AE}\rangle$ is an AE wave function and $|\psi^{PS}\rangle$ a PS wave function; $|\phi_i^{AE}\rangle$ is an AE partial wave function and $|\phi_i^{PS}\rangle$ a PS partial wave function which coincides with the corresponding AE partial wave outside the PAW sphere for each AE partial wave; $|p_i^{PS}\rangle$ is one projector function for each PS partial wave localized within the augmentation region and which obeys the relation $\langle p_i^{PS}|\phi_j^{PS}\rangle = \delta_{ij}$. $|\psi^{AE}\rangle$ and $|\psi^{PS}\rangle$ coincides each other in the region between the PAW spheres.

The partial AE wave functions are the solutions of the spherical scalar relativistic Schrödinger equation for non-polarized atom at the reference energy ε_i having an angular momentum l_i.

$$\left(-\frac{1}{2}\Delta + v_{eff}^{AE}\right)|\phi_i^{AE}\rangle = \varepsilon_i|\phi_i^{AE}\rangle \qquad (65)$$

v_{eff}^{AE} is the spherical component of the all-electron potential. The index ***i*** is a shortcut for the indexes of the reference energy ε_i, the angular momentum (l_i, m_i) and the atomic coordinates $\boldsymbol{R_i}$.

2.3.2 Modelling of solids: Supercell approach and convergence tests

2.3.2.1 Supercell approach

In principle, solid containing impurities or defects (non periodic crystal) can be approximated by means of a large cluster of atoms. For sufficiently large clusters, the quantum mechanics of the centre-most atoms approximate those in a solid. However, the size of cluster required to approximate a solid is large due to the surface over bulk atoms and electrons in small and medium sized clusters. The supercell method is a popular approach used for the electronic structure calculations of solids. Within this approach, one constructs a supercell which is a finite repetition of the unit cell over the three space directions. The supercell is then repeated throughout all space using periodic boundary conditions. However, the supercell method suffers from numerous finite size problems. Indeed, when point defects or fission gases are incorporated in the supercell for instance, they interact with their images created by the lattice periodicity. Except for the study of high defect concentration in the material, these interactions are detrimental for the defects or fission gas modelling. The interaction is cancelled as much as possible by increasing the size of the supercell as illustrated in Figure 28.

In this PhD study, a 2x2x2 supercell of the fluorite structure is used. This means that the cubic unit cell of the fluorite structure, which contains 12 atoms, has been multiplied by two along each space direction. This results in a 96-atom supercell. This size is commonly used in the literature for the study of defects and fission gas behaviour in actinide oxides such as UO_2 [9, 64, 65, 76, 120, 148, 221, 233] and PuO_2 [135, 219] as well as CeO_2 [119, 122, 234]. Moreover, Shi has demonstrated in CeO_2 that a 96-atoms supercell is large enough for the modelling of isolated defect. Other calculation parameters were set according to the convergence test presented in the next section.

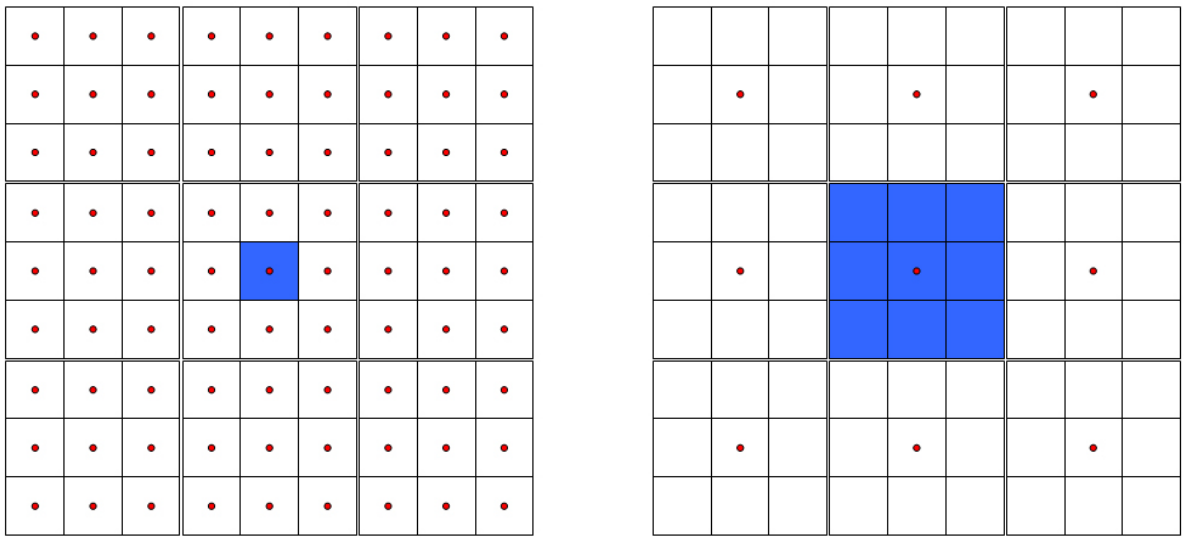

Figure 28 : 2D Illustration of the supercell method and the defect interaction with its images (red points). In the smaller supercell (left side), the interaction is more important than that yielded by a larger supercell (right side).

2.3.2.2 Convergence tests

Convergence tests are essential for DFT calculations in order to determine the optimum set of parameters necessary to have accurate results within a reasonable calculation time. These parameters are the cut-off energy and the **k**-point sampling.

Indeed, the valence electrons of each atom of the system are represented by a finite number of plane waves as explained in Section 2.3.1.2. The number of the wave functions is defined by a cut-off energy E_{cut}. This cut-off energy reduces the degrees of freedom of the system which control the convergence of the total energy toward the lowest energy. The higher the cut-off energy, the more accurate the calculation is. However, an increase in the energy cut-off also increases the calculation time. It is therefore important to determine the optimum cut-off energy for which the increase has a negligible impact on the total energy accuracy and keeping a reasonable calculation time. The number of **k**-points in the Brillouin zone presents the same challenge as for the cut-off energy. The difference between the k-points sampling and the cut-off energy is that the number of k-points depends on the supercell size. Thus, the larger the supercell, the lower the k-points number is necessary in the first Brillouin zone. In contrary, the cut-of energy only depends on the chemical elements, especially the PAW atomic data.

Before starting our study, we have conducted several convergence tests on both cut-off energy and k-point sampling on UO_2 and PuO_2. The optimal calculation parameters are obtained such that the total energy difference with the reference value is less than 1

meV/PuO_2 for the cut-off energy of PuO_2. The cut-off energies optimised by Vathonne [65] and Lei [122] for UO_2 were also considered. The criterion on the total energy difference of 1meV/MO_2, compared to the reference value, was considered for k-points. The evolution of the total energy and the calculation time as a function of the k-point mesh is shown in Figure 29.

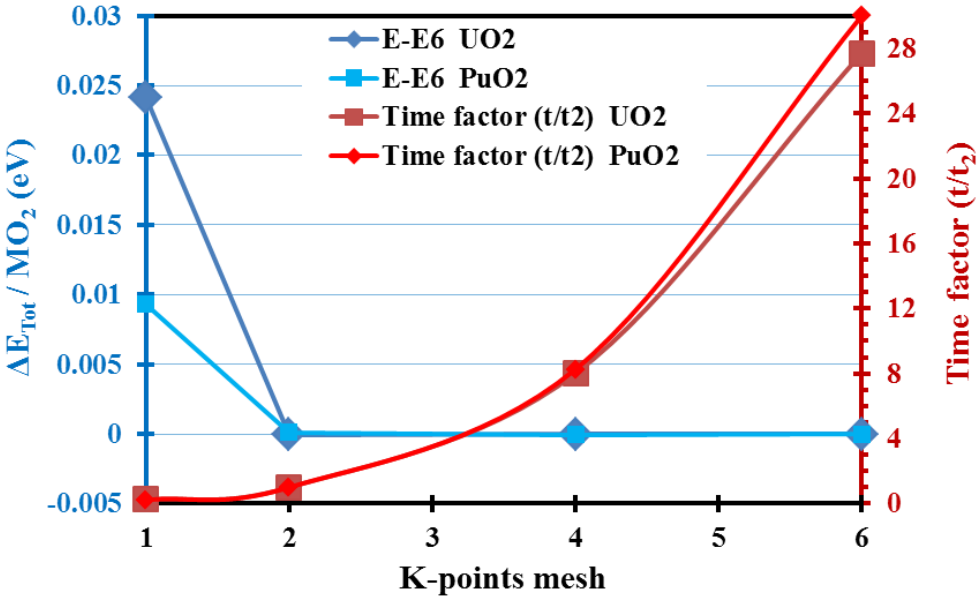

Figure 29 : Variation of total energy (blue cures) and calculation time (red curves) as a function of the k-point mesh in 96-atoms supercells. In the horizontal axis 2 corresponds to a 2x2x2 mesh.

The variation in total energy becomes smaller than our criterion of 1 meV/MO_2 from a 2x2x2 k-point mesh with a negligible time factor. On the other hand, the calculation time increases by 8 times from 2x2x2 to 4x4x4, with no significant variation in total energy. Thus the 2x2x2 k-point mesh is the optimal sampling for 96-atoms supercells of UO_2 and PuO_2. It is thus used in all our studies.

Figure 30 shows the variation of total energy (blue curve) and the calculation time (red curve) for PuO_2 as a function of the cut-off energy. From the energy cut-off of 400 eV, the variation in the total energy is almost negligible. At 500 eV, the total energy is insensitive to the increase in the cut-off energy. On the other hand, the calculation times increases slowly from 400 eV to 500 eV, by a factor of 1.2. From 500 eV to 1000 eV, the increase in calculation time is of 2.5 with non significant variation in total energy (smaller than 1 meV/MO_2). For UO_2, Vathonne [65] and Lei [122] have obtained that the cut-off energy of 500 eV is satisfactory. Thus the cut-off of 500 eV is identified as the optimal cut-off and is used for all our calculations of (U,Pu)O_2, UO_2 and PuO_2.

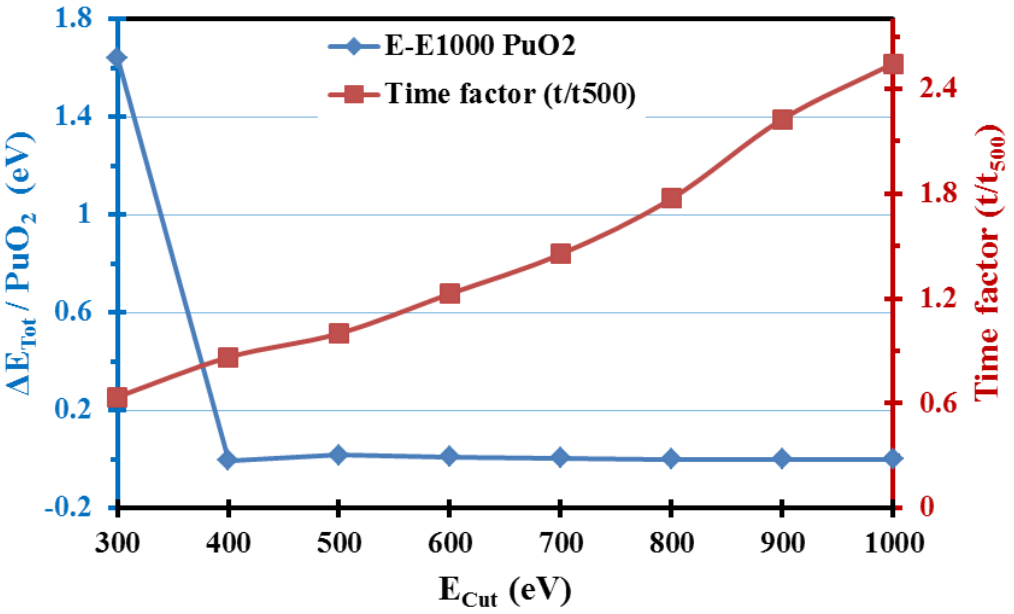

Figure 30 : Variation of total energy (blue cure) and calculation time (red curve) as a function of the cut-off energy in a 6-atom supercell of PuO_2.

2.4 Modelling of random structures: The special quasi-random structure (SQS)

Despite the miscibility gap observed for certain compositions in the phase diagram of the U-Pu-O system [4, 22, 23, 25], numerous experimental studies suggest that $(U,Pu)O_2$ is an ideal solid solution under stoichiometric conditions [34, 49]. This means that uranium and plutonium cations are randomly distributed in the cation sublattice. However, the modelling of an ideal solid solution requires a very large supercell in order to represent this random distribution in the mixture. Electronic structure calculations are currently limited to a few hundred atom supercells, especially for actinide oxides. Therefore, we use the so-called "special quasi-random structures" (SQS) developed by Zunger *et al.* [189] to model the cation sublattice of the $(U,Pu)O_2$ solid solution. This method gives a good approximate of the disorder even for a supercell containing less than ten atoms. The main idea is to find the structure which better represents a perfectly random structure. The principles of the SQS method and the atoms coordinates of binary alloys yielded are presented in the next paragraphs. We also give alternatives and perspectives to the SQS method.

2.4.1 Theory and principle of the method

The SQS method is based on the standard lattice theory where a given structure is characterised by distinct correlation functions denoted $\{\overline{\pi}_{k,m}\}$. Indeed, for a binary $A_{1-y}B_y$ alloy, any given arrangement of A and B in the lattice, which is called a configuration **σ**, is discretised into "figures" *f*. *f* is defined by the number of sites or vertices *k* and the number of neighbour distances *m (f=(k,m))*. We can define for example *f=(2,4)* which is a figure of 2 sites separated by 4 neighbour distances. Using the Ising language, a spin variable $\hat{\boldsymbol{S}}_i$ is assigned to each site of a given figure. It takes the value of +1 if the site is occupied by *A* and -1 if it is occupied by *B*. A spin product of a given figure positioned at a location ***l*** in a configuration **σ** is thus defined as follows:

$$\pi_f(\boldsymbol{l},\sigma) = \prod \hat{S}_i \qquad (66)$$

The distinct correlation function of the configuration **σ** for a given figure *f* is given by the lattice average of the spin product over all locations of symmetry-related figures of type *f*. It is expressed as follows:

$$\overline{\pi}_{k,m}(\sigma) = \overline{\pi}_f(\sigma) = \frac{1}{ND_f}\sum_l \pi_f(\boldsymbol{l},\sigma) \qquad (67)$$

where D_f is the number of figures *f* per site *i* and N the number of atoms.

The ensemble average of a physical property *P* over configurations can be rigorously expanded as follows:

$$\langle P\rangle = \sum_{k,m} D_{k,m}\langle\overline{\pi}_{k,m}\rangle\, p_{k,m} \qquad (68)$$

where $p_{k,m}$ are the interaction parameters of figures *f* and $\langle\overline{\pi}_{k,m}\rangle$ the correlation functions. For a perfectly random $A_{1-y}B_y$ alloy, the correlation functions are given as follows:

$$\langle\overline{\pi}_{k,m}\rangle_R = (2y-1)^k \qquad (69)$$

The main idea of the SQS method is to design a single "special" N-atom per cell periodic structure S (**σ**=*S*), whose distinct correlation functions $\overline{\pi}_{k,m}(S)$ best match the ensemble-average $\langle\overline{\pi}_{k,m}\rangle_R$ of the perfectly random alloy. The amount by which the property *P(S)* fails to reproduce the ensemble-average $\langle P\rangle$ of the perfectly random alloy can be represented in terms of a hierarchy of figures as follows:

$$\langle P\rangle - P(S) = \sum_{k,m} D_{k,m}\left[(2y-1)^k - \overline{\pi}_{k,m}(S)\right] p_{k,m} \qquad (70)$$

The occupation by *A* and *B* for the SQS structures (configurations) are chosen so that Equation (70) is minimized in the hierarchical manner over *m*.

2.4.2 Results on binary alloys

The SQS structures have been used for the modelling of various physical properties such as electronic and energetic properties of alloyed semiconductors [189, 235] as well as thermodynamic and elastic properties of metallic alloys [236, 237]. These studies give reliable results using relatively small supercells of a dozen atoms. Pezold *et al*. [237] have defined the interaction parameter of Equation (70) as the inverse fraction of mean distances between two vertices *i* and *j* of the figure *f*, denoted as follows:

$$\overline{d}_f = \frac{1}{N}\sum_{i,j;i<j} d_{ij} \qquad (71)$$

They thus obtained the new error function given in Equation (70) for a binary alloy as follows:

$$\langle P\rangle - P(S) = \sum_f \frac{D_f}{(k\overline{d}_f)^n}\left|(2x-1)^k - \overline{\pi}_f(S)\right| \qquad (72)$$

where n is the magnitude of the damping for different figures. Using Equation (72), Pezold *et al*. [237] have computed the atomic fractional coordinates of SQS structures of 32-atom fcc supercell of binary *A*-*B* alloys for all atomic compositions *y*. We use these SQS coordinates for uranium and plutonium/cerium cations in the cation sublattice of our 96-atom supercell. The atomic coordinates from Pezold *et al*. are given in Figure 32 and the resulting supercells for (U,Pu)O_2 with 25 % and 50 % Pu are given in Figure 31.

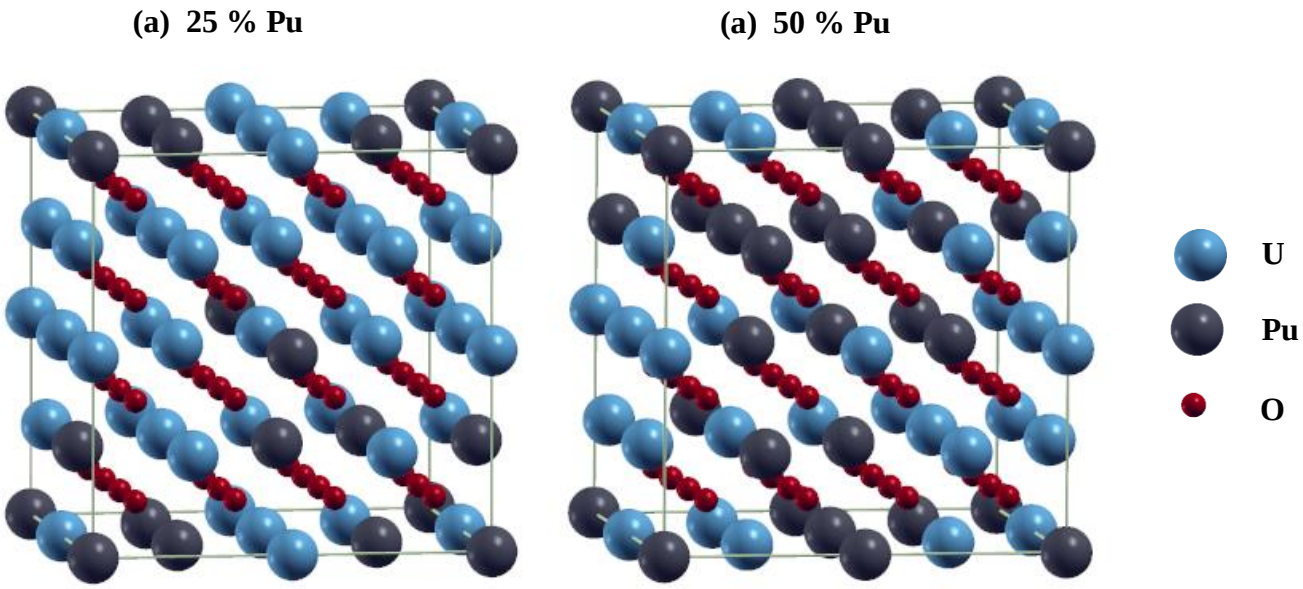

Figure 31 : SQS structures of (U,Pu)O_2 with (a) 25 % Pu and (b) 50 % Pu.

Coordinates	Concentration							
	1/16	1/8	3/16	1/4	5/16	3/8	7/16	1/2
1/4 1/2 1/4	B	B	B	B	B	B	A	B
1/4 0 1/4	B	B	B	A	B	B	B	B
1/2 1/4 1/4	B	B	B	B	B	B	B	B
1/2 3/4 1/4	B	A	A	B	A	B	A	A
3/4 1/2 1/4	B	B	A	B	B	B	B	A
3/4 0 1/4	A	A	B	B	B	B	A	A
0 1/4 1/4	B	B	B	B	B	B	B	B
0 3/4 1/4	B	B	B	B	A	A	B	A
1/4 1/4 1/2	B	B	B	B	B	B	A	B
1/4 3/4 1/2	B	B	B	B	B	B	A	A
1/2 1/2 1/2	B	B	B	B	A	B	B	A
1/2 0 1/2	B	B	B	B	B	A	A	A
3/4 1/4 1/2	B	B	B	A	B	B	B	B
3/4 3/4 1/2	B	B	A	B	B	B	A	A
0 1/2 1/2	B	B	B	B	B	B	B	B
0 0 1/2	A	B	A	B	B	A	B	B
1/4 1/2 3/4	B	B	B	B	A	A	B	A
1/4 0 3/4	B	B	B	A	B	A	A	B
1/2 1/4 3/4	B	B	B	A	B	B	B	A
1/2 3/4 3/4	B	B	B	B	B	A	B	A
3/4 1/2 3/4	B	B	B	B	B	B	B	A
3/4 0 3/4	B	A	B	A	A	A	A	B
0 1/4 3/4	B	B	B	A	B	A	A	B
0 3/4 3/4	B	B	B	B	A	B	B	B
1/4 1/4 0	B	B	B	B	B	A	B	A
1/4 3/4 0	B	B	B	B	A	A	B	A
1/2 1/2 0	B	B	B	A	B	B	A	B
1/2 0 0	B	B	B	B	B	A	A	A
3/4 1/4 0	B	A	A	B	A	A	A	B
3/4 3/4 0	B	B	A	B	A	B	B	B
0 1/2 0	B	B	B	B	A	B	B	B
0 0 0	B	B	B	A	B	B	A	A

Figure 32 : Generic SQS coordinates for the study of fcc-based random alloys by Pezold *et al.* [235]. *A* and *B* correspond to the two constituents of the binary alloy. Atomic positions are given as fractional coordinates within a 2 x 2 x 2 (32 atom) fcc supercell. Note that SQS for concentrations greater than 0.5 can be generated by interchanging the nature of constituents *A* and *B*.

2.4.3 Other approach in the modelling of random structures

Other methods for the modelling of random binary alloys can be divided into two groups. The first group is qualified as "non-structural theories" in that they only consider the average occupations by <A> or <B> of sites in the case of *A*-*B* alloys, removing the information associated with the geometrical arrangements of atoms around the sites [189, 235, 238]. Such methods are the "virtual-crystal approximation" (VCA) [239] where the alloy is assumed to have a single <AB> averaged type of atom, and the "site-coherent-potential-approximation" (SCPA) [240] where all *A*'s and separately all *B*'s are assumed equivalent and each is embedded in a uniform medium. Both these approaches are structureless since they do not take into account the local structure relaxations which impact local properties averaging. For example, even in homogenous $A_{1-y}B_y$ alloys, the average *A*-*A*, *A*-*B* and *B*-*B* distances are generally different [241]. In $(U,Pu)O_2$ for instance, it has also been shown experimentally that the local cation environments around each oxygen atom are different [49], while the cation sublattice is considered as an ideal solid solution. These methods may therefore yield a less representative description of disordered structures in $(U,Pu)O_2$ than the SQS method.

The second group, qualified as the "structural theories" are based on the direct averaging of physical properties over all or selected configurations, or using Equation (68). These are, for example, the direct sampling method, cluster expansion, the calculation of effective cluster properties and the representative structures [235].

In the direct sampling method, the measurable property <P> of a binary alloy with a lattice of N sites represents an ensemble average over all 2^N configurations σ:

$$\langle P \rangle = \sum_{\sigma}^{2^N} \rho(\sigma) P(\sigma) \qquad (73)$$

where $\rho(\sigma)$ is the probability to find the configuration σ in the system of all possible configuration. The difficulties associated with this approach are the need to relax and then average over a large number of configurations. In practice, one proceeds by either using single and sufficiently large configurations or by selecting a smaller number of "representative" configurations, such as in Monte Carlo method [242]. The molecular Monte Carlo method coupled to empirical interatomic potentials and allowing the cation exchange has, indeed, been explored as a promising perspective to SQS methods for binary supercells larger than 32 atoms. Its representative configurations can reproduce SQS structural characteristics in terms of the average number of neighbouring cations around a given atom. This can be done very accurately up to a high coordination shell (higher than the second coordination shell) as presented in Figure 33 [243, 244].

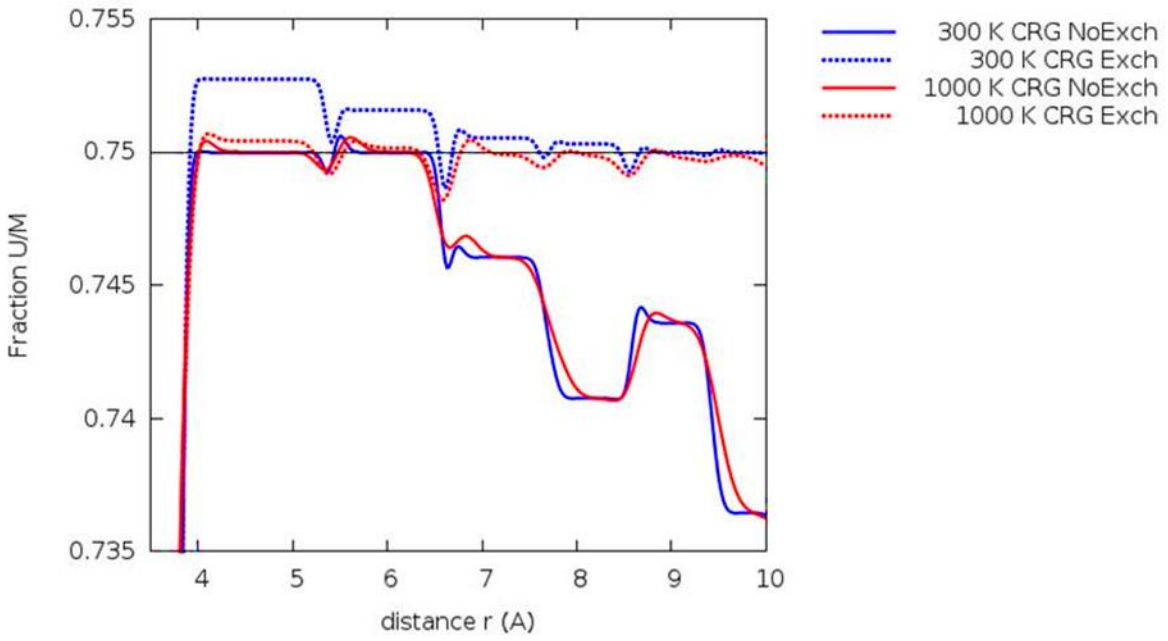

Figure 33 : Fraction of neighbouring uranium in $U_{0.75}Pu_{0.25}O_2$ with (a) cation exchange in dashed line and (b) no cation exchange in solid lines at both 300K and 1000K [241, 242].

The use of the molecular Monte Carlo method for the reproduction of SQS structures for supercells containing more than 96 atoms has been done in the framework of Takoukam's PhD [243]. It could be used to optimise the impact of the chemical environment and disorder on the modelling of the $(U,Pu)O_2$ properties.

As to the cluster expansion, the calculation of effective cluster properties and the representative structures, they all use the ensemble average of Equation (68). The only difference is found in the consideration of the interaction parameter $p_{k,m}$ of the property <*P*>. They also require the averaging over a large number of configurations [235].

2.5 Ab initio molecular dynamic method

2.5.1 Principle: use of DFT forces for the resolution of the equation of motion

The concept of *ab initio* molecular dynamics (*ab initio* MD) has been proposed by Car and Parrinello [245] in order to extend the use of pair-potential dynamics to DFT calculations. In this approach, the energy functional of the system takes into account the nuclei-nuclei interactions and external constraints. It is written as follows:

$$E[\{\psi_i\},\{\boldsymbol{R_I}\},\{\alpha_v\}] = \sum_i \int d\boldsymbol{r}\psi_i^*(\boldsymbol{r})[-\frac{\hbar^2}{2m}\boldsymbol{\nabla}^2]\psi_i(\boldsymbol{r}) + U[n(\boldsymbol{r}),\{\boldsymbol{R_I}\},\{\alpha_v\}] \quad (74)$$

Where $\{\boldsymbol{R_I}\}$ indicates the nuclei coordinates and $\{\alpha_v\}$ all the external constrains imposed to the system such as the volume Ω, the strain $\epsilon_{\mu v}$, etc. The functional U contains the Coulomb inter-nuclear repulsion and the effective potential v_{eff}.

Within this approach, all the parameters of the energy functional are considered to be time dependent, with the assumptions of the validity of classical mechanics to describe ion motion and the Born-Oppenheimer approximation to separate nuclear and electronic coordinates. Car and Parrinello [245] have thus introduced the following Lagrangian:

$$L = \sum_i \frac{1}{2}\mu \int d\boldsymbol{r}\left|\dot{\psi}_i\right|^2 + \sum_I \frac{1}{2}M_I\dot{\boldsymbol{R}}_I^2 + \sum_v \frac{1}{2}\mu_v\dot{\alpha}_v^2 - E[\{\psi_i\},\{\boldsymbol{R_I}\},\{\alpha_v\}] \quad (75)$$

where the dot indicates time derivative, M_I physical ionic mass and μ and μ_v are arbitrary parameters of appropriate units. ψ_i is subject to the holonomic constrain:

$$\int d\boldsymbol{r}\,\psi_i^*(\boldsymbol{r},t)\psi_j(\boldsymbol{r},t) = \delta_{ij} \quad (76)$$

The Lagrangian generates a dynamics for ions (M_I ionic masses) through the equation of motion as follows:

$$M_I\ddot{\boldsymbol{R}}_{\boldsymbol{I}} = -\boldsymbol{\nabla}_{\boldsymbol{R_I}}E \quad (77)$$

In other words, the equation of motion means that *ab initio* MD consists of solving the Newton's equation of motion of ions, where the forces acting on ions are computed using the DFT method, instead of empirical interatomic pair-potentials. Note that the time evolution of nuclei is efficiently coupled to the electronic minimization via an implicit adiabatic dynamic approach. In practice, this consists in introducing a fictitious dynamic for electronic orbitals such that given orbitals, initially at the minimum configuration for an initial nuclear configuration, follow the nuclear motion adiabatically. Thus, electronic orbitals are automatically at the approximately minimized configuration at each step of the *ab initio* MD evolution.

Ab initio MD allows calculations in various canonical ensembles such as NVT and NPT ensembles. For the NPT ensemble, the number of particles N, the pressure P and the temperature T are kept fixed while in the NVT, N, the volume V and T are fixed. Temperature and pressure are fixed using thermostats and barostats respectively, as presented in the next section.

2.5.2 Thermostats

In this study, the Langevin thermostat is used (MDALGO = 3 in the code VASP). Within the Langevin thermostat, temperature is maintained by modifying the Newton's equation of motion. At each time step, all particles (atoms) are submitted to a random force and have their velocities lowered using a constant friction. The equation of motion is thus written as follows:

$$M_I \ddot{\boldsymbol{R}}_{\boldsymbol{I}} = -\boldsymbol{\nabla}_{\boldsymbol{R}_I} E - M_I \Gamma \dot{\boldsymbol{R}}_{\boldsymbol{I}} + \boldsymbol{f}_{\boldsymbol{I}} \qquad (78)$$

Where Γ is the friction coefficient and f_I a random force with dispersion σ_I related to Γ through:

$$\sigma_I^2 = 2M_I \Gamma K_B T / \Delta t \,. \qquad (79)$$

The average magnitude of the random forces and the friction are related in a particular way, which guarantees that the "fluctuation-dissipation" theorem is obeyed, thereby guaranteeing NVT statistics. We have coupled Langevin thermostat to the Parrinello-Rahman (NPT) dynamics. The parameters used in VASP for the thermostat are:

- Friction coefficients (in ps^{-1}) for atomic degree of freedom: LANGEVIN_GAMMA = 10.0 10.0 10.0
- Friction coefficients (in ps^{-1}) for lattice degree of freedom: LANGEVIN_GAMMA_L = 20.0
- Fictitious mass for lattice degrees of freedom (in amu): PMASS = 1000

Other thermostats can also be used in *ab initio* MD. These are for instance the Andersen thermostat [246] where temperature is maintained via random collisions of atoms with the heat-bath at the desired temperature. The collision probability is defined as an average number of collisions per atom and time-step. We can also cite the Nosé-Hoover thermostat [247] in which an extra degree of freedom for the bath is introduced in the Lagrangian.

2.5.3 Barostats

Barostats are used to keep the pressure of a system constant during a MD simulation. It consists in coupling the system to an external bath in the same manner as for the thermostat of Andersen [246]. In the standard approach, an extra term is introduced to the equation of motion that controls the pressure change:

$$\left(\frac{dP}{dt}\right)_{bath} = \frac{P_0 - P}{\tau_P} \qquad (80)$$

where τ_P is the time constant for the coupling. The pressure is given by

$$P = \frac{2}{3V}(E_{kin} - \Xi), \quad (81)$$

where E_{kin} is the kinetic energy and Ξ is the internal virial tensor

$$\Xi = -\frac{1}{2}\sum_{i<j} \boldsymbol{r_{ij}}.\boldsymbol{F_{ij}} \quad (82)$$

$\boldsymbol{r_{ij}} = \boldsymbol{r_i} - \boldsymbol{r_j}$ and $\boldsymbol{F_{ij}}$ the force on particle *i* due to particle *j*.

Correcting the pressure in a simulation can be achieved through a change in the inner virial Ξ by scaling the inter-particle distances r_{ij}. This procedure is common for all barostats.

The Andersen barostat [246] has been developed to treat interacting particles. It was further extended to anisotropic coupling by Parrinello *et al*. [248] and later to molecular systems by Nosé *et al*. [249]. In this study, the Parrinello-Rahman barostat (ISIF = 3, IBRION = 0 in the VASP code) is used in the NPT dynamical ensemble.

2.5.4 Properties computed

Using *ab initio* MD, we have computed finite temperature properties of UO_2 and $(U,Pu)O_2$ as presented in Chapter 3. The advantage of this method compared to the phonon calculations is its ability to take directly into account the crystal anharmonicity. Therefore, the pair distribution functions of each sublattice (oxygen and actinide sublattice) can be determined even at high temperature. Thermal expansions, variations of enthalpy are also determined directly with much less adjustable parameters compared to classical dynamics using empirical interatomic potentials. Moreover, this method is transferable to systems for which thermodynamic data are not yet available.

2.6 Calculation of the formation energies of point defects in $(U,Pu)O_2$

We describe here the method developed to evaluate the formation energy of point defects in various charged states in the $(U,Pu)O_2$ fluorite phase.

2.6.1 General expression for the formation energies of point defects

The formation energy $E_f^{D_J}$ of a point defect D_J in a defective supercell related to the element *J* in a charge state *q* is expressed as follows:

$$E_f^{D_J} = E_{tot}(D_J, q) - \sum_J n_J \mu_J + q\mu_e + E_{corr} \quad (83)$$

In this equation, $E_{tot}(D_J, q)$ is the total energy of the defective supercell, n_J the number of atomic-species *J* in the defective supercell, μ_J the chemical potential of the element *J* in the perfect supercell without the defect D_J. μ_e is the electronic chemical potential of the material, i.e. the Fermi level and E_{corr} a correction energy aiming at minimizing the spurious interactions due to the finite size charged supercell [250–252]. The total energy of the defective supercell and the Fermi level can be obtained from electronic structure calculations and the correction term calculated using the structural parameters and Madelung constant. The chemical potentials of the constitutive elements in the compound, however, are not yielded by the calculations and depend on the exact composition of the compound. In mixed $(U,Pu)O_2$ oxides, a large domain of compositions with various U, Pu and O contents may exist. In order to determine the formation energies of defects in the $(U,Pu)O_2$ fluorite phase, the chemical potentials accessible for its constitutive elements (oxygen, uranium and plutonium) must therefore be evaluated.

2.6.2 Stability of $(U,Pu)O_2$ fluorite phase as a function of composition

Let us consider a $(U,Pu)O_2$ fluorite phase with composition $U_{1-y}Pu_yO_{2+x}$, where, y is the plutonium content ($0 < y < 1$), x the deviation from stoichiometry ($x<0$ corresponding to hypo-stoichiometric or O-poor compositions and $x > 0$ to hyper-stoichiometric or O-rich ones).

According to the phase diagramme of the (U-Pu-O) system, determined experimentally by Markin and Street [22] and Sari *et al.* [23] or determined using the CALPHAD method by Guéneau *et al.*[4], the stability domain of the $(U,Pu)O_2$ fluorite phase is bordered on the one hand by UO_2 and PuO_2 fluorite phases and on the other hand by reduced and oxidized (U-Pu-O) phases. This stability domain is represented schematically in Figure 34 as a function of deviation from stoichiometry *x* and of the Pu content *y*.

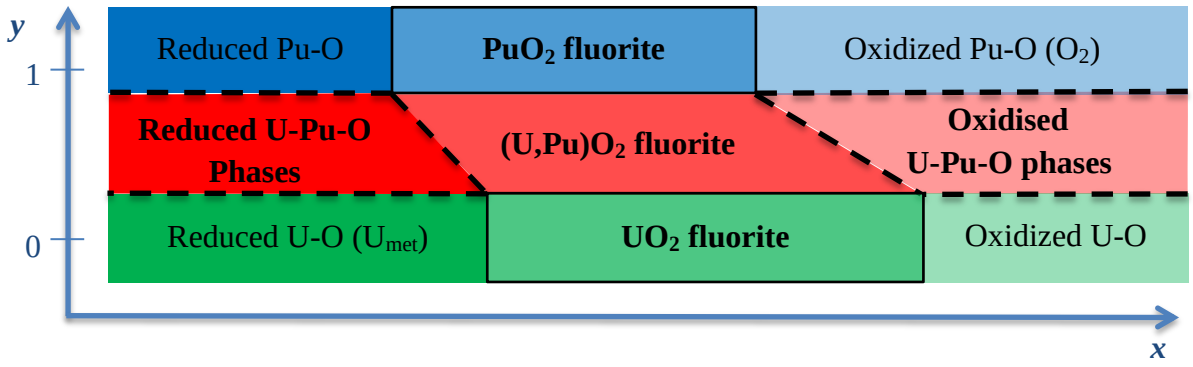

Figure 34: Schematic representation of the stability domain of the $(U,Pu)O_2$ fluorite phase and neighbouring phases as a function of the deviation from stoichiometry *x* and the Pu content y.

The limits of compositions shown in Figure 34 are only indicative and obtained by taking into account the maximum stability domain of the fluorite phases for the whole range of temperatures (from 0 K to melting temperature). This will enable us to obtain an envelope for the accessible chemical potentials.

The (U-O) and (Pu-O) systems are relatively well known and the compositions of the phase limits represented in solid lines in Figure 34 are known. The oxidized and reduced phases of the (U-Pu-O) system are, on the contrary, more complex and their compositions have not been determined exactly. The experimental [22,23] and calculated [4] phase diagrams predict that the oxidized phases are M_4O_9 and M_3O_8, where M represents a mixture of U and Pu whose exact composition is not known. The reduced phases might be the metallic ξ-(U,Pu) phase, or the $PuO_{1.52}$ or Pu_2O_3 oxide phases. Thermodynamic properties of these phases, in particular their enthalpies of formation, are also lacking. In addition, the number of possible phases and structures makes it impossible to determine them unequivocally by electronic structure calculations at this stage.

The compositions of the phase limits between $(U,Pu)O_2$ fluorite phase and the oxidized and reduced phases are therefore not known. We approximate these boundaries by straight lines between the boundaries separating the UO_2 and PuO_2 phases and their neighbouring oxidized and reduced phases, as shown in dotted lines on Figure 34. This assumption is all the more justified if the extent of the phase along the y axis is small. The limits of the $(U,Pu)O_2$ domain can then be deduced from the knowledge of the (U-O) and (Pu-O) systems.

We will therefore calculate the minimum and maximum values of the $\Delta\mu_{Pu}$, $\Delta\mu_U$ and $\Delta\mu_O$ chemical potentials corresponding to the stability domain of the $(U,Pu)O_2$ fluorite phase using the chemical potentials accessible in the U-O and Pu-O phases.

2.6.2.1 Chemical potentials at the boundaries between UO_2 and PuO_2 fluorite phases and their oxidized and reduced phases

We consider here the MO_{2+x} fluorite phases with M being U or Pu and x being the deviation from stoichiometry (x<0 corresponding to hypo-stoichiometric or O-poor compositions and x > 0 to hyper-stoichiometric or O-rich ones).

The standard enthalpy of formation of the MO_{2+x} solid solution is the change of enthalpy accompanying the formation of one mole of solid solution from its constitutive elements in their standard states. The standard states of U and Pu are the metallic α-phases and the standard state for O is the O_2 molecule. The enthalpy of formation of MO_{2+x} can then be expressed as follows:

$$\Delta H_f^{MO_{2+x}} = \mu_{MO_{2+x}}^{bulk} - \mu_M^{metal} - (2+x)\mu_O^{O_2} \qquad (84)$$

where, μ_M^{metal} and $\mu_O^{O_2}$ are the chemical potentials of M (U or Pu) and O in their reference states, respectively and $\mu_{MO_{2+x}}^{bulk}$ is the total energy of the MO_{2+x} crystal.

The latter energy can be written as a function of the atomic chemical potentials in the compound as follows:

$$\mu_{MO_{2+x}}^{bulk} = \mu_M^{MO_{2+x}} + (2+x)\mu_O^{MO_{2+x}} \qquad (85)$$

where, $\mu_M^{MO_{2+x}}$ and $\mu_O^{MO_{2+x}}$ are the chemical potentials of the metal and oxygen in MO_{2+x}, respectively.

We can therefore express the enthalpy of formation of MO_{2+x} as a function of the chemical potentials of its constitutive elements in the compound and in their reference states.

$$\Delta H_f^{MO_{2+x}} = \mu_M^{MO_{2+x}} + (2+x)\mu_O^{MO_{2+x}} - \mu_M^{metal} - (2+x)\mu_O^{O_2} \qquad (86)$$

Let us define the relative chemical potential as the difference of chemical potentials of the element j in the MO_{2+x} compound on the one hand, and in its reference state on the other hand:

$$\Delta\mu_M^{MO_{2+x}} = \mu_M^{MO_{2+x}} - \mu_M^{metal} \qquad (87)$$

$$\Delta\mu_O^{MO_{2+x}} = \mu_O^{MO_{2+x}} - \mu_O^{O_2} \qquad (88)$$

The enthalpy of formation of MO_{2+x} can then be rewritten as:

$$\Delta H_f^{MO_{2+x}} = \Delta\mu_M^{MO_{2+x}} + (2+x)\Delta\mu_O^{MO_{2+x}} \qquad (89)$$

To determine the minimal and maximal values of the relative chemical potentials $\Delta\mu_M^{MO_{2+x}}$and $\Delta\mu_O^{MO_{2+x}}$, we consider the stability of various phases in the U-O and Pu-O systems.

The various stable phases of the U-O system as a function of the oxygen content or deviation from stoichiometry *x* are synthesised inFigure 35.

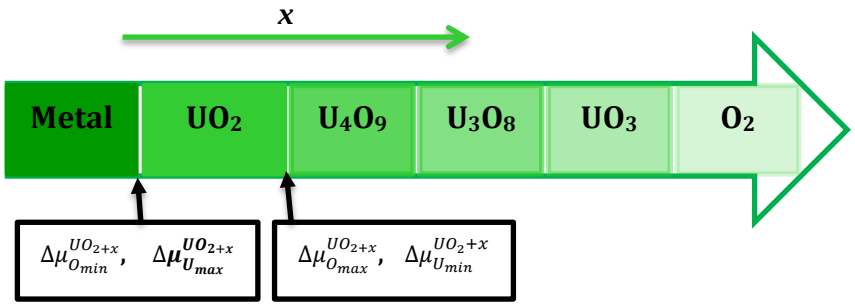

Figure 35 : Stable phases of U-O system as a function of deviation from stoichiometry *x* and positions of minimum and maximal values of the chemical potentials for U and O.

The O-rich boundary of UO_{2+x} corresponds to the co-existence of UO_{2+x} and U_4O_9. At this boundary, the chemical potentials are identical in both phases. This results in conditions as follows:

$$\begin{cases} \Delta\mu_{U_{min}}^{UO_{2+x}} + (2 + x_{max}^{UO_{2+x}})\Delta\mu_{O_{max}}^{UO_{2+x}} = \Delta H_f^{UO_{2+x}} \\ 4\Delta\mu_{U_{min}}^{UO_{2+x}} + 9\Delta\mu_{O_{max}}^{UO_{2+x}} = \Delta H_f^{U_4O_9} \end{cases} \quad (90)$$

Similarly, the O-poor boundary of UO_{2+x} corresponds to the co-existence of UO_{2+x} and with the uranium metallic phase. The chemical potential of uranium is identical in both compounds, *i.e.*:

$$\begin{cases} \Delta\mu_{U_{max}}^{UO_{2+x}} = 0 \\ (2 + x_{min}^{UO_{2+x}})\Delta\mu_{O_{min}}^{UO_2} + \Delta\mu_{U_{max}}^{UO_2} = \Delta H_f^{UO_2+x} \end{cases} \quad (91)$$

The minimum and maximum relative chemical potential values of the UO_{2+x} domain are then:

At the O-rich limit,

$$\Delta\mu_{O_{max}}^{UO_{2+x}} = \frac{1}{1-4x_{max}^{UO_{2+x}}}(\Delta H_f^{U_4O_9} - 4\Delta H_f^{UO_{2+x}}) \quad (92)$$

$$\Delta\mu_{U_{min}}^{UO_{2+x}} = \frac{1}{1-4x_{max}^{UO_{2+x}}}(9\Delta H_f^{UO_{2+x}} - (2 + 4x_{max}^{UO_{2+x}})\Delta H_f^{U_4O_9}). \quad (93)$$

And at the O-poor limit,

$$\Delta\mu_{O_{min}}^{UO_{2+x}} = \frac{1}{2+x_{min}^{UO_{2+x}}}\Delta H_f^{UO_{2+x}} \quad (94)$$

$$\Delta\mu_{U_{max}}^{UO_{2+x}} = 0. \quad (95)$$

$\Delta H_f^{UO_{2+x}}$ can be evaluated as a function of x using the phase diagram of the U-O system calculated by Guéneau *et al.* [253]. This enables us to determine the minimum and maximum relative chemical potential values of O and U accessible in the UO_{2+x} fluorite stability domain at a given temperature.

For instance, if we interpolate the thermodynamic functions of the U-O phase diagram of Guéneau *et al.* [253], $x_{min}^{UO_{2+x}} \approx x_{max}^{UO_{2+x}} \approx 0$ ($\pm 10^{-6}$) at 0 K.

Similarly, the various stable phases of the Pu-O system as a function of oxygen content are summarized in Figure 36.

At the boundary of the PuO_2 solid with the O_2 gas (O-rich), the oxygen chemical potential is identical in both PuO_2 and O_2. This results in the following conditions:

$$\begin{cases} \Delta\mu_{O_{max}}^{PuO_{2+x}} = 0 \\ \Delta\mu_{Pu_{min}}^{PuO_{2+x}} + (2 + x_{max}^{PuO_{2+x}})\Delta\mu_{O_{max}}^{PuO_{2+x}} = \Delta H_f^{PuO_{2+x}} \end{cases} \quad (96)$$

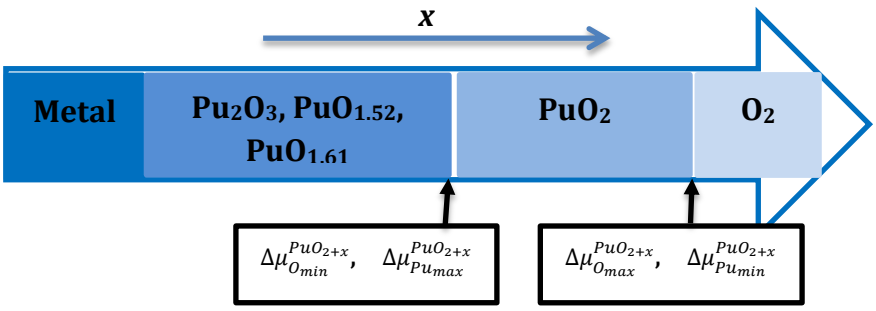

Figure 36 : Stable phases of Pu-O system as a function of deviation from stoichiometry x and positions of minimum and maximal values of the chemical potentials for Pu and O.

The O-poor boundary of PuO_{2+x} corresponds to the beginning of stability of reduced phases (Pu_2O_3, $PuO_{1.52}$, or $PuO_{1.61}$ depending on the temperature). The chemical potentials of plutonium and oxygen are identical in both phases. If we consider the Pu_2O_3 phase to obtain the largest possible stability domain over the whole range of temperature, this results in the conditions as follows:

$$\begin{cases} \Delta\mu_{Pu_{max}}^{PuO_2} + (2 + x_{min}^{PuO_{2+x}})\Delta\mu_{O_{min}}^{PuO_2} = \Delta H_f^{PuO_{2+x}} \\ 2\Delta\mu_{Pu_{max}}^{PuO_{2+x}} + 3\Delta\mu_{O_{min}}^{PuO_{2+x}} = \Delta H_f^{Pu_2O_3} \end{cases} \quad (97)$$

The chemical potential values of the boundaries of the PuO_{2+x} domain therefore are:

At the O-poor limit,

$$\Delta\mu_{O_{min}}^{PuO_{2+x}} = \frac{1}{1+2x_{min}^{PuO_{2+x}}}(2\Delta H_f^{PuO_{2+x}} - \Delta H_f^{Pu_2O_3}) \quad (98)$$

$$\Delta\mu_{Pu_{max}}^{PuO_{2+x}} = \frac{1}{1+2x_{min}^{PuO_{2+x}}}((2 + x_{min}^{PuO_{2+x}})\Delta H_f^{Pu_2O_3} - 3\Delta H_f^{PuO_{2+x}}). \quad (99)$$

At the O-rich limit,

$$\Delta\mu_{O_{max}}^{PuO_{2+x}} = 0 \quad (100)$$

$$\Delta\mu_{Pu_{min}}^{PuO_{2+x}} = \Delta H_f^{PuO_2+x} \quad (101)$$

By evaluating $\Delta H_f^{PuO_{2+x}}$ for $x_{min}^{PuO_{2+x}}$ using the phase diagram of the Pu-O system calculated by Guéneau *et al*. [254], we can determine the minimum and maximum relative chemical potential values of O and Pu accessible in the stability domain of the PuO_{2+x} fluorite phase at a given temperature.

For instance at 0 K, $x_{min}^{PuO_{2+x}} \approx 0$.

2.6.2.2 Chemical potentials in the $U_{1-y}Pu_yO_{2+x}$ fluorite phase

The standard enthalpy of formation for $U_{1-y}Pu_yO_{2+x}$, called $(U,Pu)O_{2+x}$ below, is

$$\Delta H_f^{(U,Pu)O_{2+x}} = \mu_{(U,Pu)O_{2+x}}^{bulk} - (1-y)\mu_U^{metal} - y\mu_{Pu}^{metal} - (2+x)\mu_O^{O_2} \quad (102)$$

Similarly to what was done for MO_{2+x} above,

$$\mu_{(U,Pu)O_{2+x}}^{bulk} = (1-y)\mu_U^{(U,Pu)O_{2+x}} + y\mu_{Pu}^{(U,Pu)O_{2+x}} + (2+x)\mu_O^{(U,Pu)O_{2+x}} \quad (103)$$

Where, $\mu_U^{(U,Pu)O_{2+x}}, \mu_{Pu}^{(U,Pu)O_{2+x}}$ *and* $\mu_O^{(U,Pu)O_{2+x}}$ are the chemical potentials of uranium, plutonium and oxygen in $(U,Pu)O_{2+x}$, respectively.

The enthalpy of formation of $(U,Pu)O_{2+x}$ can therefore be expressed as a function of the chemical potentials of its constitutive elements in the compound and in their reference states:

$$\Delta H_f^{(U,Pu)O_{2+x}} = (1-y)\mu_U^{(U,Pu)O_{2+x}} + y\mu_{Pu}^{(U,Pu)O_{2+x}} + (2+x)\mu_O^{(U,Pu)O_{2+x}} - (1-y)\mu_U^{metal} - y\mu_{Pu}^{metal} - (2+x)\mu_O^{O_2} \quad (104)$$

Using the relative chemical potentials $\Delta\mu_j^{(U,Pu)O_{2+x}}$:

$$\Delta\mu_U^{(U,Pu)O_{2+x}} = \mu_U^{(U,Pu)O_{2+x}} - \mu_U^{metal} \quad (105)$$

$$\Delta\mu_{Pu}^{(U,Pu)O_{2+x}} = \mu_{Pu}^{(U,Pu)O_{2+x}} - \mu_{Pu}^{metal} \quad (106)$$

$$\Delta\mu_O^{(U,Pu)O_{2+x}} = \mu_O^{(U,Pu)O_{2+x}} - \mu_O^{O_2}, \quad (107)$$

The enthalpy of formation of (U,Pu)O_2 can be rewritten as follows:

$$\Delta H_f^{(U,Pu)O_{2+x}} = (1-y)\Delta\mu_U^{(U,Pu)O_{2+x}} + y\Delta\mu_{Pu}^{(U,Pu)O_{2+x}} + (2+x)\Delta\mu_O^{(U,Pu)O_{2+x}} \quad (108)$$

Using the mixing enthalpy ΔH_{MIX}, defined as:

$$\Delta H_{MIX} = \Delta H_f^{(U,Pu)O_{2+x}} - (1-y)\Delta H_f^{UO_{2+x}} - y\Delta H_f^{PuO_{2+x}}, \quad (109)$$

$$(1-y)\Delta\mu_U^{(U,Pu)O_{2+x}} + y\Delta\mu_{Pu}^{(U,Pu)O_{2+x}} + (2+x)\Delta\mu_O^{(U,Pu)O_{2+x}} = \Delta H_{MIX} + (1-y)\Delta H_f^{UO_{2+x}} + y\Delta H_f^{PuO_{2+x}} \quad (110)$$

Then,

$$\Delta\mu_{Pu}^{(U,Pu)O_{2+x}} = \frac{1}{y}\left[(1-y)\Delta H_f^{UO_{2+x}} + y\Delta H_f^{PuO_{2+x}} + \Delta H_{MIX} - (1-y)\Delta\mu_U^{(U,Pu)O_{2+x}} - (2+x)\Delta\mu_O^{(U,Pu)O_{2+x}}\right] \quad (111)$$

and

$$\Delta\mu_U^{(U,Pu)O_{2+x}} = \frac{1}{1-y}\left[(1-y)\Delta H_f^{UO_{2+x}} + y\Delta H_f^{PuO_{2+x}} + \Delta H_{MIX} - y\Delta\mu_{Pu}^{(U,Pu)O_{2+x}} - (2+x)\Delta\mu_O^{(U,Pu)O_{2+x}}\right] \quad (112)$$

Using Equation (111) and Equation (112), the third $\Delta\mu_X^{(U,Pu)O_{2+x}}$ can be determined if the two other of them are known.

Then, these equations can be rewritten as follows when *the Pu content* tends to 0 ($y\rightarrow 0$) or 1 ($y\rightarrow 0$).

For $y\rightarrow 0$

$$\Delta\mu_{Pu}^{(U,Pu)O_{2+x}} = \Delta H_f^{PuO_{2+x}} + \frac{\Delta H_{MIX}}{y} + \frac{(1-y)}{y}\left[\Delta H_f^{UO_{2+x}} - \Delta\mu_U^{(U,Pu)O_{2+x}} - (2+x)\,\Delta\mu_O^{(U,Pu)O_{2+x}}\right] + \left[\frac{(1-y)(2+x)}{y} - \frac{(2+x)}{y}\right]\Delta\mu_O^{(U,Pu)O_{2+x}} \quad (113)$$

$$\Delta\mu_{Pu}^{(U,Pu)O_{2+x}} = \Delta H_f^{PuO_{2+x}} + \frac{\Delta H_{MIX}}{y} + \frac{(1-y)}{y}\left[\Delta H_f^{UO_{2+x}} - \Delta\mu_U^{(U,Pu)O_{2+x}} - (2+x)\,\Delta\mu_O^{(U,Pu)O_{2+x}}\right] - (2+x)\,\Delta\mu_O^{(U,Pu)O_{2+x}} \quad (114)$$

For $y \rightarrow 0$, $(U,Pu)O_{2+x} \rightarrow UO_{2+x}$, so that $\Delta\mu_U^{(U,Pu)O_{2+x}} \rightarrow \Delta\mu_U^{UO_{2+x}}$ and $\Delta\mu_O^{(U,Pu)O_{2+x}} \rightarrow \Delta\mu_O^{UO_{2+x}}$

As a consequence,

$$\Delta H_f^{UO_{2+x}} - \Delta\mu_U^{(U,Pu)O_{2+x}} - (2+x)\,\Delta\mu_O^{(U,Pu)O_{2+x}} = 0 \quad (115)$$

and

$$\Delta\mu_{Pu}^{(U,Pu)O_{2+x}} = \Delta H_f^{PuO_{2+x}} + \frac{\Delta H_{MIX}}{y} - (2+x)\,\Delta\mu_O^{(U,Pu)O_{2+x}} \quad (116)$$

As shown in Section 3.3.1.2 for x=0, ΔH_{MIX} is quadratic as a function of y and can be written as:

$$\Delta H_{MIX} = y^2(1-y)\Delta H_{sol}^{U\ in\ PuO_2+x} + y(1-y)^2\Delta H_{sol}^{Pu\ in\ UO_{2+x}} \quad (117)$$

where, $\Delta H_{sol}^{U\ in\ PuO_2}$ and $\Delta H_{sol}^{Pu\ in\ UO_2}$ are the solution enthalpies of U in PuO_2 and of Pu in UO_2, respectively.

Therefore when $y \rightarrow 0$, $\frac{\Delta H_{MIX}}{y} \rightarrow \Delta H_{sol}^{Pu\ in\ UO_{2+x}}$ and

$$\Delta\mu_{Pu}^{(U,Pu)O_{2+x}}(y \rightarrow 0) = \Delta H_f^{PuO_{2+x}} + \Delta H_{sol}^{Pu\ in\ UO_{2+x}} - (2+x)\,\Delta\mu_O^{(U,Pu)O_{2+x}} \quad (118)$$

For $y \rightarrow 1$

$$\Delta\mu_U^{(U,Pu)O_{2+x}} = \frac{1}{1-y}\left[(1-y)\Delta H_f^{UO_{2+x}} + y\Delta H_f^{PuO_{2+x}} + \Delta H_{MIX} - y\Delta\mu_{Pu}^{(U,Pu)O_{2+x}} - (2+x)\Delta\mu_O^{(U,Pu)O_{2+x}}\right] \quad (119)$$

$$\Delta\mu_U^{(U,Pu)O_{2+x}} = \Delta H_f^{UO_{2+x}} + \frac{\Delta H_{MIX}}{1-y} + \frac{y}{1-y}\left[\Delta H_f^{PuO_{2+x}} - \Delta\mu_{Pu}^{(U,Pu)O_{2+x}} - (2+x)\,\Delta\mu_O^{(U,Pu)O_{2+x}}\right] + \left[-\left(\frac{2+x}{1-y}\right) + \frac{y}{1-y}(2+x)\right]\Delta\mu_O^{(U,Pu)O_{2+x}} \quad (120)$$

For $y \rightarrow 1$, $(U,Pu)O_{2+x} \rightarrow PuO_{2+x}$,

so that $\Delta\mu_{Pu}^{(U,Pu)O_{2+x}} \rightarrow \Delta\mu_{Pu}^{PuO_{2+x}}$ and $\Delta\mu_O^{(U,Pu)O_{2+x}} \rightarrow \Delta\mu_O^{PuO_{2+x}}$

As a consequence,

$$\Delta H_f^{PuO_{2+x}} - \Delta\mu_{Pu}^{(U,Pu)O_{2+x}} - (2+x)\,\Delta\mu_O^{(U,Pu)O_{2+x}} = 0 \quad (121)$$

and

$$\Delta\mu_U^{(U,Pu)O_{2+x}} = \Delta H_f^{UO_{2+x}} + \frac{\Delta H_{MIX}}{1-y} - (2+x)\ \Delta\mu_O^{(U,Pu)O_{2+x}} \quad (122)$$

When y→ 1, according to Equation (117), $\frac{\Delta H_{MIX}}{1-y} \rightarrow \Delta H_{sol}^{U\ in\ PuO_{2+x}}$

And $\Delta\mu_U^{(U,Pu)O_{2+x}}(y \rightarrow 1) = \Delta H_f^{UO_{2+x}} + \Delta H_{sol}^{U\ in\ PuO_{2+x}} - (2+x)\ \Delta\mu_O^{(U,Pu)O_{2+x}}$ (123)

2.6.3 Boundaries of stability domain of $(U,Pu)O_2$ fluorite phase

The stability domain of $(U,Pu)O_{2+x}$ fluorite is approximated as a parallelepipedic area in the $(\Delta\mu_O, \Delta\mu_U, \Delta\mu_{Pu})$ frame. The limits of this parallelepiped are obtained from the limits of the stability domains of the UO_{2+x} and PuO_{2+x} fluorite phases, as determined in Section 2.6.2.1.

Figure 37 shows a schematic 3D representation of the stability domains of the UO_{2+x}, PuO_{2+x} and $(U,Pu)O_{2+x}$ fluorite phases as a function of the relative chemical potentials $\Delta\mu_O, \Delta\mu_U$ and $\Delta\mu_{Pu}$.

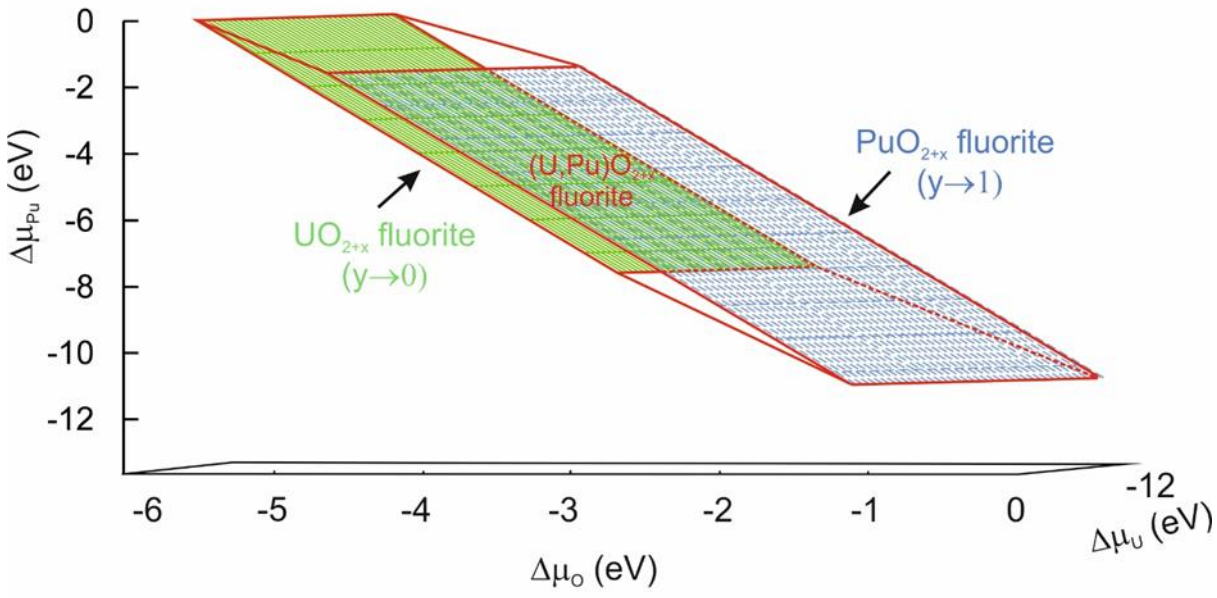

Figure 37 : Domain of stability (in red) of the $(U,Pu)O_{2+x}$ fluorite phase as a function of $\Delta\mu_O, \Delta\mu_U$ and $\Delta\mu_{Pu}$, approximated as a parallelepiped. The blue plane (above) is the PuO_{2+x} plane, the green plane (below) is the UO_{2+x} plane.

Within this approximation, the intervals of relative chemical potentials accessible for O, U and Pu can be deduced from the equations above as as follows:

From Equations (94) for UO_2 and (98) for PuO_2,

$$\Delta\mu_{O_{min}}^{(U,Pu)O_{2+x}} = \min\left[\frac{1}{2+x_{min}}\Delta H_f^{UO_{2+x_{min}}}, \frac{1}{1+2x_{min}}\left(2\Delta H_f^{PuO_{2+x_{min}}} - \Delta H_f^{Pu_2O_3}\right)\right] \quad (124)$$

From Equation (100),

$$\Delta\mu_{O_{max}}^{(U,Pu)O_{2+x}} = 0 \quad (125)$$

From Equations (93) for UO_2 and (123) for $(U,Pu)O_2$,

$$\Delta\mu_{U_{min}}^{(U,Pu)O_{2+x}} = \min\left[\frac{1}{1-4x_{max}^{UO_{2+x}}}\left(9\Delta H_f^{UO_{2+x_{max}}} - \left(2+4x_{max}^{UO_{2+x}}\right)\Delta H_f^{U_4O_9}\right),\right.$$

$$\left.\Delta H_f^{UO_{2+x_{max}}} + \Delta H_{sol}^{U\ in\ PuO_{2+x}} - \left(2+x_{max}^{(U,Pu)O_{2+x}}\right)\Delta\mu_O^{(U,Pu)O_{2+x_{max}}}\right] \quad (126)$$

From Equation (95),

$$\Delta\mu_{U_{max}}^{(U,Pu)O_{2+x}} = \Delta\mu_{U_{max}}^{UO_{2+x}} = 0 \quad (127)$$

From Equations (101) for PuO_2 and (118) for $(U,Pu)O_2$,

$$\Delta\mu_{Pu_{min}}^{(U,Pu)O_{2+x}} =$$
$$\min\left[\Delta H_f^{PuO_{2+x_{max}}}, \Delta H_f^{PuO_{2+x_{max}}} + \Delta H_{sol}^{Pu\ in\ UO_{2+x}} - (2+x)\,\Delta\mu_O^{(U,Pu)O_{2+x_{max}}}\right] \quad (128)$$

Finally, from Equations (99) for PuO_2 and (118) for $(U,Pu)O_2$,

$$\Delta\mu_{Pu_{max}}^{(U,Pu)O_{2+x}} = \max\left[\frac{1}{1+2x_{min}^{PuO_{2+x}}}\left(\left(2+x_{min}^{PuO_{2+x}}\right)\Delta H_f^{Pu_2O_3} - 3\Delta H_f^{PuO_{2+x}}\right),\right.$$

$$\left.\Delta H_f^{PuO_{2+x_{min}}} + \Delta H_{sol}^{Pu\ in\ UO_{2+x}} - (2+x_{min})\,\Delta\mu_{O_{min}}^{(U,Pu)O_{2+x_{min}}}\right] \quad (129)$$

2.6.4 Numerical application in $U_{0.75}Pu_{0.25}O_{2+x}$ and $U_{0.75}Ce_{0.25}O_{2+x}$

The values of the relative chemical potential of U, Pu and O at the boundaries of the fluorite phase of the $(U,Pu)O_2$ solid solution are summarized in Table 17. These values are calculated from Equations (124) to (129). These values are calculated at 300 K. At

this temperature, we find $x_{max\ or\ min}^{UO_{2+x}} \approx x_{max\ or\ min}^{PuO_{2+x}} \approx x_{max\ or\ min}^{CeO_{2+x}} \approx \pm 10^{-5}$ from the CALPHAD calculations. The temperature of 300 K is chosen since since the enthalpies of formation in the U-O and Pu-O system varies very little between 0 and 300 K and the energetic properties of actinide oxides calculated using the DFT+U at 0 K compare very well to the experimental and CALPHAD ones at 300 K. The values of the chemical potentials of the reference states of each species are also given.

Compound	**O-poor**			**O-rich**		
	$\Delta\mu_U$	$\Delta\mu_{Pu}$	$\Delta\mu_O$	$\Delta\mu_U$	$\Delta\mu_{Pu}$	$\Delta\mu_O$
(U,Pu)O_{2+x}	0	0.22	-5.62	-11.25	-10.99	0
Ref. states	$\mu_U^{metal} = -7.30\ eV$,		$\mu_{Pu}^{met} = -10.21\ eV$,		$\mu_O^{O_2} = -4.24\ eV$	
Solution enthalpies	$\Delta H^{U\ in\ PuO2} = -0.02\ eV$ and $\Delta H^{Pu\ in\ UO2} = -0.03\ eV$					
Conditions	T = 300 K, $x_{max\ or\ min}^{UO_{2+x}} \approx x_{max\ or\ min}^{PuO_{2+x}} \approx \pm 10^{-5}$					

Table 17 : Relative chemical potentials of uranium, plutonium and oxygen in the (U,Pu)O_2 for various Pu contents. The chemical potentials of reference states are given in the last line.

The extension of the present approach to (U,Ce)O_{2+x} gives the maximum and minimum values of the U, Ce and O relative chemical potentials shown in Table 18.

Compound	**O-poor**			**O-rich**		
	$\Delta\mu_U$	$\Delta\mu_{Ce}$	$\Delta\mu_O$	$\Delta\mu_U$	$\Delta\mu_{Ce}$	$\Delta\mu_O$
(U,Ce)O_{2+x}	0	-0.09	-5.62	-11.25	-11.30	0
Ref. states	$\mu_U^{metal} = -7.30\ eV$,		$\mu_{Ce}^{met} = -4.24\ eV$,		$\mu_O^{O_2} = -4.24\ eV$	
Solution enthalpies	$\Delta H^{U\ in\ CeO2} = -0.02\ eV$ and $\Delta H^{Ce\ in\ UO2} = -0.03\ eV$					
Concitions	T = 300 K, $x_{max\ or\ min}^{UO_{2+x}} \approx x_{max\ or\ min}^{CeO_{2+x}} \approx \pm 10^{-5}$					

Table 18 : Relative chemical potentials of uranium, plutonium and oxygen in the (U,Ce)O_2 for various Pu contents. The chemical potentials of reference states are given in the last line.

The minimum and maximum values of the chemical potentials of U, Pu, Ce and O in (U,Pu)O_{2+x} and (U,Ce)O_{2+x} calculated in this section are used in Chapters 4 and 5 for the

calculation of the formation energies of point defects. The chemical potential of given chemical species are obtained by adding the relative chemical potential to the reference state ones in the O-rich or O-poor region.

Chapter 3 : Bulk properties of uranium-plutonium mixed oxides

3.1 Introduction

The study of the perfect (U,Pu)O_2 crystal enables one to determine bulk materials properties that are not known experimentally. It is also unavoidable for the study of point defects. Indeed, in order to investigate the modifications in (U,Pu)O_2 properties induced by point defects, it is necessary to study first the perfect crystal. This study is made challenging owing to the complex electronic structure linked to the correlated *5f* electrons, and the modelling of a solid solution in this mixture. In this manuscript, the issue of strongly correlated electrons is tackled through the use of the DFT+*U* method and the mixture is taken into account through the use of SQS structures. Furthermore, as mentioned in Chapter 1, section 1.2.3.1, the magnetic properties of (U,Pu)O_2 are not yet established neither experimentally nor theoretically. Even for its end member PuO_2, the magnetic properties remain not clearly established. These properties are of course very important for the electronic structure calculations. Moreover, using LDA or GGA within the DFT+*U* method, the electronic structure calculations are known to poorly describe the energetic properties such as the enthalpy of formation [255] and the atomization energy of gas molecules [256] such as O_2, as well as solid crystals [16]. We demonstrate in this chapter that this problem can be tackled by taking into account non-local correlations through the van der Waals (vdW) corrections.

In the present chapter, we present the electronic structure calculations of the bulk properties of the perfect crystal (U,Pu)O_2 (without defects) both at 0 K and also at finite temperature. The temperature effect is taken into account using *ab initio* molecular dynamics (*ab initio MD*). A particular focus is made on the effect of plutonium content. We first analyse the 0 K properties of (U,Pu)O_2 following several steps. The first step consists in analysing the stability of magnetic configurations, namely the antiferromagnetic (AFM) and the ferromagnetic (FM) configurations. The second step consists in modelling the structural, elastic and electronic properties of (U,Pu)O_2 for various plutonium contents. The energetic properties are also studied using various functionals, namely PBE+*U* and vdW-optPBE+*U*. Next, we model the thermodynamic properties at various temperatures and for various plutonium contents. Therein, we first analyse the crystal disorder at each temperature through radial distribution functions. Further, the thermal expansion, variation of enthalpy and heat capacity are calculated as a function of the temperature for various plutonium contents. This study is the first one available using *ab initio* molecular dynamic for actinide oxides.

3.2 Magnetic, structural, elastic and electronic properties of $(U,Pu)O_2$

3.2.1 Magnetic configuration in $(U,Pu)O_2$

In this section, we study the magnetic stability of $(U,Pu)O_2$ for various Pu contents. The configurations of interest are the 1k antiferromagnetic (1k-AFM) and ferromagnetic (FM) orders. The study of magnetic stability consists in comparing ground-state energies, lattice constants and band gaps of $(U,Pu)O_2$ for each magnetic configuration. In the 1k antiferromagnetic configuration, the magnetic moments of cations are alternatively positive and negative from one crystallographic (100) plane to the next one, all collinear to a given crystallographic direction. In the ferromagnetic configuration, all magnetic moments of atoms are oriented in the same direction (with the same sign). Figure 38 illustrates the 1k-AFM and the FM configurations in $(U,Pu)O_2$.

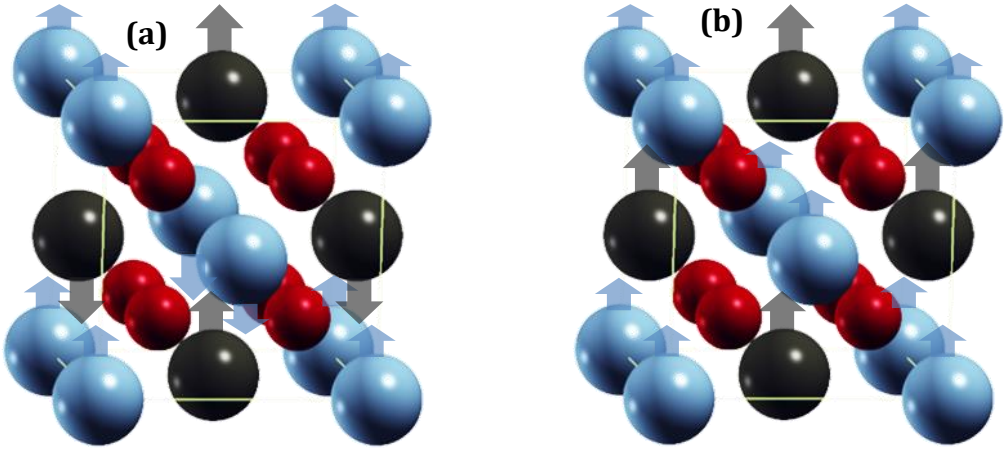

Figure 38 : (a) 1k-AFM and (b) FM configurations in $(U,Pu)O_2$ mixed oxides. The uranium atoms are represented in blue, plutonium in black and oxygen in red.

Table 19 shows the lattice constants, the band gap and the ground-state energy differences of $(U,Pu)O_2$, calculated for 1k-AFM and FM configurations, for various plutonium contents.

The ground-state energy difference E_{FM}-E_{AFM}/atom per atom, which is the difference between the FM configuration and the 1k-AFM configuration, is given in the last column in *meV* for various plutonium contents. These energies differences do not follow a clear trend. While the energy difference is positive for the pure UO_2 and PuO_2, they can be positive or negative in $(U,Pu)O_2$ for the plutonium content range investigated. Moreover, these energy differences are very small for $(U,Pu)O_2$, much smaller than the precision on energy ($\sim 10^{-2}$ meV/atom). Thus in order to well capture the magnetic configuration of $(U,Pu)O_2$, the ground-state energy of $(U,Pu)O_2$ is coupled with the

structural and electronic properties. The analysis of the structural properties in terms of lattice constants and the distortion of crystal lattice in the <001> direction, denoted by c/a, are also considered. For each plutonium concentration, the lattice constants and the distortions c/a keep similar values both in 1k-AFM and FM configurations. Thus, structural properties are not impacted by the change in magnetic configuration. However, regarding the electronic structure, a difference in the band gap between 1k-AFM and FM configurations of about 0.3 eV is observed. This difference is not negligible since it represents almost 25% of the band gap of 1k-AFM of $(U,Pu)O_2$. Therefore, we cannot consider 1k-AFM and FM to be equivalent in $(U,Pu)O_2$. We thus have to fix the magnetic configuration as close as possible to the experimental results or other calculations.

Pu content	**AFM**			**FM**			**E_{FM}-E_{AFM} /atom (meV)**
	a_0 ($Å$)	**c/a**	**Band gap (eV)**	**a_0 ($Å$)**	**c/a**	**Band gap (eV)**	
UO_2	5.543	0.987	2.5	5.547	0.986	2.2	+10.00
12.5%	5.532	0.990	1.2	5.532	0.990	0.9	+0.01
18.75%	5.526	0.992	1.2	5.526	0.992	0.9	-0.11
25%	5.520	0.994	1.2	5.520	0.994	0.9	-0.13
31.25%	5.514	0.996	1.2	5.514	0.995	0.9	-0.14
37.5%	5.509	0.997	1.2	5.509	0.997	0.9	-0.03
50%	5.497	1.001	1.2	5.495	1.001	0.9	+0.22
PuO_2	5.453	1.02	2.0	5.452	1.02	1.4	+3.31

Table 19 : Magnetic stability of $(U,Pu)O_2$ for various Pu contents. a_0 is the lattice constant and E_{FM}-E_{AFM}/atom is the difference in total energy between FM and 1k-AFM orders.

Indeed, the question of the magnetic configuration in $(U,Pu)O_2$ is of concern since it has never been experimentally investigated up to now to our knowledge. Moreover, since $(U,Pu)O_2$ is obtained by mixing UO_2 and PuO_2, the knowledge of the magnetic configurations of UO_2 and PuO_2 may give a good idea on the magnetic configuration of the mixture. If magnetic properties of UO_2 are well established experimentally and successfully reproduced by several electronic structure calculations [47, 64, 65, 76, 122, 222], the magnetic properties of PuO_2 is not yet well established as indicated in Chapter1, Section 1.2.3.1. Crystal field calculations suggest PuO_2 to be non magnetic Γ1 [55–57]. However, the anomaly in the magnetic response of PuO_2 suggests the existence of antiferromagnetic exchange interaction between plutonium cations [55]. Furthermore, electronic structure calculations predict the 1k-AFM configuration for PuO_2 [77] when the paramagnetic configuration cannot be modelled or the fluctuation of orbital occupation cannot be taken into account. On the other hand, as PuO_2, NpO_2 exhibits the same magnetic character and a similar anomaly in the magnetic response [257–259]. However, $(U,Np)O_2$ mixed oxides are magnetic. It has been established that the magnetic field from magnetic uranium cations induces a magnetic moment on

neptunium cations [259–261]. A similar phenomenon could be expected in (U,Pu)O_2. Therefore, the closest magnetic configuration of (U,Pu)O_2 to experimental and theoretical results is the AFM configuration. This configuration is used in this manuscript for the modelling of (U,Pu)O_2 in the entire plutonium content range.

3.2.2 Structural properties

We have investigated structural properties of (U,Pu)O_2 in terms of lattice constants and interatomic distances. Calculations are carried out using both PBE+*U* and vdW-optPBE+*U* functionals, in the approximation of ideal solid solution, in the entire plutonium content range. Figure 39 shows the calculated lattice constants as a function of Pu content.

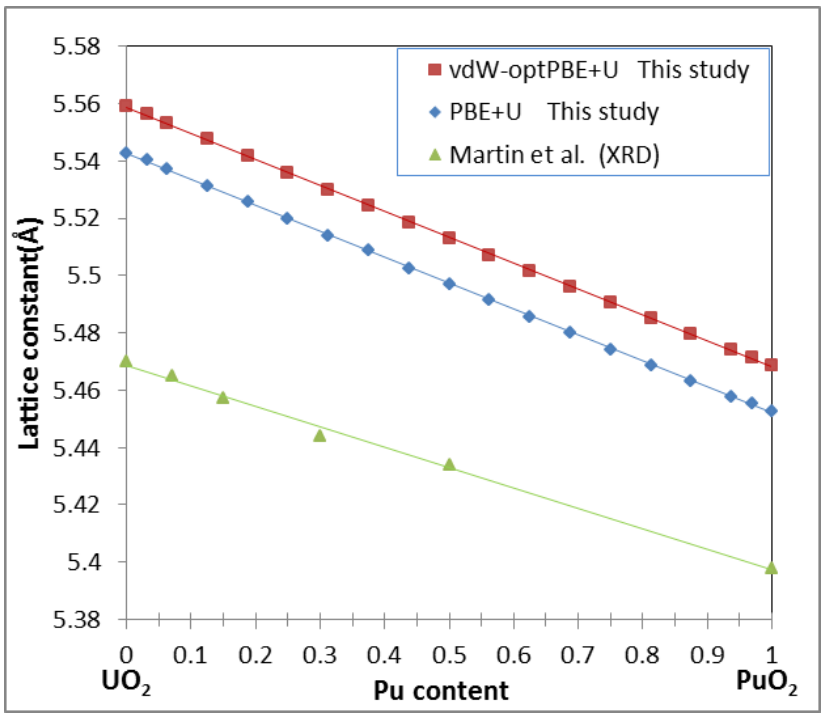

Figure 39 : Lattice parameter of (U,Pu)O_2 as a function of Pu content. Comparison with XRD experiments by Martin *et al.*[34].

It appears for both functionals that the lattice constants follow a linear evolution with respect to the Pu content, from UO_2 to PuO_2. This behaviour is known as the Vegard's law [36], and has been also found experimentally for (U,Pu)O_2 [25, 34, 37, 38, 42, 44]. Thus the DFT+*U* results using both GGA+*U* and vdW-optPBE+*U* functionals gives a consistent qualitative description of the lattice constants of (U,Pu)O_2. However, by comparing our values to the XRD experimental ones by Martin *et al.* [34], a very slight overestimation of lattice constants is observed for both functionals. This overestimation is between 1.0 % to 1.3 % for PBE+*U* and between 1.3 % to 1.6 % for vdW-optPBE+*U*.

Nevertheless, these overestimations are within the expected errors for both functionals [262] and should not affect the quality of DFT results in terms of properties calculated. The slightly larger overestimations from vdW-optPBE+*U* of 0.3 % compared to PBE+*U* could be the result of the more repulsive character of the optPBE functional than the original PBE at short separation distances [16, 263].

For the in-depth analysis of the accuracy of both PBE+*U* and vdW-optPBE+*U* functionals in the description of structural properties of actinide oxides and mixed oxides, the interatomic distances are also calculated. These results are compared to the experimental X-ray absorption spectroscopy (XAS) analysis of actinide-oxygen interatomic distances ($d_{M\text{-}O}$), in the first coordination shell. Results on UO_2, PuO_2 and $(U,Pu)O_2$ are given in the following Table 20 for the plutonium content of 25 % for the calculation and 30 % for XAS.

Compounds	**PBE+*U***		**vdW-optPBE+*U***		**Exp (XAS)** [34, 49]	
	$\mathbf{d_{U\text{-}O}}$	$\mathbf{d_{Pu\text{-}O}}$	$\mathbf{d_{U\text{-}O}}$	$\mathbf{d_{Pu\text{-}O}}$	$\mathbf{d_{U\text{-}O}}$	$\mathbf{d_{Pu\text{-}O}}$
$\mathbf{UO_2}$	2.40	--	2.41	--	2.37	--
$\mathbf{U_{0.75}Pu_{0.25}O_2}$	2.38	2.37	2.39	2.38	2.35*	2.35*
$\mathbf{PuO_2}$	--	2.36	--	2.37	--	2.33

Table 20 : Interatomic distances $d_{M\text{-}O}$ (with M = U or Pu) in the first coordination shell. Comparison of calculated values with experimental data [34, 49]. The (*) corresponds to a Pu content of 30 *wt.*%.

An interesting finding is the evolution of the M-O distances in uranium-plutonium mixed oxide. Indeed, the calculated U-O and Pu-O distances in $(U,Pu)O_2$ are different from their values in pure UO_2 and PuO_2. The addition of Pu leads to a decrease in U-O distance in comparison to its value in UO_2, and to the increase in Pu-O distance in comparison to its value in PuO_2. The calculated U-O and Pu-O distances are then almost equal in the uranium-plutonium mixed oxides with 2.38 Å for a Pu content of 25%. These results are in good agreement with the experimental results. These comparisons show that the DFT+*U* method, using both PBE+*U* and vdW-optPBE+*U* functionals, yields a satisfactory description of the structural properties of $(U,Pu)O_2$ compounds.

3.2.3 Elastic properties

In the present section, the elastic properties of UO_2 and $(U,Pu)O_2$ are investigated in terms of elastic coefficients C_{11}, C_{12} and C_{44}, and bulk modulus B_0. The elastic coefficients are calculated for rigid ions and allowing the relaxation of atoms, using the lattice distortions as proposed by Le Page and Saxe [264]. The calculation of the ionic

contribution to the elastic constants is also performed using the Hessian matrix as proposed by Wu *et al*. [265]. The vdW-optPBE+*U* is not used for the calculation of elastic coefficients since Vathonne [65] has shown that this functional gives similar results on elastic coefficients than PBE+*U*. Thus, the following results are obtained only from PBE+*U*.

Table 21 shows the values obtained for the elastic coefficients C_{11}, C_{12}, C_{44} and the bulk modulus B_0. We compare our results with available experimental data [74, 75] on UO_2 and PuO_2, as well as with available LDA+*U* results [47, 69] on UO_2, $(U,Pu)O_2$ and PuO_2.

For UO_2, our C_{11} value of 364 GPa using PBE+*U* is lower than the 389 GPa experimental one, with a difference less than 10 %. This value is also lower than the LDA+*U* value of 401 GPa obtained by Dorado *et al.* [47]. The same tendency compared to Dorado's LDA+*U* values is observed for $(U,Pu)O_2$ for all Pu contents. This tendency is expected from the difference in the binding energies yielded by LDA and GGA functionals. For C_{12} and C_{44}, our PBE+*U* results are very satisfactorily comparable to the respective experimental values of 119 GPa and 60 GPa for UO_2. The slight underestimation of elastic coefficients as compared to experimental data might be due to the overestimation of lattice constants by PBE+*U*, since it is known that the increase in lattice constant with temperature or pressure effects leads to the decrease in elastic constants.

	Functional	**UO_2**	**$(U_{0.75}Pu_{0.25})O_2$**	**$(U_{0.5}Pu_{0.5})O_2$**	**$(U_{0.25}Pu_{0.75})O_2$**	**PuO_2**
C_{11} (GPa)	PBE+*U* *	364	375	365	368	375
	LDA+*U*	401 [a]	402 [a]	---	---	---
	Exp	389 [b]	---	---	---	---
C_{12} (GPa)	PBE+*U* *	112	108	116	115	111
	LDA+*U*	132 [a]	151 [a]	---	---	---
	Exp	119 [b]	---	---	---	---
C_{44} (GPa)	PBE+*U* *	58	62	66	68	70
	LDA+*U*	94 [a]	78 [a]			
	Exp	60 [b]	---			
B_0 (GPa)	PBE+*U* *	196	197	199	199	199
	LDA+*U*	222 [a]	235 [a]	---	---	208 [e]
	Exp	207 [c]	156.9 -- 221 [f]	---	---	178 [c]

* This study; Exp Experiments; [a] Ref. [47]; [b] Ref. [74]; [c] Ref. [75]; [d] Ref. [202]; [e] Ref. [69];

[f] see ref. [266]

Table 21 : Elastic constants C_{11}, C_{12} and C_{44} and bulk modulus B_0 of UO_2, PuO_2 and $(U,Pu)O_2$ with 25%, 50% and 75% Pu. Comparison with available experimental data.

For $(U,Pu)O_2$, the results also show the increase of C_{44} with respect to Pu content, from 58 GPa for UO_2 to 70 GPa for PuO_2. Even though there are to our knowledge no experimental data on these quantities for the uranium-plutonium mixed oxides $(U,Pu)O_2$ and for PuO_2, the agreement between our PBE+*U* and the experimental results on UO_2 consolidates the fact that these results on C_{11}, C_{12} and C_{44} are a good prediction for $(U,Pu)O_2$ and PuO_2.

The PBE+*U* calculated bulk modulus for UO_2 of 196 GPa shows a good agreement with experimental one of 207 GPa. Our calculated value for PuO_2 of 199 GPa is slightly overestimated as compared to the experimental value of 178 GPa. Thus, the calculated values for UO_2 and PuO_2 are in relatively good agreement with the experimental data. For $(U,Pu)O_2$, only one composition on polycrystalline $(U,Pu)O_2$ has been studied experimentally (20 *wt*.% Pu), but the bulk modulus measured exhibits a large uncertainty since the two techniques used yield significantly different values (156.9 GPa and 221 GPa) (see Ref.[266]). Our calculated value of 197 GPa is between these results. Our values of B_0 as a function of the Pu content are good predictions, since we are able to provide relatively consistent bulk modulus in UO_2 and PuO_2.

3.2.4 Electronic properties

The electronic structure of UO_2, PuO_2 and $(U,Pu)O_2$ for various plutonium contents is investigated, in terms of electronic density of states and band gap. The electronic density of states allows a qualitative description of features of each compound such as the charge-transfer or Mott insulating character.

Table 22 presents the electronic band gap of $(U,Pu)O_2$ in the whole Pu content range, using both PBE+*U* and vdW-optPBE+*U* functionals. It appears that the band gap in the mixed oxides is lower than the value of 2.5 eV of pure UO_2 and the value of 2.0 eV of pure PuO_2. Indeed, the value of the band gap in mixed oxides is 1.2 eV using PBE+*U* and 1.4 eV using vdW-optPBE+*U* for plutonium content comprised between 3 % to 75 %. These values increase up to 2.0 eV from 75 % to pure PuO_2 for both functionals. As the calculated band gaps of UO_2 and PuO_2 compare well with the experimental ones, the values for the mixed oxides are a good prediction as experiments are lacking on these compounds.

	Functional	**UO_2**	**$(U_{0.94}Pu_{0.06})O_2$ – $(U_{0.25}Pu_{0.75})O_2$**	**$(U_{0.18}Pu_{0.82})O_2$**	**$(U_{0.06}Pu_{0.94})O_2$**	**PuO_2**
Band gap (eV)	**PBE+*U* ***	2.5	1.2	1.4	1.7	2.0
	vdW-optPBE+*U* *	2.6	1.4	1.5	1.8	2.0
	LDA+*U*	2.3[a]	1.5[a]	--	--	1.8[e]
	Exp	2.1[d]	--	--	--	1.8[f]

[a]Ref [47]; [d]Ref [202]; [e]Ref [69]; [f]Ref [66]

Table 22 : Band gap in $(U,Pu)O_2$ and its evolution as a function of the Pu content.

In order to understand the origin of the narrowing of the band gap, the electronic density of states is an indicated feature. It describes the relative energy of the electronic bands of the orbitals of atoms in the material. Figure 40 shows the projected electronic density of states (PDOS) of actinides *5f* orbitals and oxygen *2p* orbitals in UO_2, PuO_2 and $(U,Pu)O_2$ for a plutonium content of 25 % and 75 %. The PDOS for 75 % of Pu content aims at analysing the mechanism leading to the increase in the band gap from this Pu content as commented above.

The projected electronic density of states of UO_2 shows a good description of its Mott Hubbard insulating character as found experimentally [54], with the gap between the uranium *5f* states. The charge transfer insulating character is found for PuO_2, with the gap between the oxygen *2p* states and the plutonium *5f* states. For both oxides, the localized character of the *5f* states is easily identified with the presence of pronounced peaks in the density of states.

For $(U,Pu)O_2$ with a plutonium content of 25 %, the *5f* electronic density of states is a superposition of those of UO_2 and PuO_2 *5f* orbitals. In particular, all *5f* orbitals of actinides uranium and plutonium keep the same sharp features and the same hybridization character relative to the oxygen *2p* orbitals as in the pure actinide dioxides UO_2 and PuO_2. Therefore, the uranium *5f* states remain at the higher energy level compared to the oxygen *2p* states as in UO_2. The plutonium *5f* states overlap the oxygen *2p* states at the top of the valence band as in PuO_2. As a consequence, there is a shift of the plutonium *5f* valence band maximum within the valence band of uranium *5f* states and a shift of plutonium *5f* states conduction band minimum within the band gap of uranium *5f* states. Therefore, the valence band maximum (VBM) of $(U_{0.75}Pu_{0.25})O_2$ is constituted of uranium *5f* states and the conduction band minimum (CBM) constituted of plutonium *5f* states.

This result means that the presence of excess electrons in $(U,Pu)O_2$, due to the contribution of electron donor defects for example, will lead to their localization in the plutonium cations. This kind of observation has been made for hypo-stoichiometric $(U_{0.7}Pu_{0.3})O_{2-x}$ by Vigier *et al.* [49] who found the presence of Pu^{3+} cations rather than U^{3+}. This experimental result corroborates our electronic structure calculations and analysis of point defects (see Chapter 4).

The features of the electronic density of states as described above for $(U_{0.75}Pu_{0.25})O_2$ is observed for all plutonium contents lower than 75 % where the band gap is almost constant. For a Pu content of 75 %, the electronic density of states obtained is different as shown in Figure 40. In the conduction band, the uranium *5f* states vanish or become much higher in energy and the plutonium *5f* states becomes less localized than for 25 % Pu and remain at the CBM. In the valence band, the uranium *5f* states display a more localized character than for the 25 % Pu content, and remains at the VBM but come closer to the oxygen *2p* states, while plutonium *5f* states keep the same features as for 25 % Pu content.

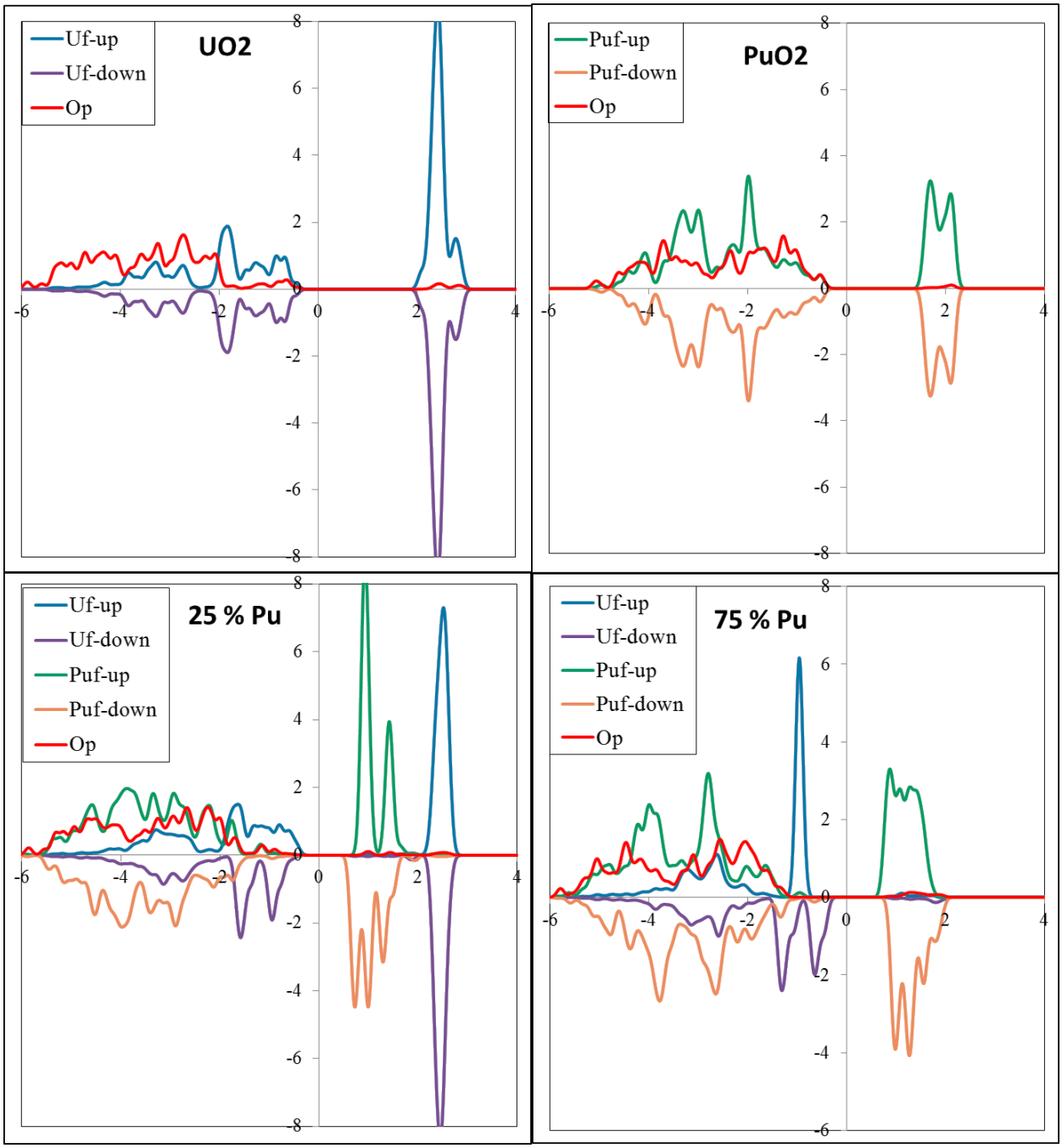

Figure 40 : Projected density of states of UO_2, $(U_{0.75}Pu_{0.25})O_2$, $(U_{0.25}Pu_{0.75})O_2$ and PuO_2 respectively for actinides *5f* orbitals and oxygen 2*p* orbitals.

Thus, $(U,Pu)O_2$ is found to be a Mott Hubard insulator, with the band gap ranging from 1.2 eV to 2.0 eV between uranium *5f* states and plutonium *5f* states. The narrowing of the band gap is the results of the hybridization of the actinides *5f* states with the oxygen *2p* states, which is maintained in the mixture.

The band gap narrowing has already been found in other semiconductor based alloys, such as $In_xAl_{1-x}N$, using first-principles calculations by Dridi *et al.* [267] and confirmed

experimentally by Iliopoulos *et al.* [268]. Indeed, the band gap of alloyed semiconductor $A_xB_{1-x}C$ can be expressed as follows:

$$\varepsilon_g^{ABC} = x\varepsilon_g^{AC} + (1-x)\varepsilon_g^{BC} - C_g x(1-x) \quad (130)$$

where C_g is a bowing parameter. For binary semiconductors, the gap is a linear function of the lattice parameter. Since the lattice parameter varies linearly with the composition of the alloy (*Vegard's law*) as it is the case for $(U,Pu)O_2$, the band gap is expected to evolve linearly with respect to the composition of alloys, which means that the bowing parameter C_g must be equal to zero. Iliopoulos *et al.* [268] have, however, found an increase in C_g with the increase in aluminium content for $In_xAl_{1-x}N$. Moreover, Dridi *et al.*[267] have obtained for $In_xGa_{1-x}N$ a bowing factor of 0.71 eV, thus a narrowing of the band gap while the lattice parameter follows the Vegard's law. Therefore, our study has shown a similar qualitative description of that phenomenon for $(U,Pu)O_2$.

3.3 Thermodynamic modelling of UO_2 and $(U,Pu)O_2$

The thermodynamic modelling in the present manuscript includes 0 K calculations of energetic quantities such as the formation enthalpies and the mixing enthalpies of uranium-plutonium mixed oxides. These are done using both PBE+*U* and vdW-optPBE+*U* functionals. We demonstrate that taking into account the van der Waals (vdW) interactions leads to the improvement of the description of energetic properties of uranium and plutonium based oxides. The finite temperature properties, namely the thermal expansion, the variations of enthalpy and the heat capacities are calculated using *ab initio* molecular dynamics within the PBE+*U* functional. The aim is to prove the efficiency of this method for the modelling of finite temperature properties of actinide based materials and thus to support the prediction of properties of these materials at high temperature.

3.3.1 Energetic properties at 0 K

3.3.1.1 Enthalpy of formation

The enthalpy of formation is calculated from the results of the electronic structure calculations as follows:

$$\Delta H_f^{U_{1-y}Pu_yO_2} = E_{Tot}^{U_{1-y}Pu_yO_2} - (1-y)E_U^{met} - yE_{Pu}^{met} - 2E_O^{O_2} \quad (131)$$

where $E_{Tot}^{U_{1-y}Pu_yO_2}$ is the DFT+U total energy of (U,Pu)O_2, E_U^{met} is the calculated chemical potential (energy per atom) of metallic uranium in the α-phase reference state, E_{Pu}^{met} the calculated chemical potential of metallic plutonium in the α-phase reference state and $E_O^{O_2}$ the calculated chemical potential of oxygen in the O_2 reference state.

In order to validate the DFT+U predictions of the enthalpy of formation for (U,Pu)O_2, we have first calculated this quantity for pure UO_2, PuO_2 and Pu_2O_3 oxides. Our results are then compared with those obtained from the CALPHAD thermodynamic modelling of UO_2 [253], PuO_2 and Pu_2O_3 [254] at room temperature. We have also compared our results to experimental data measured at room temperature as shown in Table 23.

Oxides	**ΔH_f (eV)**			
	Exp	**CALPHAD**	**PBE+U**	**vdW-optPBE+U**
UO_2	-11.24 [269]	-11.23 [253]	-10.86	-11.27
PuO_2	-10.94 [270]	-10.99 [254]	-10.10	-10.90
Pu_2O_3	-17.14±0.21 [271] *(T=1373 K)*	-17.17 [254]	-15.71	-17.11

Table 23 : Enthalpy of formation of UO_2, PuO_2 and Pu_2O_3 using both PBE+U and vdW-opt-PBE+U functionals. Comparison is made with data from Guéneau *et al*. [253, 254] and experimental data [269–271] at room temperature.

We find for the pure oxides UO_2, PuO_2 and Pu_2O_3 that the enthalpies of formation calculated using PBE+U are slightly larger than those yielded by both experiments and CALPHAD thermodynamic modelling (by 3 % for UO_2 and 8 % for both PuO_2 and Pu_2O_3). By taking into account the non-local correlations through van der Waals functional however, this overestimation is significantly decreased for the three oxides and becomes less than 0.4% compared to experiments. This means that the van der Waals dipole-dipole and dipole-quadrupole interactions are not negligible in the case of iono-covalent systems as pointed out by Moellmann *et al.* [272] and Zang *et al.* [273]. The vdW-optPBE+U results compare very well with the results of the experimental characterization and CALPHAD modelling. The improvement in the formation enthalpy of these oxides can also be explained by the improvement in the description of the binding energy of the O_2 gas molecule. The calculated chemical potential of oxygen in the O_2 reference state is improved compared to the PBE+U calculations. Furthermore, the chemical potential of uranium and plutonium in the α-phase reference states are also improved as pointed out for solids by Klimeš *et al.* [16]. In addition, the difference between the enthalpy of formation at 0 K and at room temperature is estimated to be less than 0.03 eV in UO_2, using experimental heat capacities (see Annex). This highlights the efficiency of the DFT+U method using the vdW-optPBE functional in the prediction

of the enthalpies of formation in the U-Pu-O system. We have therefore investigated the enthalpies of formation of (U,Pu)O_2 compounds, with plutonium contents of 25%, 50% and 75% as shown in Table 24.

The values obtained using the vdW-optPBE+U approach show a regular evolution from the value in UO_2 to that in PuO_2. However, the behaviour expected is a non linear curve due to the mixing enthalpy of UO_2 and PuO_2 according to the expression of the enthalpy of formation:

$$\Delta H_f^{U_{1-y}Pu_yO_2} = (1-y)\Delta H_f^{UO_2} + y\Delta H_f^{PuO_2} + \Delta H_{mix} \quad (132)$$

where $\Delta H_f^{U_{1-y}Pu_yO_2}$, $\Delta H_f^{UO_2}$ and $\Delta H_f^{PuO_2}$ are the enthalpies of formation of the three oxides and ΔH_{mix} the mixing enthalpy.

The reason of the apparent linear evolution is simply due to the fact that the mixing enthalpy ΔH_{mix} is very small (in the order of meV) compared to the enthalpy of formation, explaining why its effect cannot be captured here. The mixing enthalpy is discussed in the next section.

(U,Pu)O_2 Oxides	**ΔH_f (eV)**	
	PBE+U	**vdW-optPBE+U**
$(U_{0.75}Pu_{0.25})O_2$	-10.69	-11.18
$(U_{0.5}Pu_{0.5})O_2$	-10.51	-11.09
$(U_{0.25}Pu_{0.75})O_2$	-10.33	-10.99

Table 24 : Enthalpy of formation for (U,Pu)O_2 calculated using both PBE+U and vdW-opt-PBE+U functionals.

3.3.1.2 Mixing enthalpy

The mixing enthalpy of alloyed compounds determines their stability (negative or positive value) compared to the pure compounds and their most favourable configurations corresponding to the minimal value of the mixing enthalpy. It is calculated here for (U,Pu)O_2 mixed oxides using both the SQS configurations and a parametric model.

The parametric model is based on the polynomial approximation of the mixing enthalpy as proposed by Sluiter *et al.* [274] for alloys. Assuming a third-order cubic representation and using the limiting conditions $\Delta H_{mix}(0) = \Delta H_{mix}(1) = 0$ corresponding to pure elements, it can be shown that,

$$\Delta H_{mix}(y) = \Delta H_{sol}^{U\ in\ PuO_2}.y^2(1-y) + \Delta H_{sol}^{Pu\ in\ UO_2}.y(1-y)^2 \quad (133)$$

where $\Delta H_{sol}^{U\ in\ PuO_2} = -(\frac{\partial \Delta H_{mix}}{\partial y})_{y\to 1}$ and $\Delta H_{sol}^{Pu\ in\ UO_2} = (\frac{\partial \Delta H_{mix}}{\partial y})_{y\to 0}$ are the solution enthalpies for uranium in the lattice of PuO_2 and vice versa, respectively. Thus, the knowledge of those two solution enthalpies is sufficient to determine the mixing enthalpy in the entire range of plutonium contents. The solution enthalpies $\Delta H_{sol}^{U\ in\ PuO_2}$ and $\Delta H_{sol}^{Pu\ in\ UO_2}$ are calculated using DFT+U by substituting one uranium atom in the PuO_2 matrix and one plutonium atom in the UO_2 matrix in the 96-atom supercell. Since the composition is varying discretely in the DFT calculations, the derivatives appearing in the solution enthalpies are replaced by finite differences:

$$\Delta H_{sol}^{U\ in\ PuO_2} = \frac{1}{\Delta y}\left[\Delta H_f(1-\Delta y)\right] \text{ and } \Delta H_{sol}^{Pu\ in\ UO_2} = \frac{1}{\Delta y}[\Delta H_f(\Delta y)] \quad (134)$$

In the above equations, $\Delta H_f(\Delta y)$ is the heat of formation of $(U_{1-y}Pu_y)O_2$ calculated at y = Δy and $\Delta H_f(1-\Delta y)$ the heat of formation of $(U_{1-y}Pu_y)O_2$ calculated at y = 1-Δy. The heat of formation are calculated according to Equation (131) in a 96-atom supercell containing 32 actinide atoms, namely 1 uranium and 31 plutonium atoms or 1 plutonium and 31 uranium atoms. This corresponds to Δy = 0.03125.

Using the SQS configurations, the mixing enthalpy is also determined from direct calculations of the total energy in the entire accessible compositions of the SQS structures. This is given by the following equation:

$$\Delta H_{mix}(y) = E_{tot}^{U_{1-y}Pu_yO_2} - (1-y)E_{tot}^{UO_2} - yE_{tot}^{PuO_2} \quad (135)$$

where $E_{tot}^{U_{1-y}Pu_yO_2}$, $E_{tot}^{UO_2}$ *and* $E_{tot}^{PuO_2}$ are the total energies calculated for the three oxides.

Figure 41 shows the mixing enthalpy of the uranium-plutonium mixed oxides in the entire range of plutonium contents. PBE+U and vdW-optPBE+U calculations are carried out for both parametric (light blue and dark blue diamonds) and SQS methods (orange and dark red triangles).

The mixing enthalpy of $(U,Pu)O_2$ is found negative in the entire range of Pu contents using both SQS and parametric calculations, with very small values, at most 9 meV, which represents 0.08 % of the enthalpy of formation. This suggests that there is no demixing due to the variation of Pu content in the material. In other words, in the entire range of Pu contents, for O/(U+Pu) = 2, the actinide sublattice forms a solid solution. This has been suggested from the experimental results on $(U_{0.7}Pu_{0.3})O_2$ by Vigier *et al*. [49] and on $(U, Ce)O_2$, an experimental surrogate material for $(U,Pu)O_2$, by Martin *et al*. [275]. The present assumption agrees with the U-Pu-O phase diagram, in which the miscibility gap is observed only for oxygen content O/(U+Pu) smaller than 2. For the perfect stoichiometry, only one phase is mentioned.

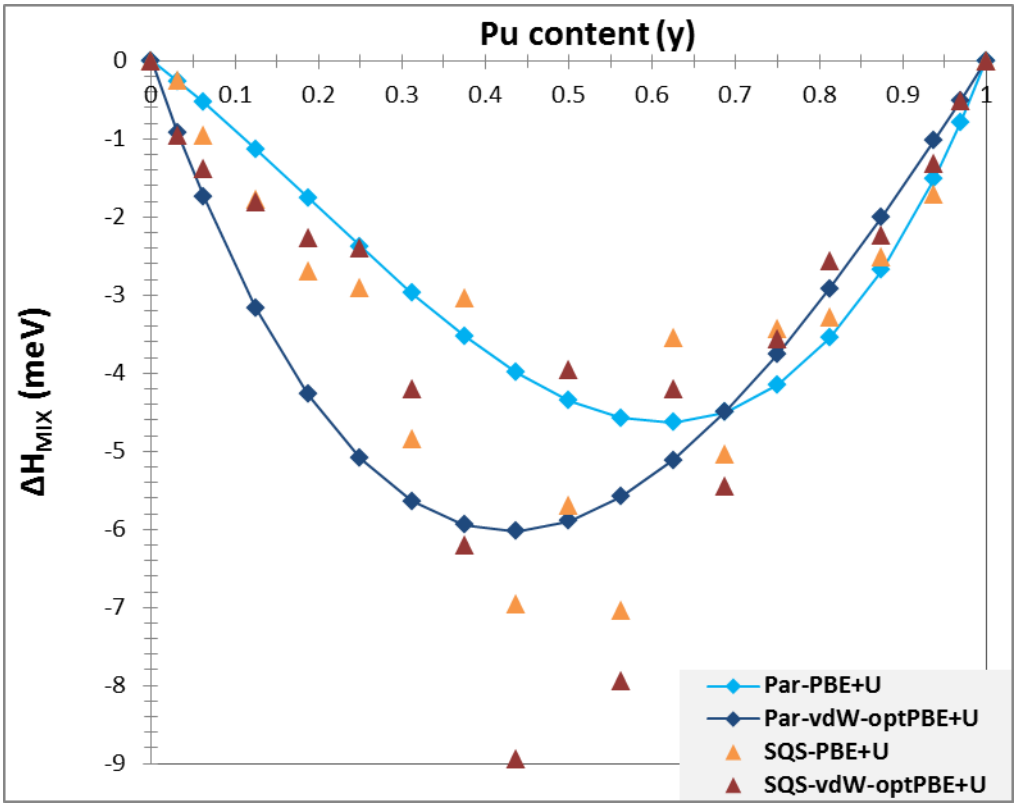

Figure 41 : Mixing enthalpy of $(U,Pu)O_2$ in the entire range of Pu contents, using both parametric method (diamonds) and SQS configurations (triangles). The parametric values are given by the light blue diamonds (PBE+*U*) and the dark blue diamonds (vdW-optPBE+*U*). The SQS values are given by the orange triangles (PBE+*U*) and dark red triangles (vdW-optPBE+*U*).

The mixing enthalpy calculations using the SQS configurations display a regular evolution as a function of the Pu content only for Pu contents close to 0 or 1, more precisely less than 0.125 and higher than 0.875. Between these two regions, the mixing enthalpy is scattered with significant energy differences between similar contents for both functionals used. These results suggest that even if the SQS configurations simulate some structural characteristics of an ideal solid solution, they remain an approximation.

By contrast to the SQS calculations, the parametric model yields regular behaviour for the mixing enthalpy as a function of the Pu content. The global minimum is however found at y= 0.625 for PBE+*U* calculations and y=0.4375 for vdW-optPBE+*U* calculations.

3.3.2 Finite temperature properties

The temperature dependent properties are calculated using *ab initio* molecular dynamics. The canonical NPT ensemble is applied within the Langevin thermostat. We have applied the 1**k** antiferromagnetic configuration, similarly to the 0 K calculations. Moreover, the occupation matrix control is used as for the 0 K calculations, aiming at properly describing the energetic properties, such as the total energy, from which essential properties of interest are derived. The time step of the simulation is fixed to 2 fs, in accordance to the optimization tests on different properties. By the same manner, the friction coefficient (γ) for atomic degrees of freedom is set to 10 and the lattice friction coefficient to 20.

The dynamic simulations are performed over 10 to 15 ps. The first 5 ps are considered as the time needed for the system to reach the equilibrium at a given temperature. Then for all finite temperature properties calculated, the statistical averaging is made over the 5 to 10 last picoseconds.

We first study the crystal disorder induced by temperature for UO_2 and $(U,Pu)O_2$ with a plutonium content of 25 % for several representative temperatures. This is achieved through the radial distribution function analysis. Secondly, the thermal expansion and the variation of enthalpy are calculated as a function of temperature and for various plutonium contents. Furthermore, the heat capacities are also calculated as a function of temperature. The specific effect of Pu content is considered.

3.3.2.1 Radial distribution functions

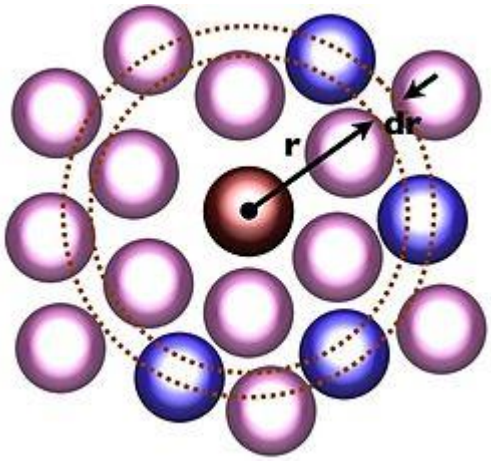

Figure 42 : Calculation of radial distribution function.

The radial distribution function (RDF), g(r), also called pair distribution function (PDF) is an important structural characteristic for a crystal. Considering a homogeneous distribution of the atoms/molecules in space, g(r) represents the probability to find an atom in a thickness dr at the distance r of another atom chosen as a reference point. This definition is illustrated by Figure 42.

In solids, atoms are packed regularly to fill the space most efficiently. This leads to regular and periodic structures, with atoms fluctuating near their lattice positions due to temperature. Thus, there is zero probability of finding a particle in regions in-between these atoms. Therefore, discrete peaks can be seen in the RDF of a crystalline solid. Each peak has a broadened shape which is caused by the atoms oscillating around their lattice sites due to temperature.

Each peak represents a coordination shell for the solid, with the nearest neighbours being found in the first coordination shell, the second nearest neighbours being found in the second and so on. On the contrary, due to the ability of atoms in liquids to move dynamically, the liquids do not maintain a constant structure and lose all of their long range structure. Especially at large values of r, the atoms become independent of each other. The first peak will be the sharpest, and indicates the first coordination sphere of the liquid while further peaks will be much smaller than the first one with the g(r) different from zero between them.

Figure 43 shows the RDF of oxygen-oxygen (O-O) pairs (a) and uranium-uranium (U-U) pairs (b) of UO_2 for various temperatures. For the O-O pairs, the increase in the peak broadening is clearly seen with the increase in temperature. In the interval between the first coordination shell (r = 2.75 Å) and the second coordination shell (r = 3.95 Å), g(r) is equal to zero up to 1000K. At 1600K and 2100K, g(r) in this interval becomes different to zero. This means that the fluctuations in the oxygen sublattice are very important so that oxygen atoms can easily move from one site to another. At 2600 K, the second minimum almost disappears. This behaviour corresponds to the liquid character in the oxygen sublattice, where oxygen atoms can almost move freely. This corresponds to the pre-melting of the oxygen sublattice which started from the Bredig transition. The temperature of 2600 K is similar to the premelting temperature obtained by Cooper *et al.* [107] and is close to the value of 2670 K found experimentally by Hiernaut *et al.* [87].

In the RDF of the U-U pairs (Figure 43.b), the slight increase in the peak broadening is observed. However, g(r) between the peaks in the first coordination shell (r = 3.95 Å) and the second coordination shell (5.55Å) is equal to or approaches zero up to 2600 K. Therefore the uranium atoms remain confined in their lattice positions. This means that the uranium sublattice remains solid up to this temperature, with an increase in the fluctuation of atoms around their equilibrium positions.

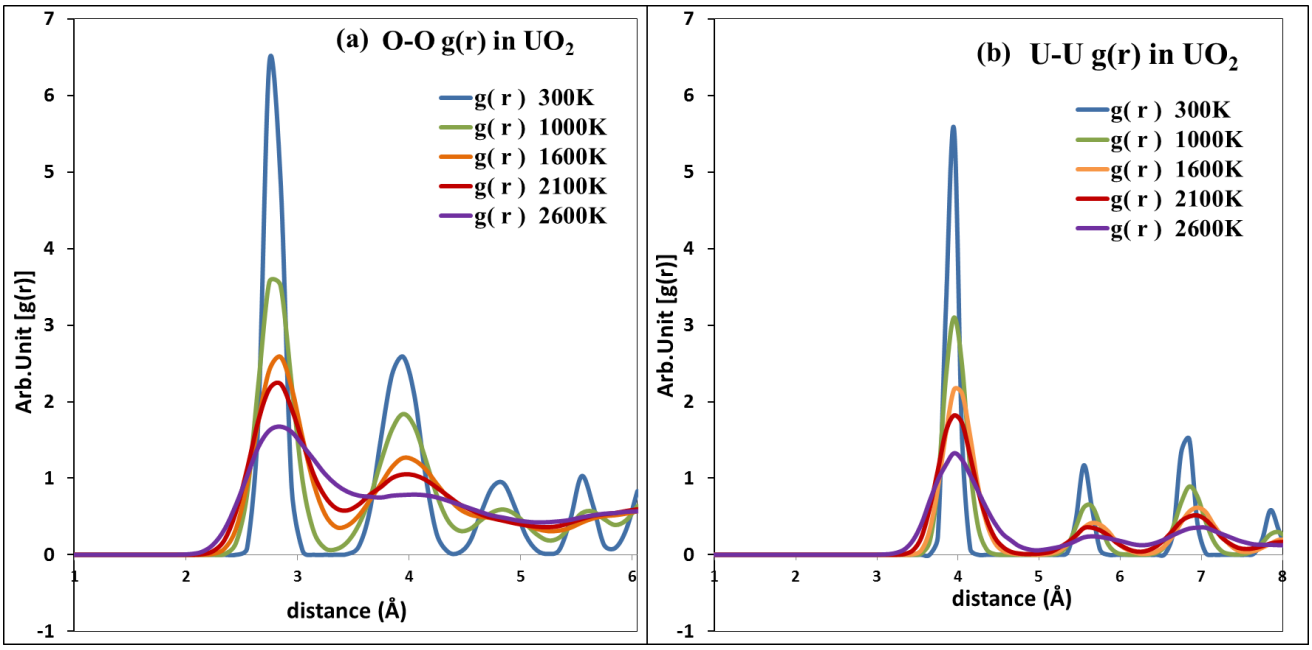

Figure 43 : Radial distribution functions g(r) of (a) the oxygen sublattice and (b) the uranium sublattice in UO_2.

In Figure 44, the RDF are plotted for $(U,Pu)O_2$ with 25 % of Pu and for the same temperature ranges. For O-O pairs (a), the RDF curves display the same shape and the same behaviour as in UO_2. However, the second minimum is slightly higher (0.05 unit) compared to the value in UO_2 at 2100 K. This means that the Bredig transition in $(U,Pu)O_2$ is expected to occur at lower temperature than in UO_2. The RDF of the U-U (b), U-Pu (c) and Pu-Pu (d) pairs displays a similar behaviour but differs a lot in absolute values. However, the solid character is maintained for the actinide sublattice up to the temperature of 2600 K. The difference in values of RDF is due to the difference in the number of U-U, U-Pu and Pu-Pu bonds in the SQS supercells of $(U,Pu)O_2$.

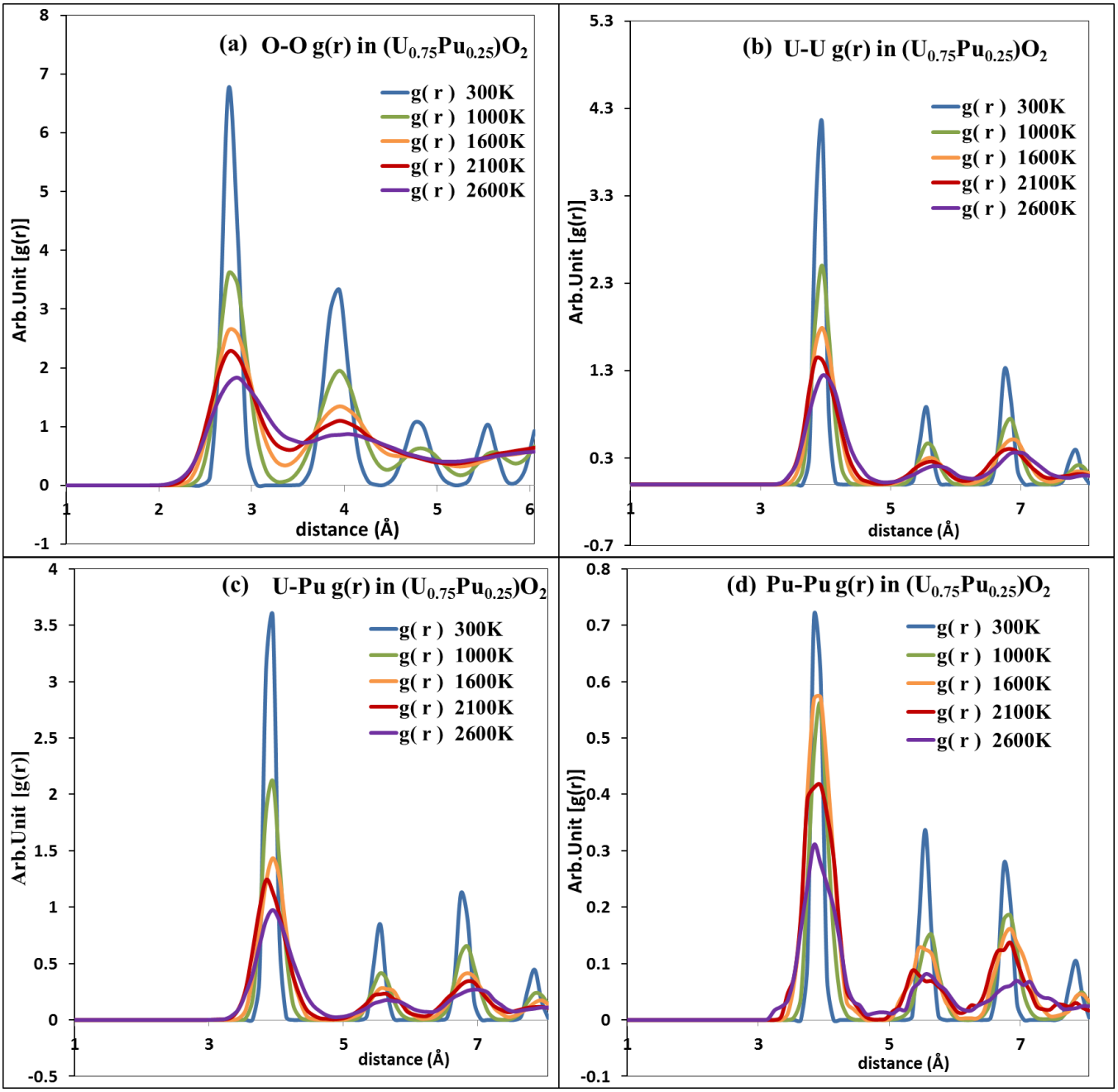

Figure 44 : Radial distribution functions g(r) of (a) the oxygen sublattice and (b), (c) and (d) the cation sublattice in $U_{0.75}Pu_{0.25}O_2$.

3.3.2.2 Thermal expansion

The linear thermal expansion is calculated using the following equation:

$$\Delta L/L_0 = \frac{a(T)-a_0}{a_0} \qquad (136)$$

where *a(T)* is the lattice constant at temperature T and a_0 corresponds to the lattice constant at room temperature. The calculated thermal expansion of UO_2 and $(U,Pu)O_2$ for various plutonium contents are shown in Figure 45. The values obtained are compared to the recommendation of D.G. Martin [90] (orange solid line) and the errors on this recommendation proposed by Fink [92] (black dashed lines).

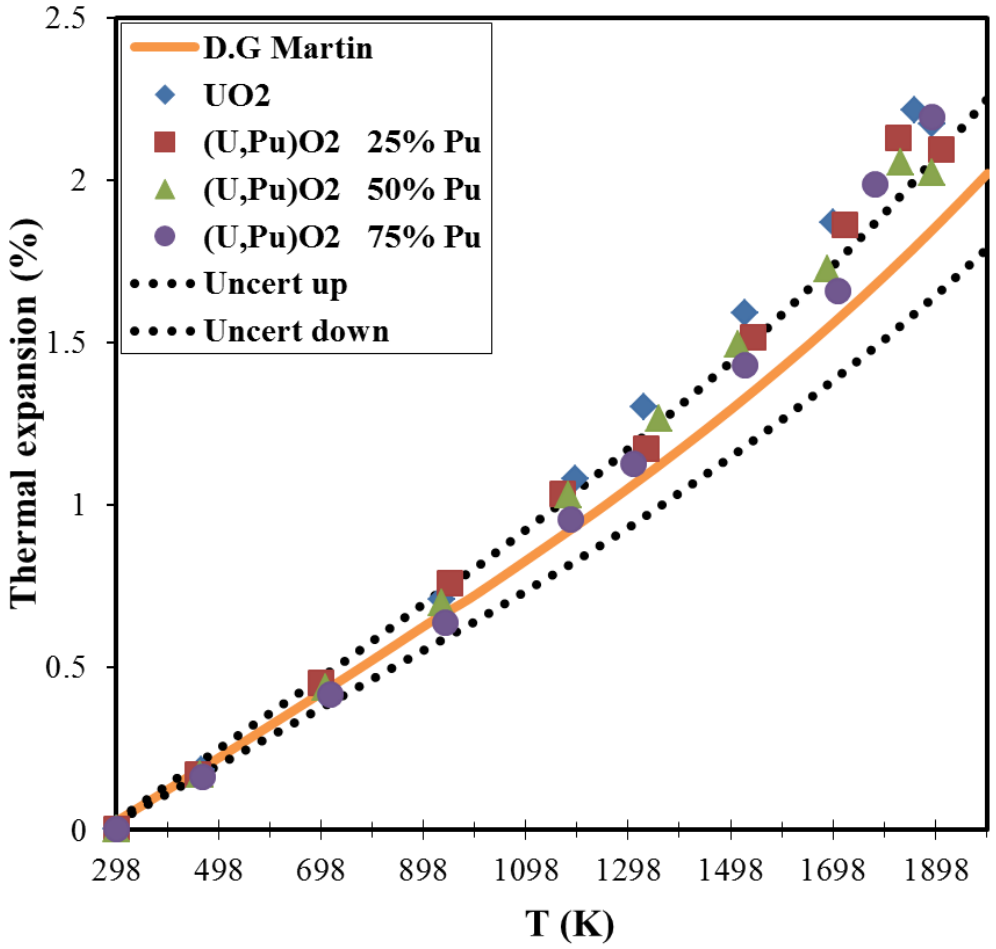

Figure 45 : Thermal expansion of UO_2 and $(U,Pu)O_2$ for various plutonium contents as a function of temperature. Results are compared to the recommendation of D. G. Martin [90]. The uncertainties assessed by Fink are also taken into account [92].

Our calculated thermal expansions fit well with Martin's recommendation at temperatures lower than 1000 K. Their evolution is regular, with a slight decrease with the increase in Pu content. At higher temperature, the calculated thermal expansion deviates slightly from the Martin recommendation [90]. The calculated values are slightly larger than the recommendation. The slight overestimation of the thermal expansion calculated using first-principles molecular dynamics has already been found in the literature [276] within the GGA [277] functional. The origin of this overestimation however, has not been clearly explained. In the case of ThO_2, Nakamura *et al.* [278]

using a larger 3x3x3 supercell and the LDA functional obtained a much better description of the thermal expansion. They thus suggest that the overestimation in Ref. [276] may be due to the small supercell size or the functional used. We think that these explanations are valuable since the GGA functional is known to overestimate the interatomic distances. This overestimation may increase at high temperature. Thus, as the crystal structure is expanded, the binding energy may be more underestimated as compare to the 0 K calculations. LDA+*U* calculations should be carried out on UO_2 in order to confirm this assumption. Also, further calculations should consider larger supercells.

We have observed a change in curvature of the thermal expansion at 1000 K, which is consistent with Martin's recommendation for all oxides studied. Moreover, the thermal expansion seems to decrease with the increase in the Pu content. However, the differences are very small, such that the effect of Pu content is negligible on the thermal expansion as recommended by D. G. Martin [90] and also suggested by Cooper *et al.* [46], and as used in the GERMINAL and ALCYONE fuel performance codes.

3.3.2.3 Variation of enthalpy and heat capacity

Figure 46 shows the calculated variation of enthalpy of UO_2 and $(U,Pu)O_2$ with Pu contents of 25%, 50 % and 75%, for various temperature range. The results are compared to Fink experimental recommendations [99] for UO_2 and $(U,Pu)O_2$ with a Pu content of 5% (solid lines).

The enthalpy H is obtained using the expression $H = E+PV$, where E is the internal energy (DFT total energy), P is the pressure and V the volume of the supercell. As the pressure is equal to zero in our *ab initio* molecular dynamic simulations, the product PV is zero and the enthalpy is equal to the internal energy.

Our calculated variation of enthalpy compares very well with the Fink experimental recommendations for a define temperature range, at least up to 2000 K for UO_2. For $(U,Pu)O_2$, the variation of enthalpy becomes slightly higher than the recommendation at 1300 K. For a temperature range higher than 1700 K, the differences become very significant and the recommendation is clearly below the calculated variation of enthalpy of $(U,Pu)O_2$ at all three Pu contents. This tendency highlights that the variation of enthalpy increases with the increase in Pu content. This results is consistent with the experimental recommendation where the variation of enthalpy of $(U,Pu)O_2$ with a Pu content of 5 % is slightly higher than that of UO_2. As our calculations are limited to 2000 K, the effect of the Bredig transition which is in general observed in the variation of enthalpy of many compounds [278] cannot be seen here.

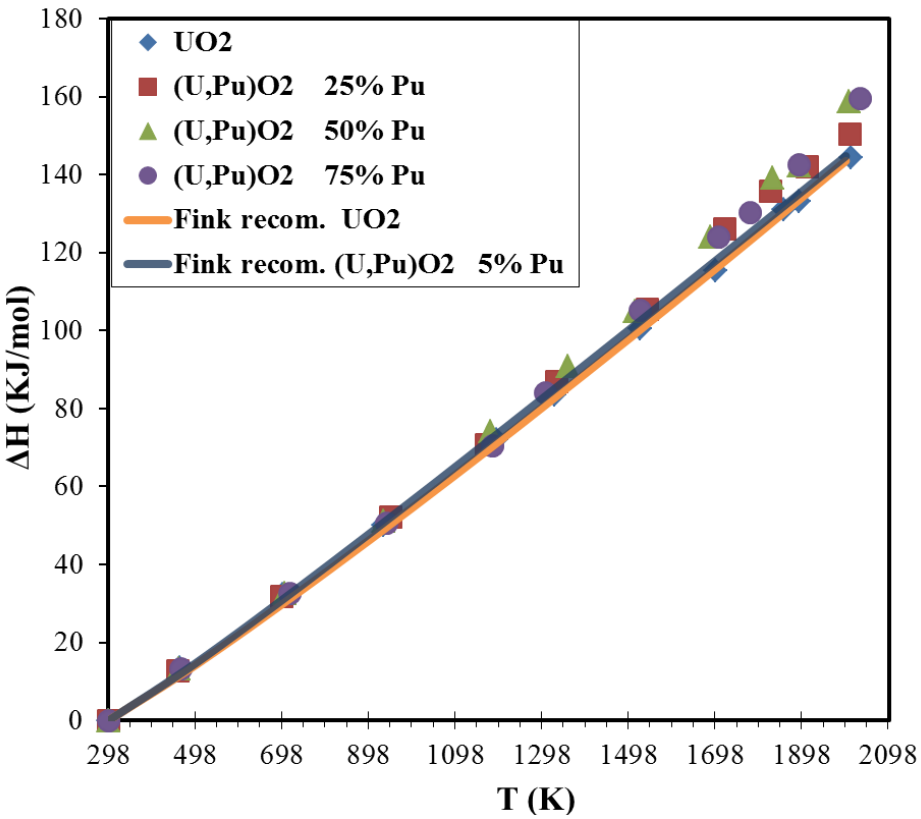

Figure 46 : Variation of enthalpy of UO_2 and $(U,Pu)O_2$ for various plutonium contents as a function of temperature. The calculated results are compared to Fink's recommendation for UO_2 and $(U,Pu)O_2$ with 5% Pu content [99].

Figure 47 shows the derived heat capacities of UO_2, $U_{0.75}Pu_{0.25}O_2$ (squares and diamonds) and the comparison to the Fink experimental recommendations [99] (solid lines) for UO_2 and PuO_2, as well as CALPHAD [26] calculations of UO_2 and $U_{0.75}Pu_{0.25}O_2$. The CALPHAD calculations are performed using the THERMOCALC software within the TAF-ID database [28].

The *ab initio* MD heat capacities have been derived by fitting the variations of enthalpy, using the general expression proposed by Fink [99] in Equation (12). The parameters of this equation where optimized using the variation of enthalpies for the calculation of the heat capacities.

For both UO_2 and $(U,Pu)O_2$, the calculated heat capacity increases fairly rapidly up to around 600 K. Above this temperature, the slope becomes relatively small. This variation is similar to the experimental recommendation and CALPHAD calculations.

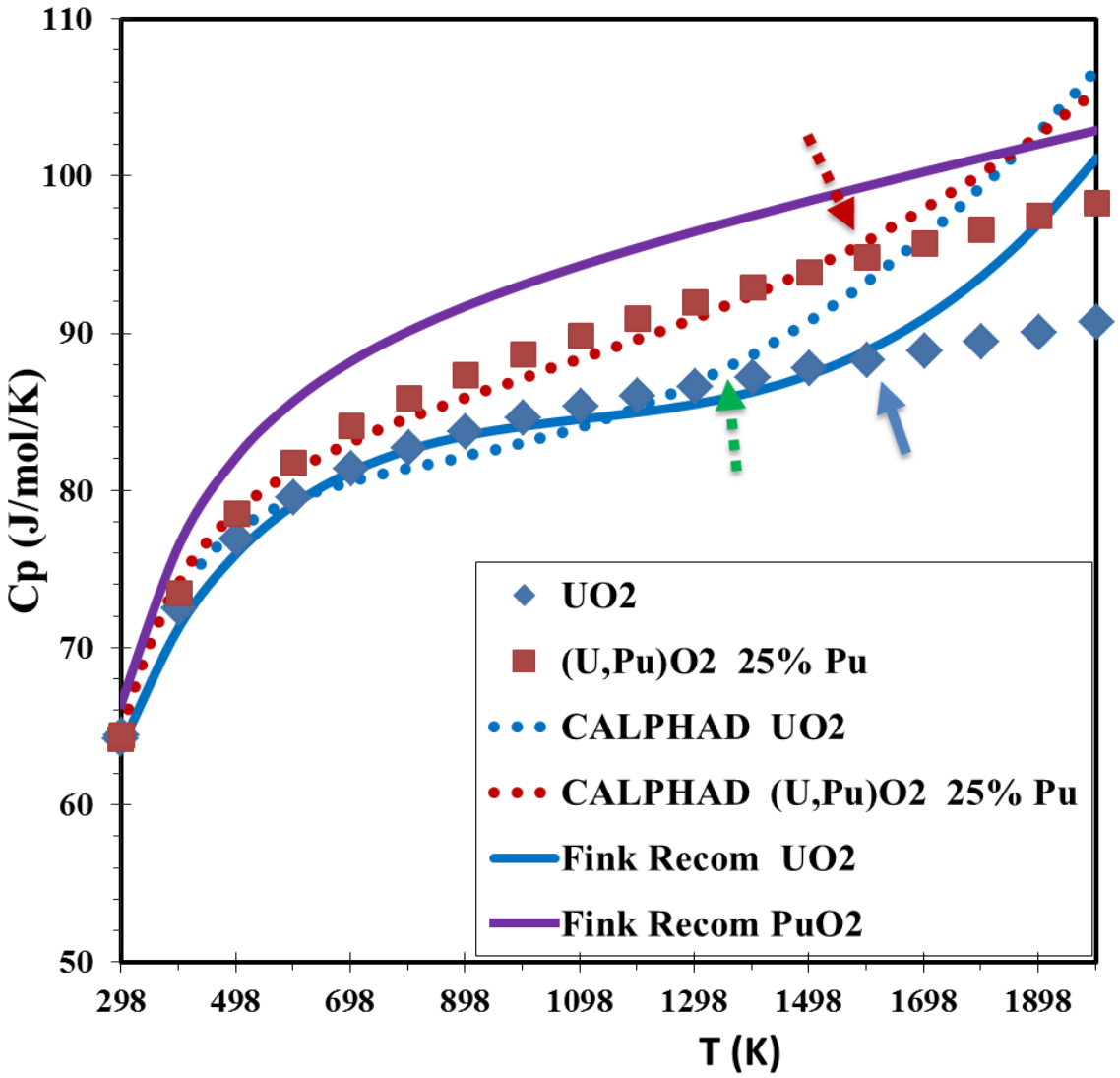

Figure 47 : Heat capacity of UO_2 (blue diamonds) and $(U,Pu)O_2$ with 25% Pu content (red squares) calculated using *ab initio* MD. Results are compared with Fink's recommendations for UO_2 (blue line) and PuO_2 (purple line) as well as CALPHAD calculations for UO_2 (blue dotted lines) and $(U,Pu)O_2$ with 25% Pu content (red dotted lines).

Globally, the calculated heat capacity for UO_2 (blue squares) compare very well with the Fink recommendation up to 1600 K. Above this temperature range, the slope of the recommendation increases significantly while the calculated value keeps the same slope (solid blue arrow). The significant increase in Cp for UO_2 is observed earlier at around 1350 K for CALPHAD values (dashed green arrow). However, the *ab inito* MD values do not yield this rapid increase in Cp. The same tendency is observed for $U_{0.75}Pu_{0.25}O_2$ as compared to the CALPHAD results (dashed red arrow), with the Cp values of $(U,Pu)O_2$ found between those of the UO_2 and PuO_2 experimental recommendations. The increase in the Cp at high temperature (recommendation/CALPHAD) is due to the contribution

of the oxygen Frenkel pairs to the heat capacity, as demonstrated in PuO_2 by Kato *et al.* [94]. Therefore, given the small supercell size for which one oxygen Frenkel pair will correspond to a very large concentration of around 1 %, and as the *ab initio* MD simulation time is not large enough (few ps) to allow the Frenkel pairs formation, their contribution to the heat capacity is not taken into account directly. In order to include the contribution of the oxygen Frenkel pairs, the enthalpies of formation as well as the entropies of this defect have to be calculated. Even if the enthalpy of formation of the oxygen Frenkel pair can be calculated in our study (V_O+I_O in Chapter 4), the entropy of this defect is not yet known for $(U,Pu)O_2$. This constitutes a perspective for further PhD study. The good description of the heat capacity is an important step for the *ab initio* calculation of the thermal conductivity of actinide oxides, especially for the complex mixed compounds such as $(U,Pu,Am)O_2$ for which the thermodynamic data are missing.

3.4 Conclusion

We have discussed in this chapter various material properties of pristine $(U,Pu)O_2$, namely the calculated static 0 K properties such as the stability of magnetic configurations, the structural, elastic, electronic and energetic properties. Finite temperature properties such as the radial distribution functions of the various sublattices, the thermal expansion, the variation of enthalpy and the heat capacity have been also investigated using *ab initio* molecular dynamics. Our DFT+*U* calculated properties compare very satisfactorily with experimental data, especially for UO_2 and to a certain extent for PuO_2. This agreement therefore supports our prediction of similar properties for $(U,Pu)O_2$. We have, for instance, highlighted the narrowing of the band gap in $(U,Pu)O_2$ and also calculated its elastic constants, its enthalpies of formation and its mixing enthalpies for various Pu contents. As to the finite temperature properties, we have shown the efficiency of *ab initio* MD coupled to DFT+*U* to provide reliable results for strongly correlated actinide oxides compounds, compared to experimental ones and to thermodynamic modelling methods such as CALPHAD. Our results have for instance corroborated the D. G. Martin recommendation for the thermal expansion of UO_2. This recommendation is used in ALCYONE and GERMINAL fuel performance codes. Given the transferability of the *ab initio* MD method, it is envisaged to be used for the calculation of more complex mixed compounds for which experimental thermodynamic data are missing. These are for instance $(U,Pu,Am)O_2$.

Chapter 4: Defect structure, stability and migration in PuO_2 and $(U,Pu)O_2$

4.1 Introduction

The knowledge of defect properties is an important step for the description of various phenomena that occur in the material at the atomic scale. Indeed, the study of point defect stability allows to identify the defects which accommodate the deviation from stoichiometry and constitute traps for fission gases, and also allows to capture modifications induced on the cation valences. Such studies on $(U,Pu)O_2$ will contribute to the interpretation of experiments, especially X-ray absorption spectroscopy (XAS) [279] or positon annihilation spectroscopy [2] for the identification of point defects and fission gas traps in $(U,Pu)O_2$. Furthermore, point defect investigation is an essential step for the study of atomic transport properties since they govern the mobility of atoms in the material. In addition, point defect formation and migration energies are key quantities for the calculation of the activation energies of diffusion. This latter quantity is used for the determination of diffusion coefficients [127]. The atomic transport properties are essential for the description of microstructural evolution under irradiation.

The study of defects in the mixed oxide $(U,Pu)O_2$ is more challenging compared to pure UO_2 and PuO_2. Indeed, the actinide sublattice is constituted of two different atomic species. This leads to the presence of various chemical environments for each defect site in $(U,Pu)O_2$. Moreover, the cation composition can vary. These two features can lead to changes in defect properties in $(U,Pu)O_2$. Thus a complete investigation of defects in $(U,Pu)O_2$ requires the analyses of these features on the defect properties.

The goal of this chapter is to give an as exhaustive as possible characterisation of point defect stability in PuO_2 and $(U,Pu)O_2$ as well as the electronic and structural modifications induced by their formation. In this study, the volume is allowed to relax for neutral defects and then the same volume is maintained constant for charged defects. A specific focus is made on the effect of chemical environments and the plutonium content on the defect formation. Furthermore, the atomic migration is investigated. For this latter topic, the migration mechanisms are identified and the activation energies of diffusion are calculated for various atomic species in $(U,Pu)O_2$.

4.2 Defect structure

4.2.1 Electronic and structural modifications induced by oxygen Vacancies

An oxygen vacancy is a missing oxygen atom in the oxygen sublattice. In the actinide oxide fluorite structure, the oxygen vacancy is located in a tetrahedral site, surrounded by four actinide cations in the first coordination shell. In $(U,Pu)O_2$, the actinide cations surrounding the oxygen vacancy can be uranium or plutonium cations. The defect can be in a pure U or Pu chemical environment, or in a mixed chemical environment. The possible chemical environments of oxygen vacancies are summarized in Figure 48. As for the second coordination shell, the oxygen vacancy is surrounded by six oxygen ions.

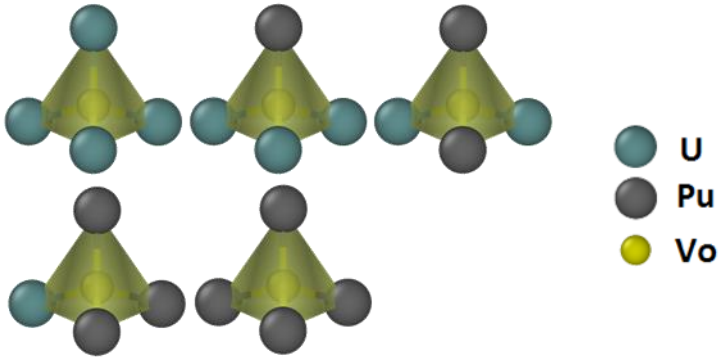

Figure 48 : Chemical environments of the oxygen vacancies in in $(U,Pu)O_2$.

The presence of an oxygen vacancy leads to electronic and structural modifications of the actinide oxides. In the present subsection, the cases of PuO_2 and $(U,Pu)O_2$ are studied. UO_2 was already studied in detail by Dorado [64] and Vathonne [65].

The neutral oxygen vacancy is a two-electron donor. When it is formed in PuO_2 or $(U,Pu)O_2$, the two electrons released localize on two plutonium cations. These Pu cations are reduced from Pu^{4+} to Pu^{3+}. The electronic optimisation in our calculations for both PuO_2 and $(U,Pu)O_2$ shows that the Pu^{3+} cations formed are always located as close as possible to the oxygen vacancy. Therefore, for PuO_2, Pu^{3+} cations are always in the first coordination shell of the vacancy. They are presented in Figure 50 by the green balls. In $(U,Pu)O_2$, if there are not enough Pu in the first coordination shell, Pu^{3+} can be found in the higher coordination shell, as presented in Figure 50 by green balls. U^{3+} cations have never been obtained in our calculation of $(U,Pu)O_2$. This result is consistent with the X-ray absorption spectroscopy (XAS) of Vigier *et al.* [49] where only reduced Pu^{3+} cations are found in the hypo-stoichiometric $U_{0.7}Pu_{0.3}O_{2-x}$. The reduction of Pu

cations can be compensated when a formal charge +2 is considered for the oxygen vacancy defects. The stability of such charged defects will be presented in Section 4.3.

The presence of oxygen neutral vacancies also induces changes in the electronic density of states (DOS) of PuO_2 and $(U,Pu)O_2$. Figure 49 depicts the total electronic density of states of $U_{0.75}Pu_{0.25}O_{2-x}$ containing a neutral and a formally charged (+2) oxygen vacancy compared to the perfect $U_{0.75}Pu_{0.25}O_2$.

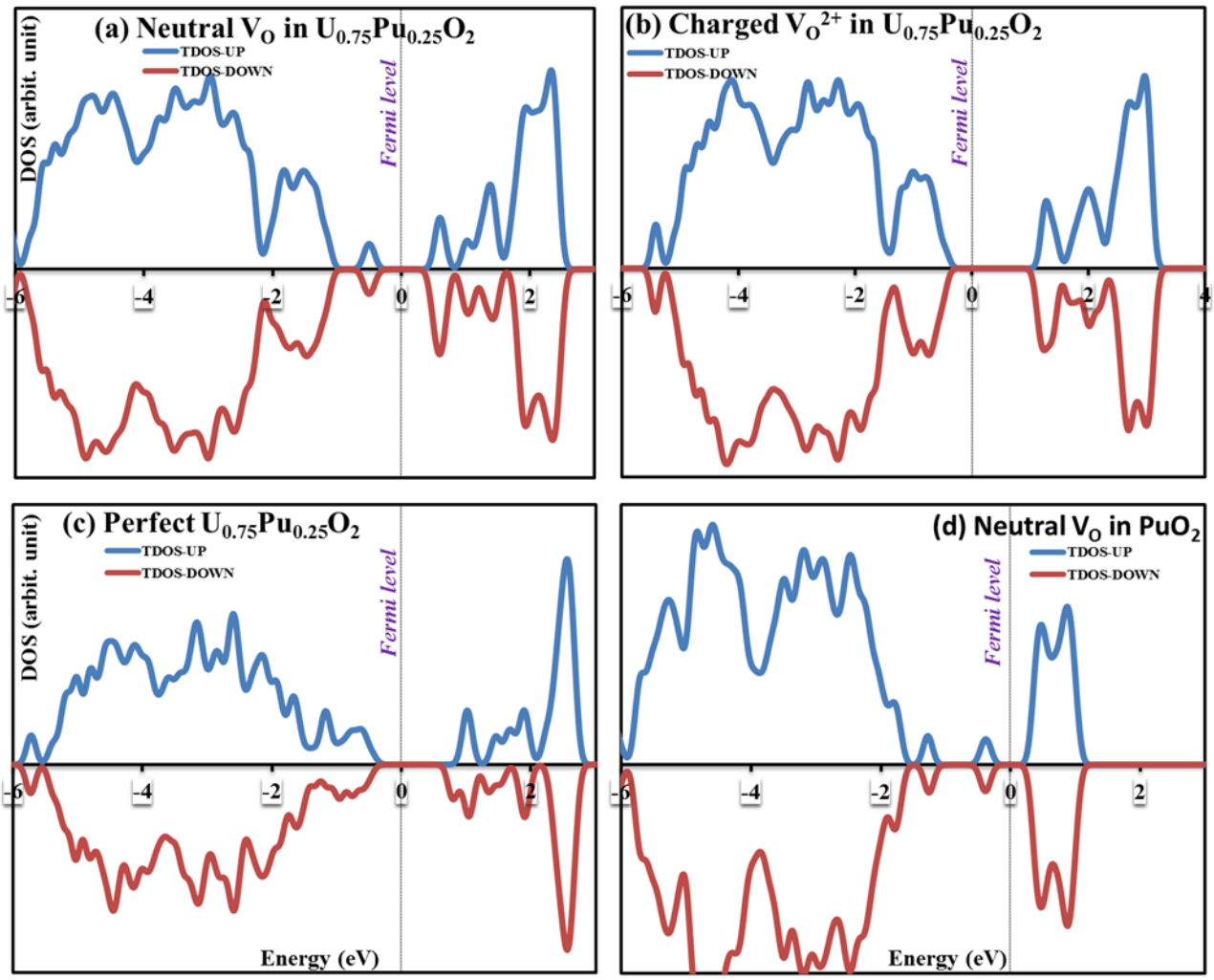

Figure 49 : Total density of states (TDOS) of $U_{0.75}Pu_{0.25}O_2$ containing (a) a neutral oxygen vacancy, (b) a formally charged (+2) oxygen vacancy, (c) no defect (perfect $(U,Pu)O_2$ supercell) and (d) a neutral oxygen vacancy in PuO_2.

The results show that additional electronic defect states appear in the band gap above the valence band in the presence of neutral oxygen vacancies in PuO_2 (Figure 49.d) and $(U,Pu)O_2$ (Figure 49.a). These states are not observed for the formally charged (+2) defects (Figure 49.b). Moreover, for the neutral defects, the Fermi level shifts and becomes closer to the conduction band minimum of both PuO_2 and $(U,Pu)O_2$. In the case

of the formally charged defects, the band gap and the density of states are not significantly modified compared to the perfect compound.

In PuO_2 containing a neutral oxygen vacancy, two localized states are observed within the band gap. The analysis of the partial DOS shows that for each Pu^{3+} formed, both states observed correspond to localized *5f* states. One of these two states is due to the presence of the additional electron on the *5f* orbital of the Pu^{4+} cation (which transforms into Pu^{3+}). The second state is probably due to the electrostatic repulsion between this additional electron and the initial four electrons of the Pu^{4+} *5f* shell. This repulsion destabilizes the electronic configuration by introducing this additional localized state. Our result contrasts with the one of Lu *et al.* [135] who have found only one state localized close to the conduction band minimum. Indeed, Lu *et al*. [135] have not treated the electrons as localized on two Pu cations. In their study, the electrons released are distributed on the four neighbouring Pu. This may explain the difference with our results.

In $(U,Pu)O_2$, only one state is observed within the band gap. This state is localized on the *f* shell of Pu^{3+} cations. The analysis of the partial DOS shows that, in fact, two states are created on the *f* shell of two Pu^{3+} cations which accommodate the excess electrons. However, as mentioned in Chapter 3, Section 3.2.4, the electronic density of states of Pu cations is shifted towards lower energies in $(U,Pu)O_2$ and the additional state localized at the lower energy goes into the valence band of $(U,Pu)O_2$. That is why only one state is observed in the band gap instead of two states as in PuO_2.

Compound	Defect	Displacements δ (Å)	Displacement direction (Δ)	Number of oxygen displaced
PuO_2	V_O	-0.15	<100>	6
	V_O^{2+}	-0.23	<100>	6
	Pu^{3+}	--	--	--
$U_{0.75}Pu_{0.25}O_2$	V_O	-0.15	<100>	6
	V_O^{2+}	-0.22	<100>	6
	Pu^{3+}	+0.07	<100>	8
Lattice expansion	V_O	$a(MO_{2-x}) = a(MO_2) + 0.29\,x$ (in Å)		

Table 25 : Atomic distortions induced by neutral and charged oxygen vacancies in the oxygen sublattice. The displacements around Pu^{3+} are observed only when Pu^{3+} is not in the first coordination shell of the defect.

Table 25 shows the local distortions in the oxygen sublattice induced by the neutral and formally charged oxygen vacancies in PuO_2 and $U_{0.75}Pu_{0.25}O_2$. The algebraic displacements δ and the direction of displacements of the first neighbouring oxygen atoms are both given.

The displacements around Pu^{3+} which are localized beyond the first coordination shell of the defect are also given, although such a configuration only exists for $(U,Pu)O_2$ with defect chemical environments containing less than 2 Pu cations.

The negative value of the algebraic displacement means that the surrounding oxygen atom around comes closer to the defect.

The difference in atomic displacements between the neutral and the formal charge oxygen vacancy is the result of three phenomena: The elastic interaction with defects, the electrostatic interaction with Pu^{3+} and the steric effect of Pu^{3+}. Firstly, the elastic interaction between the defect and the surrounding oxygen ions tends to bring oxygen ions into the defect site. Secondly, the electrostatic interaction between oxygen ions and first neighbouring cations has the following effects: For neutral vacancies, the two Pu^{3+} in the first coordination shell of the oxygen vacancy are less charged compared to Pu^{4+}. This generates a lower electrostatic attraction on oxygen ions compared to Pu^{4+}. Thirdly, the atomic radius of Pu^{3+} (114 pm) is larger than that of Pu^{4+} (110 pm), creating a steric effect. The electrostatic interaction and the steric effect reduce the displacements of oxygen ions. In the case of the formally charged defects, the +2 charge compensates the two electrons available from the vacancy formation and avoid the formation of Pu^{3+}. Therefore, the electrostatic attraction become higher with Pu^{4+} compared to Pu^{3+} and the steric effect is cancelled. Thus, the displacement is more important in the charged defect case. Figure 50 shows the oxygen atoms displaced (pink balls) around an oxygen vacancy, the Pu^{3+} formed (green balls) as well as the oxygen atoms displaced next to Pu^{3+} (purple balls) in PuO_2 (Figure 50.a) and $(U,Pu)O_2$ (Figure 50.b).

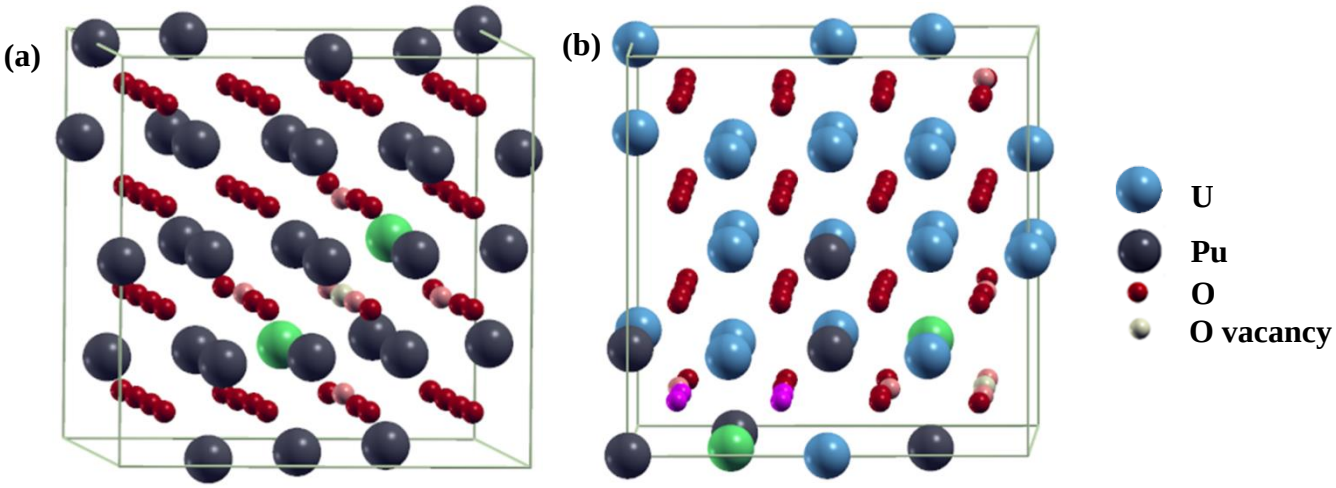

Figure 50 : Oxygen atoms displaced (pink balls) around oxygen vacancies, the Pu^{3+} formed (green balls) and oxygen atoms displaced around Pu^{3+} (purple balls) in (a) PuO_2 and (b) $(U,Pu)O_2$.

The displacements observed next to Pu^{3+} is the consequence of the formation of the small electron polaron which is accompanied by the local distortion in the lattice as found in CeO_2 [234, 280].

No significant displacement is found in the actinide sublattice. Nevertheless, it is to be noted that the distances between the actinide cations in the first coordination shell and the oxygen vacancy are slightly increased compared to the perfect compound. This results in the increase in the lattice constant. The calculation of the slope of the variation of the lattice constant as a function of the deviation from stoichiometry gives the value of 0.29, which is consistent with the experimental value of 0.32 by Vauchy *et al.* [52] (see Chapter 1, Equation (1)).

4.2.2 Electronic and structural modifications induced by oxygen interstitials

An octahedral oxygen interstitial corresponds to an oxygen ion in an octahedral site of the fluorite structure. In actinide oxides, the oxygen interstitials are surrounded by eight oxygen ions in the first coordination shell. The second coordination shell is constituted of six actinide cations, which for the mixed actinide oxides corresponds to the cation chemical environment of the interstitial (see Figure 51). The second coordination shell is thus important for interstitials in the mixed actinide oxides, since it can vary from defect site to another according to the number of U or Pu cations. For the oxygen interstitials, we distinguish seven different chemical environments, going from the pure U environment to the pure Pu environment.

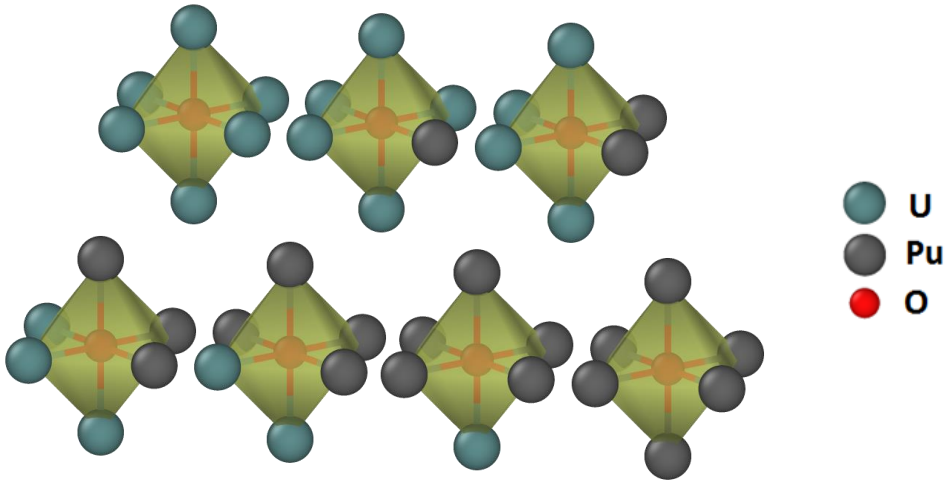

Figure 51 : Chemical environments of the oxygen interstitial in $(U,Pu)O_2$.

In the present section, we present the electronic and structural modifications induced by the presence of an oxygen interstitial in PuO_2 and $(U,Pu)O_2$ respectively.

The oxygen interstitial is a two-electron acceptor. Its formation leads to the release of two holes, which means that the oxygen interstitial captures two electrons to form O^{2-}. In $(U,Pu)O_2$, these electrons are taken from two U cations which oxidize into U^{5+}. The electronic optimisation in our study has shown that the U^{5+} cations are always localized in the second cation coordination shell of the defect as presented by the green balls in Figure 53. For $U_{0.75}Pu_{0.25}O_2$, each U^{5+} is localized at 4.76 Å from the oxygen interstitial. In PuO_2, no Pu^{5+} can form and the electrons are partially taken from oxygen ions in the lattice. However, the two electrons are not completely captured and the charge absolute value on the oxygen interstitial remains smaller than 2|e|. Thus, in PuO_2 the oxygen interstitial possesses a less negative charge compared to lattice O^{2-} ions. Bader charge analysis shows a charge loss of 0.47|e| on the oxygen interstitial compared to other oxygen ions of the lattice. It is to be noted that the oxidized PuO_{2+x} is found unstable experimentally [281].

Oxygen interstitials also induce modifications on the electronic density of states of $(U,Pu)O_2$ and PuO_2 as presented in Figure 52.

For PuO_2, the presence of neutral oxygen interstitials induces unoccupied electronic states above the valence band maximum. These states come from unoccupied *2p* states of the oxygen interstitial itself. The Fermi level also shifts towards the valence band maximum as shown in Figure 52 (a). As for the formally charged -2 oxygen interstitials, occupied states are obtained in the band gap together with a shift of the Fermi level towards the conduction band minimum. This latter electronic modification is shown in Figure 52 (b). The presence of occupied states near the valence band maximum means that the -2 charge state of I_0 brings a p-type doping effect on PuO_2. These results are similar to those obtained by Lu *et al.* [135].

There are no electronic states found in the band gap according to the TDOS of $(U,Pu)O_2$. Detailed analyses of the partial DOS (not shown here) highlight the presence of unoccupied states on the uranium *f* states just below the conduction band minimum of uranium *5f* states. These states disappear when the oxygen interstitial is charged -2. However, as the Pu *5f* states are shifted towards low energies to form the conduction band minimum (CBM) of $(U,Pu)O_2$ far below the CBM of uranium *5f* cations, the above unoccupied uranium *f* states are ultimately localized in the conduction band of $(U,Pu)O_2$. Therefore, the presence of a charged or neutral oxygen interstitials has no impact on the electronic density of states of $(U,Pu)O_2$.

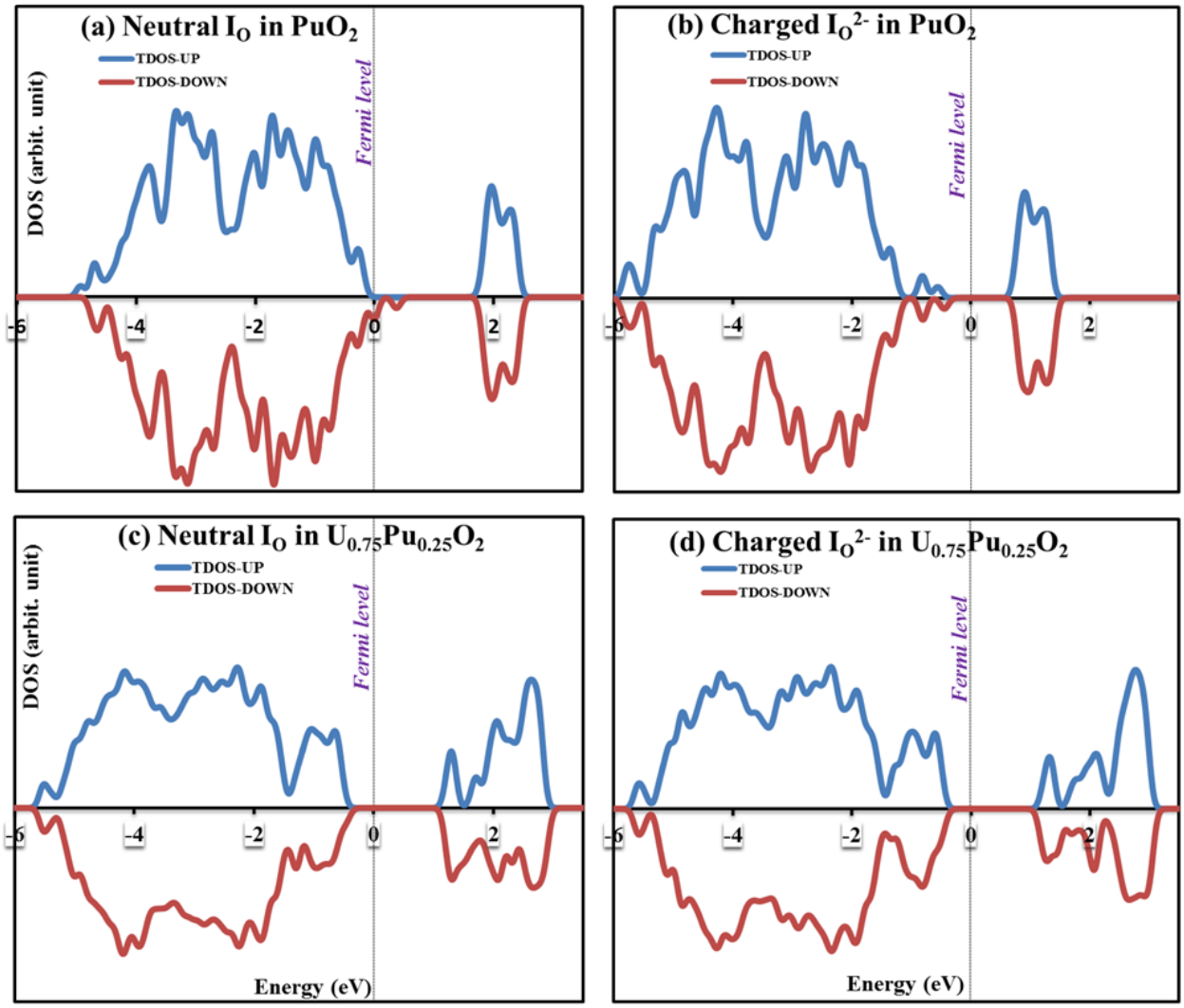

Figure 52 : Total density of states (TDOS) of PuO_2 containing (a) a neutral oxygen interstitial, (b) a formally charged (-2) oxygen interstitial, and TDOS of $(U,Pu)O_2$ containing (c) a neutral oxygen interstitial and (d) a formally charged (-2) oxygen interstitial.

Table 26 depicts the local distortions induced by the presence of neutral and formally charged oxygen interstitials in PuO_2 and $(U,Pu)O_2$. These results show significant differences in the lattice distortion for neutral and formally charged oxygen interstitials in PuO_2 while there are no difference between the distortions for neutral and formally charged oxygen interstitials in $(U,Pu)O_2$. Positive displacements mean that oxygen atoms are pushed away from the defect.

The difference found in the displacements owing to the formal charge state in PuO_2 is due to the smaller electrostatic repulsion exerted by the less negatively charged oxygen interstitial for the neutral defect, compared to the formally charged one. This smaller repulsion combines with the elastic repulsion generated by the presence of the defect. The resulting displacement is therefore smaller compared to the effect of the elastic repulsion and the electrostatic repulsion of O^{2-}. For the formally charge state -2, the

addition of two negative charges compensates the charge loss of the defect and thus increases the electrostatic repulsion on surrounding O^{2-}. The displacement induced is therefore larger than that of the neutral oxygen interstitial. In $(U,Pu)O_2$, the similarity in displacements for the neutral and charge defect is due to the absence of charge loss on the O interstitial, since a O^{2-} interstitial with a complete -2 charged is formed through the oxidation of two U^{4+} into U^{5+} far from the defect site. U^{5+} cations are presented by green balls in Figure 53. Therefore, the attraction of oxygen ions by the oxygen interstitial as observed in PuO_2 does not occur in $(U,Pu)O_2$. The displacements observed are thus very close to the ones obtained in PuO_2 for a formally charged oxygen interstitial.

Compound	Defect	Displacements δ (Å)	Displacement direction (Δ)	Number of oxygen displaced
PuO_2	I_O	+0.09	<111>	8
	I_O^{2-}	+0.14	<111>	8
$U_{0.75}Pu_{0.25}O_2$	I_O	+0.16	<111>	8
	I_O^{2+}	+0.16	<111>	8
Lattice constant	I_O	$a\,(MO_{2+x}) = a\,(MO_2) - 0.1369\,x$ (in Å)		

Table 26 : Atomic distortions induced by neutral and charged oxygen interstitials in the oxygen sublattice. The impact of the hyper-stoichiometry is also shown.

In the actinide sublattice, the bonding length of actinide cations surrounding the oxygen interstitial decreases from 5.54 Å in the perfect fluorite structure to 5.34 Å. This results in the decrease in the lattice constant as obtained experimentally on UO_2 by Teske *et al*. [282], with the following relationship between the lattice constant and the deviation from the stoichiometry:

$$a = (5.4705 - 0.1306x)\text{Å} \qquad (137)$$

By generalizing this expression as $a = (a_0 + bx)$Å, we found the slope b = -0.1369, which is similar to the experimental value obtained for UO_2.

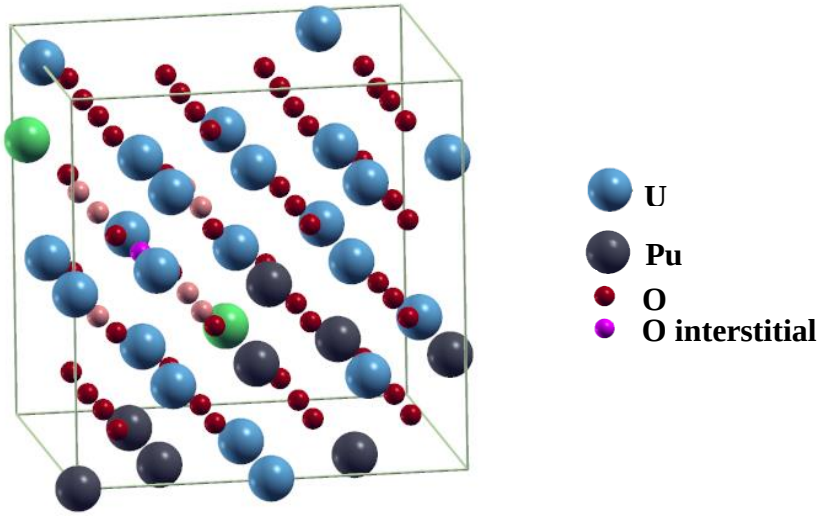

Figure 53 : Local distortions induced by an oxygen interstitial in PuO_2 and $(U,Pu)O_2$. The eight oxygen ions displaced in the first coordination shell are presented in pink for $(U,Pu)O_2$.

4.2.3 Electronic and structural modifications induced by plutonium and uranium interstitials

Plutonium or uranium interstitials are surrounded by eight oxygen ions in the first coordination shell. The second coordination shell is constituted of six actinide cations. The modifications induced by plutonium interstitials in PuO_2 and $(U,Pu)O_2$, as well as uranium interstitials in $(U,Pu)O_2$ are shown in this section.

Neutral actinide interstitials in PuO_2 and $(U,Pu)O_2$ are electron donors and release four electrons. Each electron released is localized on neighbouring Pu cations (never U cations) which in turn are reduced into Pu^{3+}. When the neutral interstitial cation is Pu, it keeps one of the four electrons released. Therefore, the neutral Pu interstitial is always found in the reduced Pu^{3+} state. In that case, in PuO_2, the three other electrons released are localized on three plutonium cations in the first coordination shell of the defect (three Pu^{3+} indicated by the yellow balls in Figure 54). For $(U,Pu)O_2$, the positions of the three Pu^{3+} depend on the defect environment. The U interstitial keeps the U^{4+} valence and the four electrons released are localized on four Pu cations at the closest neighbour sites of the defect which become Pu^{3+}. The modifications induced in the electronic density of states are similar to those obtained for oxygen vacancies since both types of defects are electron donors.

The local distortions induced in the lattice are shown in Table 27. They are determined by the atomic displacements of the defect first neighbouring actinide cations in PuO_2

and (U,Pu)O_2. The local environment of the defect is highlighted in Figure 54. It appears clearly that the formally charged plutonium interstitials, which are Pu^{4+} cations, are more repulsive than the Pu^{3+} ones in the interstitial position (corresponding to the neutral defect configuration). The displacements induced by the uranium interstitials are similar for neutral and formally charged interstitials. Moreover, the elastic repulsion generated by U interstitials is slightly larger than that generated by Pu interstitials. This can be seen from the larger displacements induced by U interstitials compared to Pu interstitials.

Compound	Defect	Displacements δ (Å)	Displacement direction (Δ)	Number of oxygen displaced
PuO_2	I_{Pu}	+0.26	<100>	6
	I_{Pu}^{4+}	+0.31	<100>	6
$U_{0.75}Pu_{0.25}O_2$	I_{Pu}	+0.27	<100>	6
	I_{Pu}^{4+}	+0.30	<100>	6
	I_U	+0.36	<100>	6
	I_U^{4+}	+0.36	<100>	6

Table 27 : Atomic displacements in the cation sublattice induced by neutral and charged actinide interstitials. The sign (+) means that the atoms are pushed away from the defect.

Near the neutral plutonium interstitial, the displacements are a combination of the elastic repulsion in the Pu sublattice, and the electrostatic attraction, owing to the intrinsic negative charged character of the Pu^{3+} interstitial compared to Pu^{4+} or U^{4+}. For the formally charged defect, the intrinsic charge is compensated and the electrostatic attraction is cancelled out. For U interstitials, there is no U^{3+} formed. Therefore, no electrostatic attraction occurs. This results in equal local distortions for neutral and formally charged U interstitials. Note that no oxygen displacement is observed.

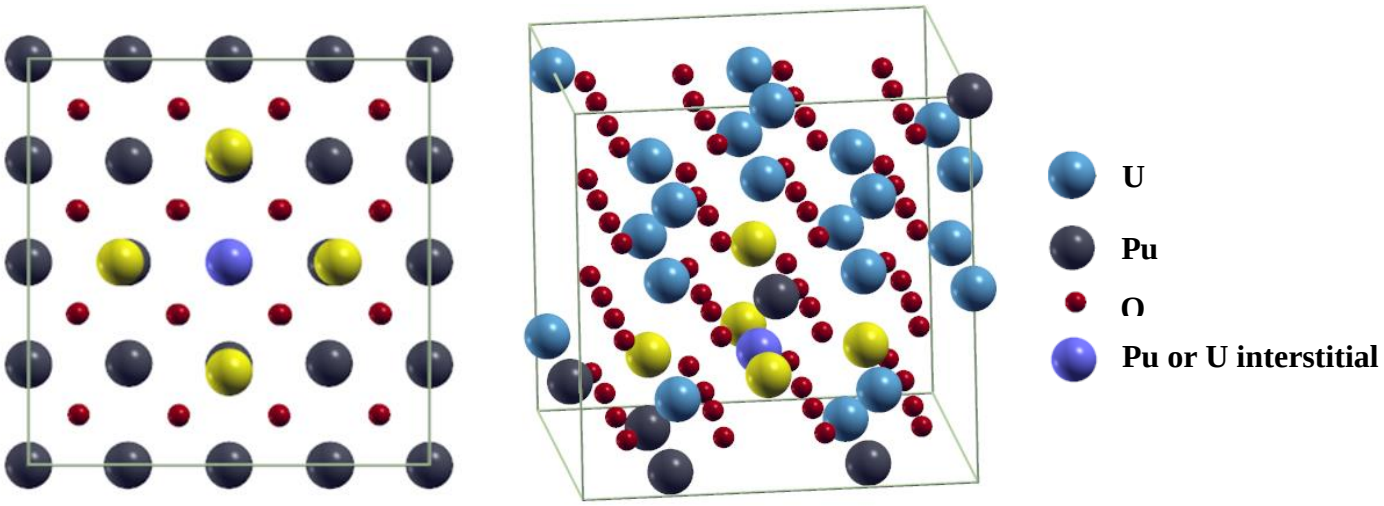

Figure 54 : Local environment of Pu or U interstitials in PuO_2 and $(U,Pu)O_2$. The yellow balls are the displaced actinide cations.

4.2.4 Electronic and structural modifications induced by plutonium and uranium vacancies

The actinide vacancy (U or Pu) is defined by a missing actinide atom in the actinide sublattice. Uranium and plutonium vacancies are surrounded by eight oxygen ions in the first coordination shell, and yield an oxidizing character. As the oxidized phase PuO_{2+x} of PuO_2 is found to be unstable experimentally [281], we will only analyse the electronic and structural modifications induced in $(U,Pu)O_2$.

U and Pu vacancies are electron acceptors which release four holes in the defective compound. This means that four electrons are missing in the lattice. We found that the missing electrons are accommodated by four U cations in the nearest coordination shell. The latter U cations oxidize into U^{5+} cations. The modifications on the electronic density of states are similar to those obtained for oxygen interstitials, which are also electron acceptors.

The formation of an actinide vacancy induces the displacement of the eight oxygen ions located in the first coordination shell of the defect. For both uranium and plutonium vacancies, the displacement is almost the same, with a value of +0.24 Å in the <111> direction for both neutral and formally charged actinide vacancy. The oxygen atoms displaced are highlighted in Figure 55 by small green balls.

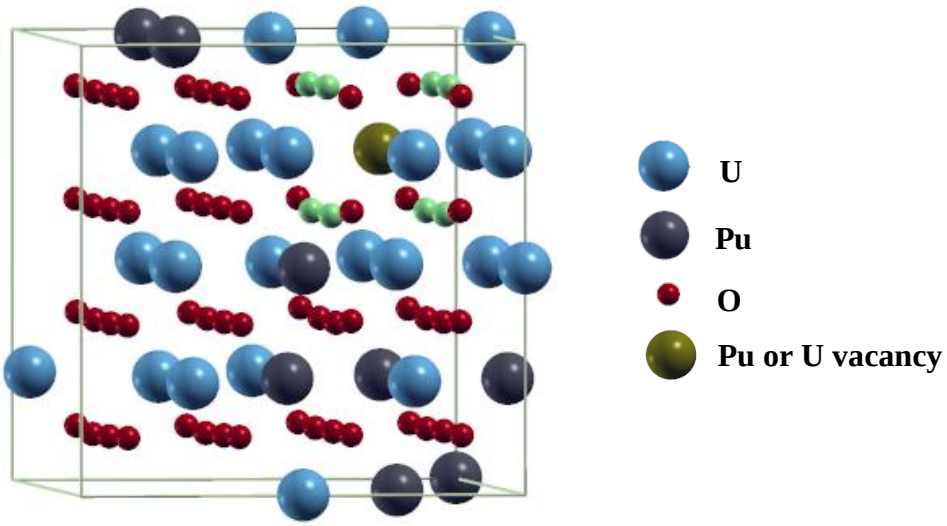

Figure 55 : Atomic displacements induced by the Pu or U vacancies in $(U,Pu)O_2$. The small green balls are the displaced oxygen ions.

4.2.5 Electronic and structural modifications induced by Bound Schottky defects in PuO_2 and $(U,Pu)O_2$

The bound Schottky defects (BSD) in actinide oxides are the defects constituted of an actinide vacancy and two oxygen vacancies. The two oxygen vacancies are localized in the first coordination shell of the actinide vacancy. As actinide oxides possess a fluorite structure, there are three possible configurations for the BSDs as presented schematically in Figure 56 for $(U,Pu)O_2$. The first configuration denoted BSD1 corresponds to the oxygen vacancies oriented in the <100> direction. The second configuration BSD2 corresponds to the oxygen vacancies oriented in the <110> direction and the third configuration BSD3 corresponds to the oxygen vacancies oriented in the <111> direction. For BSDs in $(U,Pu)O_2$ the actinide vacancy can be U or Pu, leading to the U-BSDs types or Pu-BSD types.

BSD defects are neither electron donor nor electron acceptor defects. Thus there are no electronic modifications induced by BSD defects.

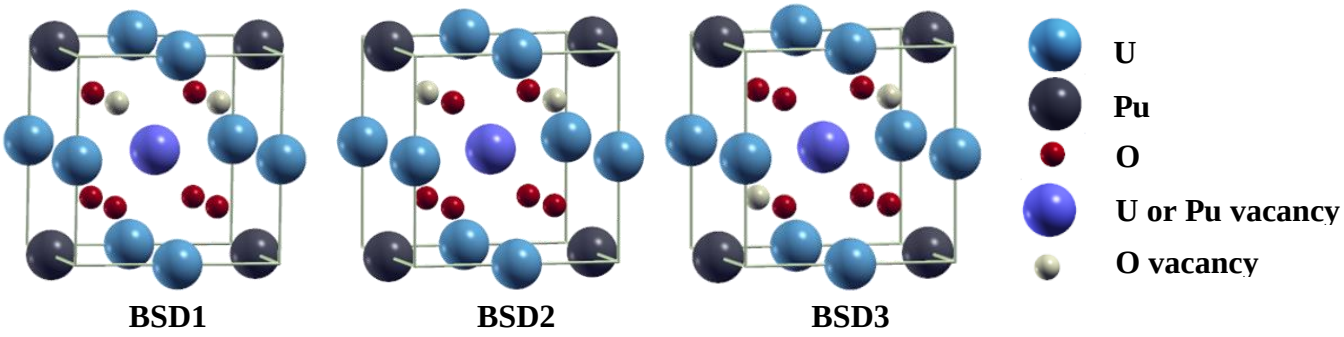

Figure 56 : Bound Schottky Defect (BSD) configurations in $(U,Pu)O_2$.

We have studied the impact of various BSDs on the structural properties of PuO_2 and $(U,Pu)O_2$. Local distortions in the oxygen sublattice are shown in Table 28. These distortions are expressed in terms of atomic displacements.

Compound	Defect	Displacements δ (Å)	Displacement direction (Δ)	Number of oxygen displaced
PuO_2	BSD1	+0.18	<111>	6
		-0.18	<111>	6
	BSD2	+0.18	<111>	6
		-0.24	<111>	6
	BSD3	+0.21	<111>	6
		-0.24	<111>	6
$U_{0.75}Pu_{0.25}O_2$	BSD1	+0.30	<111>	6
		-0.27	<111>	6
	BSD2	+0.30	<111>	6
		-0.31	<111>	6
	BSD3	+0.28	<111>	6
		-0.31	<111>	6

Table 28 : Local distortions of oxygen sublattice induced by BSD defects. The displacements of oxygen ions pushed away from cation vacancies are shown in black and those pushed closer to the oxygen vacancies are shown in red.

The presence of the BSDs in PuO_2 and $(U,Pu)O_2$ leads to a complex distortion of the oxygen sublattice. The oxygen atoms are displaced in two different manners as we can observe in Figure 57 for the BSD2. The first group of displacement involves six oxygen

atoms in the first coordination shell of the actinide vacancy, represented in Figure 57 by the small green balls (data in black in Table 28). On the order hand, six oxygen ions located in the first coordination shell of the oxygen vacancies of the BSD defects are pulled closer to the oxygen vacancies (red data in Table 28). The displacements are slightly different between the BSD1, BSD2 and BSD3 configurations and are larger for $(U,Pu)O_2$ than PuO_2. Moreover, the BSD2 and BSD3 configurations present quite similar distortions in the oxygen sublattice. Therefore, their configurational energies are close to each other and explain the similarity in their formation energies as obtained in Section 4.3.2.3.

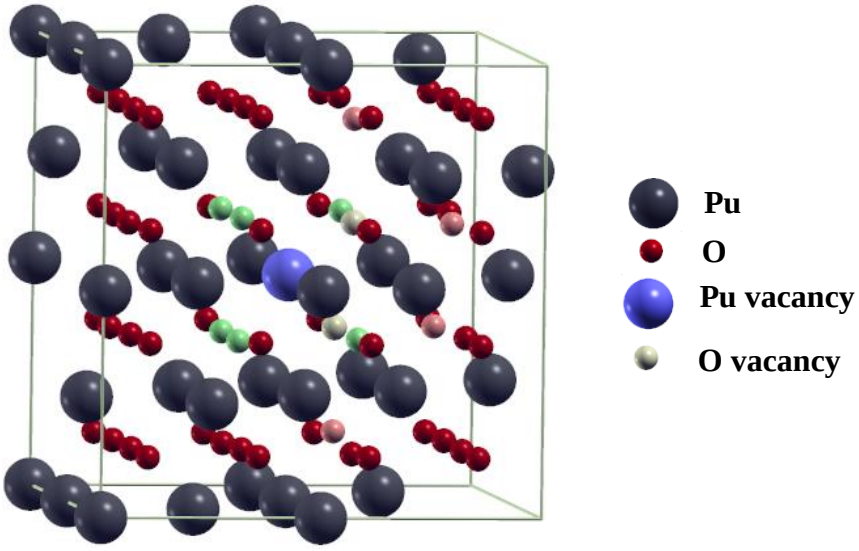

Figure 57 : Atomic displacements induced by BSDs in PuO_2. The small green balls are oxygen atoms located in the first coordination of Pu vacancy and the small pink balls corresponds to the oxygen atoms nearby the oxygen vacancies of the BSD.

4.3 Point defect stability in PuO_2 and $(U,Pu)O_2$

4.3.1 Point defect stability four various charge states in PuO_2

Figure 58 shows the plot of the formation energies of various point defects in PuO_2, under neutral and formal charge state in the whole accessible oxygen chemical potential range of the fluorite structure of the Pu-O system, as calculated in Section 2.6.2.2. The formation energy is shown for the Fermi level in the middle of the band gap. In the

notation Y^{q}_{atom}, Y is the defect type. These are vacancies (V), interstitials (I), bound Schottky defects (BSD2). *atom* is the associated atomic type of the defect. These are oxygen (O) and plutonium (Pu). q is the charge state of the defect. Ioo is the oxygen di-interstitial. The charge states are neutral (X) or formally charged states (+2 for O vacancies, -2 for O interstitials, +4 for Pu interstitials). The oxygen chemical potential at the stoichiometry is the value at which the oxygen vacancies and interstitials have the same concentration. This value is assumed to be at the intersection of their formation energies for the most stable charge states. The stoichiometry is represented by the dotted line.

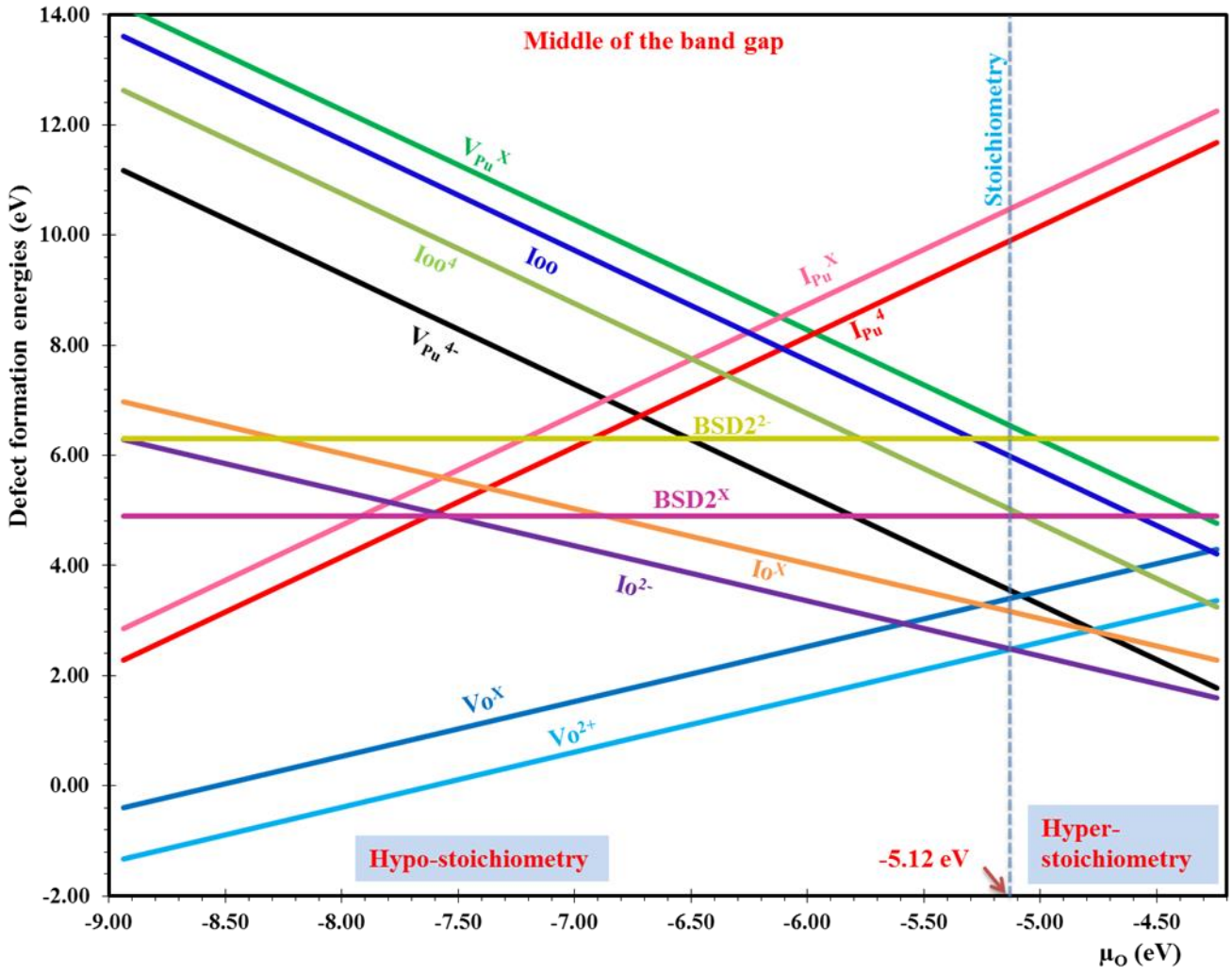

Figure 58 : Formation energies of neutral and formally charged defects in PuO_2 as a function of the oxygen chemical potential (Fermi level in the middle of the band gap).

Firstly, the results on the stability of defect charge states show a completely charged behaviour of point defects in PuO_2 for the Fermi level in the middle of the band gap, in

the whole oxygen chemical potential range. For all point defects considered, the formal charge states Vo^{2+}, Io^{2-}, Ioo^{4-}, Vpu^{4-}, Ipu^{4+} and $BSD2^{X}$ are the most favourable. This behaviour is linked to the fact that the plutonium oxidation state +IV is always the most favourable one found in PuO_2 instead of +III , even in hypo-stoichiometric conditions. Secondly, Figure 58 depicts the defect types which are expected to be the most stable in the various stoichiometry domains. From the lower limit of the hypo-stoichiometry conditions to the oxygen chemical potential of -7.60 eV, the order of stability of the defects is the following: Vo – Ipu – BSD2 – Io – Vpu – Ioo. The stability of the first two defects results in the decrease of the O/Pu ratio in PuO_2, corresponding to a hypo-stoichiometric or reducing character. Therefore, in this domain, the reducing defects are the most favourable. Moreover, the formation energies of oxygen vacancies are negative. This behaviour confirms the ease of PuO_2 to reduce into Pu_2O_3 phase.

For the oxygen chemical potential around the stoichiometry, namely from -7.60 eV to -5.12 eV, the oxygen vacancies remain the most favourable defects. At the hyper-stoichiometry (chemical potential larger than -5.12 eV), oxidizing defects such as oxygen interstitials become more favourable than the reducing V_O, I_{Pu} and the neutral BSD2. On the order hand, the width of the hyper-stoichiometry domain is much smaller (by the factor of 4) than that of the hypo-stoichiometry domain. This result is probably due to the fact that PuO_2 is the highest stable oxidized phase of the Pu-O system. Thus, it cannot be further oxidized, unless a very constraining oxidizing condition is reached. This may corresponds to a very high oxygen chemical potential. The formation of PuO_{2+x} has been reported to be unstable even at high temperature [281]. This experimental observation supports our results and our assumption.

4.3.2 Point defect stability in $(U,Pu)O_2$

Defect formation in $(U,Pu)O_2$ are impacted by various features. As introduced in the previous Section 4.2, defects in $(U,Pu)O_2$ possess a large variety of chemical environments. This is due to the fact that the cation sublattice is mixed. In addition, the Pu contents constitute an additional parameter for $(U,Pu)O_2$ compared to pure oxides. Beside the formation energies of various defects and charge states in $(U,Pu)O_2$, the impact of the chemical environments and the Pu contents will be subsequently addressed on oxygen defects. These analyses allow, on the one hand, to identify stable environments for each defect, and, on the other hand, the effect of Pu content on atomic scale irradiation damage can be captured.

4.3.2.1 Effect of chemical environment on point defect formation in $(U,Pu)O_2$

In the present section, we present the impact of the chemical environments of defects in terms of the variation of the formation energies with respect to the number of plutonium cations in the first coordination shell of the defect. All the formation energies are calculated using the oxygen chemical potential identified at the stoichiometry for $U_{0.75}Pu_{0.25}O_2$ (see Sub-section 4.3.2.3).

Figure 59 presents the formation energies of an oxygen vacancy in various chemical environments containing respectively 0, 1, 2 and 3 Pu cations in the first coordination shell. The decrease in the formation energy with the increase in Pu/(U+Pu) ratio is highlighted. The chemical environments containing at least 2 Pu are the most favourable. The energy difference between the most stable environments (lowest energy) and the less stable one (highest energy) is 0.5 eV. This difference is high, meaning that the effect of chemical environment cannot be neglected. We also observe that the environment with one Pu cation is more stable than the pure uranium environment.

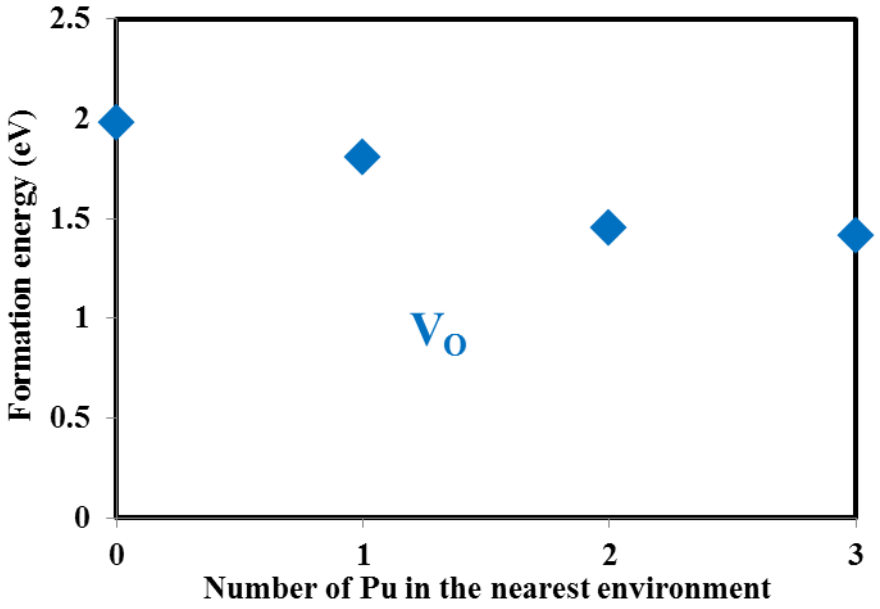

Figure 59 : Evolution of the formation energy of a neutral oxygen vacancy with the chemical environments. Four environments containing 0, 1, 2 and 3 Pu cations are assessed. The formation energies are calculated for the stoichiometry condition as shown in the Section 4.3.2.3.

The variation of the formation energies for various chemical environments can be explained by the formation of small electron polarons. Their formation leads to local

distortions around the atoms (or cations) with which the electron is interacting [234]. These distortions accommodate the electron polarons. In the defective $(U,Pu)O_2$, the formation of an oxygen vacancy is accompanied by the release of two electrons and these electrons are always localized on Pu cations in $(U,Pu)O_2$, never on U cations (see Section 4.2.1). When the small electron polarons are formed in the first coordination shell of oxygen vacancies, it benefits from the presence of the free space yielded by the vacancies. Therefore, local distortions are not observed and the formation energy associated to the polaron is low. In contrary, when electron polarons are formed far from the oxygen vacancies, there is no free space and local distortions are observed as mentioned in Section 4.2.1. The formation energy associated to the polaron in that case is higher than in the previous case. It is thus expected to find the highest formation energy when all the two electron polarons associated to a neutral oxygen vacancy are not in its first coordination shell (pure uranium environment), and the lowest formation energy for two electron polarons formed in the first coordination shell of the oxygen vacancy (at least 2 Pu in the environment). This is in line with our results.

Figure 60 depicts the evolution of formation energies of a neutral oxygen interstitial in $U_{0.75}Pu_{0.25}O_2$ with respect to various chemical environments. Chemical environments are identified in terms of the number of Pu cations in the first cation shell of oxygen interstitials. The results highlight the increase in the formation energies of neutral oxygen interstitials with the increase of the number of Pu in the environment. The energy difference of 0.6 eV is obtained between the most favourable environment (uranium pure environment) and the least favourable one (four Pu).

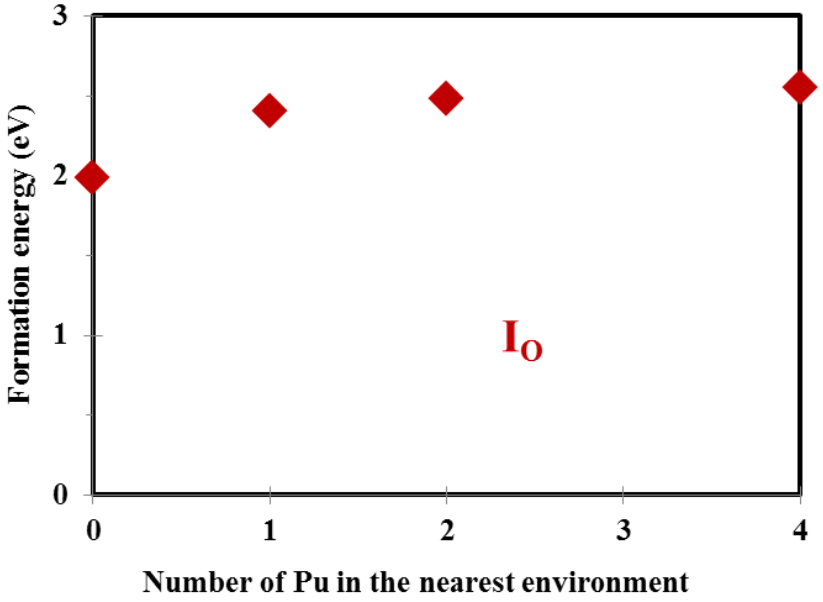

Figure 60 : Evolution of the formation energy of a neutral oxygen interstitial with the chemical environments. Four environments containing 0, 1, 2 and 4 Pu cations are assessed. The formation energies are calculated for the stoichiometry condition as shown in the Section 4.3.2.3.

The increase in the formation energy of neutral oxygen interstitials is due to the stainless nature of Pu cations. Indeed, oxygen interstitials are oxidizing defects. A low oxidation of $(U,Pu)O_2$ has been found experimentally to induce the formation of defect structure around uranium cations [34], never around the Pu cations. By analogy, we can reasonably expect the presence of Pu cations in the interstitial environment to be less favourable for the formation of the defect structure. This may explain the loss of stability with the increase in Pu in the defect environment.

4.3.2.2 Effect of Pu content on point defect formation

Figure 61 shows the plot of the formation energies of a neutral oxygen vacancy as a function of Pu contents. Formation energies are calculated at stoichiometry and for the most stable chemical environments provided by the SQS configurations [189, 237]. The chemical environments possess once Pu for 12.5% Pu and two Pu for 25 and 50 % Pu. The results highlight that the formation energies of oxygen vacancies in $(U,Pu)O_2$ are lower than those in the UO_2 and PuO_2 pure oxides. In $(U,Pu)O_2$ especially, the formation energies are much smaller in $(U,Pu)O_2$ than in pure UO_2. This tendency is probably due to the favourable reducing environment provided by Pu cations.

Figure 62 depicts the evolution of the formation energy of a neutral oxygen interstitial with the Pu content in $(U,Pu)O_2$. Here again, the most favourable chemical environment is considered for each defect. The formation energies of O interstitial in $(U,Pu)O_2$ are found lower than in PuO_2. On the other hand, these energies are very close (slightly larger) to that in UO_2 (see Ref. [65] at stoichiometry). The lower formation energies in $(U,Pu)O_2$ compared to PuO_2 is indeed due to the presence of uranium cations which can accommodate the hyper-stoichiometry.

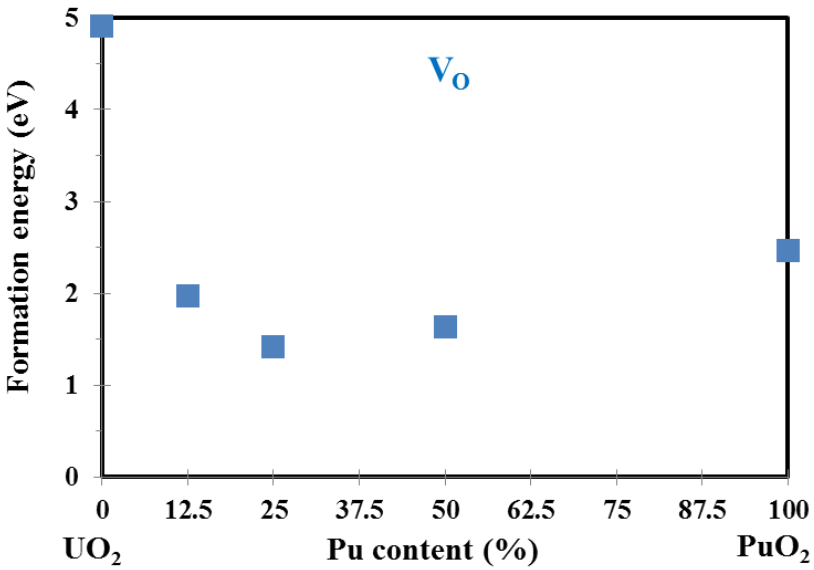

Figure 61 : Formation energy of a neutral oxygen vacancy as a function of Pu content.

The variation of the formation energies of neutral oxygen interstitials with the Pu content is negligible. This result suggests that plutonium cations in the second and higher coordination shell have no impact on the formation of oxygen interstitials.

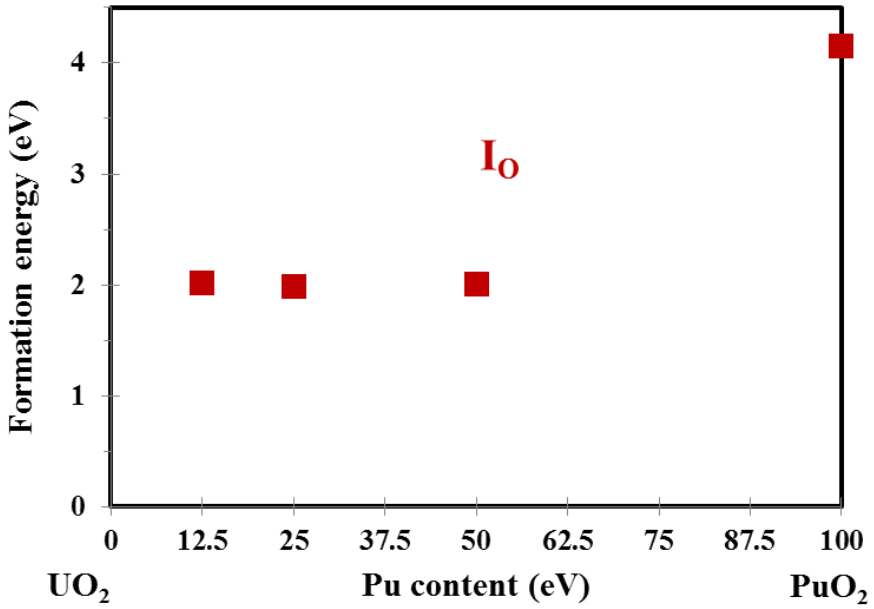

Figure 62 : Formation energies of a neutral oxygen interstitial as a function of Pu content.

4.3.2.3 Point defect formation energies for various charge states in $(U,Pu)O_2$

Figure 63 shows the plot of the formation energies of various point defects in $U_{0.75}Pu_{0.25}O_2$, under neutral and formally charged states as a function of the O chemical potential. These energies are calculated in the entire accessible oxygen chemical potential range of the fluorite phase of the U-Pu-O system. The formation energies are assessed for the Fermi level in the middle of the band gap. The notation Y_{atom}^{q} has the same meaning as for PuO_2 (see Section 4.3.1). The defect charge states are neutral (X) or formally charge states (+2 for O vacancy, -2 for O interstitial, +4 for U and Pu interstitials and -4 for U or Pu vacancies). The stoichiometry is defined in the same manner as for PuO_2 (see Section 4.3.1) and is represented by the dotted line.

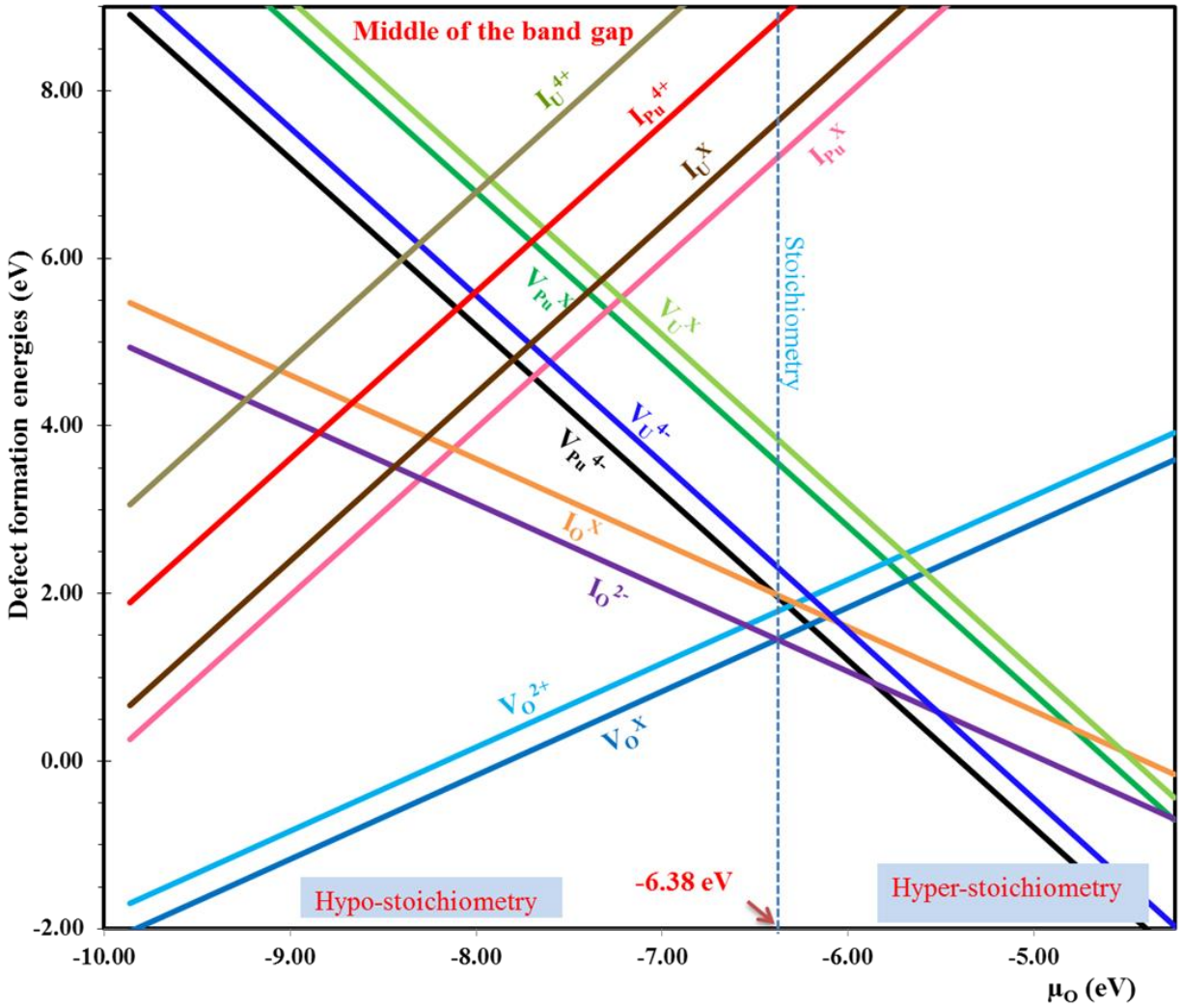

Figure 63 : Formation energies of neutral and formal charge point defects in $U_{0.75}Pu_{0.25}O_2$ as a function of the oxygen chemical potential.

The stability of defects shows two different charge behaviour for oxidizing and reducing defects for the Fermi level in the middle of the band gap. Indeed, for reducing defects such as oxygen vacancies and actinide interstitials, the neutral charge states are the most favourable in the whole chemical potential range. Next, for oxidizing point defects such as oxygen interstitials and actinide vacancies, the formal charge states are the most favourable ones for the Fermi level in the middle of the band gap, for the entire oxygen chemical potential range. This result means that Pu^{3+} cations, which are induced by neutral reducing defects, are the most favorable cations in $(U,Pu)O_2$ to accommodate the presence of reducing defects. On the other hand, U^{4+} cations, which are found for formally charged oxidizing defects, are the most stable U cations in $(U,Pu)O_2$ for the various stoichiometry conditions. Therefore, the oxidizing states +III and +IV of Pu and +IV of U can be found in $(U,Pu)O_2$ depending on the deviation from stoichiometry. This conclusion agrees well with the experimental result of Vigier *et al.* [49] where Pu^{3+}

cations were obtained in hypo-stoichiometric $U_{0.7}Pu_{0.3}O_{2-x}$. The stability of U^{4+} also agrees with theoretical results of Vathonne *et al*. [283], Crocombette *et al*. [284] and Nerikar *et al*. [121] on UO_2.

Figure 63 also depicts the defect types which are stable at various stoichiometry conditions. From the lower limit of the hypo-stoichiometry to the oxygen chemical potential of -8.30 eV, the order of stability of the defects is the following: V_O - I_{Pu} - I_U - I_O - V_{Pu} - V_U. This ranking highlights that all the reducing defects are more favourable. The formation energies of oxygen vacancies are negative up to the chemical potential of -7.80 eV, suggesting a spontanneous reduction of the $(U,Pu)O_{2-x}$ fluorite phase into the reducing structural phase. For the oxygen chemical potential range from -7.80 eV to the stoichiometry (-6.38 eV), the order of stability of the defects become the following: V_O - I_O - V_{Pu} - V_U - I_{Pu} - I_U. In this region, the oxygen vacancies remain the most stable defects with a positive formation energies. This domains corresponds to the stability of $(U,Pu)O_{2-x}$ fluorite structure phase. In both cases the hypo-stoichiometry is accomodated by oxygen vacancies. In the hyper-stoichiometry region, for the oxygen chemical potential ranged from -6.38 eV to -5.87 eV, the defect stability ranking is as follows: I_O - V_O ↔ V_{Pu} - V_U - I_{Pu} - I_U. Oxygen interstitials become the most stable defects and thus, accommodate the hyper-stoichiometry. The formation energy of this stable defect remains positive, meaning that $(U,Pu)O_{2+x}$ does not oxidize spontaneously. For the oxygen chemical potential higher than -5.87 eV, the defect stability is ranked as follows: V_{Pu} - V_U - I_O - V_O - I_{Pu} - I_U. The plutonium vacancy becomes the most stable defect, with a positive formation energy up to the oxygen chemical potential of -5.40 eV. Above -5.40 eV, the formation energy of V_{Pu} defect becomes negative, meaning that $(U,Pu)O_{2+x}$ oxidizes spontaneously into an oxidized phase structure.

We can also mention the larger oxygen chemical potential range which corresponds to the stability of the $(U,Pu)O_{2-x}$ fluorite phase (-7.80 eV ≤ μ_O ≤ -6.38 eV) in the hypo-stoichiometry, compared to that of the $(U,Pu)O_{2+x}$ fluorite phase (-6.38 eV ≤ μ_O ≤ -5.40 eV) in the hyper-stoichiometry. This result agrees with the phase diagram of the U-Pu-O system where the reduced fluorite phase $(U,Pu)O_{2-x}$ is stable in a larger oxygen content range than the oxidized fluorite phase $(U,Pu)O_{2+x}$ [22, 285, 286], especially for 25 % Pu.

We have also studied the stability of various bound Schottky defects (BSD) in the $(U,Pu)O_{2+x}$ fluorite phase. The results are shown in Table 29 for the Fermi level in the middle of the band gap. The BSD formation energies do not vary with the deviation from stoichiometry.

The formation energies of -2 charged BSD are found more favourable than that of neutral ones (formal charge state) for the Fermi level in the middle of the band gap. This confirms the stability of Pu^{3+} cations in $(U,Pu)O_2$. Indeed, the formation of the -2 charge state induces the reduction of two Pu^{4+} cations into two Pu^{3+}. On the other hand, the BSD2_Pu is found to be the most stable defect. Globally, the BSD2 configuration (see

Section 4.2.5) is found to be the most stable configuration of BSD. This result agrees with other theoretical results on UO_2 [64, 283].

Defect formation energy (eV)	Neutral	-2 charge state
BSD1_Pu	4.08	3.55
BSD2_Pu	3.35	2.97
BSD3_Pu	3.74	3.21
BSD1_U	3.93	3.57
BSD2_U	3.51	3.14
BSD3_U	3.51	3.25

Table 29 : Formation energies (in eV) of various bound Schottky defects types in $(U,Pu)O_2$. The neutral and -2 charge states are assessed for the Fermi level in the middle of the band gap.

The defect formation energies and stable charge states are impacted by the Fermi level, as found for UO_2, PuO_2 and CeO_2 [119, 283, 284]. Figure 64 shows the plot of the defect formation energies as a function of the Fermi level in the entire band gap of $U_{0.75}Pu_{0.25}O_2$. Only the most favourable BSD2_Pu type is presented, as all BSD types follow the same evolution and their charge state does not depend on the stoichiometry conditions.

The position of the Fermi level impacts strongly the defect charge state. When the Fermi energy evolves from the middle of the band gap towards the valence band maximum, defects tend to be electron deficient compared to their behaviour for the Fermi level in the middle of the band gap. This corresponds to the p-type semiconductor behaviour. Contrary, when the Fermi energy evolves towards the conduction band minimum, defects tend to be in surplus of electrons. This corresponds to the n-type semiconductor behaviour.

The formation of point defects is essential for the migration process since point defects assist the atomic migration. Moreover, the formation energies are combined to the migration energies for the description of atomic diffusion in the materials. Atomic migration and diffusion are presented in the next section.

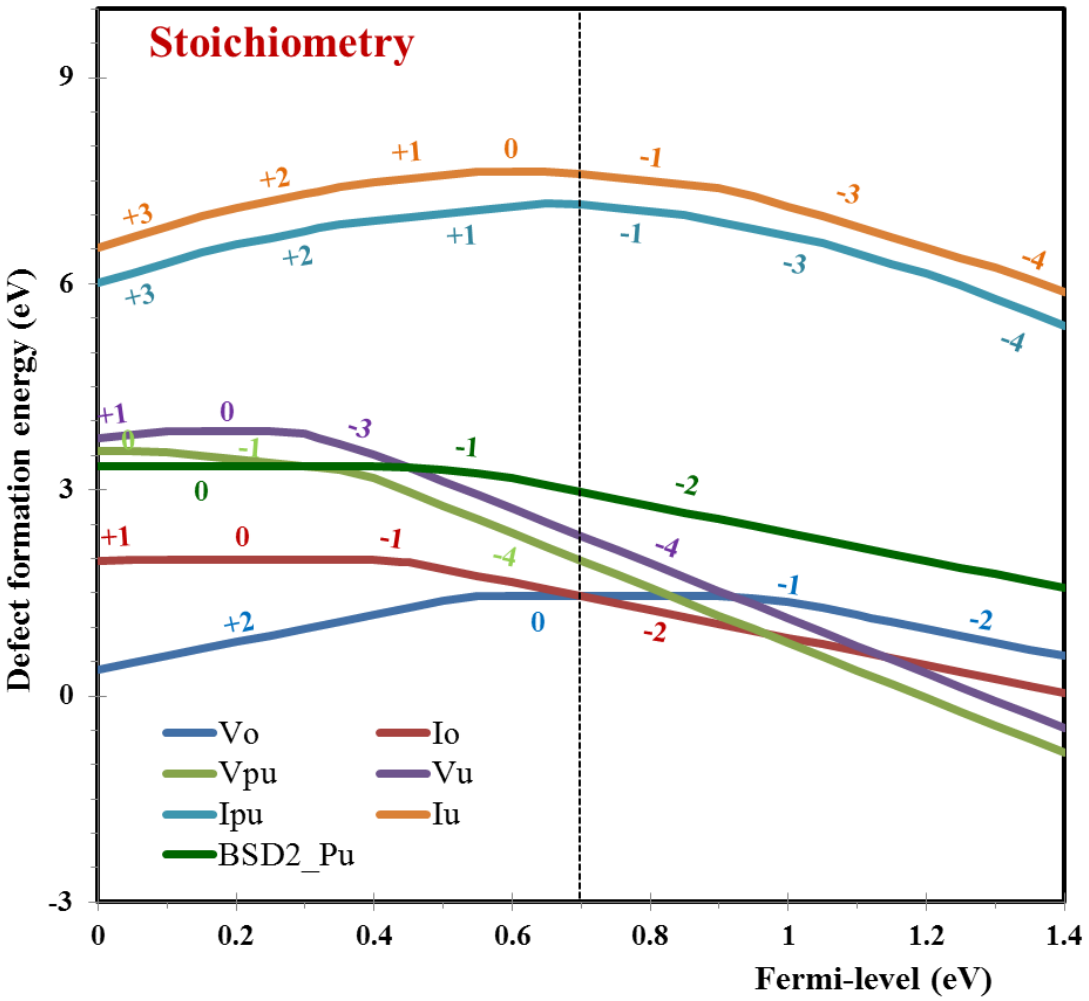

Figure 64 : Stability of defects and their charge states as a function of the Fermi level. The formation energies are calculated in the stoichiometric condition, for the Fermi level in the entire band gap of $U_{0.75}Pu_{0.25}O_2$.

4.4 Migration of point defects in $(U,Pu)O_2$

The migration of atomic species defines the elementary mechanisms in atomic diffusion processes in materials. It corresponds to the elementary jumps of an atom from one site to another site of the crystal lattice. The jumping frequency of an atom, which defines the probability for this atom to hop from its site to another site in the lattice is linked to the migration barrier as follows:

$$\nu = \nu_0 \exp(-\frac{E_m}{K_B T}) \qquad (138)$$

where ν_0 is a prefactor and E_m the migration barrier.

The atomic migration is assisted by defects and the jump of an atom can be assimilated to that of the defect which assists the migration. For each defect, the optimal migration path corresponds to the lowest migration barrier.

The complete atomic diffusion is described by the diffusion coefficient, which takes into account both the concentration of the defect assisting the diffusion and its probability to jump from one site to another. The diffusion coefficient can be written as follows:

$$D = D_0 \exp(-\frac{E_a}{K_B T}) \qquad (139)$$

where D_0 is the prefactor which accounts for all vibrational and entropic terms. E_a is the activation energy of the diffusion. The activation energy of the diffusion is thus a key transport property which is crucial for nuclear fuels, especially in our case for $(U,Pu)O_2$ MOX fuel since atomic diffusion governs the microstructural restructuring under operation. The simplest estimate of E_a is the some of the formation and the migration energies of the defect which assists the diffusion.

In the present Section, we present our results on the migration of oxygen and actinide cations, calculated using the Nudged Elastic Band method (NEB), in stoichiometric $(U,Pu)O_2$ assisted by defects under neutral and formal charge states. The migration barriers are also combined to the formation energies as calculated in the previous section, for the determination of the activation energies of the diffusion. Then, diffusion mechanisms are determined for each species of $(U,Pu)O_2$. The effects of charge state, Pu content and deviations from stoichiometry on the atomic diffusion in $(U,Pu)O_2$ are also discussed.

4.4.1 Oxygen migration: mechanisms involved

We have investigated two different diffusion mechanisms for oxygen, namely the vacancy and interstitial mechanisms. For each mechanism, neutral and formal charge state of vacancies and interstitials are considered.

Figure 65 shows the migration barrier of neutral oxygen vacancy (V_O^X, blue curve) and formally charged oxygen vacancy (V_O^{2+}, red curve) in the <100> direction. Only the <100> direction is considered for the O vacancy mechanism since it corresponds to the migration between nearest neighbour O sites and it was already shown for UO_2 that it is the most favourable O vacancy mechanism [287].

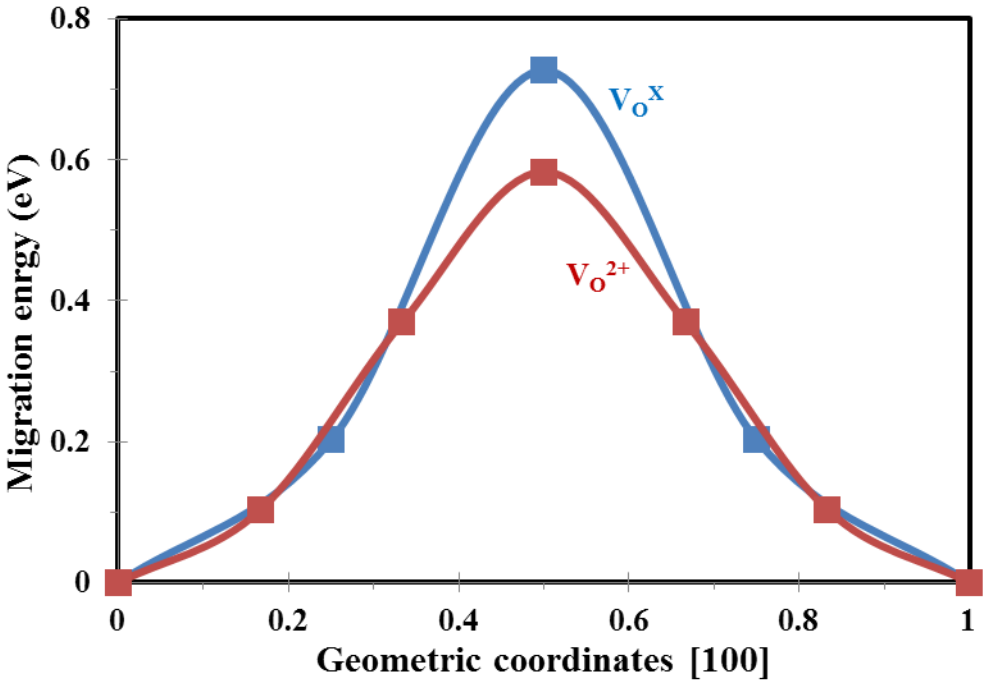

Figure 65 : Migration barrier of neutral (blue) and formal charge +2 (red) oxygen vacancies in $U_{0.75}Pu_{0.25}O_2$. The migration direction is <100>.

Our calculations highlight that the formally charged oxygen vacancies migrate easier than the neutral ones. The migration barriers obtained for the neutral and the formally charged oxygen vacancy are 0.73 eV and 0.58 eV, respectively. These values are similar to the value of 0.67 eV obtained for the neutral vacancy in UO_2 by Dorado *et al.* [287] using GGA+*U* and by Moore *et al.* [128] using DICTRA model.

Figure 66 depicts the migration barriers of neutral (blue curve) and formally charged –2 (red curve) oxygen interstitials through the direct mechanism in the <110> direction (a) and the indirect or interstitialcy mechanism in the <111> direction (b). In the direct mechanism, the oxygen atom in the octahedral interstitial position jumps directly to the nearest empty octahedral interstitial position. In the indirect mechanism, the oxygen in the interstitial position moves to replace a nearest oxygen atom of the lattice, which in turn is pushed to the nearest octahedral interstitial site.

The migration barriers obtained for both mechanisms in $U_{0.75}Pu_{0.25}O_2$ show that, in the direct mechanism, the neutral oxygen interstitials migrate more favourably than the formally charged ones. On the contrary, in the indirect mechanism, the migration of the formally charged oxygen interstitials is favoured. The phenomena behind these different behaviours are linked to the fact that the U^{5+} cations induced by neutral oxygen interstitial are smaller than U^{4+} and also slightly increase the cation-oxygen electrostatic interaction in the lattice, even at relatively high coordination shell of U^{5+}. Therefore, it is more difficult in the case of neutral interstitial to push the oxygen atom from its lattice position in the interstitialcy mechanism, compared to the formally charged interstitial where only U^{4+} are found. This favours the migration of formal

charge defect. For the direct mechanism, the presence of U^{5+} may be favourable to the local distortion in the oxygen sublattice along the migration path. This favours the migration of neutral defect.

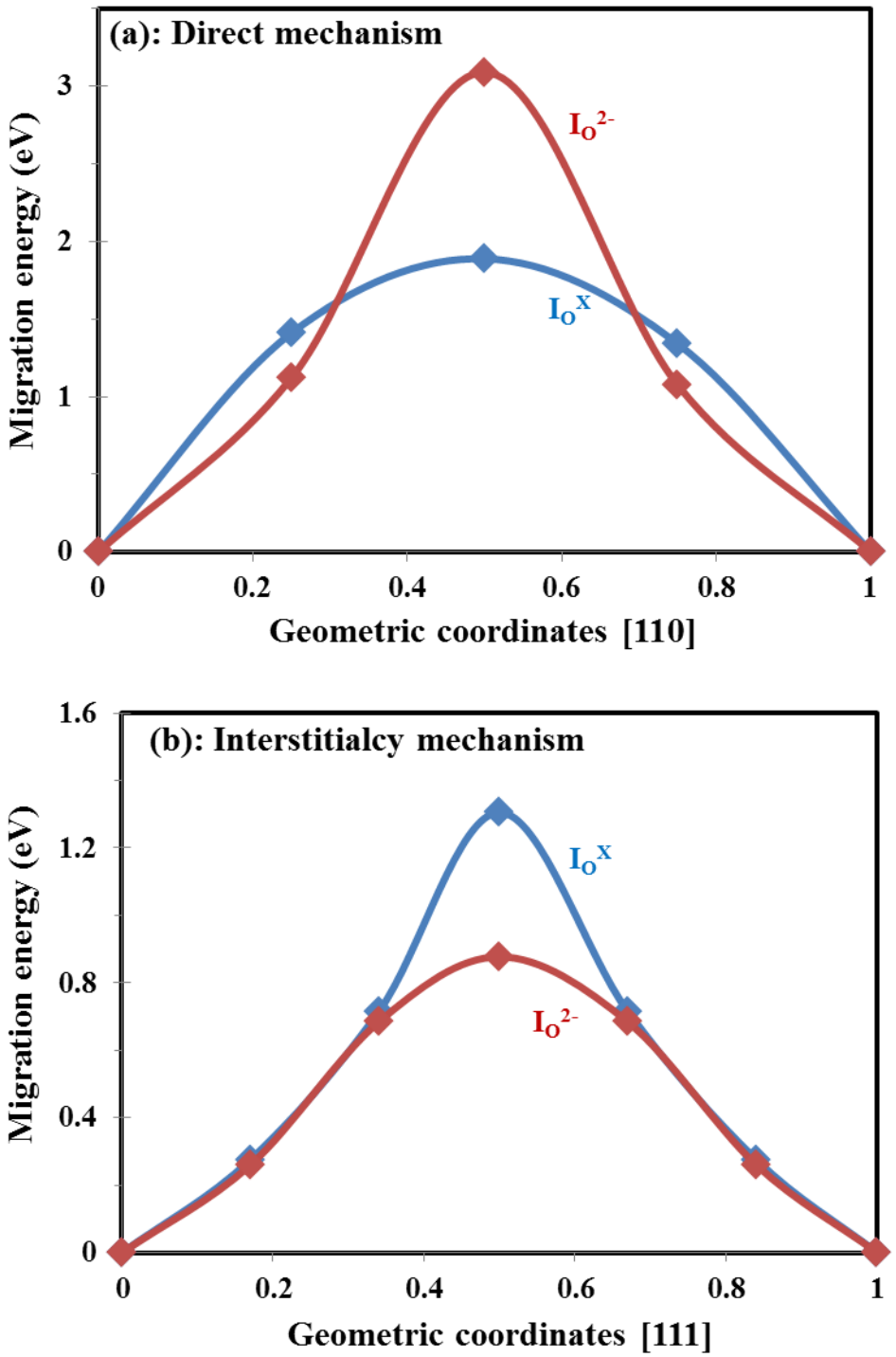

Figure 66 : Migration barrier of neutral (blue) and formal charge -2 (red) oxygen interstitials in $U_{0.75}Pu_{0.25}O_2$. The migration follows (a) direct mechanism (interstitial-interstitial) along the <110> direction and (b) indirect mechanism (interstitial-lattice-interstitial) along the <111> direction.

The migration barriers are lower for the indirect mechanism than for direct mechanism. This means that in $(U,Pu)O_2$, the migration of oxygen interstitials follows the indirect (or interstitialcy) mechanism. This mechanism is the same one as the one obtained for oxygen interstitials in UO_2 by Dorado *et al*. [287].

The activation energies of diffusion for both vacancy and interstitials diffusion mechanisms are shown in Table 30 at the stoichiometric condition.

Mechanisms		E_f (eV)	E_m (eV)	E_a (eV)	Litterature E_a (eV)
V_O	Neutral	1.45	0.73	2.18	**2.6** by Matzke [123], UO_2
	Formal charge	1.78	0.58	2.36	
Direct I_O	Neutral	1.98	1.89	3.87	**3.32** by Dorado [11], UO_2
	Formal charge	1.45	3.09	4.54	
Interstitialcy I_O	Neutral	1.98	1.31	3.29	**1.81** by Moore [127], PuO_2
	Formal charge	1.45	0.88	2.33	

Table 30 : Formation energies (E_f), migration energies (E_m) and activation energies of the diffusion (E_a) of stoichiometric $U_{0.75}Pu_{0.25}O_2$. Data of activation energies of diffusion of stoichiometric UO_2 and PuO_2 are shown for comparison.

It appears that the neutral oxygen vacancies possess the lowest activation energies of diffusion of 2.18 eV. This means that the diffusion of oxygen in the stoichiometric $(U,Pu)O_2$ is vacancy assisted. This result agrees with the experimental assumption of Vauchy *et al*. [181] and the DICTRA modelling of Moore *et al*. [127].

Our activation energy of diffusion of oxygen is comprised between the experimental measurement by Matzke [123] on UO_2 and the DICTRA value by Moore *et al*. [127] on PuO_2. This agreement supports the accuracy of our results on both the definition of the stoichiometry for the defect formation energies and the calculations of the migration barriers.

Few experimental studies on the activation energies of diffusion of oxygen in non-stoichiometric $(U,Pu)O_2$ are available in the literature (see Chapter 1, Table 15). These studies show much lower values compared to our values. These differences are justified since our results only correspond to the stoichiometry condition. If we assume that the migration energy of oxygen ions is constant in the stable domain of the fluorite phase of $(U,Pu)O_{2\pm x}$, considering the variation of the formation energy of neutral oxygen vacancies and the formally charged interstitials, the activation energy of diffusion of oxygen will vary as in Figure 67 below. Within this hypostesis on the migration energy,

we obtain that the diffusion of oxygen atoms in $(U,Pu)O_2$ is vacancy assisted under hypo-stoichiometry and stoichiometry conditions. Under hyper-stoichiometry condition, the interstitialcy mechanism governs the diffusion of oxygen atoms in $(U,Pu)O_2$.

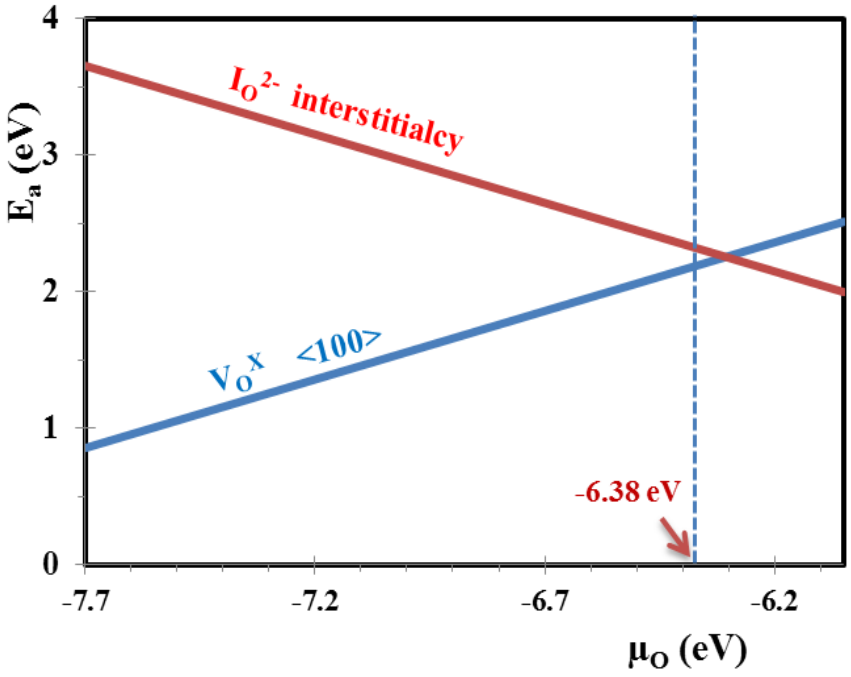

Figure 67 : Activation energies of diffusion of oxygen in $(U,Pu)O_2$ as a function of the oxygen chemical potential, for the vacancy and the indirect interstitial mechanisms. The dashed line at -6.38 eV correspond to the stoichiometry condition.

4.4.2 Uranium and plutonium migration: mechanisms involved

The migration of uranium and plutonium vacancies and interstitials in $(U,Pu)O_2$ is investigated in this section. The neutral and formally charged states of both defects are considered. The effect of Pu content is only considered for the neutral uranium vacancies and the neutral plutonium interstitials.

Figure 68 presents the migration barriers of neutral (blue curve) and formally charged -4 (red curve) uranium vacancies (a) and plutonium vacancies (b) in $U_{0.75}Pu_{0.25}O_2$ under stoichiometric condition. In all cases, the migration barriers of neutral actinide vacancies in the <110> direction are lower than those of formally charged ones. This means that at the stoichiometric conditions, the neutral actinide vacancies migrate easier than the formally charged ones. Indeed, as mentioned in Section 4.2.4, the neutral actinide vacancies are surrounded by U^{5+} cations which are smaller, and then offer more free space in the migration path, than U^{4+} in the case of the formally charged vacancies. This explains the lower migration barriers for the neutral actinide vacancies compared to the formally charged ones. On the other hand, the migration barriers of neutral uranium and plutonium vacancies are similar, with values of 4.71 eV and 4.90 eV, respectively. These values are smaller compared to those of 5.5 eV and 5.8 eV obtained in UO_2 by Dorado *et al.* [288] using both GGA+*U* and LDA+*U* respectively.

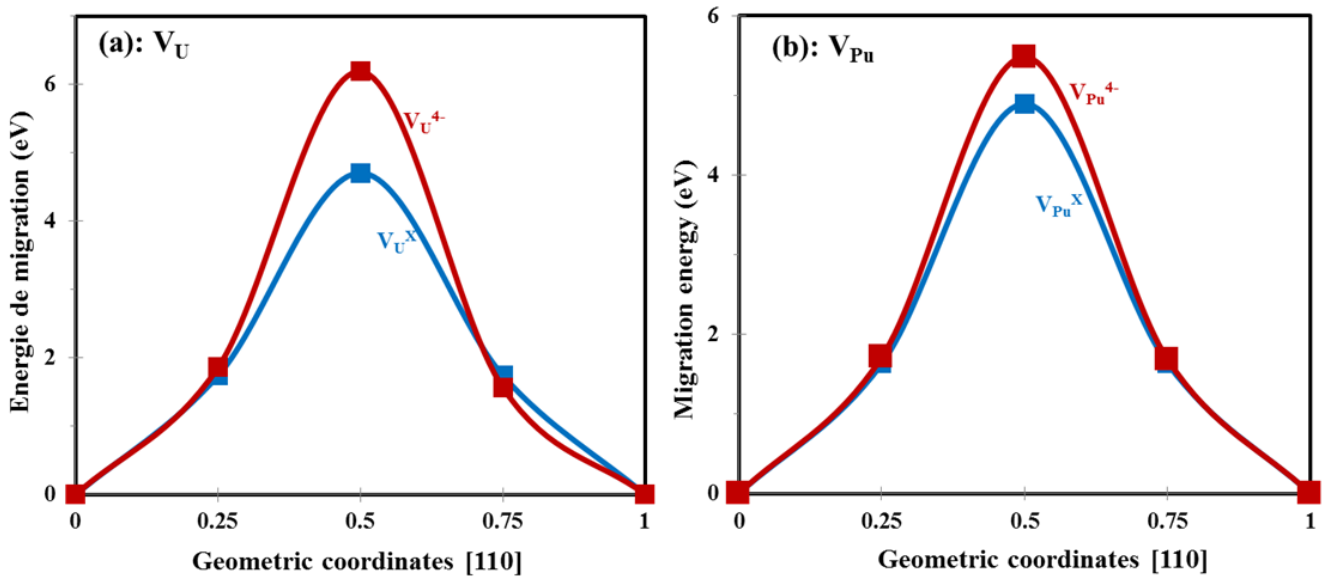

Figure 68 : Migration barrier of (a) uranium and (b) plutonium vacancies in $U_{0.75}Pu_{0.25}O_2$. The migration barriers of neutral vacancies are in blue and the formal charge vacancies are in red.

The effect of plutonium content on the migration barrier of neutral uranium vacancies is shown in Figure 69. The difference in migration barriers for 25 % Pu (blue curve) and

50 % Pu (green curve) is of about 0.2 eV, which is very small compared to the large energies involved.

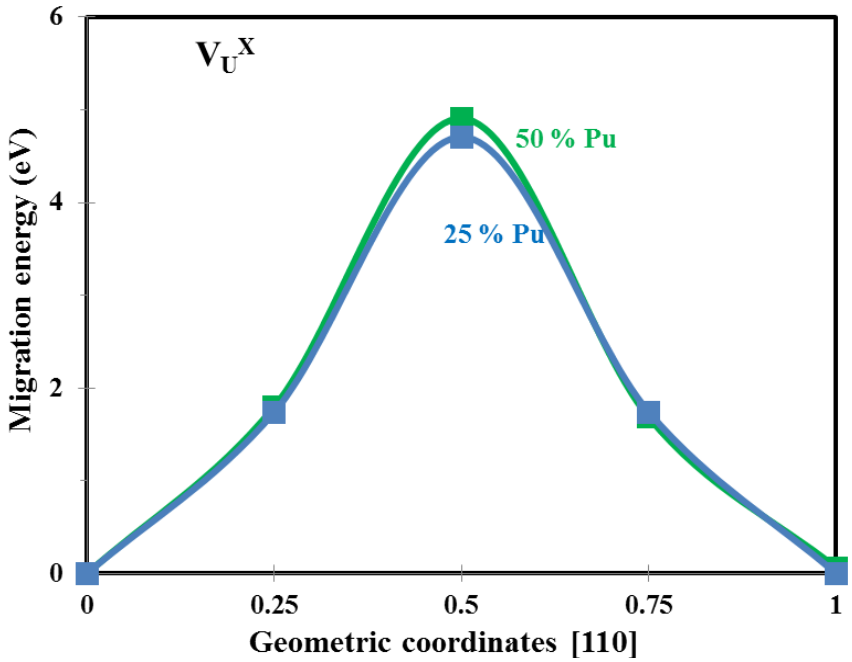

Figure 69 : Migration barrier of neutral uranium vacancies for Pu contents of 25 % (blue) and 50 % (green).

This result highlights the negligible impact of Pu content on the migration of actinide vacancies in the stoichiometric $(U,Pu)O_2$. The slight increase in migration barrier might be due to the increase in the number of Pu cation in the local environment of the migrating defect at 50 % Pu.

Figure 70 (a) depicts the migration barriers of neutral and charged uranium interstitials in the stoichiometric $U_{0.5}Pu_{0.5}O_2$. In Figure 70 (b), the migration barriers of neutral plutonium interstitials are given for plutonium contents of 50 % (green curve) and 31 % (blue curve).

First of all, the migration barrier of neutral uranium interstitials is slightly lower than that of the formally charged I_U. The energy difference is less than 0.3 eV. On the other hand, the migration barriers of neutral Pu interstitials for 31 % Pu and 50 % Pu differ by 0.1 eV. This difference is negligible compared to the high energies involved. It can be reasonably assumed that the Pu content has no impact on the migration of plutonium cations. On the other hand, the migration barrier of neutral plutonium interstitials is lower than that of neutral uranium interstitials. This means that plutonium interstitials migrate easier in the stoichiometric $(U,Pu)O_2$ than uranium interstitials.

In order to determine the actinide diffusion mechanism, the activation energies of diffusion of actinide cations are given for each defect in Table 31.

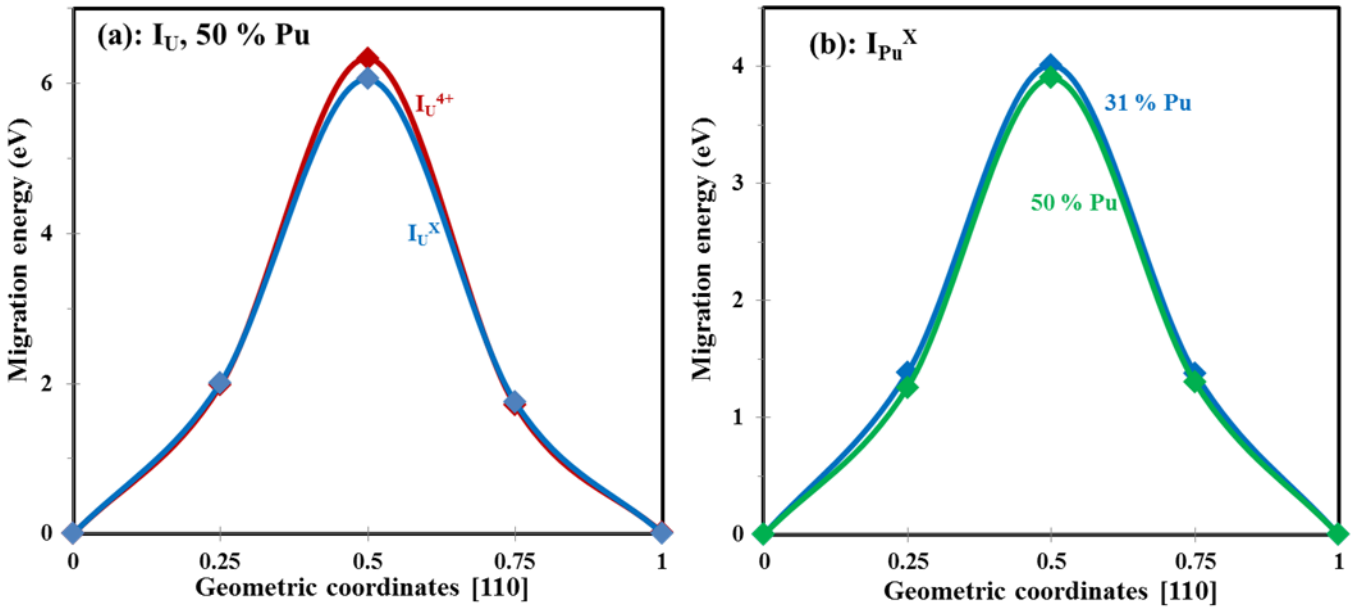

Figure 70 : Migration barrier of (a) neutral and formal charge uranium interstitials for 50 % Pu and (b) neutral plutonium interstitials for two Pu contents.

The activation energies of diffusion of actinide vacancies are lower than those of actinide interstitials. This means that the migration of actinides cations in the stoichiometric $(U,Pu)O_2$ is vacancy assisted. This result agrees with other theoretical studies by Dorado *et al*. [288] on U migration in UO_2. Besides, the activation energy of diffusion of plutonium vacancies under formal charge state is lower than those of neutral and charged uranium vacancies. The difference is around 1.0 eV, which is significant.

Therefore, the diffusion of formally charged plutonium cation is easier than that of uranium in stoichiometric $(U,Pu)O_2$. The activation energy of diffusion is of the same order of magnitude for the neutral V_{Pu} and neutral V_U as for the charged V_U.

Experimental and theoretical data on actinide diffusion in $(U,Pu)O_2$ are scarce and scattered. The diffusion of Pu in $(U,Pu)O_{2-x}$ was measured experimentally but Matzke [123] reports numerous uncertainties [123]. Owing to that, we compare our results to the calculated uranium diffusion properties of UO_2. Our value of 8.52 eV for the diffusion of U cations in $(U,Pu)O_2$ is higher than that of 5.3 eV obtained by Moore *et al*. [128] on UO_2 using the DICTRA model, as well as the values obtained by Dorado *et al*. [288]ranging from 3.4 eV to 6.4 eV using LDA+*U* on UO_2. As the formation energies of actinide vacancies decrease from the stoichiometry to the hyper-stoichiometry, the activation energies of diffusion of actinides follow the same trend. This tendency agrees with the DICTRA results of Moore *et al*. [128] on UO_2. In their study, a decrease by 2 eV of the activation energy of diffusion of uranium from the stoichiometry to O/U = 2.20 were pointed out. A similar tendency was also seen by Dorado *et al*. [288] using LDA+*U*.

On the other hand, experimental data on the diffusion of uranium in UO_2 are scattered as mentioned by the review of Matzke [123]. It is therefore difficult to make a consistent comparison of our results with experiments. Beyond the uncertainties on the experimental diffusion data of UO_2, the results might highlight the lower actinide diffusion in $(U,Pu)O_2$ compared to UO_2.

Mechanisms		E_f (eV)	E_m (eV)	E_a (eV)	Litterature E_a (eV)
V_U	Neutral	3.86	4.71	8.57	5.3 by Moore [128], UO_2
	Formal charge	2.33	6.19	8.52	
V_{Pu}	Neutral	3.57	4.90	8.47	
	Formal charge	1.97	5.48	7.45	
I_U	Neutral	7.63	6.06	13.69	
	Formal charge	10.02	6.34	16.36	
I_{Pu}	Neutral	7.19	4.01	11.20	
	Formal charge	8.20	--	--	

Table 31 : Activation energies of diffusion of actinide cations in stoichiometric $U_{0.75}Pu_{0.25}O_2$. Various diffusion mechanisms are analysed for both neutral and formal charge state of each cation.

Our results also confirm that the diffusion of oxygen atoms is largely more favourable than that of actinide atoms in $(U,Pu)O_2$, by a factor of around 4 on the activation energy of diffusion. This tendency is in line with experimental conclusions by Matzke [123] on the diffusion coefficients.

4.5 Conclusion

The electronic and structural modifications induced by point defects as well as the formation and migration energies of point defects in PuO_2 and $(U,Pu)O_2$ were presented in this chapter. Electron-donor and electron-acceptor defects yield different defect electronic states in the band gap of PuO_2 and $(U,Pu)O_2$. Furthermore, point defects induce various structural modifications shown in this chapter in terms of atomic

displacements. The formation energies of point defects under various charge states were investigated in the entire oxygen chemical potential range in PuO_2 and $(U,Pu)O_2$. We found that the hypo-stoichiometry is accommodated by oxygen vacancies while the hyper-stoichiometry is accommodated by oxygen interstitials both in PuO_2 and $(U,Pu)O_2$. The stable oxidation states of cations were also discussed, highlighting differences for $(U,Pu)O_2$, UO_2 and PuO_2. Next, the migration properties were investigated for both oxygen and actinides point defects. This study was combined to the one on the defect formation for the complete investigation of the atomic self-diffusion in the $(U,Pu)O_2$ MOX fuel. The oxygen diffusion through vacancy mechanism in the hypo-stoichiometry and through interstitialcy mechanism in the hyper-stoichiometry was highlighted. The results presented here are of first concern for higher scale modelling techniques. On the one hand, the results on the structural modifications as well as defect formation energies are crucial as reference values for the development of interatomic empirical potentials or numerical potentials for the study of charged defects in $(U,Pu)O_2$. On the other hand, the results on the atomic migration and diffusion will be used as database for thermokinetic models, especially the CALPHAD/DICTRA model, for the calculation of the atomic self-diffusion coefficients of the uranium-plutonium mixed oxide fuels. As perspectives, the influence of defect clusters on the atomic transport properties would be an important step in order to complete our conclusion on the diffusion mechanisms of various species. This kind of studies cannot be currently treated using DFT calculations, but might be possible soon regarding the rapid development of computational resources. It is however planned to be conducted at the CEA-SESC/LM2C laboratory using interatomic empirical potentials calculations which are simpler and less computationally demanding compared to the DFT method. Our studies could also be extended to a more detailed analysis of the chemical environments (considering the second and third coordination shell of defect for instance) in the defect formation and migration properties. This will also require a larger supercell and then a faster calculation method such as interatomic empirical potential calculations. Finally, the effect of americium on the atomic transport properties can also be analysed following our study [281]. Indeed, americium is always found with a non-negligible amount in the fast breeder reactors MOX fuel. The study of its effects on the formation and migration of atomic species is therefore required.

Chapter 5: Defect stability and migration in $(U,Ce)O_2$, comparison to $(U,Pu)O_2$

5.1 Introduction

Cerium is commonly used as a surrogate for plutonium for experimental studies of $(U,Pu)O_2$ MOX fuel [275]. This choice is motivated by the combination of safety in using Ce instead of Pu, and the similarities between various properties of these elements. Indeed, on the one hand, Ce has no radiotoxicity issue compared to Pu. This results in the simpler experimental handling of $(U,Ce)O_2$ compared to $(U,Pu)O_2$. On the other hand, the atomic radius of Ce and its chemical properties related to its *4f* electrons are very close to those of Pu. The phase diagrams of the Ce-O and Pu-O systems are also very close to each other [254, 289, 290]. Moreover, UO_2 and CeO_2 are known to form a $(U,Ce)O_2$ solid solution [275, 291, 292]. The above similarities listed do not consider the behaviour of $(U,Ce)O_2$ under irradiation. Indeed, the in-reactor behaviour of fuels is highly impacted by the irradiations which generate an important number and variety of damage in the material. It is therefore important to analyse the irradiation damage properties in $(U,Ce)O_2$ in order to confirm the adequacy of the experimental use of this material as surrogate of $(U,Pu)O_2$ MOX fuels. Previous studies on bulk and defect properties in CeO_2 and $(U,Ce)O_2$ have been conducted at the CEA-SESC/LM2C by Shi [122], using LDA+*U*. These studies revealed a higher lattice constant, a lower mixing enthalpies and a lower formation energy of oxygen vacancy for $(U,Ce)O_2$ compared to $(U,Pu)O_2$.

In the present chapter, we investigate various point defect properties in $(U,Ce)O_2$ as well as their impact on the structural and electronic properties of the material. Careful comparison is made with the results on $(U,Pu)O_2$ presented in Chapter 4. In the first part of this chapter, the electronic modifications and lattice distortions induced by various point defects in $(U,Ce)O_2$ are investigated. In the second part, defect formation energies are determined under various defect charge states, and in the entire oxygen chemical potential range. The effect of the chemical environment is also highlighted.

5.2 Defect structure in $(U,Ce)O_2$: comparison to $(U,Pu)O_2$

5.2.1 Electronic and structural modifications induced by oxygen vacancy in $(U,Ce)O_2$

The presence of a neutral oxygen vacancy in $(U,Ce)O_2$ induces the reduction of two cerium Ce^{4+} cations into Ce^{3+} located in the nearest coordination shell of the vacancy. In that case, cerium cations play the same role as Pu cations in $(U,Pu)O_2$. Uranium cations are always found under U^{4+} valence states. Figure 71 shows the projected density of states (PDOS) of uranium *5f*, cerium *4f* and oxygen *2p* orbitals. The perfect supercell and the defective ones with the neutral and the formally charged oxygen vacancies are analysed.

Rigorously, the projected electronic density of states of bulk $(U,Ce)O_2$ differs slightly to that of $(U,Pu)O_2$ (see Chapter 3, Figure 40). Indeed, the *4f* orbitals of Ce^{4+} are unoccupied, contrary to $(U,Pu)O_2$ where the plutonium *5f* orbitals are occupied in the valence band. Despite this slight difference, the PDOS of $(U,Ce)O_2$ and $(U,Pu)O_2$ yield the same features. For instance, the valence band maximum (VBM) is constituted of uranium *5f* states, and the conduction band minimum (CBM) constituted of cerium *4f* states. The band gap is thus narrowed as for $(U,Pu)O_2$.

In $(U,Ce)O_2$ containing a neutral oxygen vacancy, a defect state forms at the VBM (see the indication by arrows in Figure 71. b). This defect state superimposes with the VBM and thus cannot be observed distinctly in the band gap, contrary to $(U,Pu)O_2$ where the defect electronic state is clearly located in the band gap. In the PDOS, only one defect state is observed on the Ce^{3+} *4f* states, instead of two. This is also the case for $(U,Pu)O_2$. This means that the two electron polarons Ce^{3+} possess the same configuration. The removal of two electrons in the formally charged oxygen vacancy (V_O^{2+}) cancels the defect state in the band gap leading to the same PDOS as the perfect crystal.

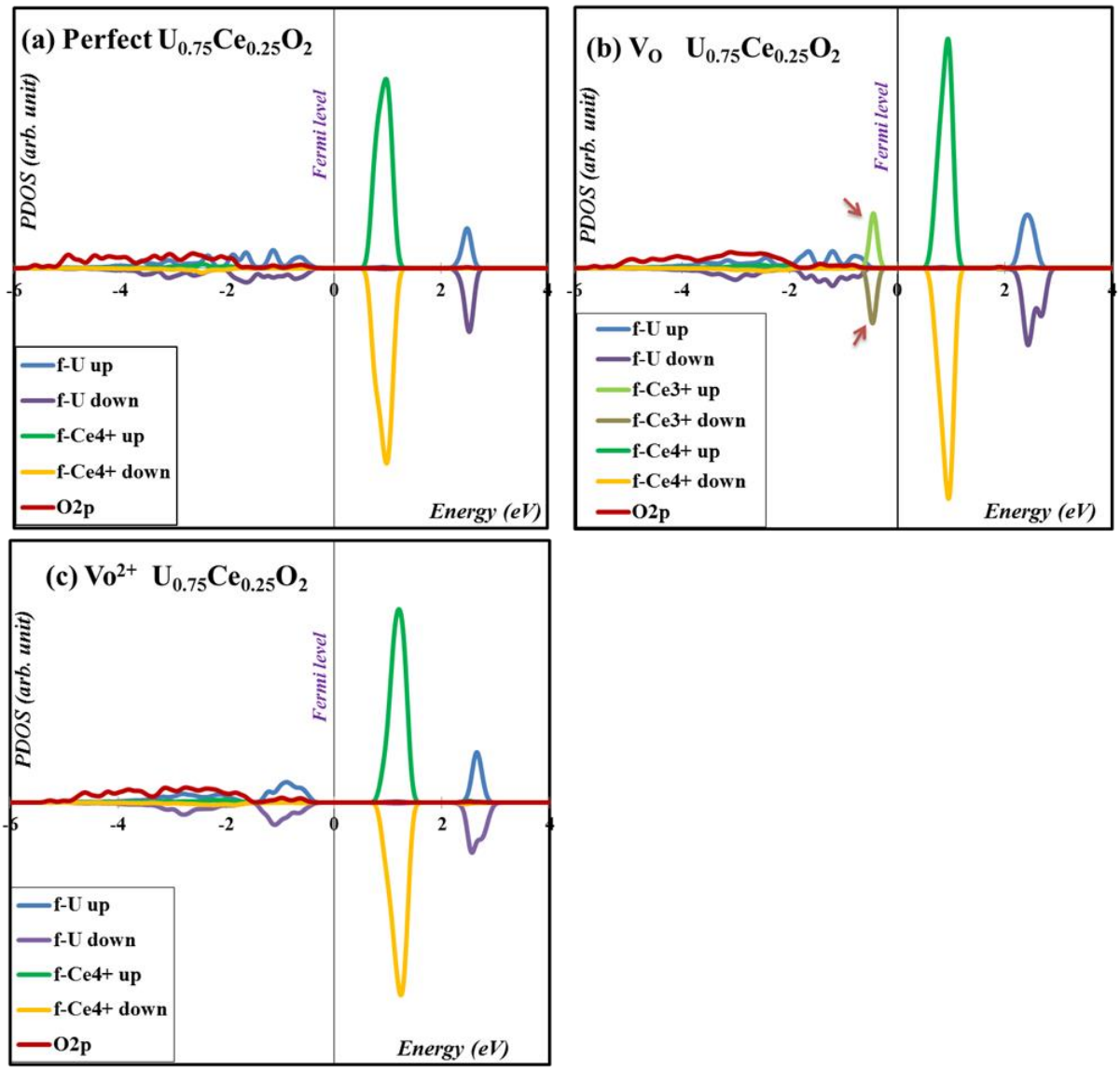

Figure 71 : Projected density of states of (a) perfect $U_{0.75}Ce_{0.25}O_2$ and $U_{0.75}Ce_{0.25}O_2$ containing (b) a neutral oxygen vacancy and (b) a formally charged 2+ oxygen vacancy.

Table 32 presents the lattice distortions induced by a neutral and a formally charged oxygen vacancy (V_O^{2+}) in $(U,Ce)O_2$. The distortions are analysed in terms of atomic displacements in the oxygen sublattice. Comparison is made with the previous results on $(U,Pu)O_2$.

Compound	Defect	Displacements δ (Å)	Displacement direction (Δ)	Number of oxygen displaced
$U_{0.75}Ce_{0.25}O_2$	V_O	-0.11	<100>	6
	V_O^{2+}	-0.20	<100>	6
	Ce^{3+}	+0.09	<111>	8
Lattice expansion	V_O	a (MO_{2-x}) = a (MO_2) + 0.40 x (in Å)		
$U_{0.75}Pu_{0.25}O_2$	V_O	-0.15	<100>	6
	V_O^{2+}	-0.22	<100>]	6
	Pu^{3+}	+0.07	<111>	8
Lattice expansion	V_O	a (MO_{2-x}) = a (MO_2) + **0.29** x (in Å)		

Table 32 : Atomic displacements induced by a neutral and a formally charged oxygen vacancy in the oxygen sublattice of $(U,Ce)O_2$. Results are compared to those of $(U,Pu)O_2$ (in red).

The displacements shown here for a neutral oxygen vacancy correspond to the chemical environment with at least two cerium cations in the first coordination shell. The sign minus means that oxygen atoms come closer to the defect while the sign plus means that oxygen atoms are pushed away from the defect. The neutral oxygen vacancy induces less displacement compared to the formally charged one. This is due to the same phenomena explained for $(U,Pu)O_2$ in Chapter 4, namely the elastic interaction of the defect and the oxygen sublattice and the smaller electrostatic attraction of O^{2-} by Ce^{3+} localized near the vacancy, compared to Ce^{4+}. The removal of two electrons from the supercell cancels the formation of Ce^{3+} cations and thus increases electrostatic attractions. As a result, the formally charged oxygen vacancy induces a more important distortion. In general, the distortions observed are in the same order of magnitude as in $(U,Pu)O_2$. On the other hand, when Ce^{3+} is not in the first coordination shell of the vacancy, a lattice distortion is observed around the Ce^{3+} cation. This distortion is slightly larger than that around Pu^{3+} in $(U,Pu)O_2$.

The presence of an oxygen vacancy also results in a lattice expansion. The calculation of the slope of the lattice constant as a function of the deviation from stoichiometry gives the value of 0.40. This value is larger than that of $(U,Pu)O_2$ (0.29). Thus, the oxygen vacancy induces a more important increase of the interatomic distances of the first neighbouring cations in $(U,Ce)O_2$ than $(U,Pu)O_2$.

In summary, oxygen vacancy leads to different electronic modifications in $(U,Ce)O_2$ and $(U,Pu)O_2$ and yield the same qualitative lattice distortions. However, the amplitudes of

the distortions are different. The lattice expansion with the deviation from stoichiometry is also more important in $(U,Ce)O_2$, suggesting that this compound is more sensitive to elastic distortion than $(U,Pu)O_2$.

5.2.2 Electronic and structural modifications induced by oxygen interstitials in $(U,Ce)O_2$

The presence of a neutral oxygen interstitial in the $(U,Ce)O_2$ lattice leads to the oxidation of two uranium U^{4+} cations into U^{5+}. The U^{5+} are localized in the second cation coordination shell, similarly as in $(U,Pu)O_2$.

The analyses of the projected electronic density of states in Figure 72 (b) show the same behaviour of the neutral oxygen interstitial than that observed in $(U,Pu)O_2$. Indeed, unoccupied defect states appear in the *5f* orbitals of uranium cations (indicated by arrows in Figure 72 (b)). These defect states are above the unoccupied *4f* states of cerium cations which constitute the CBM. There are therefore no defect states in the band gap. The formally charged -2 oxygen interstitial in Figure 72 (c) induces an occupied defect state (indicated by green arrow) in the band gap. Our calculations show that when two electrons are added to the neutral oxygen interstitial, all the U^{5+} are not reduced back into U^{4+}. One electron is captured by Ce^{4+} which is reduced into Ce^{3+}. This Ce^{3+} introduces an occupied state in the band gap. This behaviour is probably due to the pre-existing hole polaron trap distortions around the oxidized U cation. The compensation of this trap distortion might be less energetically favourable than the formation of electron polaron in Ce^{3+}. The role of pre-existing hole polaron trap distortion is in line with the procedure aiming at localizing a hole polaron on a chosen atom, as pointed out by Geneste *et al*. [293]. This marks a significant difference with the perfect crystal where there is no hole polaron trap distortions and all cations keep the +4 charge state. The simultaneous formation of U^{5+} and Ce^{3+} indicates that Ce cations yield more reducing character than Pu cations. This behaviour shows a significant difference between $(U,Ce)O_2$ and $(U,Pu)O_2$.

Table 33 presents the atomic displacements induced by the formation of a neutral and formally charge -2 oxygen interstitial in $(U,Ce)O_2$.

Both the neutral and formally charged oxygen interstitial yield similar atomic displacements in the oxygen sublattice. Eight oxygen atoms in the first coordination shell of the defect are pushed away from it by +0.16 Å. This elastic distortion around the oxygen interstitial is similar to the one observed in $(U,Pu)O_2$ and have the same origin.

In the actinide sublattice, the bonding length of cations surrounding the oxygen interstitial decreases from 5.50 Å for the perfect crystal to 5.33 Å, resulting in the decrease in the lattice constant. The expression of lattice constant as a function of the

deviation from stoichiometry, using the Equation (137) proposed by Teske *et al.* [282], shows similar contraction compared to $(U,Pu)O_2$.

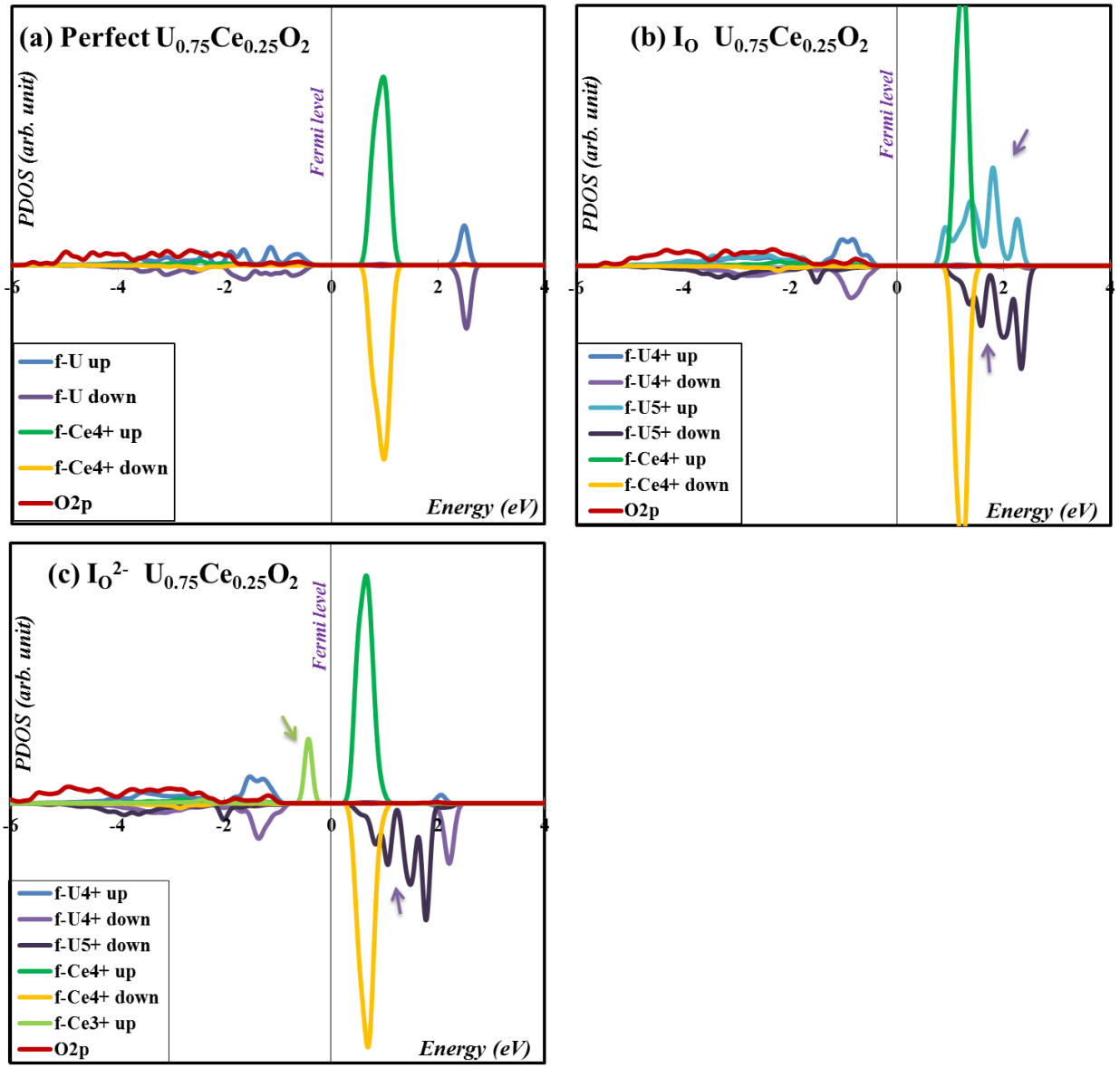

Figure 72 : Projected density of states of (a) perfect $U_{0.75}Ce_{0.25}O_2$ and $U_{0.75}Ce_{0.25}O_2$ containing (b) a neutral oxygen interstitial and (b) a formally charged -2 oxygen interstitial.

Finally, $(U,Ce)O_2$ and $(U,Pu)O_2$ yield slightly different electronic modifications in the presence of a neutral or formally charged oxygen interstitials. The most significant one is the valence of the cations in presence of a charged oxygen interstitial. On the other hand, the lattice distortion as well as the lattice contraction induced by oxygen interstitials are similar in both $(U,Ce)O_2$ and $(U,Pu)O_2$.

Compound	Defect	Displacements δ (Å)	Displacement direction (Δ)	Number of oxygen displaced
$U_{0.75}Ce_{0.25}O_2$	I_O	+0.16	<111>	8
	I_O^{2-}	+0.16	<111>	8
Lattice constant	I_O	a (MO_{2+x}) = a (MO_2) - **0.1331** x (in Å)		
$U_{0.75}Pu_{0.25}O_2$	I_O	+0.16	<111>	8
	I_O^{2+}	+0.16	<111>	8
Lattice constant	I_O	a (MO_{2+x}) = a (MO_2) - **0.1369** x (in Å)		

Table 33 : Atomic displacements induced by a neutral and a formally charged oxygen interstitial in the oxygen sublattice of $(U,Ce)O_2$. Results are compared to those of $(U,Pu)O_2$ (in red).

5.2.3 Electronic and structural modifications induced by uranium and cerium vacancies

The uranium and cerium vacancies are four-electron acceptors. Their formation leads to the loss of electrons on four uranium cations in the first cation coordination shell of the cation vacancy. As a result, these four uranium cations have a valence U^{5+}. The modifications induced by cation vacancies in the electronic density of states are similar to those induced by oxygen interstitials, for both neutral and formally charged cation vacancies (see Figure 72). These modifications are thus different from those in $(U,Pu)O_2$.

The cation vacancies induce lattice distortions, especially in the oxygen sublattice. Table 34 shows atomic displacement, the direction of the displacements and the number of oxygen displaced by the neutral and formally charged cation vacancies.

The formation of cation vacancies results in the displacement of eight neighbouring oxygen ions in the first coordination shell. The sign plus means that the oxygen atoms are pushed away from the defect. The oxygen displacements are almost identical for the neutral and formally charged defects. This is due to the fact that for both defects, the same phenomenon comes into play, namely the loss of the electrostatic attraction between the eight oxygen ions and the U^{4+} vacant cation. As the four U^{5+} are farther from the defect compared to the oxygen atoms displaced, they do not participate to the lattice distortion. The lattice distortions are similar in $(U,Ce)O_2$ and $(U,Pu)O_2$.

It therefore appears that the electronic modifications induced by cations vacancies in the electronic density of states are different between $(U,Ce)O_2$ and $(U,Pu)O_2$. On the other hand, the two compounds yield similar lattice distortions in the presence of cation vacancies.

Compound	Defect	Displacements δ (Å)	Displacement direction (Δ)	Number of oxygen displaced
$U_{0.75}Ce_{0.25}O_2$	V_U	+0.24	<111>	8
	V_U^{4-}	+0.24	<111>	8
	V_{Ce}	+0.21	<111>	8
	V_{Ce}^{4-}	+0.21	<111>	8
$U_{0.75}Pu_{0.25}O_2$	V_U	+0.24	<111>	8
	V_U^{4-}	+0.24	<111>	8
	V_{Pu}	+0.24	<111>	8
	V_{Pu}^{4-}	+0.24	<111>	8

Table 34 : Atomic displacements induced by neutral and formally charged uranium and cerium vacancies in the oxygen sublattice of $(U,Ce)O_2$. Results are compared to those of $(U,Pu)O_2$ (in red).

5.2.4 Electronic and structural modifications induced by uranium and cerium interstitials

Neutral uranium and cerium interstitials are electron donors. Their formation leads to the excess of 4 electrons which localize on cerium Ce^{4+} cations, which reduce into Ce^{3+}, in the first cation coordination shell. The modifications induced by cation interstitials in the electronic density of states are similar to those induced by oxygen vacancies, for both neutral and formally charged cation interstitials (see Figure 71). The defect energy state in the band gap is thus lower than that obtained for $(U,Pu)O_2$. Neutral cerium interstitials are under Ce^{3+} valence state while the formally charged ones are under Ce^{4+} valence state. Uranium interstitials are always under U^{4+} valence state, as in $(U,Pu)O_2$.

The lattice distortions induced by cation interstitials are presented in Table 35 in terms of atomic displacements in the actinide sublattice.

For both Ce and U interstitials, six nearest cations are pushed away from the defect. Cerium interstitials induce lower lattice distortions than uranium interstitials in $(U,Ce)O_2$, similarly as plutonium interstitials in $(U,Pu)O_2$. Moreover, the formally charged Ce interstitial is more repulsive than the neutral one. This is surprisingly uncorrelated to the expected steric effect which might inverse the tendency, due to the larger ionic radius of Ce^{3+} (107 pm) in the case of neutral interstitial compared to that of Ce^{4+} (94 pm) in the case of the formally charged one. Therefore, the dominant phenomenon is electrostatic repulsion between cations. Indeed, the Ce^{3+} in the neutral Ce interstitial configuration possesses less positive charge than Ce^{4+} in the formally charged Ce interstitial configuration. Thus Ce^{3+} yields lower electrostatic repulsions on the neighbouring cations. Therefore the cation displacements are lower in the neutral defect configuration than the formally charged one. This tendency is qualitatively similar to that observed in $(U,Pu)O_2$ for Pu interstitials.

Compound	Defect	Displacements δ (Å)	Displacement direction (Δ)	Number of oxygen displaced
$U_{0.75}Ce_{0.25}O_2$	I_{Ce}	+0.34	<100>	6
	I_{Ce}^{4+}	+0.37	<100>	6
	I_U	+0.40	<100>	6
	I_U^{4+}	+0.40	<100>	6
$U_{0.75}Pu_{0.25}O_2$	I_{Pu}	+0.27	<100>	6
	I_{Pu}^{4+}	+0.30	<100>	6
	I_U	+0.36	<100>	6
	I_U^{4+}	+0.36	<100>	6

Table 35 : Atomic displacements induced by neutral and formally charged uranium and cerium vacancies in the oxygen sublattice of $(U,Ce)O_2$. Results are compared to those of $(U,Pu)O_2$ (in red).

The atomic displacements are identical for the uranium neutral and formally charged interstitials. This is obviously due to the fact that uranium keeps its U^{4+} valence state at the interstitial position in both cases. The result is qualitatively similar to the one obtained in $(U,Pu)O_2$.

Finally, we can conclude that Ce and Pu cation interstitials yield different electronic modifications in the electronic density of states in $(U,Ce)O_2$ and $(U,Pu)O_2$ respectively. They only yield similar qualitative tendency in the lattice distortion for both materials.

However, looking at the amplitude of the distortions, $(U,Ce)O_2$ is more elastically sensitive to cation interstitials than $(U,Pu)O_2$ since it presents larger lattice distortion.

5.2.5 Electronic and structural modifications induced by uranium and cerium BSD defects

As mentioned for $(U,Pu)O_2$, BSD defects are neither electron donors, nor electron acceptors. Hence their have no impact on the electronic properties of the $(U,Ce)O_2$ mixed oxides.

The lattice distortions induced by BSDs defects in $(U,Ce)O_2$ are summarized in Table 36 in terms of the atomic displacements in the oxygen sublattice. The nature of the distortions is similar to that observed and discussed for $(U,Pu)O_2$ in Chapter 4 Section 4.2.5 in that, oxygen atoms get displaced in two different ways. The oxygen cage around the cation vacancy expands in the <111> direction while the oxygen atoms around the oxygen vacancies of the BSDs are pushed close to these oxygen vacancies.

The major differences between $(U,Ce)O_2$ and $(U,Pu)O_2$ regarding the lattice distortions induced by BSD defects is the amplitude of the distortions which is lower in $(U,Ce)O_2$ by the order of magnitude of 0.1 Å. This difference is significant and can be attributed to the difference in the cohesive energies in both compounds or to the magnitude of the elastic self-interactions between defect images, owing to the finite supercell size as pointed out by Burr *et al.* [294].

Compound	Defect	Displacements δ (Å)	Displacement direction (Δ)	Number of oxygen displaced
$U_{0.75}Ce_{0.25}O_2$	BSD1	+0.20	<111>	6
		-0.15	<100>	6
	BSD2	+0.22	<111>	6
		-0.17	<100>	6
	BSD3	+0.21	<111>	6
		-0.15	<100>	6

Table 36 : Local distortions of oxygen sublattice induced by BSD defects in $(U,Ce)O_2$. The displacements of oxygen ions pushed away from cation vacancies are shown in black and those pushed closer to the oxygen vacancies are shown in red.

5.3 Point defect stability in $(U,Ce)O_2$: comparison to $(U,Pu)O_2$

We analyse in the following sections the point defect properties in terms of formation energies. We take into account various charge states and the effect of the deviation from stoichiometry. We present in the two first sections the effect of the chemical environment (number of Ce cations in the first coordination shell of the defect) and the impact of cerium content on the formation energy of oxygen vacancies and interstitials. Since the aim is to compare the defect properties in $(U,Ce)O_2$ and $(U,Pu)O_2$, we use in these two first sections the same oxygen chemical potential of -6.38 eV as in Chapter 4, Section 4.3.2.3. This oxygen chemical potential corresponds to the stoichiometry condition for $(U,Pu)O_2$. Further, the stability of various point defects under various charge states is presented, with a brief discussion of the stable cations valence states in the presence of defects in $(U,Ce)O_2$.

5.3.1 Effect of chemical environment on point defects formation energy

Figure 73 presents the formation energy of a neutral oxygen vacancy in various chemical environments containing respectively 0, 1, 2 and 3 Ce cations in the first coordination shell of the vacancy. A small variation in the formation energy with the increase in Ce/(U+Ce) ratio is highlighted. For all the chemical environments investigated, the ones containing at least 2 Ce are the most favourable.

The energy difference between the most stable environments (lowest energy) and the least stable one (highest energy) is 0.14 eV. This difference, even if not negligible, is smaller than that obtained for $(U,Pu)O_2$ (0.50 eV). The variation in formation energy with the number of Ce cation in the first coordination shell of the vacancy can be attributed to the formation of electronic polarons as explained in Chapter 4, Section 4.3.2.1. We also observe that the environment with one Ce cation is slightly less stable than the pure uranium environment.

We find that for a similar oxygen chemical potential, the oxygen vacancy forms more favourably in $(U,Ce)O_2$ (0.69 eV) than in $(U,Pu)O_2$ (1.45 eV). The formation energy in $(U,Ce)O_2$ is lower by the factor of two compared to that of $(U,Pu)O_2$. This means that $(U,Ce)O_2$ is easier to reduce than $(U,Pu)O_2$.

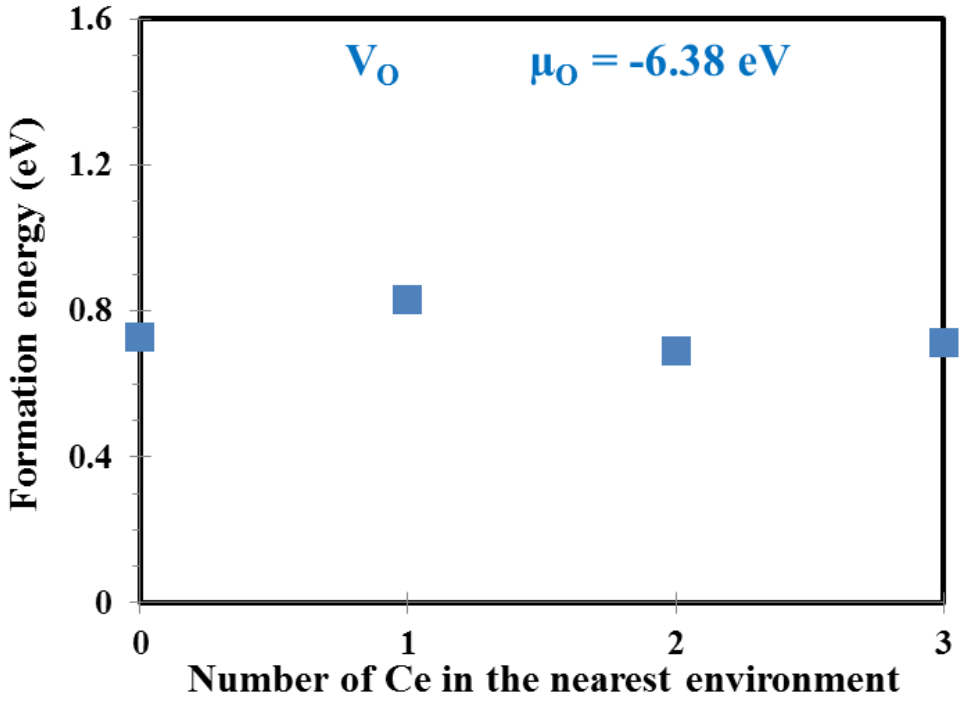

Figure 73 : Evolution of the formation energy of a neutral oxygen vacancy with the chemical environments. Four environments containing 0, 1, 2 and 3 Ce cations are assessed. The formation energies are calculated for the hyper-stoichiometry condition as shown in the Section 5.3.3.

Figure 74 presents the formation energy of a neutral oxygen interstitial in various chemical environments of $U_{0.75}Ce_{0.25}O_2$. Chemical environments are identified in terms of the number of Ce cations in the first cation shell of oxygen interstitials, as in $(U,Pu)O_2$ (see Chapter 4). The results show small variations of the formation energies of neutral oxygen interstitials with the increase of the number of Ce in the environment. An energy difference less than 0.15 eV is obtained between the most favourable environment and the less favourable one. We can therefore conclude that, in contrary to $(U,Pu)O_2$ (see Chapter 4, Section 4.3.2.1), the presence of Ce cations around an oxygen interstitial has a very small impact on the formation of this defect. The values of the formation energies obtained for all chemical environments in $(U,Ce)O_2$ are similar to those of the less favourable environments in $(U,Pu)O_2$. The difference in the formation energies of the oxygen interstitial between the most favourable environments of both compounds is 0.6 eV. We can therefore conclude that the oxidation conditions of $(U,Ce)O_2$ and $(U,Pu)O_2$ are quite similar.

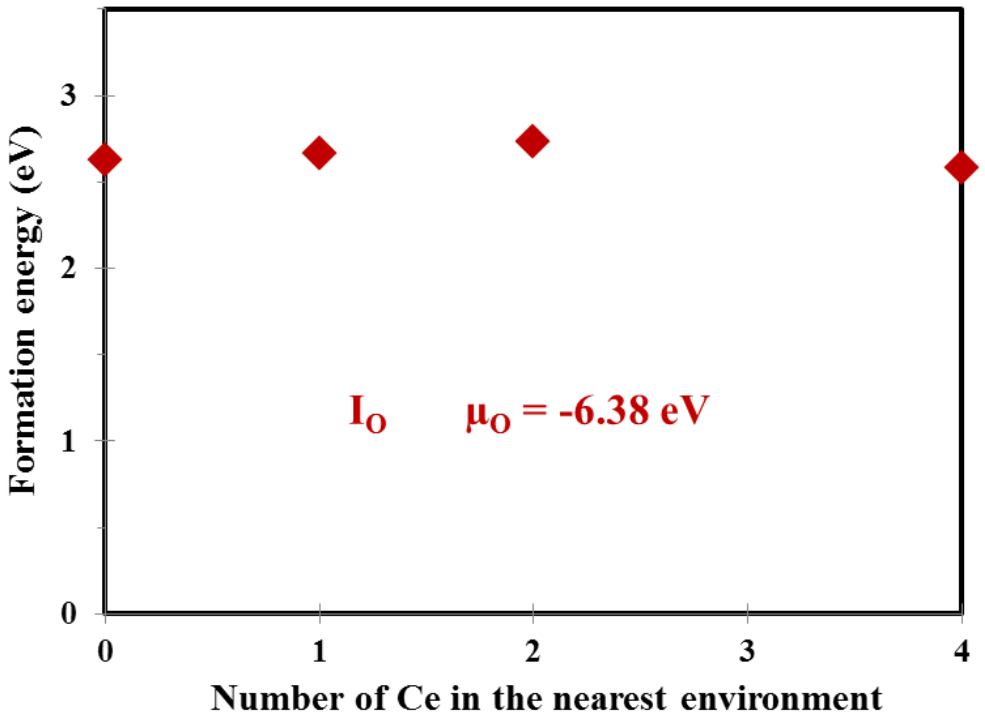

Figure 74 : Evolution of the formation energy of a neutral oxygen interstitial with the chemical environments. Four environments containing 0, 1, 2 and 4 Ce cations are assessed. The formation energies are calculated for the stoichiometry condition as shown in the Section 5.3.3.

5.3.2 Effect of Ce content on point defect formation

Figure 75 shows the plot of the formation energies of a neutral oxygen vacancy as a function of Ce contents. Formation energies are calculated for an oxygen chemical potential of -6.38 eV, and for the most stable chemical environments provided by the SQS configurations [189, 237]. These chemical environments possess one Ce cation for 12.5 % Ce content and two Ce cations for 25 % and 50 % Ce content. The results highlight that the formation energies of oxygen vacancies in $(U,Ce)O_2$ are much lower than those in pure UO_2 oxide. This decrease in formation energy is also observed for $(U,Pu)O_2$. In $(U,Ce)O_2$, however, a small variation in the formation energy with the increase in Ce content is observed, with the energy difference of around 0.2 eV between 12.5 % and 50 % Ce content.

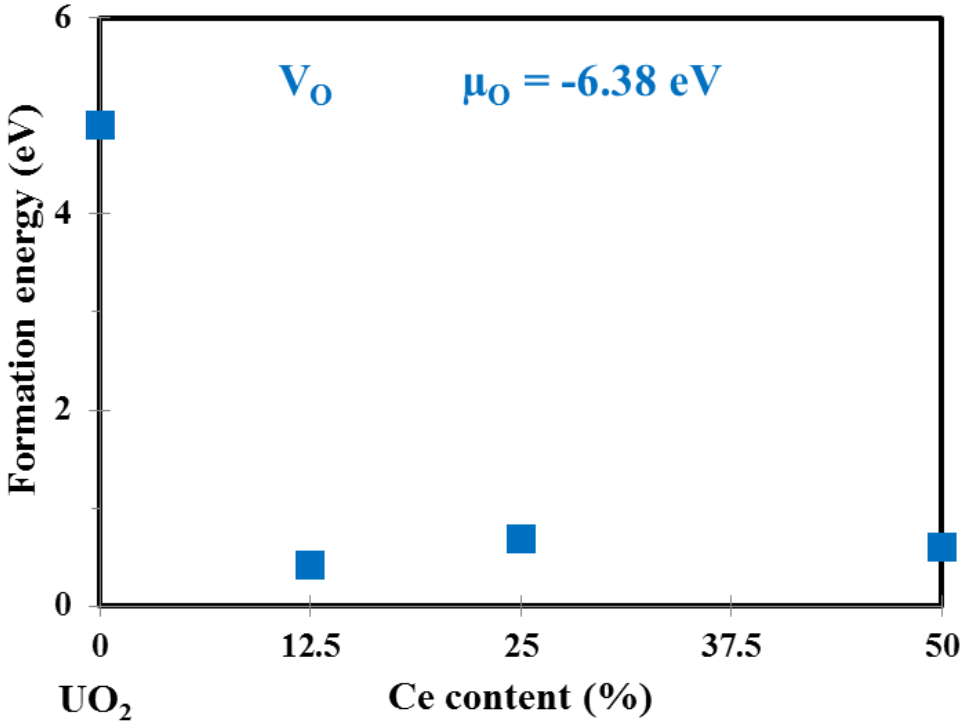

Figure 75 : Formation energy of a neutral oxygen vacancy as a function of Ce content.

The variation of the formation energies of the oxygen vacancy with the Ce content in $(U,Ce)O_2$ shows a smaller value (least than 0.27 eV) compared to that in $(U,Pu)O_2$ (up to 0.56 eV).

5.3.3 Point defect stability for various charge states

Figure 76 shows the plot of the formation energies of various point defects in $U_{0.75}Ce_{0.25}O_2$, under neutral and formally charged states as a function of the O chemical potential (μ_O). These energies are calculated in the entire accessible oxygen chemical potential range of the fluorite phase of the U-Ce-O system. The formation energies are assessed for the Fermi level in the middle of the band gap. The notation $\boldsymbol{Y^q_{atom}}$ has the same meaning as in Chapter 4. The defect charge states are neutral (X) or formally charged (+2 for O vacancy, -2 for O interstitial, +4 for U and Ce interstitials and -4 for U or Ce vacancies).

The stability of defects shows two different charge behaviours for oxidizing and reducing defects for the Fermi level in the middle of the band gap. For reducing defects such as oxygen vacancies and cation interstitials, the neutral charge state is the most favourable one in the whole chemical potential range. For oxidizing point defects such as oxygen interstitials and uranium vacancy, the formal charge states are the most

favourable ones for the Fermi level in the middle of the band gap, for the entire oxygen chemical potential range. The neutral and formally charged cerium vacancies have similar formation energy. This result means that cerium cation with the valence state Ce^{3+}, which are induced by neutral reducing defects, are the most favourable cations in $(U,Ce)O_2$ to accommodate the presence of reducing defects. On the other hand, U^{4+} cations, which are found for formally charged oxidizing defects, are the most stable U cations in $(U,Ce)O_2$ for the various stoichiometry conditions. Therefore, the oxidizing states +III and +IV of Ce and +IV of U can be found in $(U,Ce)O_2$ depending on the deviation from stoichiometry. This conclusion is similar to that obtained for $(U,Pu)O_2$.

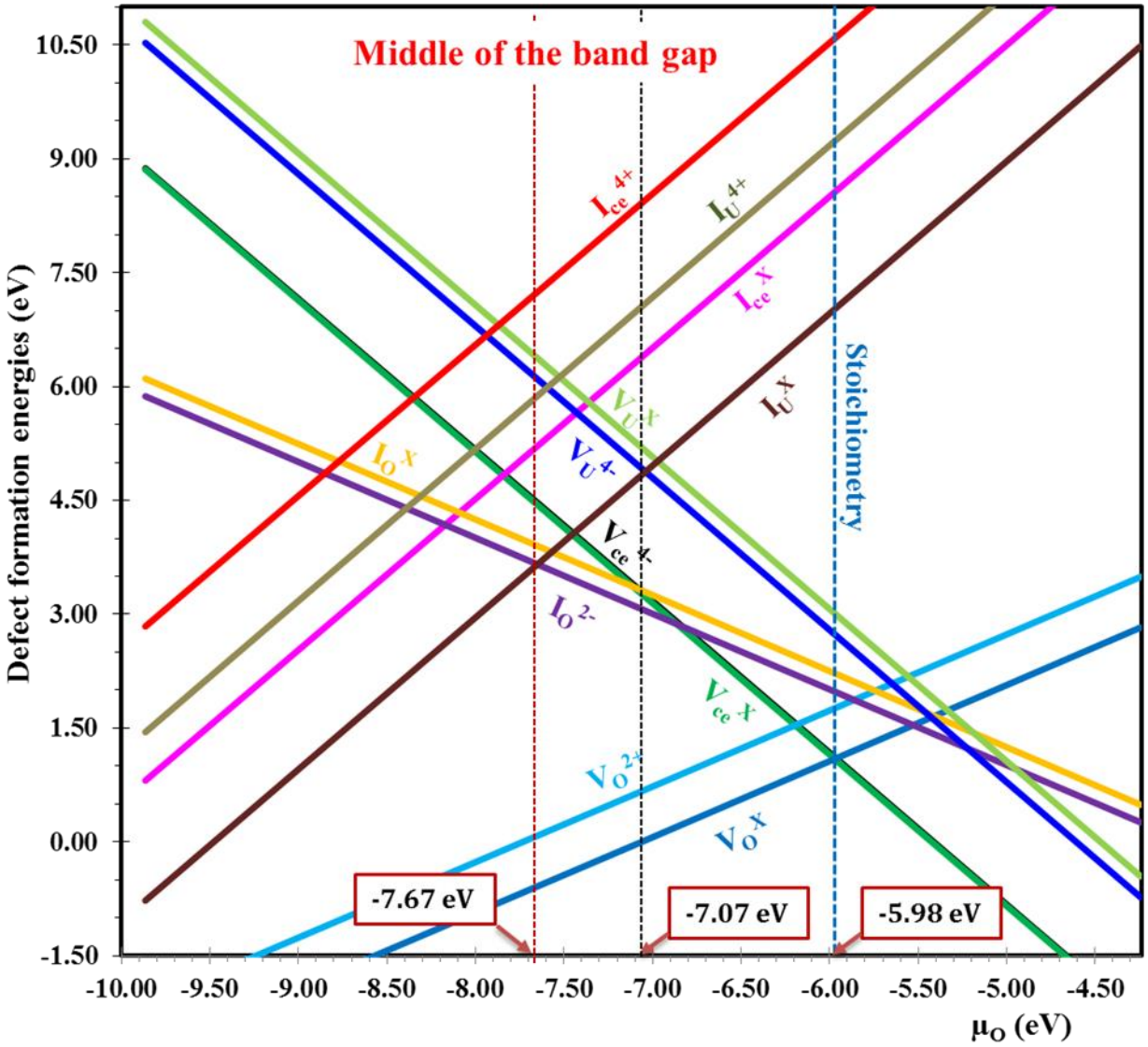

Figure 76 : Formation energy of neutral and formally charged point defects in $U_{0.75}Ce_{0.25}O_2$ as a function of oxygen chemical potential.

The defect types which are stable at various oxygen chemical potential ranges are also depicted in Figure 76. Two main regions are observed. The first one is the hypo-stoichiometry region, observed for the oxygen chemical potential ranging from the

lower limit to the value of -5.98 eV. This hypo-stoichiometry region is accommodated by the oxygen vacancy. The second one is the hyper-stoichiometry region, obtained for the oxygen chemical potential ranging fron -5.98 eV to the upper limit. This hyper-stoichiometry region is accommodated by the cerium vacancy. This result is different to that obtained in $(U,Pu)O_2$, where the hyper-stoichiometry is first accommodated by the oxygen interstitial.

In the hypo-stoichiometry region, other remarkable domains are observed: the domain at which the formation energy of the oxygen vacancy is negative ($\mu_O \leq$ -7.07 eV) and the domain where this formation energy is positive ($\mu_O \geq$ -7.07 eV). From the lower limit to the oxygen chemical potential of -7.67 eV, the order of stability of the defects is $V_O - I_U -$ (I_O or I_{Ce}) $- V_{Ce} - V_U$. For the oxygen chemical potential ranging from -7.67 eV to -7.07 eV, the stability of the defects is as follows: $V_O - I_O -$ (I_U or V_{Ce}) $-$ (I_{Ce} or V_U). The negative value of the formation energy of oxygen vacancy up to the chemical potential of -7.07 eV suggests a very favourable reduction of the $(U,Ce)O_{2-x}$ fluorite phase. In the second domain, where $\mu_O \geq$ -7.07 eV, the formation energies of oxygen vacancies become positive and remain the lowest compared to other point defects up to the stoichiometry condition (μ_O = -5.98 eV). The order of stability of the defects becomes $V_O - I_O - V_{Ce} - V_U - I_U - I_{Ce}$ in a short interval of the oxygen chemical potential [-7.07 eV, -6.85 eV] and $V_O - V_{Ce} - I_O - V_U - I_U - I_{Ce}$ from -6.85 eV to the stoichiometry.

In the hyper-stoichiometry region, we distinguish two domains: in the first domain, which corresponds to the oxygen chemical potential ranging from -5.98 eV to -5.44 eV, the formation energy of the cerium vacancy is positive. This suggests than $(U,Ce)O_{2+x}$ fluorite phase is stable, since cerium vacancy accommodates the hyper-stoichiometry. In the second domain ($\mu_O \geq$ -5.44 eV), the formation energy of the cerium vacancy is negative, suggesting a very favourable oxidation of $(U,Ce)O_{2+x}$ fluorite phase.

It appears from the above results that the defect stability in $(U,Ce)O_2$ is completely different from that obtained in $(U,Pu)O_2$. First, in the hyper-stoichiometry, for $(U,Ce)O_2$, the cerium vacancy is the most stable defect, contrary to the oxygen interstitial for $(U,Pu)O_2$. Second, the oxygen chemical potential corresponding to the stoichiometry condition for $(U,Ce)O_2$ (-5.98 eV) is higher than that obtained for $(U,Pu)O_2$ (-6.38 eV). Last, the relative order of stability of defects compared to each other is very different in both compounds. Owing to these differences, we can conclude that regarding the enthalpy of formation of point defects, $(U,Ce)O_2$ and $(U,Pu)O_2$ are not perfect surrogates.

Table 37 gives the formation energies of various neutral BSDs in $U_{0.75}Ce_{0.25}O_2$. For comparison, the values for $U_{0.75}Pu_{0.25}O_2$ are also given. Note that the formation energies of BSD defects do not vary with the deviation from stoichiometry, and in an equivalent way with the oxygen chemical potential.

Defect formation energy (eV)	**Neutral BSDs**	
BSD types	**$U_{0.75}Ce_{0.25}O_2$**	**$U_{0.75}Pu_{0.25}O_2$**
BSD1_Ce/Pu	2.14	4.08
BSD2_Ce/Pu	1.91	3.35
BSD3_Ce/Pu	1.98	3.74
BSD1_U	4.42	3.93
BSD2_U	3.71	3.51
BSD3_U	3.97	3.51

Table 37 : Formation energies (in eV) of various neutral bound Schottky defect types in $(U,Ce)O_2$ and $(U,Pu)O_2$.

In $(U,Ce)O_2$, the most stable BSD configuration for each cation vacancy type is the BSD2 and the most stable vacancy type is the Ce-type. This result is qualitatively similar to that obtained in $(U,Pu)O_2$. However, the Ce-type BSDs of $(U,Ce)O_2$ yield lower formation energies than the Pu-type BSDs of $(U,Pu)O_2$ as we can see in Table 37. On the contrary, the U-type BSDs yield the higher formation energies in $(U,Ce)O_2$ than in $(U,Pu)O_2$.

The last point investigated is the impact of the Fermi level on the formation energy and the stability of defect charge states in $(U,Ce)O_2$. The results are shown in Figure 77 for $U_{0.75}Ce_{0.25}O_2$.

The same sensitivity to the Fermi level as for $(U,Pu)O_2$ is obtained for $(U,Ce)O_2$. Indeed, when the Fermi energy evolves from the middle of the band gap (dashed line) towards the valence band maximum, defects tend to be electron deficient compared to their behaviour for the Fermi level in the middle of the band gap. This corresponds to the p-type semiconductor behaviour. On the contrary, when the Fermi energy evolves towards the conduction band minimum, defects tend to be in surplus of electrons. This corresponds to the n-type semiconductor behaviour.

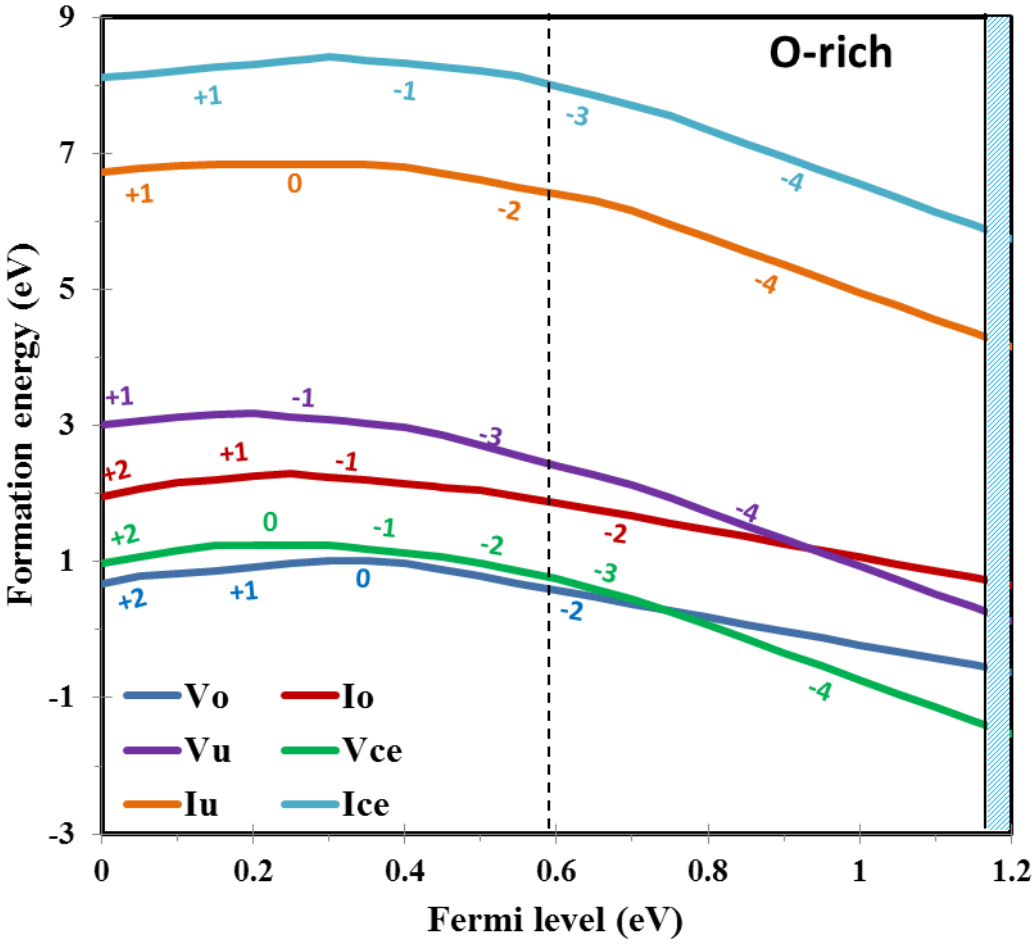

Figure 77 : Stability of defects in $U_{0.75}Ce_{0.25}O_2$ and their charge states as a function of the Fermi level. The formation energies are calculated for the highest oxygen chemical potential, for the Fermi level in the entire band gap.

5.4 Conclusion

In the present Chapter, a comparison of defect properties in $(U,Ce)O_2$ and $(U,Pu)O_2$ was performed. In particular, the impact of point defects on the electronic properties such as the electronic density of states, and structural properties in terms of the lattice distortions around the defect environment in $(U,Ce)O_2$ were investigated. The point defect formation energies were also investigated in the entire accessible oxygen chemical potential ranges, taking into account the effect of chemical environments and cerium contents for oxygen defects as well as the defect charge states and the impact of the position of the Fermi level. The aim of this study was to draw a larger comparison

between $(U,Ce)O_2$ and $(U,Pu)O_2$ in view of the point defect properties and their impact on materials properties.

We have first obtained for reducing defects completely different modifications in the electronic density of states for both compounds, especially the position of the defect electronic state in the band gap for neutral ones. For the oxidizing defects, while the formally charged defects lead to the complete M^{4+} valence state for cations in $(U,Pu)O_2$, we found for $(U,Ce)O_2$ the presence of Ce^{3+} valence state for their formal charge states, as well as Ce^{4+} and U^{4+}. As to the structural modifications, we have shown that the magnitude of distortions were very different for both compounds even if the distortion types induced were qualitatively similar for each point defect. The calculated defect formation energies have also highlighted the differences in the defect stability, thus in equilibrium defect concentrations, as well as the effect of Ce/Pu contents in both compounds. This study highlights the fact that the behaviour of $(U,Pu)O_2$ under irradiation cannot be expected to be experimentally perfectly well simulated using $(U,Ce)O_2$. The deviation from stoichiometry induced locally under irradiation can lead to very different behaviour for both mixed oxides. In order to gain more insight in the limitation of $(U,Ce)O_2$ to be considered as a surrogate for $(U,Pu)O_2$, further investigations should consider the defect entropy and the atomic transport properties in $(U,Ce)O_2$. This consideration, in first approximate, will improve the understanding of atomic diffusion and thus whether the $(U,Pu)O_2$ restructuring under operating condition can be represented or well simulated using $(U,Ce)O_2$ as a surrogate.

Chapter 6: Fission gas trapping in $(U,Pu)O_2$

6.1 Introduction

Fission gases (FG) such as Kr, Xe are found in the fuel under normal operating condition owing to the fission reactions of actinide elements. The krypton gas, especially the krypton-85 (^{85}Kr) isotope, is one of the fission products of radioactive nuclei such as ^{235}U. The xenon gas is formed in the fuel directly from the fission reaction of ^{235} U or indirectly through the β decay of iodine ^{135} I. Kr and Xe gas are estimated to be almost 15 % of fission products yielded in UO_2 [295]. These gases are first accommodated by point defects in the fuel. At finite temperature, they also migrate through the fuel matrix to form bubbles inside the grains and on the grain boundaries, and they can finally be released toward the cladding. The presence of fission gas bubbles has a significant impact on fuel properties as well as on the nuclear plant operation. On the one hand, the accumulation of fission gas bubbles alters the mechanical properties of the fuel and also causes fuel swelling. Furthermore, the fission gases released are known to fill the fuel–cladding gap and thus alter the thermal transfer from the fuel to the cladding and further to the coolant. This phenomenon can lead to an increase in temperature in the fuel matrix. On the other hand, the accumulation of ^{135}Xe with its high neutron cross section [296] accelerate the decrease in fission reaction, if a sudden drop in power occurs in the reactor. This phenomenon is known as the "xenon poisoning of the reactor". Helium is produced under normal operating condition and mostly during long term storage of spent fuel [297, 298]. Helium atoms are produced through phenomena such as α-decay of actinides and ternary fission [297, 299]. Experimental studies highlight the trapping of He within the fuel matrix. The increase in helium production in the $(U,Pu)O_2$ MOX fuel compared to its homologue UO_2 [299] is also pointed out. Moreover, in the Pu aggregates of the MOX fuel, the production of He is much higher. Therefore, it is crucial to understand phenomena which accompany the trapping of these gases in the $(U,Pu)O_2$ fuel matrix.

The trapping of fission gases has been investigated in UO_2 [65, 300], CeO_2 [119, 122] and ThO_2 [297, 301] using first-principles calculations. For all these studies, the most favorable defects which accommodate the fission gases and He are bound Schottky defects (BSD). These defects are formed by one actinide (U or Pu) vacancy and two oxygen vacancies. In this chapter, we use electronic structure calculations to investigate the fission gas trapping behaviour in $(U,Pu)O_2$. We have limited our study to Bound Schottky Defects (BSD) by analising all the BSDs configurations (3 configurations) and cation vacancy types (U or Pu) as detailed in Chapter 4, Section 4.2.5. This choice is justified by the fact that BSDs are found to be the most stable incorporation site for fission gases and helium in UO_2 [64, 65, 225] and other actinide oxides [119, 122, 297, 301]. We first recall how the incorporation and the solution energies are calculated. We then give the results on the incorporation and the solubility of Kr, Xe and He in the $(U,Pu)O_2$ matrix.

6.2 Generalities on the incorporation and solubility calculations of fission gases

The incorporation and solubility of fission gases (FG) are investigated in the present chapter in terms of the incorporation energies and the solution energies of each gas in a given defect site. The incorporation energy of a fission gas atom represents the energy needed for the trapping of this fission gas in an existing defect site. This is, for instance, the case of irradiated fuels containing prior irradiation damage. For the calculation of the solution energy, the formation of the incorporation defect site is also taken into account. The solubility is representative for materials without pre-existing defects such as non-irradiated fresh fuels. The incorporation energy of a fission gas *FG* in a defect site *X* is given by the following expression:

$$E_I(FG,X) = E_{Tot}(FG,X) - E_{Tot}(X) - \mu_{FG} \qquad (140)$$

where $E_{Tot}(FG,X)$ is the total energy of the supercell containing the fission gas in the defect site X, $E_{Tot}(X)$ is the total energy of the supercell containing the defect X and μ_{FG} the chemical potential of fission gas atom. The lower the incorporation energy, the higher the stability of the FG in the incorporation site.

The solution energy is obtained by adding to the incorporation energy the formation energy of the defect in which the FG is incorporated:

$$E_{Sol}(FG,X) = E_I(FG,X) + E_f(X) \qquad (141)$$

where $E_f(X)$ is the formation energy of the defect *X*, calculated according to Equation (83) (see Section 2.6). The lower the solution energy, the more soluble the fission gas.

The incorporation energy of fission gas does not explicitly depend on the chemical potential of the atoms of (U,Pu)O_2. Therefore, this quantity is independent of the stoichiometry conditions. On the other hand, the solution energy is sensitive to the stoichiometry conditions through the defect formation energy. However, the formation energy of BSDs is independent of the stoichiometry as highlighted in Chapter 4 Section 4.3.2.3.

6.3 Fission gas trapping behaviour in $(U,Pu)O_2$

6.3.1 Incorporation of Kr, Xe and He at BSD sites

The incorporation of fission products (FP) can be understood in general as a competition between various phenomena. The first one is the steric effect. It is related to the local strain induced by the size of the FP atom incorporated. This phenomenon leads to atomic displacements around the FP atom. The second one is the chemical interaction of the FP atom with the neighbouring atoms, such as the van der Waals interactions and the coulomb interactions [225, 302]. In the case of fission gases, the coulomb interactions cannot be envisaged since the noble gases are not charged and their valence electron shells are full. The incorporation energies of Kr, Xe and He are discussed in the following sections.

6.3.1.1 Incorporation of Kr

The incorporation energies of Kr in various BSD sites of $(U,Pu)O_2$ with 25 % Pu are reported in Table 38. These energies are determined in two different ways. In the first case, the van der Waals interactions are taken into account (vdW), through the use of the vdW-optPBE+*U* functional. In the second case, vdW interactions are neglected (no vdW) and the PBE+*U* functional is used. Comparison is further made with literature data on the incorporation of Kr in UO_2 BSD sites.

The most favourable BSD incorporation site for Kr in $(U,Pu)O_2$ is found to be the BSD1_U site, with the lowest incorporation energy of 0.03 eV and 0.67 eV with and without taking into account the van der Waals interactions, respectively. Globally, the stability of BSD incorporation sites vis-à-vis the Kr atom is ranked as follows: BSD1_U – BSD1_Pu – BSD3_Pu – BSD2_U – BSD3_U – BSD2_Pu.

The stability of the compact BSD1 configuration for the incorporation of Kr in $(U,Pu)O_2$ follows the same trend as found for Kr in UO_2 by Vathonne *et al.* [65] and Thompson and Wolverton [225]. Among the BSD types (U or Pu), the uranium BSD type is the most favourable BSD for the accommodation of Kr in $(U,Pu)O_2$. For uranium BSD type, the stability of configurations can be ranked as BSD1 – BSD2 – BSD3, consistently with previous published studies in UO_2 [64, 65, 225]. For plutonium BSD type, their ability to accommodate Kr follows the stability order BSD1 – BSD3 – BSD2, at least when the vdW interactions are considered.

Defects sites	Refs.	BSD1_U	BSD2_U	BSD3_U	BSD1_Pu	BSD2_Pu	BSD3_Pu
$U_{0.75}Pu_{0.25}O_2$	This work *(vdW)*	0.03	1.72	1.90	0.25	2.31	1.08
	This work *(no vdW)*	0.67	2.43	2.57	0.84	2.96	1.77
	ΔE_I	-0.64 (-96 %)	-0.71 (-29 %)	-0.67 (-26 %)	-0.59 (-70 %)	-0.65 (-22 %)	-0.69 (-39 %)
UO_2	Vathonne *(vdW)* [65]	0.01	0.58	0.86	--	--	--
	Vathonne *(no vdW)* [65]	0.61-0.77	1.18-1.37	1.38-1.48			
	Thompson *(no vdW)* [225]	0.66	1.25	1.63	--	--	--
	Dorado *(no vdW)* [64]	0.64	1.26	1.38	--	--	--
	Brillant *(no vdW)* [302]	--	1.43	--	--	--	--

Table 38 : Incorporation energies (in eV) of krypton in various BSD defects of $(U,Pu)O_2$ with 25 % Pu. In the first line, the van der Waals interactions are taken into account while for the second line this effect is neglected. ΔE_I is the vdW contribution to the incorporation energy. Comparison is made between $(U,Pu)O_2$ and UO_2.

The analysis of the effect of the van der Waals interactions on the incorporation energies of Kr is shown through ΔE_I in Table 38. It appears that the absolute effect of the van der Waals interactions is in the same order of magnitude (-0.64 to - 0.77 eV) for all configurations except for BSD1_Pu. However, their relative contribution to the incorporation energies varies from 22% to the maximum value of 96 %. This result highlights the fact that the interaction between the electronic cloud of Kr and that of the first neighbouring atoms are not identical for all incorporation sites. In order to well capture the influence of the van der Waals interactions we have analysed the localisation of Kr in the BSD defect and the charge distribution according to Bader charge repartition analysis.

Figure 78 shows the Kr atom trapped in the three most favourable BSD sites. The krypton atom is in orange.

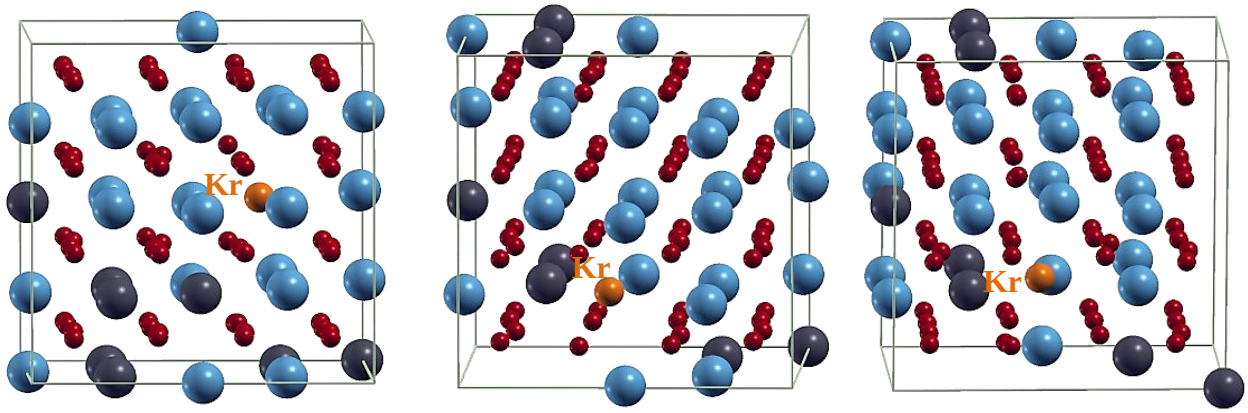

Figure 78 : Krypton gas trapped in three most favourable BSD incorporation sites. Kr atom is in orange, U in blue and Pu in dark grey.

The Kr atom does not localise in the actinide vacancy of the BSD defects, even for BSD3 where the actinide vacancy is the centre of gravity of the defect. Kr is positioned closer to one actinide cation than other cations in the first coordination shell of the BSD site. This reorganisation may affect the interaction between the electronic cloud of Kr and that of its nearest neighbouring actinide cation. The smallest krypton-uranium distance of 3.16 Å is obtained for the most stable BSD1_U site in contrast to 3.92 Å for uranium-uranium first neighbouring distance.

The Bader charge analysis is presented in Table 39 where the average atomic volume, according to Bader charge repartition, is presented for the actinides in the first coordination shell of the Kr atom (M[near Kr]) and far from Kr (M[far Kr]). The corresponding atomic radius and the algebraic distance between electronic cloud of Kr and the nearest actinide (*EC*[Kr-M]) according to Bader charge repartition are also shown. The algebraic distance between electronic clouds is defined as the distance between krypton and cation nuclei minus the sum of the Bader atomic radius of krypton and cation. This quantity characterises the overlap between both electronic clouds. This algebraic distance can be negative if the electronic clouds of both krypton and a given cation overlap. This overlap suggests that both atoms share their electronic densities, leading to a weak vdW interaction.

An expansion of 11 % of the Bader charge volume of actinide atoms around the Kr atom incorporated in the BSD site is observed. This expansion is due to the relatively small size of Kr incorporated in a large BSD site. The distance between the electronic cloud of Kr and that of the closest uranium cation is negative (-0.36 Å), meaning that they overlap each other. This may lead to a weaker van der Waals interactions. This distance

is positive (0.20 Å) for the rest of the cations surrounding the Kr incorporation BSD site, suggesting a larger van der Waals interactions than the previous case.

Actinides and Kr atoms	*An*[near Kr]	*An*[far Kr]	Kr
Atomic volumes (Å^3)	17.82	16.07	28.58
Atomic radius (Å)	1.62	1.57	1.90
Distance *EC*[Kr-M] (Å)	-0.36 and 0.20	--	-0.36 and 0.20

Table 39 : Atomic parameters according to the Bader charge repartition analysis of actinide atoms and Kr atom incorporated in the BSD1_U site. *EC*[Kr-M] is the algebraic distance between the electronic cloud of Kr and of the nearest actinide neighbours.

Globally, as we can see in Table 38, the BSD1 configurations present the largest vdW contribution to the incorporation energy (higher than 70 %). This can be explained by the fact that this configuration is the most compact. Thus, BSD1 offers the largest free volume for the incorporation of FG, and disadvantages the overlap between the FG and the matrix electronic densities.

The incorporation of Kr atom in the BSD sites leads to the displacement of the first neighbouring oxygen atoms by 0.55 Å farther from the Kr atom as compared to the U-O distance. This displacement is two times larger than those observed around actinide vacancies of the free BSD defects (see Chapter 4 Section 4.2.5). This means that the incorporation of Kr is made difficult by steric effect which causes oxygen displacements around the Kr atom.

6.3.2 Incorporation of Xe

Table 40 depicted the incorporation energies of Xe in various BSD sites of (U,Pu)O_2 with 25 % Pu. The van der Waals interactions are considered (vdW) or neglected (no vdW). Comparisons are made between our results and available incorporation energies of Xe in the BSD site of UO_2 from the literature.

The most favourable incorporation sites of Xe in (U,Pu)O_2 are found to be the BSD1_U and the BSD3_Pu. Globally, the stability of BSD defect sites for the accommodation of Xe in (U,Pu)O_2 can be ranked as follows: BSD1_U and BSD3_Pu – BSD2_U – BSD1_Pu – BSD2_Pu – BSD3_U. In order to compare our results to the available data for UO_2, we analyse the incorporation energies for each BSD type.

For the U-type BSD, the BSD1 configuration is the most favourable for the accommodation of Xe when the van der Waals interactions are taken into account. The U type BSD configurations can be ranked according to the accommodation of Xe as BSD1 – BSD2 – BSD3. We can clearly see that this ranking is similar between (U,Pu)O_2 and UO_2 [64, 225] as shown in Table 40. If we ignore the van der Waals interactions, the

most favourable configuration for $(U,Pu)O_2$ is the BSD2_U while the BSD1 is predicted in UO_2. For Pu-type BSD, the BSD3 is the most favourable configuration for the accommodation of Xe gas atom. By taking into account the van der Waals interactions, the incorporation energy obtained is similar to that of BSD1_U. Therefore, both BSD1_U and BSD3_Pu are the most favourable incorporation sites for Xe. In all the cases, the effect of the van der Waals interactions is smaller than that of Kr. It represents less than 70 % of the incorporation energy.

Defects sites	**Refs.**	**BSD1_U**	**BSD2_U**	**BSD3_U**	**BSD1_Pu**	**BSD2_Pu**	**BSD3_Pu**
$\mathbf{U_{0.75}Pu_{0.25}O_2}$	This work *(vdW)*	0.60	0.97	1.87	1.19	1.62	0.61
	This work *(no vdW)*	1.96	1.72	2.56	2.04	2.29	1.49
	ΔE_I	-1.36 (-69 %)	-0.75 (-44 %)	-0.69 (-30 %)	-0.85 (-42 %)	-0.67 (-29 %)	-0.88 (-59 %)
$\mathbf{UO_2}$	Vathonne (vdW) [65]	0.45	1.03	1.68	--	--	--
	Thompson *(no vdW)* [225]	1.06	1.82	1.92	--	--	--
	Dorado (no vdW) [64]	1.18	1.82	2.25	--	--	--
	Nerikar (no vdW) [303]	1.38	--	--	--	--	--
	Andersson (no vdW) [169]	0.18	--	--	--	--	--
	Brillant *(no vdW)* [302]	--	1.63	--	--	--	--

Table 40 : Incorporation energies (in eV) of xenon in BSD defects of $(U,Pu)O_2$. Comparison is made with values obtained on UO_2.

The Xe incorporated in BSD defects does not localise in the actinide vacancy of the defect. The Xe atom moves slightly to localise nearby one actinide atoms as depicted in Figure 79. This position is similar to the one observed previously for the Kr atom. The smallest distance between Xe and its nearest actinide neighbour is about 3.22 Å rather than 3.92 Å for actinide-actinide interatomic distance in $(U,Pu)O_2$.

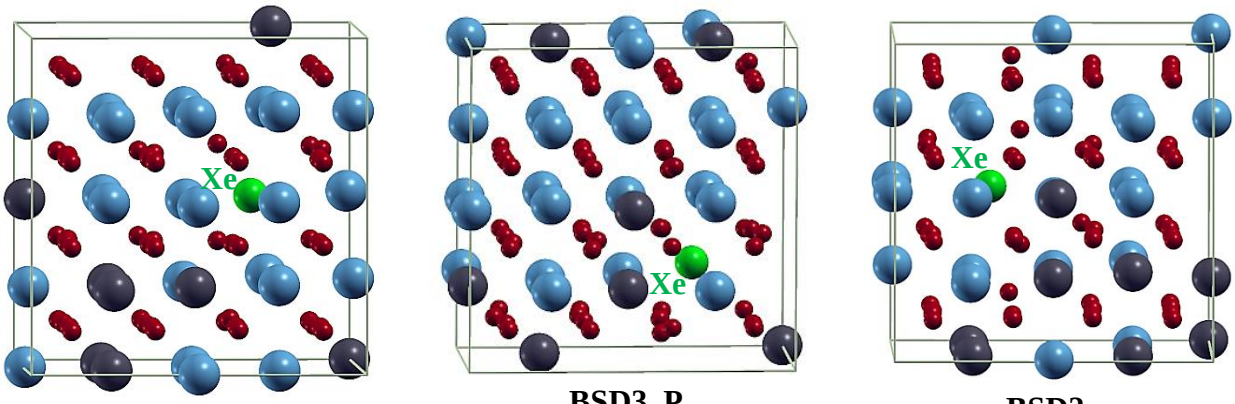

Figure 79 : Xe trapped in the three most favourable BSD defects, namely BSD1_U, BSD3_Pu and BSD2_U. Xe atom is in green, U in blue and Pu in dark grey.

In order to capture the van der Waals interactions effect, the same Bader charge analysis is performed for Xe and shown in Table 41.

Actinides and Xe atoms	***An*[near Xe]**	***An*[far Xe]**	**Xe**
Atomic volumes (Å³)	17.71	16.74	33.75
Atomic radius (Å)	1.62	1.59	2.00
Distance *EC*[Xe-M] (Å)	-0.40 and 0.10	--	-0.40 and 0.10

Table 41 : Atomic parameters according to the Bader charge repartition of actinide atoms and Xe atom incorporated in the BSD1_U defect. *EC*[Xe-M] is the algebraic distance between the electronic cloud of Xe and of the nearest actinide neighbours.

A slight increase by 6 % in Bader charge volume for actinide atoms nearby Xe is observed. This expansion is smaller by the factor 2 than the one yielded by Kr. This is due to the larger size of xenon atom compared to krypton, leaving less free space in the BSD incorporation site. Table 41 shows that the electronic cloud of Xe overlaps with that of the nearest uranium cation. The overlap is larger than the one for Kr, in line with the larger radius of the Xe atom. This larger overlap yields a smaller contribution for Xe than for Kr of the van der Waals interactions to the incorporation energies, as can be seen in Table 40. This is highlighted by the negative distance (-0.40 Å) between both electronic clouds according to the Bader charge repartition. Other actinide atoms in the first coordination shell of the BSD incorporation site yield a gap of 0.10 Å between their electronic cloud and that of Xe.

The displacements of oxygen atoms in the first coordination shell are presented in Table 42. These displacements are more linked to the BSD configuration than to the incorporation energy. This means that the formation of the BSD incorporation site has more impact on the lattice distortions than the incorporated Xe atom. This issue will be discussed in the Section 6.3.4.2 on the solution energy.

BSD types	BSD1_U	BSD2_U	BSD3_U	BSD1_Pu	BSD2_Pu	BSD3_Pu
Oxygen displacements (Å)	0.68	0.63	0.58	0.70	0.63	0.55

Table 42 : Displacement of oxygen atoms in the first coordination shell of the Xe atom.

6.3.3 Incorporation of He

Table 43 presents the incorporation energies of helium atom in various BSD sites. Similar features as for Kr and Xe are considered. Other theoretical studies on the incorporation of He in UO_2 and PuO_2 BSD sites are presented in order to compare with our results on $(U,Pu)O_2$.

Defects sites	Refs.	BSD1_U	BSD2_U	BSD3_U	BSD1_Pu	BSD2_Pu	BSD3_Pu
$U_{0.75}Pu_{0.25}O_2$	This work *(vdW)*	0.09	-0.18	0.04	0.65	0.01	-0.02
	This work *(no vdW)*	0.24	-0.04	0.24	0.81	0.12	0.12
	ΔE_I	-0.15 (-63 %)	-0.14 (-350 %)	-0.20 (-83 %)	-0.16 (-20 %)	-0.11 (-92 %)	-0.14 (-117 %)
UO_2	Vathonne (vdW) [65]	-0.07	0.01	-0.05	--	--	--
	Thompson *(no vdW)* [225]	0.04	0.13	0.16	--	--	--
	Brillant *(no vdW)* [302]	--	-0.02	--	--	--	--
PuO_2	Tian *(no vdW)* [71]	--	--	--	--	--	0.49

Table 43 : Incorporation energies of He in various BSD sites of $(U,Pu)O_2$. ΔE_I give the contribution of vdW interaction to the incorporation energies. Available data for UO_2 and PuO_2 are shown.

The results show that the BSD2_U site, which is the bound Schottky defect constituted of an uranium vacancy and two oxygen vacancies in the <110> direction, is the most favourable one for the accommodation of a helium atom in $(U,Pu)O_2$. This result remains the same irrespective to the consideration of the van der Waals interactions or not. The least favourable BSD site for the incorporation of He is the BSD1_Pu site.

The U-type BSD sites in $(U,Pu)O_2$ can be ranked as follows, regarding their stability for the accommodation of He atom: BSD2_U – BSD3_U – BSD1_U. In contrast, in UO_2 the ranking is different and is BSD1_U – BSD3_U – BSD2_U according to Vathonne [65]. The incorporation of He exhibits an exothermic character (negative incorporation energy) in the most favourable site in $(U,Pu)O_2$ as in UO_2. Another data from Brillant *et al*. [302] also gives an exothermic character for the incorporation of He on UO_2. However, Thompson *et al.* [225] have found positive values of the incorporation energy for all BSD configurations in UO_2. The discrepancies observed in the literature might be due to the existence of multiple energy minima in UO_2 as pointed out by Dorado *et al*. [222]. The ranking of the stability of the Pu-type BSD sites, for the accommodation of He atom in $(U,Pu)O_2$ is as follows: BSD3_Pu – BSD2_Pu – BSD1_Pu. The result of He incorporation in BSD3 site of PuO_2 investigated by Tian *et al*. [71] is shown in Table 43. This value is higher than the one obtained in $(U,Pu)O_2$ despite the fact that the authors use the occupation matrix control scheme. This difference can be due to the fact that the environment of He in PuO_2 is different to that in $(U,Pu)O_2$. Thus, the behaviour of He is probably mostly impacted by the presence of the uranium in the lattice.

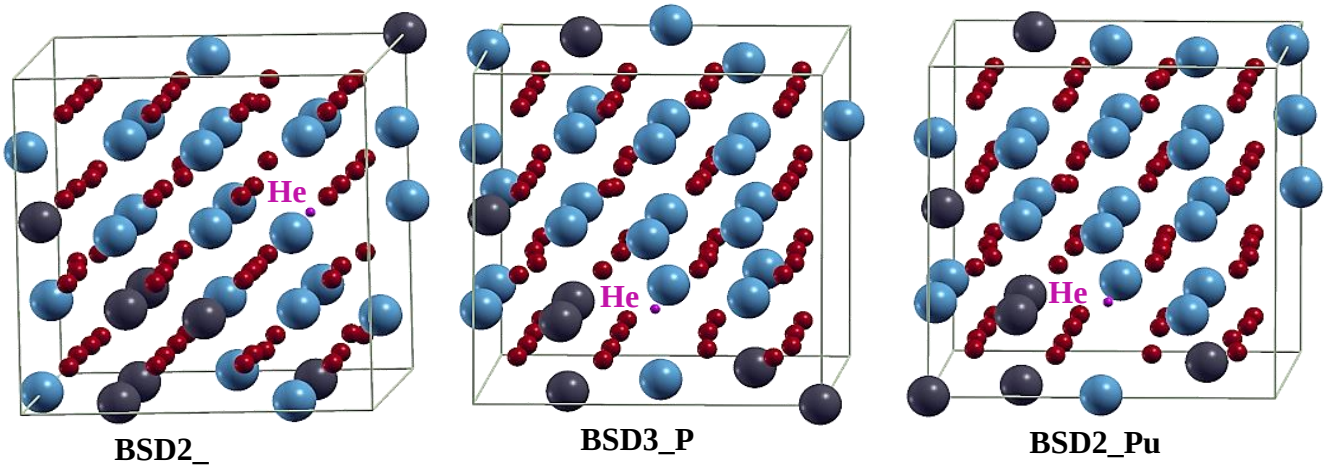

Figure 80 : Helium atom trapped in the three most favourable BSD sites, namely BSD2_U, BSD3_Pu and BSD2_Pu. He is the purple ball, U the blue balls, Pu the dark grey balls and O the red balls.

Another factor in the calculated incorporation of He in $(U,Pu)O_2$ is the contribution of the van der Waals interactions which is given in Table 43 as ΔE_I. The contribution of the van der Waals interactions in the incorporation of He is expected to be much larger than those of Kr and Xe which have a larger atomic radius than He. Our results show that this contribution is indeed almost 4 to 6 times larger for He (up to 350 %) than for Kr (no higher than 96 %) and Xe (less than 70 %). The origin of this large contribution is analysed considering the stable position of He in the most favourable BSD trapping site as highlighted by Figure 80.

The detailed analysis of the localisation of He shows that for the most stable BSD sites, He atom is localised at the actinide U or Pu vacancies of the BSD sites, contrary to Kr and Xe. The distance to the nearest actinide atom is 3.92 Å which is identical to the actinide-actinide interatomic distance. To investigate the origin of the larger van der Waals contribution to the incorporation of He, we have analysed the Bader charge distribution around the He and its nearest neighbouring actinide atoms in the most favourable incorporation site. Results are shown in Table 44. The Bader analysis is similar to that conducted for Kr and Xe.

Actinides and He atoms	*An*[near He]	*An*[far He]	He
Atomic volumes (Å^3)	18.04	16.69	10.52
Atomic radius (Å)	1.63	1.59	1.36
Distance *EC*[He-M] (Å)	0.93	--	0.93

Table 44 : Atomic parameters according to the Bader charge analysis of actinide atoms and He atom incorporated in the BSD2_U site. *EC*[He-M] is the algebraic distance between the electronic cloud of He and of the nearest actinides neighbours.

The slight Bader charge volume expansion of about 8 % in actinide atoms around the He atom in the BSD site is due to the free volume available owing to the small size of He. The electronic clouds of both He and the nearest actinides are located at 0.93 Å from each other. Contrary to Kr and Xe atoms, this distance is positive, meaning that there is no overlapping between both electronic clouds. This situation is favourable for the van der Waals interactions, which are non local. The relative value of the van der Waals contribution to the incorporation of He (in %) is thus higher as compared to the cases of Kr and Xe. One should note, however, the smaller values of the incorporation energies of He compared to other gases.

Another contribution to the incorporation of He is the atomic displacements of the first neighbouring oxygen atoms around He. We found this displacement to be strongly linked to the BSD configurations. The most favourable BSD2 and BSD3 configurations yield displacements of around 0.3 Å, which are identical to those obtained in the free BSD2 and BSD3 defects as shown in Chapter 4 Section 4.2.5. Therefore, the steric effect due to the presence of He is negligible.

6.3.4 Solubility of Kr, Xe and He in (U,Pu)O_2

In this section, we complete the analyses of fission gases behaviour in terms of their solubility in (U,Pu)O_2. Indeed, the incorporation energies correspond to the case in which the number of available trap sites for the gas atoms is larger than the number of gas atoms. If this criterion is exceeded, in other words, if the number of gas atoms becomes larger than the trap sites, the need for the creation of defect site appears

necessary. This situation corresponds to the solubility of fission gases in the $(U,Pu)O_2$ matrix, which is assessed by the solution energy calculated according to Equation (141). This latter is described in the following sections. The steric effect and the van der Waals interactions are also analysed.

6.3.4.1 Solubility of Kr in $(U,Pu)O_2$

Table 45 below presents the solution energies of the Kr atom in the $(U,Pu)O_2$ matrix, with a Pu content of 25 %. The Kr gas atom is located at the BSD sites.

Defects sites	Refs.	BSD1_U	BSD2_U	BSD3_U	BSD1_Pu	BSD2_Pu	BSD3_Pu
$U_{0.75}Pu_{0.25}O_2$	This work *(vdW)*	3.96	5.22	5.41	4.33	5.65	4.81
	This work *(no vdW)*	3.33	4.68	4.84	3.11	4.64	3.78
UO_2	Vathonne *(vdW)* [65]	4.02	3.91	4.29	--	--	--
	Vathonne *(no vdW)* [65]	3.86 - 4.02	3.66 - 3.85	3.98-4.08			
	Thompson *(no vdW)* [225]	4.74	4.58	5.08	--	--	--
	Dorado *(no vdW)* [64]	3.96	3.80	4.20	--	--	--
	Brillant *(no vdW)* [302]	--	2.93	--	--	--	--

Table 45 : Solution energies (in eV) of Kr in the BSD sites of $(U,Pu)O_2$ with 25 % Pu. vdW means that the van der Waals interactions have been considered. Some theoretical results on UO_2 from the literature are shown for comparison to our results.

First of all, the solution energies of Kr in all BSD sites are positive and large. This means that the noble gas Kr is largely insoluble in $(U,Pu)O_2$. The most favourable solution site is the BSD1 configurations, mostly the BSD1_Pu one. This result is consistent with that obtained by Kuganathan *et al.* [301] in thoria, and differs with the results on UO_2 where the BSD2 configuration is found favourable (see Table 45). Furthermore, the solution energies increase when the van der Waals interactions are taken into account for each

BSD site. Thus this interaction enhance the insolubility of Kr in the $(U,Pu)O_2$ matrix. The steric effect also contributes to that insolubility, as mentioned in the Section 6.3.1.1 for the incorporation of Kr.

Our results on the solubility are in line with those found in UO_2 by several authors [64, 65, 225, 302] who also found positive solution energies for Kr in the BSD sites. Moreover, Vathonne [65] has also found an increase in the solution energy of Kr in BSD sites of UO_2 when the vdW interactions are considered. Globally, the smallest solution energy of Kr in $(U,Pu)O_2$ is in the same order of magnitude as the one found in UO_2, even though the preferred solution sites are different.

6.3.4.2 Solubility of Xe

Table 46 presents the solution energies of the Xe atom in the $(U,Pu)O_2$ matrix, with a Pu content of 25 %. The Xe gas atom is located at the BSD sites.

Our results show that all the solution energies of Xe at BSD sites are positive and large, meaning that Xe is largely insoluble in $(U,Pu)O_2$. The most favourable solution sites are respectively the BSD3_Pu and BSD2_U. This result is consistent with that obtained by Vathonne *et al.* [65] in UO_2. Furthermore, the solution energies slightly increase when the van der Waals interactions are taken into account for each BSD site, except for BSD1_U. Thus this interaction only slightly increases the insolubility of Xe in the $(U,Pu)O_2$ matrix compared to the case of Kr. This is expected, since in the incorporation energies calculated in Section 6.3.1, the vdW contribution is smaller for Xe than for Kr. The analysis of the contribution of the steric effect shows for the Pu-type BSD sites that the solution energy increases when the displacements of oxygen atoms localised in the first coordination shell of Xe increase. They range from 0.55 Å for the solution energy of 4.35 eV to 0.70 Å for the solution energy of 5.26 eV. Moreover, these displacements are larger for Xe than for Kr, as well as the solution energies. These results highlight the impact of the steric effect in the solubility of fission gases in $(U,Pu)O_2$.

Our results on the solubility of Xe in BSD sites compare very satisfactorily to those obtained by Vathonne [65] and Dorado [64] in UO_2. The values obtained when the van der Waals interactions are neglected also compare very well with other DFT studies by Andersson *et al.* [169] and Brillant *et al.* [302].

Defects sites	Refs.	BSD1_U	BSD2_U	BSD3_U	BSD1_Pu	BSD2_Pu	BSD3_Pu
$U_{0.75}Pu_{0.25}O_2$	This work *(vdW)*	4.52	4.47	5.38	5.26	4.96	4.35
	This work *(no vdW)*	4.63	3.97	4.83	4.32	3.96	3.50
UO_2	Vathonne (vdW) [65]	4.46	4.36	5.11	--	--	--
	Thompson *(no vdW)* [225]	5.15	5.16	5.39	--	--	--
	Dorado (no vdW) [64]	4.50	4.36	5.07	--	--	--
	Nerikar (no vdW) [303]	3.88	--	--	--	--	--
	Andersson (no vdW) [169]	4.75	--	--	--	--	--
	Brillant *(no vdW)* [302]	--	3.57	--	--		

Table 46 : Solution energies (in eV) of Kr in the BSD sites of $(U,Pu)O_2$ with 25 % Pu. vdW means that the van der Waals interactions have been considered. Some theoretical results on UO_2 from the literature are included.

6.3.4.3 Solubility of He

Table 47 below presents the solution energies of the He atom in the $(U,Pu)O_2$ matrix, with a Pu content of 25 %. The He gas atom is located at the BSD sites.

The solution energies are large and positive, meaning that He is insoluble in the $(U,Pu)O_2$ matrix. The most favourable solution sites are BSD2_Pu and BSD2_U respectively. These results are consistent with those obtained for UO_2 by Vathonne [65] and Thompson *et al.* [225]. The stability of the BSD2 sites is also in line with the results obtained in ThO_2 by Kuganathan *et al*. [297] on He trapping. Here again, the van der Waals interactions increase the solution energies as for Kr and Xe ones. The atomic displacements of neighbouring oxygen atoms yield a value of 0.60 Å for the least

favourable BSD1 configurations and 0.30 Å for BSD2 and BSD3 configurations which are more favourable. The solution energy of He in PuO_2 of 4.86 eV obtained by Tian *et al.* [71] is larger than that of UO_2 for the BSD3 configuration without vdW. Our results also show that Tian *et al.*'s value of the solution energy of He in PuO_2 is more than twice the solution energy of He in $(U,Pu)O_2$. This means that the solubility of He in $(U,Pu)O_2$ is more favourable than in PuO_2.

Defects sites	Refs.	BSD1_U	BSD2_U	BSD3_U	BSD1_Pu	BSD2_Pu	BSD3_Pu
$U_{0.75}Pu_{0.25}O_2$	This work *(vdW)*	4.02	3.21	3.55	4.73	3.35	3.72
	This work *(no vdW)*	2.90	2.21	2.51	3.09	1.79	2.13
UO_2	Vathonne *(vdW)* [65]	3.94	3.34	3.38	--	--	--
	Thompson *(no vdW)* [225]	4.13	3.45	3.62	--	--	--
	Brillant *(no vdW)* [302]	--	1.48	--	--	--	--
PuO_2	Tian *(no vdW)* [71]	--	--	--	--	--	4.86

Table 47 : Solution energies (in eV) of He in the BSD sites of $(U,Pu)O_2$ with 25 % Pu. vdW means that the van der Waals interactions have been considered. Other DFT results from the literature on UO_2 and PuO_2 are shown in order to compare with our results.

6.4 Conclusion

In this chapter we have studied the fission gases (Kr and Xe) and helium trapping behaviour in $(U,Pu)O_2$ in various bound Schottky defect (BSD) sites. We have first analysed the incorporation energies and the associated contribution of the van der Waals interactions and the steric effect. We found for the krypton atom that the most favourable incorporation site is BSD1_U and that the BSD1 configurations are more favourable in general for the Kr incorporation. For xenon in $(U,Pu)O_2$, the BSD1_U and the BSD3_Pu are found to be the most favourable incorporation sites. For both Kr and

Xe, the gas atom is not located at the actinide vacancy of the BSD, but closer to a cation of the matrix. The electronic clouds of the gas atom and of this close cation overlap. We found that the larger the overlap, the smaller the vdW contribution to the incorporation energy. This is in line with analyses of rare gas incorporation in small molecules by Bertolus *et al.* [304] and rare gases in UO_2 by Vathonne *et al*. [65]. In the case of the helium atom, the most favourable incorporation sites are BSD2_U and BSD3_Pu. These sites yield negative incorporation energies for He, meaning that these incorporations are exothermic, contrary to those of Kr and Xe for which the most favourable traps yield positive incorporation energies. Finally, we found that the fission gas incorporation energies in $(U,Pu)O_2$ have the same order of magnitude as the values in UO_2. The calculation of the solution energy of fission gases and helium in the $(U,Pu)O_2$ matrix highlight a large insolubility of each gas in the $(U,Pu)O_2$ matrix due to the large positive values of formation energies of traps. This insolubility is found to be increased by the vdW interactions. The solution energies of Kr, Xe and He are found to be in the same order of magnitude as their values in UO_2. However, the solution energy of He in PuO_2 from the literature is much higher than that found in $(U,Pu)O_2$. These results lead to the conclusion that the fission gas trapping behaviour in $(U,Pu)O_2$ is closer to that in UO_2 than that in PuO_2. A perspective to this chapter is the investigation of the migration of fission gases in $(U,Pu)O_2$. The intra-granular migration of fission gas atoms constitutes an elementary mechanism for the fission gas release in the $(U,Pu)O_2$ fuel.

General conclusion

The goal of our study was to contribute to a better understanding of the evolution of the properties of the $(U,Pu)O_2$ MOX fuel under irradiation. To this aim, using the DFT+*U* associated to the SQS method or *ab initio* molecular dynamics, we have first investigated structural, electronic, elastic and thermodynamic properties of $(U,Pu)O_2$. Secondly, we have studied the energetic properties of point defects, as well as the modifications induced by their creation both on the electronic and structural properties of $(U,Pu)O_2$. Third, we have studied the atomic transport properties in $(U,Pu)O_2$ calculating migration energies and mechanisms, as well as the activation energies for self-diffusion. Then, we have determined point defect energetic properties of $(U,Ce)O_2$ and modifications induced on the electronic and structural properties. We have therefore improved the comparison of the point defects properties between $(U,Pu)O_2$ and it experimental surrogate $(U,Ce)O_2$. Finally, we have investigated the fission gases (Kr and Xe) and helium trapping behaviour and solubility in the $(U,Pu)O_2$ matrix. All our results were compared to experimental results or higher scale modelling and major conclusions and perspectives were drawn.

In the first part dedicated to the material properties of pristine $(U,Pu)O_2$, we have first shown the very good description of properties by the DFT+*U* method and the effect of Pu content on these properties. The linear evolution of the lattice parameter as a function of the Pu content was obtained in this study. The electronic properties of $(U,Pu)O_2$, especially a narrowing of the band gap compared to the pure UO_2 and PuO_2 oxides, were also predicted. The narrowing of the band gap is explained by the shift of the Pu *5f* states towards lower energies. Furthermore, we have determined the elastic constants and the bulk modulus of $(U,Pu)O_2$ for various Pu contents. Next, energetic properties of $(U,Pu)O_2$ for various Pu contents were calculated, in particular the enthalpy of formation and the mixing enthalpy, in the entire Pu content range. An excellent accuracy was reached on the enthalpies of formation of the pure oxides UO_2, PuO_2 and Pu_2O_3, with a relative error less than 0.4 % when taking into account the van der Waals long range interactions. The calculation of mixing enthalpy of $(U,Pu)O_2$ yields negative values in the entire Pu content range – using both the direct SQS configurations or a parametric method – in agreement with the formation of a solid solution observed in uranium-plutonium mixed oxides.

A second aspect of the study of bulk $(U,Pu)O_2$ is the calculations of finite temperature properties of $(U,Pu)O_2$ using *ab initio* Molecular Dynamics. We have investigated the radial distribution functions (RDF) of the oxygen and cation sublattices for various temperatures up to 2600 K. For the oxygen sublattice, the RDFs show a solid character up to 2100 K, with a large peak broadening due to the thermal agitation. At 2600 K, a liquid character was found in the RDF. This result means that the oxygen sublattice is already molten at this temperature, suggesting that the Bredig transition has already been reached. As to the cation sublattice, the solid character was observed in the RDFs for all temperatures studied (up to 2600 K). This means that this sublattice is not yet molten and that, in turn, the melting temperature of the compound was not yet reached. The linear thermal expansion of UO_2 and $(U,Pu)O_2$ were also investigated for various

temperatures up to 2000 K. Up to 1000 K, our results agree very well with D. G Martin recommendations used in particular in the ALCYONE and GERMINAL fuel performance codes. Above 1000 K, our results are higher than the recommendations, but within the uncertainties interval of the recommendation as determined by Fink. These higher values are in line with recent measurements of the thermal expansion on UO_2. Qualitatively, we have found a change in the slope of the thermal expansion at around 1000 K, consistent with the evolution of Martin's recommendations. The results on the variation of enthalpy up to 2000 K also show a very good agreement with Fink's experimental recommendations for UO_2 and $(U,Pu)O_2$. For $(U,Pu)O_2$ especially, an increase in the variation of enthalpy is observed for temperatures higher than 1300 K. Finally, the heat capacity of UO_2 and $(U,Pu)O_2$ was investigated up to a temperature of 2000 K. Results were compared to Fink's experimental recommendations for UO_2 and PuO_2, as well as with CALPHAD calculations using the TAF-ID database. Our *ab initio* MD results agree with the recommendations and CALPHAD values up to 1600 K. The increase of the heat capacity at this temperature range is not well captured by our calculations due to the fact that the simulation time does not allow the creation of Frenkel pairs, which are responsible for this increase.

All these results and their agreements with experimental or other modelling results highlight the maturity of the electronic structure calculations and the *ab initio* MD in the description of finite temperature properties of bulk actinide mixed oxides. It thus constitutes a good complement to experimental characterisations. Given their transferability, further studies are envisaged for the study of thermodynamic properties of complex mixed actinide oxides, such as $(U,Pu,Am)O_2$ for which thermodynamic data are scarce. Our *ab initio* MD parametrisation for actinide oxides can also be used for the study of point defects properties at high temperature, as well as the impact of point defects on thermodynamic properties of nuclear fuels.

In the second part, devoted to the point defects and atomic transport properties in PuO_2 and $(U,Pu)O_2$, we have first analysed the modifications induced by the creation of point defects on the electronic and structural properties of $(U,Pu)O_2$. We distinguish three types of defects: the reducing defects (oxygen vacancy (V_O) and actinide interstitials (I_M)), the oxidising defects (oxygen interstitials (I_O) and actinide vacancies (V_M)) and the stoichiometric defects (bound Schottky defects (BSD)). Our study has shown that the presence of neutral reducing defects leads to the reduction of two (for V_O) or four (for I_M) Pu^{4+} cations into Pu^{3+}, accompanied by the introduction of a defect occupied state in the band gap. The Pu^{3+} cations and the defect occupied states disappear when the reducing defects are under formal charge states (Vo^{2+} or I_M^{4+}), where two or four electrons are removed from the supercell. The oxidizing defects, under neutral charge state, induce the oxidation of two (for I_O) or four (for V_M) U^{4+} cations into U^{5+}, without defect electronic state in the band gap. When the defects are under formal charge states, the U^{5+} disappear and an unoccupied defect state is observed in the uranium *5f* density of states. This defect state is not found in the band gap since it is placed at higher energy compared to the plutonium *5f* conduction band which constitutes the conduction band

minimum of the $(U,Pu)O_2$ mixed oxide. For PuO_2, an unoccupied defect state is observed in the band gap for neutral oxidizing defects. Since Pu cations do not oxidize into Pu^{5+}, unoccupied oxygen *2p* states are created on the interstitial itself. When the defects are formally charged, the previous unoccupied state transforms into an occupied state in the band gap. The stoichiometric bound Schottky defects do not yield electronic modifications in $(U,Pu)O_2$. The creation of point defects also induces structural modifications, especially lattice distortions. These distortions are measured in terms of atomic displacements. The displacements affect the oxygen atoms in the first coordination shell of the defects which are pushed closer to the defect (for Vo) or pushed away from the defect (for I_O and V_M). For I_M, first neighbour actinide atoms are pushed away from the defect. These displacements are isotropic for single point defects. Furthermore, the oxygen vacancies lead to an expansion of the lattice parameter while the oxygen interstitials lead to a contraction of the lattice parameter. For the BSD defects, the elastic distortions are anisotropic.

The second aspect of the study of defects is devoted to the energetic properties of point defects. We have first developed a model for the calculation of the range of chemical potentials of each atomic species found in the $(U,Pu)O_2$ mixed oxides. Then, we have shown that the formation energy of oxygen point defects (Io and Vo) depends on the immediate chemical environment, *i.e* the number of Pu cations in the first neighbour position. The formation energy of Vo decreases when the number of Pu in the first coordination sphere increases while the formation energy of Io increases with the increase in the number of Pu cations first neighbours. The effect of the Pu content was also analysed. The formation energy of the oxygen vacancy in $(U,Pu)O_2$ is lower than in pure UO_2 and PuO_2, with a slight variation in the formation energy when the Pu content increases in $(U,Pu)O_2$. The formation energy of the oxygen interstitial is very close to that in UO_2 and lower than that in PuO_2, and its variation with the Pu content is negligible. In $(U,Pu)O_2$, The oxygen vacancy is the most stable defect in hypo-stoichiometric conditions and is stable under neutral charge state for the Fermi level in the middle of the band gap. This indicates that the most stable valence states of cations are U^{4+}, Pu^{3+} and Pu^{4+} in hypo-stoichiometry. This is consistent with the experimental results obtained using X-ray absorption spectroscopy (XAS). For hyper-stoichiometric $(U,Pu)O_2$, the oxygen interstitial is the most favourable defect and is stable under its formal I_O^{2-} charge state for the Fermi level in the middle of the band gap. This indicates that in the hyper-stoichiometric regime, the most stable valence states of cations are U^{4+} and Pu^{4+}. The most stable configuration of the BSD defects is the BSD2 with oxygen vacancies in <110> direction, and those formed with a Pu vacancy are the most stable BSD types.

The last aspect of the defect study is devoted to the determination of migration energies and mechanisms, as well as the activation energies, of the self-diffusion in $(U,Pu)O_2$. We have highlighted the easier migration of the formally charged oxygen vacancy than the neutral one. The oxygen interstitial was also found to migrate easier through the indirect (interstitialcy) mechanism than the direct mechanism under its

formal charge state. The calculation of the activation energy for the self-diffusion in various stoichiometric conditions have shown that the oxygen self-diffusion is vacancy-assisted in the hypo-stoichiometric regime while it is assisted by oxygen interstitials in the hyper-stoichiometric regime, and it takes place through an indirect mechanism. For the cations, the migration energy of neutral vacancies and interstitials (migration of U^{4+} and Pu^{3+}) are lower than those of the formally charged ones (only U^{4+} and Pu^{4+} in the lattice). The increase in Pu content tends to increase the migration energy of cation vacancies, while its impact is negligible for the cation interstitials. Globally, the activation energies for the self-diffusion of cation vacancies are lower than those of cation interstitials. This means that actinide cations migrate through a vacancy mechanism.

The results of this part on point defects and atomic transport properties are of first concern for higher scale modelling techniques. On the one hand, the results on the structural modifications, as well as defect formation energies, are crucial as reference data for the development of interatomic empirical potentials or numerical potentials for the study of charged defects in $(U,Pu)O_2$. On the other hand, the results on the atomic migration and diffusion will be used as database for thermokinetic models, especially the CALPHAD/DICTRA model, for the calculation of the atomic self-diffusion coefficients of the uranium-plutonium mixed oxide fuels.

As perspectives, the influence of defect clusters on the atomic transport properties would be an important step in order to complete our conclusion on the diffusion mechanisms of various species. This kind of studies cannot be currently treated using DFT calculations, but might be possible soon regarding the rapid development of computational resources. It is however planned to be conducted using empirical potentials based techniques which are less computationally demanding compared to the electronic structure calculation methods. Our studies could also be extended to a more detailed analysis of the chemical environments (considering the second and third coordination shell of defect for instance) in the defect formation and migration properties. This will also require a larger supercell and therefore a faster calculation method such as interatomic empirical potential calculations.

In the third part of our study, the modifications induced by the creation of point defects in $(U,Ce)O_2$, as well as the energetic properties of point defects, were treated, and thorough comparisons were made between $(U,Pu)O_2$ and $(U,Ce)O_2$. Our results show that neutral and formally charged reducing defects lead to the same qualitative modifications of the electronic properties as in $(U,Pu)O_2$, and that Pu cations have a similar behaviour as Ce ones. The difference is the lower energy of the defect state in the band gap for the neutral reducing defects. The neutral charge states of the oxidizing defects have a similar impact on the electronic properties as for $(U,Pu)O_2$. However, for the formally charged defects, one U^{5+} and one Ce^{3+} cations are obtained, with an occupied defect state in the band gap. The impact of point defects on the electronic properties of $(U,Ce)O_2$ is thus different to that of $(U,Pu)O_2$. The lattice distortions

induced by point defects in $(U,Ce)O_2$ are also qualitatively similar to those obtained in $(U,Pu)O_2$. However, the amplitude of the distortions in $(U,Ce)O_2$ are different to those obtained for $(U,Pu)O_2$.

Concerning the energetic properties of point defects in $(U,Ce)O_2$, our results show that for the same oxygen chemical potential, the formation energy of the oxygen vacancy is twice as smaller as its value in $(U,Pu)O_2$ while the formation of the oxygen interstitial is similar in both oxides. In the entire range of chemical potentials, the oxygen vacancy is the most favourable defect. Its neutral charge state is the most stable for the Fermi level in the middle of the band gap. This suggests the stability of U^{4+}, Ce^{3+} and Ce^{4+} cation valence states. Moreover, for oxygen chemical potentials higher than -6.86 eV, the cerium vacancy becomes more stable than the oxygen interstitial while the oxygen vacancy remains the most stable defect. This behaviour is different to that obtained in $(U,Pu)O_2$ where the oxygen interstitial was the most favourable defect at higher oxygen chemical potential. The BSD2 configuration and Ce-type of the BSD defects is the most favourable one similarly to $(U,Pu)O_2$. However, the formation energies in the two oxides are quite different, with the energy of BSD_Ce in $(U,Ce)O_2$ lower than that of BSD_Pu in $(U,Pu)O_2$, and the energy of BSD_U slightly higher in $(U,Ce)O_2$ compared to $(U,Pu)O_2$. All these results highlight the notable difference of $(U,Ce)O_2$ and $(U,Pu)O_2$ concerning the point defect properties and their impact on material properties. This suggests in first approximate that these oxides may have different behaviour under irradiation. In order to gain more insight in the limitation of $(U,Ce)O_2$ as a surrogate for $(U,Pu)O_2$, further investigations should consider the defect entropy and the atomic transport properties in $(U,Ce)O_2$. These considerations will improve the understanding of atomic diffusion and thus whether $(U,Pu)O_2$ restructuring under operating condition can be represented or well simulated using $(U,Ce)O_2$ as surrogate.

In the last part of this PhD thesis, we focused on the fission gases (Kr and Xe) and helium (He) trapping and solubility behaviour in the $(U,Pu)O_2$ matrix. We have first studied the incorporation of Kr, Xe and He in six BSD defects, considering the non-local correlations. The BSD1 configuration within the U-type vacancy (BSD1_U) is found favourable for the incorporation of Kr while BSD1_U and BSD3_Pu were found favourable for the incorporation of Xe. The BSD2_U and BSD3_Pu configurations accommodate more favourably the incorporation of He. The solution energies, which take into account the energy needed to create the defect in the perfect crystal, were found to be positive and large, meaning that these gases are highly insoluble in a pristine $(U,Pu)O_2$ matrix. The van der Waals interactions tend to increase this insolubility. The comparison to available results on UO_2 show that our values on $(U,Pu)O_2$ are in the same order of magnitude. Further studies should consider the incorporation of a cluster of fission gases in the BSDs or more extended defects, and the migration of fission gases in $(U,Pu)O_2$ MOX fuel in order to draw consistent fission gas bubble formation and release mechanisms for this compound.

Globally, we can first note the improvement of the predictive character of the electronic structure calculations, within the DFT method, highlighted through this PhD thesis. Therefore, following this PhD, the effect of americium on the defect formation and atomic transport properties will be analysed. Indeed, americium is always found with a non-negligible amount in the fast breeder reactor MOX fuel. The study of its effects on the defect formation and migration of atomic species is therefore required. Then, the method we developed for the calculation of the atomic chemical potentials in $(U,Pu)O_2$ will be extended to other actinide mixed oxides, such as $(U,Am)O_2$, for the investigation of point defects energetic properties for various stoichiometry conditions. Moreover, the combination of our DFT results and the empirical interatomic potentials will allow to develop empirical interatomic potentials enabling the variation of the cation valence state in actinide oxides. Such advance is crucial for the description of the evolution of defects concentration in nuclear fuels under irradiation. The results obtained in our work can also serve as reference database for numerical potentials in machine learning method, for the investigation of point defects properties in $(U,Pu)O_2$. Second, the development of functionals (such as vdW-DF) and methods (such as DMFT) with higher accuracy compared to the currently most used ones, and the rapid development of computational resources, announce a promising future for electronic structure calculations for the description of nuclear fuel materials. In this context, DFT+*U* coupled to *ab initio* MD will rapidly extend its efficiency in the modelling of extended defects as well as temperature-dependent phenomena in actinide oxides and other complex materials. Within these advances, the energetic properties of defects linked to the temperature such as the free energies of formation and migration could be directly calculated using the DFT method. Diffusion coefficients and thermodynamics data will be more readily accessible. Moreover small defect clusters (nano-voids, fission gas clusters, dislocations) and their impact on the material properties could also be analysed. The investigation of the finite temperature properties, which is very resource consuming, would result in an advance in the prediction or refinement of phase diagrams of innovative materials.

References

[1] Onofri, C., Legros, M., Léchelle, J., Palancher, H., Baumier, C., Bachelet, C., and Sabathier, C.,. Full characterization of dislocations in ion-irradiated polycrystalline UO_2. *J. Nucl. Mater.* **494,** 252–259 (2017).

[2] Wiktor, J., Barthe, M.-F., Jomard, G., Torrent, M., Freyss, M., and Bertolus, M. Coupled experimental and DFT+U investigation of positron lifetimes in UO2. *Phys. Rev. B* **90,** 184101 (2014).

[3] Noirot, L. MARGARET: An Advanced Mechanistic Model of Fission Gas Behavior in Nuclear Fuel. *J. Nucl. Sci. Technol.* **43,** 1149–1160 (2006).

[4] Guéneau, C., Dupin, N., Sundman, B., Martial, C., Dumas, J.-C., Gossé, S., Chatain, S., Bruycker, F.D., Manara, D., and Konings, R.J.M. Thermodynamic modelling of advanced oxide and carbide nuclear fuels: Description of the U–Pu–O–C systems. *J. Nucl. Mater.* **419,** 145–167 (2011).

[5] Blöchl, P. E. Projector augmented-wave method. *Phys. Rev. B* **50,** 17953–17979 (1994).

[6] Kresse, G., Hafner, J. Ab initio molecular dynamics for liquid metals. *Phys. Rev. B* **47,** 558–561 (1993).

[7] Kresse, G. and Furthmüller, J. Efficiency of ab-initio total energy calculations for metals and semiconductors using a plane-wave basis set. *Comput. Mater. Sci.* **6,** 15–50 (1996).

[8] Gonze, X., Beuken, J.-M., Caracas, R., Detraux, F., Fuchs, M., Rignanese, G.-M., Sindic, L., Verstraete, M., Zerah, G., and Jollet, F.. First-principles computation of material properties: the ABINIT software project. *Comput. Mater. Sci.* **25,** 478–492 (2002).

[9] Cooper, M. W. D., Murphy, S. T. and Andersson, D. A. The defect chemistry of $UO_{2\pm x}$ from atomistic simulations. *J. Nucl. Mater.* **504,** 251–260 (2018).

[10] Bertolus, M. *et al.* Linking atomic and mesoscopic scales for the modelling of the transport properties of uranium dioxide under irradiation. *J. Nucl. Mater.* **462,** 475–495 (2015).

[11] Dorado, B. *et al.* First-principles calculation and experimental study of oxygen diffusion in uranium dioxide. *Phys. Rev. B* **83,** 035126 (2011).

[12] Bès, R. *et al.* Experimental evidence of Xe incorporation in Schottky defects in UO_2. *Appl. Phys. Lett.* **106,** 114102 (2015).

[13] EC 7FP F-Bridge (2008 - 2012) - University of Latvia. (2018). Available at: https://www.cfi.lu.lv/eng/projects/ec-framework-projects/ec-7fp-f-bridge-2008-2012/. (Accessed: 4th September 2018)

[14] Investigations Supporting MOX Fuel Licensing in ESNII Prototype Reactors | Projects | H2020. *CORDIS | European Commission* (2018). Available at: https://cordis.europa.eu/project/rcn/210822_en.html. (Accessed: 4th September 2018)

[15] Klimeš, J., Bowler, D. R. and Michaelides, A. Chemical accuracy for the van der Waals density functional. *J. Phys. Condens. Matter* **22,** 022201 (2010).

[16] Klimeš, J., Bowler, D. R. and Michaelides, A. Van der Waals density functionals applied to solids. *Phys. Rev. B* **83,** 195131 (2011).

[17] Martin, P. *et al. Catalog on MOX properties for fast reactors*. (ESNII+ report, 2017).

[18] Noirot, J., Desgranges, L. and Lamontagne, J. Detailed characterisations of high burn-up structures in oxide fuels. *J. Nucl. Mater.* **372,** 318–339 (2008).

[19] Riglet-Martial, C. *et al.* Experimental evidence of oxygen thermo-migration in PWR UO_2 fuels during power ramps using in-situ oxido-reduction indicators. *J. Nucl. Mater.* **480**, 32-39 (2016).

[20] Parrish, R. and Aitkaliyeva, A. A review of microstructural features in fast reactor mixed oxide fuels. *J. Nucl. Mater.* doi:10.1016/j.jnucmat.2018.05.076

[21] Garcia, P. *et al.* Nucleation and growth of intragranular defect and insoluble atom clusters in nuclear oxide fuels. *Nucl. Instrum. Methods Phys. Res. Sect. B Beam Interact. Mater. At.* **277,** 98–108 (2012).

[22] Markin, T. L. and Street, R. S. The uranium-plutonium-oxygen ternary phase diagram. *J. Inorg. Nucl. Chem.* **29,** 2265–2280 (1967).

[23] Sari, C., Benedict, U. and Blank, H. A study of the ternary system $U0_2$-$Pu0_2$-Pu_20_3. *J. Nucl. Mater.* **35,** 267–277 (1970).

[24] Belin, R. C. *et al.* In situ high temperature X-Ray diffraction study of the phase equilibria in the UO_2–PuO_2–Pu_2O_3 system. *J. Nucl. Mater.* **465,** 407–417 (2015).

[25] Truphémus, T. *et al.* Structural studies of the phase separation in the UO_2–PuO_2–Pu_2O_3 ternary system. *J. Nucl. Mater.* **432,** 378–387 (2013).

[26] Lukas, H. L., Fries, S. G. and Sundman, B. *Computational thermodynamics: the CALPHAD method*. (Cambridge University Press, 2007).

[27] Devanathan, R. *et al.* Modeling and simulation of nuclear fuel materials. *Energy Environ. Sci.* **3,** 1406 (2010).

[28] NEA Nuclear Science Commitee and OECD. Thermodynamics of Advanced Fuels – International Database (TAF-ID). Available at: https://www.oecd-nea.org/science/taf-id/. (Accessed: 11th July 2018)

[29] Komeno, A. *et al.* Phase separation behaviour of $(U_{0.7}Pu_{0.3})O_{2-x}$ (1.92<x<2.00) based fuels containing actinides and/or lanthanides. *IOP Conf. Ser. Mater. Sci. Eng.* **9,** 012016 (2010).

[30] Dean, G., Boivineau, J. C., Chereau, P. and Marcon, J. P. Contribution à l'étude du système U-Pu-0. *Fourth International Conference on Plutonium and other Actinides* (1970).

[31] Strach, M., Belin, R. C., Richaud, J.-C. and Rogez, J. High Temperature X-ray Diffraction Study of the Oxidation Products and Kinetics of Uranium–Plutonium Mixed Oxides. *Inorg. Chem.* **53,** 12757–12766 (2014).

[32] McEachern, R. J. and Taylor, P. A review of the oxidation of uranium dioxide at temperatures below 400°C. *J. Nucl. Mater.* **254,** 87–121 (1998).

[33] Desgranges, L., Baldinozzi, G., Rousseau, G., Nièpce, J.-C. and Calvarin, G. Neutron Diffraction Study of the in Situ Oxidation of UO_2. *Inorg. Chem.* **48,** 7585–7592 (2009).

[34] Martin, P. *et al.* XAS study of $(U_{1-y}Pu_y)O_2$ solid solutions. *J. All. Comp.* **444–445,** 410–414 (2007).

[35] Vauchy, R., Robisson, A.-C., Audubert, F. and Hodaj, F. Ceramic processing of uranium–plutonium mixed oxide fuels $(U_{1-y}Pu_y)O_2$ with high plutonium content. *Ceram. Int.* **40,** 10991–10999 (2014).

[36] Vegard, L. Die Konstitution der Mischkristalle und die Raumfüllung der Atome. *Z. Für Phys.* **5,** 17–26 (1921).

[37] Thuemmler, F., Kleykamp, H. and Hofmann, P. Chemical factors influence on the irradiation behaviour of oxide fuels. *J. Nucl. Mater.* **81,** 215–230 (1979).

[38] Brett, N. H. and Fox, A. C. Oxidation products of plutonium dioxide-uranium dioxide solid solutions in air at 750°C. *J. Inorg. Nucl. Chem.* **28,** 1191–1203 (1966).

[39] Lyon, W. L. and Baily, W. E. The solid-liquid phase diagram for the UO2-PuO2 system. *J. Nucl. Mater.* **22,** 332–339 (1967).

[40] Nakayama, Y. A phase study on the tie line of U_3O_7-PuO_2. *J. Inorg. Nucl. Chem.* **33,** 4077–4084 (1971).

[41] Jayadevan, N. C., Hadap, R. G. and Chackraburtty, D. M. The oxidation behaviour of 30 wt% PuO-UO_2 solid solution. *J. Nucl. Mater.* **82,** 195–198 (1979).

[42] Duriez, C., Alessandri, J.-P., Gervais, T. and Philipponneau, Y. Thermal conductivity of hypostoichiometric low Pu content (U,Pu)O_{2-x} mixed oxide. *J. Nucl. Mater.* **277,** 143–158 (2000).

[43] Grandjean, S. *et al.* Structure of mixed U(IV)–An(III) precursors synthesized by co-conversion methods (where An=Pu, Am or Cm). *J. Nucl. Mater.* **385,** 204–207 (2009).

[44] Kato, M. and Konashi, K. Lattice parameters of (U, Pu, Am, Np)O_{2-x}. *J. Nucl. Mater.* **385,** 117–121 (2009).

[45] Beauvy, M. Nonideality of the solid solution in (U, Pu)O_2 nuclear fuels. *J. Nucl. Mater.* **188,** 232–238 (1992).

[46] Cooper, M. W. D., Murphy, S. T., Rushton, M. J. D. and Grimes, R. W. Thermophysical properties and oxygen transport in the (U_x,Pu_{1-x})O_2 lattice. *J. Nucl. Mater.* **461,** 206–214 (2015).

[47] Dorado, B. and Garcia, P. First-principles DFT+*U* modeling of actinide-based alloys: Application to paramagnetic phases of UO_2 and (U,Pu) mixed oxides. *Phys. Rev. B* **87,** 195139 (2013).

[48] Yang, Y., Wang, B. and Zhang, P. Electronic and mechanical properties of ordered (Pu, U) O_2 compounds: A density functional theory +U study. *J. Nucl. Mater.* **433,** 345–350 (2013).

[49] Vigier, J.-F. *et al.* Structural Investigation of ($U_{0.7}Pu_{0.3}$)O_{2-x} Mixed Oxides. *Inorg. Chem.* **54,** 5358–5365 (2015).

[50] Sali, S. K., Kulkarni, N. K., Phatak, R. and Agarwal, R. Oxidation behaviour of plutonium rich (U, Pu)C and (U, Pu)O_2. *J. Nucl. Mater.* **479,** 623–632 (2016).

[51] Ma, J. *et al.* Molecular dynamical study of physical properties of ($U_{0.75}Pu_{0.25}$)O_{2-x}. *J. Nucl. Mater.* **452,** 230–234 (2014).

[52] Vauchy, R. *et al.* Room-temperature oxidation of hypostoichiometric uranium–plutonium mixed oxides $U_{1-y}Pu_yO_{2-x}$ – A depth-selective approach. *J. Nucl. Mater.* **465,** 349–357 (2015).

[53] Freyss, M., Petit, T. and Crocombette, J.-P. Point defects in uranium dioxide: Ab initio pseudopotential approach in the generalized gradient approximation. *J. Nucl. Mater.* **347,** 44–51 (2005).

[54] Yu, S.-W. *et al.* f-f origin of the insulating state in uranium dioxide: X-ray absorption experiments and first-principles calculations. *Phys. Rev. B* **83,** 165102 (2011).

[55] Santini, P. *et al.* Multipolar interactions in f-electron systems: The paradigm of actinide dioxides. *Rev. Mod. Phys.* **81,** 807–863 (2009).

[56] Colarieti-Tosti, M., Eriksson, O., Nordström, L., Wills, J. and Brooks, M. S. S. Crystal-field levels and magnetic susceptibility in PuO_2. *Phys. Rev. B* **65,** 195102 (2002).

[57] Kern, S. *et al.* Crystal-field transition in PuO_2. *Phys. Rev. B* **59,** 104–106 (1999).

[58] Ma, L. and Ray, A. K. An ab initio study of $PuO_{2\pm0.25}$, $UO_{2\pm0.25}$, and $U_{0.5}Pu_{0.5}O_{2\pm0.25}$. *Eur. Phys. J. B* **81,** 103 (2011).

[59] Baer, Y. and Schoenes, J. Electronic structure and Coulomb correlation energy in UO_2 single crystal. *Solid State Commun.* **33,** 885–888 (1980).

[60] Myers, H. P., Jonsson, T. and Westin, R. Intrinsic semiconduction in uranium dioxide. *Solid State Commun.* **2,** 321–322 (1964).

[61] Bates, J. L., Hinman, C. A. and Kawada, T. Electrical Conductivity of Uranium Dioxide. *J. Am. Ceram. Soc.* **50,** 652–656 (1967).

[62] Killeen, J. C. The effect of niobium oxide additions on the electrical conductivity of UO_2. *J. Nucl. Mater.* **88,** 185–192 (1980).

[63] Jollet, F. *et al.* The electronic structure of uranium dioxide: an oxygen K-edge X-ray absorption study. *J. Phys. Condens. Matter* **9,** 9393 (1997).

[64] Dorado, B. Étude des propriétés de transport atomique dans la dioxyde d'uranium par le calcul de structure électronique: influence des fortes corrélations. (PhD thesis, Aix-Marseille Université, 2010).

[65] Vathonne, E. Étude par calcul de structure électronique des dégâts d'irradiation dans le combustible nucléaire UO_2: comportement des défauts ponctuels et gaz de fission. (PhD thesis, Aix-Marseille Université, 2014).

[66] McNeilly, C. E. The electrical properties of plutonium oxides. *J. Nucl. Mater.* **11,** 53–58 (1964).

[67] McCleskey, T. M. *et al.* Optical band gap of NpO_2 and PuO_2 from optical absorbance of epitaxial films. *J. Appl. Phys.* **113,** 013515 (2013).

[68] Wen, X.-D., Martin, R. L., Henderson, T. M. and Scuseria, G. E. Density Functional Theory Studies of the Electronic Structure of Solid State Actinide Oxides. *Chem. Rev.* **113,** 1063–1096 (2013).

[69] Sun, B., Zhang, P. and Zhao, X.-G. First-principles local density approximation+*U* and generalized gradient approximation+U study of plutonium oxides. *J. Chem. Phys.* **128,** 084705 (2008).

[70] Ao, B. *et al.* First-Principles Energetics of Some Nonmetallic Impurity Atoms in Plutonium Dioxide. *J. Phys. Chem. C* **119,** 14879–14889 (2015).

[71] Tian, X., Gao, T., Lu, C., Shang, J. and Xiao, H. First principle study of the behavior of helium in plutonium dioxide. *Eur. Phys. J. B* **86,** 179 (2013).

[72] Hernandez, S. C. and Holby, E. F. DFT+*U* Study of Chemical Impurities in PuO_2. *J. Phys. Chem. C* **120,** 13095–13102 (2016).

[73] Wachtman, J. B., Wheat, M. L., Anderson, H. J. and Bates, J. L. Elastic constants of single crystal UO_2 at 25° C. *J. Nucl. Mater.* **16,** 39–41 (1965).

[74] Fritz, I. J. Elastic properties of UO_2 at high pressure. *J. Appl. Phys.* **47,** 4353–4358 (1976).

[75] Idiri, M., Le Bihan, T., Heathman, S. and Rebizant, J. Behavior of actinide dioxides under pressure: UO_2 and ThO_2. *Phys. Rev. B* **70,** 014113 (2004).

[76] Andersson, D. A., Lezama, J., Uberuaga, B. P., Deo, C. and Conradson, S. D. Cooperativity among defect sites in AO_{2+x} and A_4O_9 (A=U, Np, Pu): Density functional calculations. *Phys. Rev. B* **79,** 024110 (2009).

[77] Zhang, P., Wang, B.-T. and Zhao, X.-G. Ground-state properties and high-pressure behavior of plutonium dioxide: Density functional theory calculations. *Phys. Rev. B* **82,** 144110 (2010).

[78] Martin, D. G. The elastic constants of polycrystalline UO_2 and (U,Pu) mixed oxides: a review and recommendations. *High Temp. - High Press.* **21,** 13–24 (1989).

[79] Ma, L., Atta-Fynn, R. and Ray, A. K. Elemental and mixed actinide dioxides: an *ab* initio study. *J. Theor. Comput. Chem.* **11,** 611–629 (2012).

[80] Arima, T., Yamasaki, S., Inagaki, Y. and Idemitsu, K. Evaluation of thermal conductivity of hypostoichiometric (U, Pu)O_{2-x} solid solution by molecular dynamics simulation at temperatures up to 2000 K. *J. Alloys Compd.* **415,** 43–50 (2006).

[81] Balboa, H., Van Brutzel, L., Chartier, A. and Le Bouar, Y. Assessment of empirical potential for MOX nuclear fuels and thermomechanical properties. *J. Nucl. Mater.* **495,** 67–77 (2017).

[82] Hausner, H. Determination of the melting point of uranium dioxide. *J. Nucl. Mater.* **15,** 179–183 (1965).

[83] Latta, R. E. and Fryxell, R. E. Determination of solidus-liquidus temperatures in the UO_{2+x} system (- 0.50< x< 0.20). *J. Nucl. Mater.* **35,** 195–210 (1970).

[84] Carbajo, J. J., Yoder, G. L., Popov, S. G. and Ivanov, V. K. A review of the thermophysical properties of MOX and UO_2 fuels. *J. Nucl. Mater.* **299,** 181–198 (2001).

[85] Hough, A. and Marples, J. A. C. The pseudo binary phase diagrams of PuO_2 with alumina, beryllia and magnesia and the pseudo ternary PuO_2-ThO_2-BeO. *J. Nucl. Mater.* **15,** 298–309 (1965).

[86] De Bruycker, F. *et al.* Reassessing the melting temperature of PuO_2. *Mater. Today* **13,** 52–55 (2010).

[87] Hiernaut, J. P., Hyland, G. J. and Ronchi, C. Premelting transition in uranium dioxide. *Int. J. Thermophys.* **14,** 259–283 (1993).

[88] Basak, C. B. and Kolokol, A. S. A Novel Pseudo-Ion Approach in Classical MD Simulation: A Case Study on $(U_{0.8}Pu_{0.2})O_2$ Mixed Oxide. *J. Am. Ceram. Soc.* **95,** 1435–1439 (2012).

[89] Kato, M., Ikusawa, Y., Sunaoshi, T., Nelson, A. T. and McClellan, K. J. Thermal expansion measurement of $(U,Pu)O_{2-x}$ in oxygen partial pressure-controlled atmosphere. *J. Nucl. Mater.* **469,** 223–227 (2016).

[90] Martin, D. G. The thermal expansion of solid UO_2 and (U, Pu) mixed oxides — a review and recommendations. *J. Nucl. Mater.* **152,** 94–101 (1988).

[91] Oetting, F. L. The chemical thermodynamics of nuclear materials. VII. the high-temperature enthalpy of plutonium dioxide. *J. Nucl. Mater.* **105,** 257–261 (1982).

[92] Fink, J. K. Thermophysical properties of uranium dioxide. *J. Nucl. Mater.* **279,** 1–18 (2000).

[93] Yamashita, T., Nitani, N., Tsuji, T. and Inagaki, H. Thermal expansions of NpO_2 and some other actinide dioxides. *J. Nucl. Mater.* **245,** 72–78 (1997).

[94] Kato, M. *et al.* Thermal expansion measurement and heat capacity evaluation of hypo-stoichiometric $PuO_{2.00}$. *J. Nucl. Mater.* **451,** 78–81 (2014).

[95] Konings, R. J. M. and Beneš, O. The heat capacity of NpO_2 at high temperatures: The effect of oxygen Frenkel pair formation. *J. Phys. Chem. Solids* **74,** 653–655 (2013).

[96] Nakamura, H., Machida, M. and Kato, M. First-Principles Calculation of Phonon and Schottky Heat Capacities of Plutonium Dioxide. *J. Phys. Soc. Jpn.* **84,** 053602 (2015).

[97] Leibowitz, L., Fischer, D. F. and Chasanov, M. G. Enthalpy of uranium-plutonium oxides: $(U_{0.8}Pu_{0.2})O_{1.97}$ from 2350 to 3000 K. *J. Nucl. Mater.* **42,** 113–116 (1972).

[98] Gibby, R. L., Leibowitz, L., Kerrisk, J. F. and Clifton, D. G. Analytical expressions for enthalpy and heat capacity for uranium-plutonium oxide. *J. Nucl. Mater.* **50,** 155–161 (1974).

[99] Fink, J. K. Enthalpy and heat capacity of the actinide oxides. *Int. J. Thermophys.* **3,** 165–200 (1982).

[100] Harding, J. H., Martin, D. G. and Potter, P. E. Report EUR 12402 EN: Thermophysical and thermochemical properties of fast reactor materials. (1989).

[101] Kandan, R., Babu, R., Nagarajan, K. and Vasudeva Rao, P. R. Calorimetric measurements on uranium–plutonium mixed oxides. *J. Nucl. Mater.* **324,** 215–219 (2004).

[102] Vasudeva Rao, P. R., Anthonysamy, S., Krishnaiah, M. V. and Chandramouli, V. Oxygen potential and thermal conductivity of (U, Pu) mixed oxides. *J. Nucl. Mater.* **348,** 329–334 (2006).

[103] Morimoto, K., Kato, M. and Ogasawara, M. Thermal diffusivity measurement of (U, Pu)O_{2-x} at high temperatures up to 2190 K. *J. Nucl. Mater.* **443,** 286–290 (2013).

[104] Green, M. S. Markoff Random Processes and the Statistical Mechanics of Time-Dependent Phenomena. II. Irreversible Processes in Fluids. *J. Chem. Phys.* **22,** 398–413 (1954).

[105] Washington, A. B. . UKAEA, TRG Report. **2236,** (1973).

[106] Philipponneau, Y. Thermal conductivity of (U,Pu)O_{2-x} mixed oxyde fuel. *J. Nucl. Mater* **188,** 194–197 (1992).

[107] Cooper, M. W. D., Middleburgh, S. C. and Grimes, R. W. Modelling the thermal conductivity of (U_xTh_{1-x})O_2 and (U_xPu_{1-x})O_2. *J. Nucl. Mater.* **466,** 29–35 (2015).

[108] Klemens, P. G. The Thermal Conductivity of Dielectric Solids at Low Temperatures (Theoretical). *Proc. R. Soc. Lond. Math. Phys. Eng. Sci.* **208,** 108–133 (1951).

[109] Klemens, P. G. The Scattering of Low-Frequency Lattice Waves by Static Imperfections. *Proc. Phys. Soc. Sect. A* **68,** 1113 (1955).

[110] Klemens, P. G. Thermal Resistance due to Point Defects at High Temperatures. *Phys. Rev.* **119,** 507–509 (1960).

[111] Callaway, J. Model for Lattice Thermal Conductivity at Low Temperatures. *Phys. Rev.* **113,** 1046–1051 (1959).

[112] Callaway, J. and von Baeyer, H. C. Effect of Point Imperfections on Lattice Thermal Conductivity. *Phys. Rev.* **120,** 1149–1154 (1960).

[113] Abeles, B. Lattice Thermal Conductivity of Disordered Semiconductor Alloys at High Temperatures. *Phys. Rev.* **131,** 1906–1911 (1963).

[114] Adachi, S. Lattice thermal resistivity of III–V compound alloys. *J. Appl. Phys.* **54,** 1844–1848 (1983).

[115] Adachi, S. Lattice thermal conductivity of group-IV and III–V semiconductor alloys. *J. Appl. Phys.* **102,** 063502 (2007).

[116] Crocombette, J. P., Jollet, F., Nga, L. T. and Petit, T. Plane-wave pseudopotential study of point defects in uranium dioxide. *Phys. Rev. B* **64,** 104107 (2001).

[117] Crocombette, J.-P., Torumba, D. and Chartier, A. Charge states of point defects in uranium oxide calculated with a local hybrid functional for correlated electrons. *Phys. Rev. B* **83,** 184107 (2011).

[118] Vathonne, E., Wiktor, J., Freyss, M., Jomard, G. and Bertolus, M. DFT+*U* investigation of charged point defects and clusters in UO_2. *J. Phys. Condens. Matter* **26,** 325501 (2014).

[119] Shi, L., Vathonne, E., Oison, V., Freyss, M. and Hayn, R. First-principles DFT+*U* investigation of charged states of defects and fission gas atoms in CeO_2. *Phys. Rev. B* **94,** 115132 (2016).

[120] Crocombette, J.-P. Influence of charge states on energies of point defects and clusters in uranium dioxide. *Phys. Rev. B* **85,** 144101 (2012).

[121] Nerikar, P., Watanabe, T., Tulenko, J. S., Phillpot, S. R. and Sinnott, S. B. Energetics of intrinsic point defects in uranium dioxide from electronic-structure calculations. *J. Nucl. Mater.* **384,** 61–69 (2009).

[122] Lei, S. Études par calcul de structure électronique des dioxydes d'uranium et de cérium contenant des défauts et des impuretés. (PhD thesis, Aix Marseille Université, 2016).

[123] Matzke, H. Atomic transport properties in UO_2 and mixed oxides $(U, Pu)O_2$. *J. Chem. Soc. Faraday Trans. 2 Mol. Chem. Phys.* **83,** 1121–1142 (1987).

[124] Bayoglu, A. S., Giordano, A. and Lorenzelli, R. Mesure de l'autodiffusion de l'oxygene dans $PuO_{2.00}$ par echange isotopique. *J. Nucl. Mater.* **113,** 71–74 (1983).

[125] Bayoglu, A. S. and Lorenzelli, R. Etude de la diffusion chimique de l'oxygene dans PuO_{2-x} par dilatometrie et thermogravimetrie. *J. Nucl. Mater.* **82,** 403–410 (1979).

[126] Kim, K. C. and Olander, D. R. Oxygen diffusion in UO_{2-x}. *J. Nucl. Mater.* **102,** 192–199 (1981).

[127] Moore, E., Guéneau, C. and Crocombette, J.-P. Oxygen diffusion model of the mixed (U,Pu)$O_{2\pm x}$: Assessment and application. *J. Nucl. Mater.* **485,** 216–230 (2017).

[128] Moore, E., Guéneau, C. and Crocombette, J.-P. Diffusion model of the non-stoichiometric uranium dioxide. *J. Solid State Chem.* **203,** 145–153 (2013).

[129] Dorado, B. *et al.* Advances in first-principles modelling of point defects in UO_2 : f electron correlations and the issue of local energy minima. *J. Phys. Condens. Matter* **25,** 333201 (2013).

[130] Iwasawa, M. *et al.* First-Principles Calculation of Point Defects in Uranium Dioxide. *Materials Transactios* **47,** 2651–2657 (2006).

[131] Gupta, F., Brillant, G. and Pasturel, A. Correlation effects and energetics of point defects in uranium dioxide: a first principle investigation. *Philos. Mag.* **87,** 2561–2569 (2007).

[132] Tiwary, P., van de Walle, A. and Grønbech-Jensen, N. *Ab* initio construction of interatomic potentials for uranium dioxide across all interatomic distances. *Phys. Rev. B* **80,** 174302 (2009).

[133] Yu, J., Devanathan, R. and Weber, W. J. First-principles study of defects and phase transition in UO 2. *J. Phys. Condens. Matter* **21,** 435401 (2009).

[134] Petit, T., Lemaignan, C., Jollet, F., Bigot, B. and Pasturel, A. Point defects in uranium dioxide. *Philos. Mag. B* **77,** 779–786 (1998).

[135] Lu, Y., Yang, Y. and Zhang, P. Charge states of point defects in plutonium oxide: A first-principles study. *J. Alloys Compd.* **649,** 544–552 (2015).

[136] Grégory, G., François, B. and Marc, T. Oxygen vacancies and self-trapped electronic polarons in PuO_2.

[137] Petit, L., Svane, A., Szotek, Z. and Temmerman, W. M. First-Principles Calculations of PuO2±x. *Science* **301,** 498 (2003).

[138] Sun, B. *et al.* The environmental dependence of redox energetics of PuO_2 and α-Pu_2O_3: A quantitative solution from. *Phys. Lett. A* **376,** 2672–2676 (2012).

[139] Taylor, S. E. and Bruneval, F. Understanding and correcting the spurious interactions in charged supercells. *Phys. Rev. B* **84,** (2011).

[140] Freyss, M., Vergnet, N. and Petit, T. Ab initio modeling of the behavior of helium and xenon in actinide dioxide nuclear fuels. *J. Nucl. Mater.* **352,** 144–150 (2006).

[141] Tiwary, P., van de Walle, A., Jeon, B. and Grønbech-Jensen, N. Interatomic potentials for mixed oxide and advanced nuclear fuels. *Phys. Rev. B* **83,** 094104 (2011).

[142] Na-Phattalung, S. *et al.* First-principles study of native defects in anatase TiO_2. *Phys. Rev. B* **73,** 125205 (2006).

[143] Hong, M. *et al.* Solubility and clustering of ruthenium fission products in uranium dioxide as determined by density functional theory. *Phys. Rev. B* **85,** (2012).

[144] Finnis, M. W., Lozovoi, A. Y. and Alavi, A. The oxidation of NIAL: What Can We Learn from Ab Initio Calculations? *Annu. Rev. Mater. Res.* **35,** 167–207 (2005).

[145] Nerikar, P., Watanabe, T., Tulenko, J. S., Phillpot, S. R. and Sinnott, S. B. Energetics of intrinsic point defects in uranium dioxide from electronic-structure calculations. *J. Nucl. Mater.* **384,** 61–69 (2009).

[146] Lidiard, A. B. Self-diffusion of uranium in UO_2. *J. Nucl. Mater.* **19,** 106–108 (1966).

[147] Garcia, P. *et al.* A defect model for UO_{2+x} based on electrical conductivity and deviation from stoichiometry measurements. *J. Nucl. Mater.* **494,** 461–472 (2017).

[148] Bruneval, F., Freyss, M. and Crocombette, J.-P. Lattice constant in nonstoichiometric uranium dioxide from first principles. *Phys. Rev. Mater.* **2,** 023801 (2018).

[149] Geng, H. Y. *et al.* Point defects and clustering in uranium dioxide by LSDA+*U* calculations. *Phys. Rev. B* **77,** 104120 (2008).

[150] Geng, H. Y., Chen, Y., Kaneta, Y. and Kinoshita, M. Stability mechanism of cuboctahedral clusters in UO_{2+x} : First-principles calculations. *Phys. Rev. B* **77,** (2008).

[151] Ma, Y. A study of point defects in UO_{2+x} and their impact upon fuel properties. (PhD thesis, Aix Marseille Université, 2017).

[152] Amsel, G. and Samuel, D. Microanalysis of the stable isotopes of oxygen by means of nuclear reactions. *Anal. Chem.* **39,** 1689–1698 (1967).

[153] Yajima, S., Furuya, H. and Hirai, T. Lattice and grain-boundary diffusion of uranium in UO_2. *J. Nucl. Mater.* **20,** 162–170 (1966).

[154] Auskern, A. B. and Belle, J. Oxygen ion self-diffusion in uranium dioxide. *J. Nucl. Mater.* **3,** 267–276 (1961).

[155] Matzke, H. On uranium self-diffusion in UO_2 and UO_{2+x}. *J. Nucl. Mater.* **30,** 26–35 (1969).

[156] Schmitz, F. and Lindner, R. Diffusion of heavy elements in nuclear fuels: actinides in UO_2. *J. Nucl. Mater.* **17,** 259–269 (1965).

[157] Sabioni, A. C. S., Ferraz, W. B. and Millot, F. First study of uranium self-diffusion in UO_2 by SIMS. *J. Nucl. Mater.* **257,** 180–184 (1998).

[158] Berthinier, C., Rado, C., Chatillon, C. and Hodaj, F. Thermodynamic assessment of oxygen diffusion in non-stoichiometric $UO_{2\pm x}$ from experimental data and Frenkel pair modeling. *J. Nucl. Mater.* **433,** 265–286 (2013).

[159] Willis, B. T. M. The defect structure of hyper-stoichiometric uranium dioxide. *Acta Crystallogr. A* **34,** 88–90 (1978).

[160] Fryxell, R. E., Joyce, D. E. and Szwarc, R. *J. Nucl. Mater* **25,** 97 (1968).

[161] Contamin, P., Bacmann, J. J. and Marin, J. F. Autodiffusion de l'oxygene dans le dioxyde d'uranium surstoechiometrique. *J. Nucl. Mater.* **42,** 54–64 (1972).

[162] Murch, G. E., Bradhurst, D. H. and Bruin, H. J. D. Oxygen self-diffusion in non-stoichiometric uranium dioxide. *Philos. Mag. J. Theor. Exp. Appl. Phys.* **32,** 1141–1150 (1975).

[163] Garcia, P. *et al.* Oxygen diffusion in relation to p-type doping in uranium dioxide. *J. Nucl. Mater.* **400,** 112–118 (2010).

[164] Morelon, N.-D., Ghaleb, D., Delaye, J.-M. and Brutzel, L. V. A new empirical potential for simulating the formation of defects and their mobility in uranium dioxide. *Philos. Mag.* **83,** 1533–1555 (2003).

[165] Alcock, C. B., Hawkins, R. J., Hills, A. W. D. and McNamara, P. A Study of Cation Diffusion in Stoichiometric UO_2 Using α-Ray Spectrometry. *Thermodyn. Vol II Proc. Symp. Thermodyn. Emphas. Nucl. Mater. At. Transp. Solids* (1966).

[166] Matzke, H. Lattice disorder and metal self-diffusion in non-stoichiometric UO_2 and (U, Pu)O_2 | Supplément au Journal de Physique Colloques. *J. Phys. Colloq.* **34,** C9-317-C9-325 (1973).

[167] Lindner, R. and Schmitz, F. Diffusion von Uran-233 in Urandioxyd. *Z. Für Naturforschung A* **16,** 1373–1378 (1961).

[168] Dorado, B. *et al.* First-principles calculations of uranium diffusion in uranium dioxide. *Phys. Rev. B* **86,** 035110 (2012).

[169] Andersson, D. A., Uberuaga, B. P., Nerikar, P. V., Unal, C. and Stanek, C. R. U and Xe transport in $UO_{2\pm x}$: Density functional theory calculations. *Phys. Rev. B* **84,** (2011).

[170] Deaton, R. L. and Wiedenheft, C. J. Self-diffusion of oxygen in $^{238}PuO_2$. *J. Inorg. Nucl. Chem.* **35,** 649–650 (1973).

[171] Chereau, P. and Wadier, J.-F. Mésures de résistivite et de cinétique d'oxydation dans PuO_{2-x}. *J. Nucl. Mater.* **46,** 1–8 (1973).

[172] Kutty, T. R. G. *et al.* Densification behaviour and sintering kinetics of PuO_2 pellets. *J. Nucl. Mater.* **297,** 120–128 (2001).

[173] Kato Masato, Uchida Teppei and Sunaoshi Takeo. Measurement of oxygen chemical diffusion in PuO_{2-x} and analysis of oxygen diffusion in PuO_{2-x} and $(Pu,U)O_{2-x}$. *Phys. Status Solidi C* **10,** 189–192 (2012).

[174] Crank, J. *The Mathematics of Diffusion*. (Clarendon Press, 1979).

[175] D'Annucci, F. and Sari, C. Oxygen diffusion in uranium-plutonium oxide fuel at low temperature. *J. Nucl. Mater*. **68**, 357-359 (1977)

[176] Sari, C. Oxygen chemical diffusion coefficient of uranium-plutonium oxides. *J. Nucl. Mater.* **78,** 425–426 (1978).

[177] Bayoglu, A. S. and Lorenzelli, R. Diffusion chimique de l'oxygène dans $(U, Pu)O_{2-x}$. *J. Nucl. Mater.* **79,** 437–438 (1979).

[178] Bayoglu, A. S. and Lorenzelli, R. Diffusion chimique de l'oxygène dans $(U,Pu)\ O_{2+x}$. *J. Nucl. Mater.* **88,** 315–316 (1980).

[179] Bayoğlu, A. S. and Lorenzelli, R. Oxygen diffusion in fcc fluorite type nonstoichiometric nuclear oxides $MO_{2\pm x}$. *Solid State Ion.* **12,** 53–66 (1984).

[180] Kato, M. *et al.* Oxygen chemical diffusion in hypo-stoichiometric MOX. *J. Nucl. Mater.* **389,** 416–419 (2009).

[181] Vauchy, R. *et al.* Oxygen self-diffusion in polycrystalline uranium–plutonium mixed oxide $U_{0.55}Pu_{0.45}O_2$. *J. Nucl. Mater.* **467, Part 2,** 886–893 (2015).

[182] Vauchy, R. Etude du rapport O/M dans des nouveaux combustibles oxydes à base d'U et Pu : élaboration et caractérisation de matériaux modèles $U_{1-y}Pu_yO_{2-x}$. (PhD thesis, Université de Grenoble, 2014).

[183] Kato, M., Konashi, K. and Nakae, N. Analysis of oxygen potential of $(U_{0.7}Pu_{0.3})O_{2\pm x}$ and $(U_{0.8}Pu_{0.2})O_{2\pm x}$ based on point defect chemistry. *Thermochem. Thermophys. Nucl. Mater. Twelfth Symp. Thermochem. Thermophys. Nucl. Mater.* **389,** 164–169 (2009).

[184] Kofstad, P. Nonstoichiometry, diffusion, and electrical conductivity in binary metal oxides. (1972).

[185] Schmitz, F. and Marajofsky, A. Self-diffusion of plutonium in (U,Pu)O_{2-x}: role of the oxygen potential and the plutonium content. *Thermodyn. Nucl. Mater. 1974* (1975).

[186] Matzke, H. Lattice defects and irradiation damage in ThO_2, UO_2 and (U,Pu)O_2. *Plutonium 1975 Actin.* (1976).

[187] A. Jackson, R., A. Catlow, C. R. and Dixon Murray, A. Point-defect calculations on UO 2. *J. Chem. Soc. Faraday Trans. 2 Mol. Chem. Phys.* **83,** 1171–1176 (1987).

[188] Jackson, R. A., Murray, A. D., Harding, J. H. and Catlow, C. R. A. The calculation of defect parameters in UO2. *Philos. Mag. A* **53,** 27–50 (1986).

[189] Zunger, A., Wei, S.-H., Ferreira, L. G. and Bernard, J. E. Special quasirandom structures. *Phys. Rev. Lett.* **65,** 353–356 (1990).

[190] Hohenberg, P. and Kohn, W. Inhomogeneous Electron Gas. *Phys. Rev.* **136,** B864–B871 (1964).

[191] Kohn, W. and Sham, L. J. Self-Consistent Equations Including Exchange and Correlation Effects. *Phys. Rev.* **140,** A1133–A1138 (1965).

[192] Wigner, E. On the Interaction of Electrons in Metals. *Phys. Rev.* **46,** 1002–1011 (1934).

[193] Ceperley, D. M. and Alder, B. J. Ground State of the Electron Gas by a Stochastic Method. *Phys. Rev. Lett.* **45,** 566–569 (1980).

[194] Hedin, L. and Lundqvist, B. I. Explicit local exchange-correlation potentials. *J. Phys. C Solid State Phys.* **4,** 2064 (1971).

[195] Barth, U. von and Hedin, L. A local exchange-correlation potential for the spin polarized case. i. *J. Phys. C Solid State Phys.* **5,** 1629 (1972).

[196] Vosko, S. H., Wilk, L. and Nusair, M. Accurate spin-dependent electron liquid correlation energies for local spin density calculations: a critical analysis. *Can. J. Phys.* **58,** 1200–1211 (1980).

[197] Perdew, J. P. and Zunger, A. Self-interaction correction to density-functional approximations for many-electron systems. *Phys. Rev. B* **23,** 5048–5079 (1981).

[198] Becke, A. D. Density-functional exchange-energy approximation with correct asymptotic behavior. *Phys. Rev. A* **38,** 3098–3100 (1988).

[199] Lee, C., Yang, W. and Parr, R. G. Development of the Colle-Salvetti correlation-energy formula into a functional of the electron density. *Phys. Rev. B* **37,** 785–789 (1988).

[200] Perdew, J. P. and Wang, Y. Accurate and simple analytic representation of the electron-gas correlation energy. *Phys. Rev. B* **45,** 13244–13249 (1992).

[201] Perdew, J. P., Burke, K. and Ernzerhof, M. Generalized Gradient Approximation Made Simple. *Phys. Rev. Lett.* **77,** 3865–3868 (1996).

[202] Schoenes, J. Optical properties and electronic structure of UO2. *J. Appl. Phys.* **49,** 1463–1465 (1978).

[203] McNeilly, C. E. The electrical properties of plutonium oxides. *J. Nucl. Mater.* **11,** 53–58 (1964).

[204] Butterfield, M. T. *et al.* Photoemission of surface oxides and hydrides of delta plutonium. *Surf. Sci.* **571,** 74–82 (2004).

[205] Kelly, P. J. and Brooks, M. S. S. Cohesive properties of uranium dioxide. *Phys. BC* **102,** 81–83 (1980).

[206] J. Kelly, P. and S. Brooks, M. S. Electronic structure and ground-state properties of the actinide dioxides. *J. Chem. Soc. Faraday Trans. 2 Mol. Chem. Phys.* **83,** 1189–1203 (1987).

[207] Becke, A. D. Density-functional thermochemistry. III. The role of exact exchange. *J. Chem. Phys.* **98,** 5648–5652 (1993).

[208] Adamo, C. and Barone, V. Toward reliable density functional methods without adjustable parameters: The PBE0 model. *J. Chem. Phys.* **110,** 6158–6170 (1999).

[209] Heyd, J., Scuseria, G. E. and Ernzerhof, M. Hybrid functionals based on a screened Coulomb potential. *J. Chem. Phys.* **118,** 8207–8215 (2003).

[210] Georges, A., Kotliar, G., Krauth, W. and Rozenberg, M. J. Dynamical mean-field theory of strongly correlated fermion systems and the limit of infinite dimensions. *Rev Mod Phys* **68,** 13–125 (1996).

[211] Kotliar, G. *et al.* Electronic structure calculations with dynamical mean-field theory. *Rev. Mod. Phys.* **78,** 865–951 (2006).

[212] Anisimov, V. I., Zaanen, J. and Andersen, O. K. Band theory and Mott insulators: Hubbard U instead of Stoner I. *Phys. Rev. B* **44,** 943–954 (1991).

[213] Mott, N. F. and Friedman, L. Metal-insulator transitions in VO_2, Ti_2O_3 and $Ti_{2-x}V_xO_3$. *Philos. Mag.* **30,** 389–402 (1974).

[214] Hubbard, J. Electron Correlations in Narrow Energy Bands. II. The Degenerate Band Case. *Proc. R. Soc. Lond. Math. Phys. Eng. Sci.* **277,** 237–259 (1964).

[215] Lichtenstein, A. I. and Katsnelson, M. I. Ab initio calculations of quasiparticle band structure in correlated systems: LDA++ approach. *Phys. Rev. B* **57,** 6884–6895 (1998).

[216] Dudarev, S. L., Botton, G. A., Savrasov, S. Y., Humphreys, C. J. and Sutton, A. P. Electron-energy-loss spectra and the structural stability of nickel oxide: An LSDA+*U* study. *Phys. Rev. B* **57,** 1505–1509 (1998).

[217] Amadon, B., Applencourt, T. and Bruneval, F. Screened Coulomb interaction calculations: cRPA implementation and applications to dynamical screening and self-consistency in uranium dioxide and cerium. *Phys. Rev. B* **89,** 125110 (2014).

[218] Kotani, A. and Ogasawara, H. Theory of core-level spectroscopy in actinide systems. *Phys. B Condens. Matter* **186,** 16–20 (1993).

[219] Jomard, G., Amadon, B., Bottin, F. and Torrent, M. Structural, thermodynamic, and electronic properties of plutonium oxides from first principles. *Phys. Rev. B* **78,** 075125 (2008).

[220] Amadon, B., Jollet, F. and Torrent, M. γ and β cerium: LDA+U calculations of ground-state parameters. *Phys. Rev. B* **77,** 155104 (2008).

[221] Wiktor, J. dentification of equilibrium and irradiation-induced defects in nuclear ceramics: electronic structure calculations of defect properties and positron annihilation characteristics. (PhD thesis, Aix-Marseille Université, 2015).

[222] Dorado, B., Amadon, B., Freyss, M. and Bertolus, M. DFT+*U* calculations of the ground state and metastable states of uranium dioxide. *Phys. Rev. B* **79,** 235125 (2009).

[223] Yaguang, L. Modelling of structural and electronic modiffication induced by point defects in mixed oxides of uranium and plutonium. (Internship, CEA of Cadarache, 2015).

[224] Meredig, B., Thompson, A., Hansen, H. A., Wolverton, C. and van de Walle, A. Method for locating low-energy solutions within DFT+*U*. *Phys. Rev. B* **82,** 195128 (2010).

[225] Thompson, A. E. and Wolverton, C. First-principles study of noble gas impurities and defects in UO 2. *Phys. Rev. B* **84,** (2011).

[226] Geng, H. Y., Chen, Y., Kaneta, Y., Kinoshita, M. and Wu, Q. Interplay of defect cluster and the stability of xenon in uranium dioxide from density functional calculations. *Phys. Rev. B* **82,** 094106 (2010).

[227] Gryaznov, D., Heifets, E. and Kotomin, E. The first-principles treatment of the electron-correlation and spin–orbital effects in uranium mononitride nuclear fuels. *Phys. Chem. Chem. Phys.* **14,** 4482–4490 (2012).

[228] Dion, M., Rydberg, H., Schröder, E., Langreth, D. C. and Lundqvist, B. I. Van der Waals Density Functional for General Geometries. *Phys. Rev. Lett.* **92,** 246401 (2004).

[229] Langreth, D. C. *et al.* A density functional for sparse matter. *J. Phys. Condens. Matter* **21,** 084203 (2009).

[230] Monkhorst, H. J. and Pack, J. D. Special points for Brillouin-zone integrations. *Phys. Rev. B* **13,** 5188–5192 (1976).

[231] Milman, V. *et al.* Electronic structure, properties, and phase stability of inorganic crystals: A pseudopotential plane-wave study. *Int. J. Quantum Chem.* **77,** 895–910 (2000).

[232] Kresse, G. and Joubert, D. From ultrasoft pseudopotentials to the projector augmented-wave method. *Phys. Rev. B* **59,** 1758–1775 (1999).

[233] Andersson, D. A., Watanabe, T., Deo, C. and Uberuaga, B. P. Role of di-interstitial clusters in oxygen transport in UO_{2+x} from first principles. *Phys. Rev. B* **80,** 060101 (2009).

[234] Sun, L., Huang, X., Wang, L. and Janotti, A. Disentangling the role of small polarons and oxygen vacancies in CeO_2. *Phys. Rev. B* **95,** 245101 (2017).

[235] Wei, S.-H., Ferreira, L. G., Bernard, J. E. and Zunger, A. Electronic properties of random alloys: Special quasirandom structures. *Phys. Rev. B* **42,** 9622–9649 (1990).

[236] Chandran, M., Subramanian, P. R. and Gigliotti, M. F. First principles calculation of mixing enthalpy of β-Ti with transition elements. *J. Alloys Compd.* **550,** 501–508 (2013).

[237] von Pezold, J., Dick, A., Friák, M. and Neugebauer, J. Generation and performance of special quasirandom structures for studying the elastic properties of random alloys: Application to Al-Ti. *Phys. Rev. B* **81,** 094203 (2010).

[238] Jaros, M. Electronic properties of semiconductor alloy systems. *Rep. Prog. Phys.* **48,** 1091–1154 (1985).

[239] Nordheim, L. Zur Elektronentheorie der Metalle. II. *Ann. Phys.* **401,** 641–678 (1931).

[240] Soven, P. Coherent-Potential Model of Substitutional Disordered Alloys. *Phys. Rev.* **156,** 809–813 (1967).

[241] Mikkelsen, J. C. and Boyce, J. B. Atomic-Scale Structure of Random Solid Solutions: Extended X-Ray-Absorption Fine-Structure Study of $Ga_{1-x}In_xAs$. *Phys. Rev. Lett.* **49,** 1412–1415 (1982).

[242] Metropolis, N. and Ulam, S. The Monte Carlo Method. *J. Am. Stat. Assoc.* **44,** 335–341 (1949).

[243] Takoukam, T. C. and Bourasseau, E. On going PhD at the CEA of Cadarache, DEC/SESC/LM2C, supervised by Emeric Bourasseau. (2017).

[244] Bourasseau, E. *CEA technical report*. DEC/SESC/LLCC, NT 17-011 (2017).

[245] Car, R. and Parrinello, M. Unified Approach for Molecular Dynamics and Density-Functional Theory. *Phys. Rev. Lett.* **55,** 2471–2474 (1985).

[246] Andersen, H. C. Molecular dynamics simulations at constant pressure and/or temperature. *J. Chem. Phys.* **72,** 2384–2393 (1980).

[247] Hoover, W. G. Canonical dynamics: Equilibrium phase-space distributions. *Phys. Rev. A* **31,** 1695–1697 (1985).

[248] Parrinello, M. and Rahman, A. Polymorphic transitions in single crystals: A new molecular dynamics method. *J. Appl. Phys.* **52,** 7182–7190 (1981).

[249] Nosé, S. and Klein, M. L. Constant pressure molecular dynamics for molecular systems. *Mol. Phys.* **50,** 1055–1076 (1983).

[250] Taylor, S. E. and Bruneval, F. Understanding and correcting the spurious interactions in charged supercells. *Phys. Rev. B* **84,** 075155 (2011).

[251] Leslie, M. and Gillan, N. J. The energy and elastic dipole tensor of defects in ionic crystals calculated by the supercell method. *J. Phys. C Solid State Phys.* **18,** 973 (1985).

[252] Lany, S. and Zunger, A. Accurate prediction of defect properties in density functional supercell calculations. *Model. Simul. Mater. Sci. Eng.* **17,** 084002 (2009).

[253] Guéneau, C., Baichi, M., Labroche, D., Chatillon, C. and Sundman, B. Thermodynamic assessment of the uranium–oxygen system. *J. Nucl. Mater.* **304,** 161–175 (2002).

[254] Guéneau, C., Chatillon, C. and Sundman, B. Thermodynamic modelling of the plutonium–oxygen system. *J. Nucl. Mater.* **378,** 257–272 (2008).

[255] Wang, L., Maxisch, T. and Ceder, G. Oxidation energies of transition metal oxides within the GGA+*U* framework. *Phys. Rev. B* **73,** 195107 (2006).

[256] Kurth, S., Perdew, J. P. and Blaha, P. Molecular and Solid-State Tests of Density Functional Approximations: LSD, GGAs, and Meta-GGAs. *Int. J. QUANTUM Chem.* **75,** 21

[257] Osborne, D. W. and Westrum, E. F. The Heat Capacity of Thorium Dioxide from 10 to 305°K. The Heat Capacity Anomalies in Uranium Dioxide and Neptunium Dioxide. *J. Chem. Phys.* **21,** 1884–1887 (1953).

[258] Ross, J. W. and Lam, D. J. The Magnetic Susceptibility of Neptunium Oxide and Carbide between 4.2° and 350°K. *J. Appl. Phys.* **38,** 1451–1453 (1967).

[259] Tabuteau, A., Jové, J., Pagès, M., de Novion, C. H. and Gal, J. Mössbauer and magnetization studies of the $U_{1-x}Np_xO_2$ fluorites. *Solid State Commun.* **50,** 357–361 (1984).

[260] Tabuteau, A. *et al.* Neutron diffraction study on $U_{0.5}Np_{0.5}O_2$ at low temperatures. *J. Phys. Lett.* **45,** 373–378 (1984).

[261] Boeuf, A. *et al.* Neutron Diffraction Study of the $U_{1-x}Np_xO_2$ Fluorites. *Europhys. Lett.* **3,** 221 (1987).

[262] Haas, P., Tran, F. and Blaha, P. Calculation of the lattice constant of solids with semilocal functionals. *Phys. Rev. B* **79,** (2009).

[263] Murray, É. D., Lee, K. and Langreth, D. C. Investigation of Exchange Energy Density Functional Accuracy for Interacting Molecules. *J. Chem. Theory Comput.* **5,** 2754–2762 (2009).

[264] Le Page, Y. and Saxe, P. Symmetry-general least-squares extraction of elastic data for strained materials from *ab initio* calculations of stress. *Phys. Rev. B* **65,** (2002).

[265] Wu, X., Vanderbilt, D. and Hamann, D. R. Systematic treatment of displacements, strains, and electric fields in density-functional perturbation theory. *Phys. Rev. B* **72,** (2005).

[266] Martin, D. G. The elastic constants of polycrystalline UO_2 and (U, Pu) mixed oxides: a review and recommendations. *High temperatures-High pressures* **21,** 13–24 (1989).

[267] Dridi, Z., Bouhafs, B. and Ruterana, P. First-principles investigation of lattice constants and bowing parameters in wurtzite $Al_xGa_{1-x}N$, $In_xGa_{1-x}N$ and $In_xAl_{1-x}N$ alloys. *Semicond. Sci. Technol.* **18,** 850 (2003).

[268] Iliopoulos, E., Adikimenakis, A., Giesen, C., Heuken, M. and Georgakilas, A. Energy bandgap bowing of InAlN alloys studied by spectroscopic ellipsometry. *Appl. Phys. Lett.* **92,** 191907 (2008).

[269] Huber, E. J. and Holley, C. E. Enthalpies of formation of triuranium octaoxide and uranium dioxide. *J. Chem. Thermodyn.* **1,** 267–272 (1969).

[270] Johnson, G. K., Van Deventer, E. H., Kruger, O. L. and Hubbard, W. N. The enthalpies of formation of plutonium dioxide and plutonium mononitride. *J. Chem. Thermodyn.* **1,** 89–98 (1969).

[271] Chereau, P., Déan, G., De Franco, M. and Gerdanian, P. High-temperature microcalorimetric measurements of partial molar enthalpy of solution, $\Delta H(O_2)$, in plutonium + oxygen. *J. Chem. Thermodyn.* **9,** 211–219 (1977).

[272] Moellmann, J., Ehrlich, S., Tonner, R. and Grimme, S. A DFT-D study of structural and energetic properties of TiO_2 modifications. *J. Phys. Condens. Matter* **24,** 424206 (2012).

[273] Zhang, G.-X., Tkatchenko, A., Paier, J., Appel, H. and Scheffler, M. van der Waals Interactions in Ionic and Semiconductor Solids. *Phys. Rev. Lett.* **107,** 245501 (2011).

[274] Sluiter, M. H. F. and Kawazoe, Y. Prediction of the mixing enthalpy of alloys. *EPL Europhys. Lett.* **57,** 526 (2002).

[275] Martin, P. *et al.* A XAS study of the local environments of cations in $(U, Ce)O_2$. *J. Nucl. Mater.* **312,** 103–110 (2003).

[276] Szpunar, B. and Szpunar, J. A. Theoretical investigation of structural and thermo-mechanical properties of thoria up to 3300 K temperature. *Solid State Sci.* **36,** 35–40 (2014).

[277] Wu, Z. and Cohen, R. E. More accurate generalized gradient approximation for solids. *Phys. Rev. B* **73,** (2006).

[278] Nakamura, H. and Machida, M. High-temperature properties of thorium dioxide: A first-principles molecular dynamics study. *J. Nucl. Mater.* **478,** 56–60 (2016).

[279] Vauchy, R. *et al.* Impact of the cation distribution homogeneity on the americium oxidation state in the $U_{0.54}Pu_{0.45}Am_{0.01}O_{2-x}$ mixed oxide. *J. Nucl. Mater.* **456,** 115–119 (2015).

[280] Plata, J. J., Márquez, A. M. and Sanz, J. F. Electron Mobility via Polaron Hopping in Bulk Ceria: A First-Principles Study. *J. Phys. Chem. C* **117,** 14502–14509 (2013).

[281] Gouder, T., Seibert, A., Havela, L. and Rebizant, J. Search for higher oxides of Pu: A photoemission study. *Surf. Sci.* **601,** L77–L80 (2007).

[282] Teske, K., Ullmann, H. and Rettig, D. Investigation of the oxygen activity of oxide fuels and fuel-fission product systems by solid electrolyte techniques. Part I: Qualification and limitations of the method. *J. Nucl. Mater.* **116,** 260–266 (1983).

[283] Vathonne, E., Wiktor, J., Freyss, M., Jomard, G. and Bertolus, M. DFT+*U* investigation of charged point defects and clusters in UO_2. *J. Phys. Condens. Matter* **26,** 325501 (2014).

[284] Crocombette, J.-P. Influence of charge states on energies of point defects and clusters in uranium dioxide. *Phys. Rev. B* **85,** 144101 (2012).

[285] Sari, C., Benedict, U. and Blank, H. A study of the ternary system $U0_2$-$Pu0_2$-Pu_20_3. *J. Nucl. Mater.* **35,** 267–277 (1970).

[286] Guéneau, C. *et al.* Thermodynamic modelling of advanced oxide and carbide nuclear fuels: Description of the U–Pu–O–C systems. *J. Nucl. Mater.* **419,** 145–167 (2011).

[287] Dorado, B. *et al.* First-principles calculation and experimental study of oxygen diffusion in uranium dioxide. *Phys. Rev. B* **83,** 035126 (2011).

[288] Dorado, B. *et al.* First-principles calculations of uranium diffusion in uranium dioxide. *Phys. Rev. B* **86,** 035110 (2012).

[289] Zinkevich, M., Djurovic, D. and Aldinger, F. Thermodynamic modelling of the cerium–oxygen system. *Solid State Ion.* **177,** 989–1001 (2006).

[290] Sørensen, O. T. Thermodynamic studies of the phase relationships of nonstoichiometric cerium oxides at higher temperatures. *J. Solid State Chem.* **18,** 217–233 (1976).

[291] Markin, T. L., Street, R. S. and Crouch, E. C. The uranium-cerium-oxygen ternary phase diagram. *J. Inorg. Nucl. Chem.* **32,** 59–75 (1970).

[292] Lorenzelli, R. and Touzelin, B. Sur le système UO_2-CeO_2; étude cristallographique à haute température. *J. Nucl. Mater.* **95,** 290–302 (1980).

[293] Geneste, G., Amadon, B., Torrent, M. and Dezanneau, G. DFT+*U* study of self-trapping, trapping, and mobility of oxygen-type hole polarons in barium stannate. *Phys. Rev. B* **96,** 134123 (2017).

[294] Burr, P. A. and Cooper, M. W. D. Importance of elastic finite-size effects: Neutral defects in ionic compounds. *Phys. Rev. B* **96,** 094107 (2017).

[295] Grimes, R. W. Simulating the Behaviour of Inert Gases in UO_2. in *Fundamental Aspects of Inert Gases in Solids* 415–429 (Springer, Boston, MA, 1991). doi:10.1007/978-1-4899-3680-6_36

[296] Kheradmand Saadi, M., Shahriari, M. and Zolfaghari, A. R. Xenon transient simulation of the VVER-1000 nuclear reactor using adiabatic approximation. *Ann. Nucl. Energy* **37,** 753–761 (2010).

[297] Kuganathan, N., Ghosh, P. S., Arya, A. and Grimes, R. W. Helium trapping and clustering in ThO_2. *J. Nucl. Mater.* (2018). doi:10.1016/j.jnucmat.2018.05.006

[298] Garrido, F., Nowicki, L., Sattonnay, G., Sauvage, T. and Thomé, L. Lattice location of helium in uranium dioxide single crystals. *Nucl. Instrum. Methods Phys. Res. Sect. B Beam Interact. Mater. At.* **219–220,** 196–199 (2004).

[299] Roudil, D. *et al.* Diffusion of radiogenic helium in natural uranium oxides. *J. Nucl. Mater.* **378,** 70–78 (2008).

[300] Vathonne, E. *et al.* Determination of Krypton Diffusion Coefficients in Uranium Dioxide Using Atomic Scale Calculations. *Inorg. Chem.* **56,** 125–137 (2017).

[301] Kuganathan, N. *et al.* Fission gas in thoria. *J. Nucl. Mater.* **485,** 47–55 (2017).

[302] Brillant, G., Gupta, F. and Pasturel, A. Fission products stability in uranium dioxide. *J. Nucl. Mater.* **412,** 170–176 (2011).

[303] Nerikar, P. V. *et al.* Thermodynamics of fission products in $UO_{2\pm x}$. *J. Phys. Condens. Matter* **21,** 435602 (2009).

[304] Bertolus, M., Major, M. and Brenner, V. Assessment of density functional theory for bonds formed between rare gases and open-shell atoms: a computational study of small molecules containing He, Ar, Kr and Xe. *Phys. Chem. Chem. Phys.* **14,** 553–561 (2011).

[305] "CAPACITE CALORIFIQUE MOLAIRE A PRESSION CONSTANTE |," 11-Sep-2018. [Online]. Available: http://www.edu.upmc.fr/chimie/lc101-202-301/communs/public/ capcalo.htm . [Accessed: 11-Sep-2018].

[306] Sanati, M., R. Albers, T. Lookman, A. Saxena. Elastic constants, phonon density of states, and thermal properties of UO_2, *Physical Review B*, **84**, 014116(2011)

[307] Wang, B.-T., P. Zhang, R. Lizárraga, I. Di Marco, O. Eriksson., *Physical Review B*, **88**, 104107(2013)

[308] Jones, W. M., Gordon, J and Long, E. A. The Heat Capacities of Uranium, Uranium Trioxide, and Uranium Dioxide from 15°K to 300°K ., *J. Chem. Phys*. **20**, 695 (1952).

[309] Howard, E. F and Harold, R. L .The heat capacity and thermodynamic functions of uranium from 5 to 350°K., *J. Phys. Chem.*, **64** , 904–906 (1960)

Annex:

Evaluation of the variation of the enthalpy of formation of UO_2 between 0 K and 300 K

The enthalpy of formation of UO_2 at a given temperature T is:

$$\Delta H_f^{UO_2}(T) = H^{UO_2}(T) - H^U(T) - H^{O_2}(T)$$

Where, , $H^{UO_2}(T)$ is the enthalpy of UO_2, $H^U(T)$ the enthalpy of U and $H^{O_2}(T)$ the enthalpy of O_2 molecule at temperature T.

The variation of the enthalpy of formation between 0 K and a given temperature T can be written as follows:

$$\Delta H_f^{UO_2}(T) - \Delta H_f^{UO_2}(0) = H^{UO_2}(T) - H^{UO_2}(T) - (H^U(T) - H^U(0)) - (H^{O_2}(T) - H^{O_2}(0))$$

$$\Delta H_f^{UO_2}(T) - \Delta H_f^{UO_2}(0) = \Delta H^{UO_2}(T) - \Delta H^U(T) - \Delta H^{O_2}(T)$$

$$\Delta H_f^{UO_2}(T) - \Delta H_f^{UO_2}(0) = \int_0^T C_p^{UO_2} d\theta - \int_0^T C_p^U d\theta - \int_0^T C_p^{O_2} d\theta$$

Thus, the variation of the enthalpy of formation of UO_2 between 0 K and 300 K can be calculated if the expressions of the heat capacities of UO_2, U and O_2 with temperature are known.

For the oxygen molecule O_2, the interrelation between the heat capacity and temperature is known [305], and given by the following equation:

$C_p^{O_2}(T) \approx 25.73 + 12.97\text{x}10^{-3}T - 3.77\text{x}10^{-6}T^2$ (J.mol^{-1}.K^{-1}),

So that $\int_0^T C_p^{O_2} d\theta = 25.73T + 6.45\text{x}10^{-3}T^2 - 1.2567\text{x}10^{-6}T^3$ (J. mol^{-1})

For the uranium dioxide, the heat capacity can be approximated as a linear function of the temperature up to room temperature,, as shown for UO_2 by Sanati *et al*. [306] and Wand *et al*. [307] through phonon calculations using LDA+*U* and GGA+*U*, and from experimental data at low temperature [308].

We can therefore write $C_p^{UO_2}(T) \approx aT + b$

Since $C_p^{UO_2}(0) = 0$ and $C_p^{UO_2}(298.15\ K) = 63.98\ J.mol^{-1}.K^{-1}$

$$a = 0.2146 \ and \ \ b = 0$$

And

$$C_p^{UO_2}(T) \approx 0.2198T$$

So that $\int_0^T C_p^{UO_2} d\theta = 0.1073T^2$ J.mol^{-1}

Using the same expression for metallic U, we have

$C_p^U(T) \approx a^U T + b^U$

$C_p^U(0) = 0$ and $C_p^U(300\ K) = 27.6939\ J.mol^{-1}.K^{-1}$ from Ref. [309]

$$a^U = 0.092313 \ and \ \ b^U = 0$$

So that $\int_0^T C_p^U d\theta = 0.04616T^2$ J.mol^{-1},

Finally,

$\Delta H_f^{UO_2}(T) - \Delta H_f^{UO_2}(0) = -25.73T + (0.1073 - 0.04616 - 6.45\text{x}10^{-3})T^2 + 1.2567\text{x}10^{-6}T^3$ (in J.mol^{-1})

At 300 K, we have $\Delta H_f^{UO_2}(300K) - \Delta H_f^{UO_2}(0) = -2762{,}9691\ J.mol^{-1} = -0.029\ eV$

This difference is less than 0.3 % of $\Delta H_f^{UO_2}(300K)$. The energetic properties of UO_2 and more generally of actinide oxides calculated at 0K can therefore be considered good approximations of room temperature properties.